Delft University of Technology

Sorption enhanced CO_2 methanation for large scale energy storage
Catalyst and Process development

Wei, L.

DOI
10.4233/uuid:e6d8a29b-0e7f-4093-b007-027b23e40b3f

Publication date
2022

Document Version
Final published version

Citation (APA)
Wei, L. (2022). *Sorption enhanced CO_2 methanation for large scale energy storage: Catalyst and Process development*. [Dissertation (TU Delft), Delft University of Technology]. https://doi.org/10.4233/uuid:e6d8a29b-0e7f-4093-b007-027b23e40b3f

Important note
To cite this publication, please use the final published version (if applicable).
Please check the document version above.

Copyright
Other than for strictly personal use, it is not permitted to download, forward or distribute the text or part of it, without the consent of the author(s) and/or copyright holder(s), unless the work is under an open content license such as Creative Commons.

Takedown policy
Please contact us and provide details if you believe this document breaches copyrights.
We will remove access to the work immediately and investigate your claim.

This work is downloaded from Delft University of Technology.
For technical reasons the number of authors shown on this cover page is limited to a maximum of 10.

Sorption enhanced CO_2 methanation for large scale energy storage

Catalyst & Process development

Liangyuan WEI
魏良元

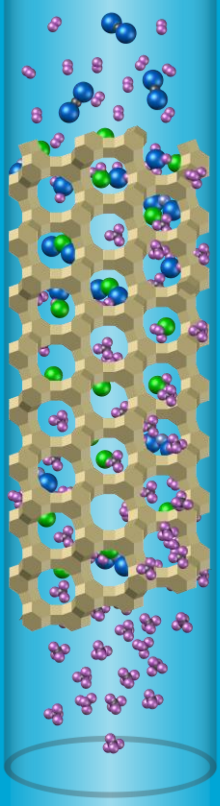

TUDelft Delft University of Technology

Sorption enhanced CO_2 methanation for large scale energy storage

Catalyst & Process development

Liangyuan WEI
魏良元

Sorption enhanced CO_2 methanation for large scale energy storage

Catalyst & Process development

Dissertation

for the purpose of obtaining the degree of doctor
at Delft University of Technology,
by the authority of the Rector Magnificus, prof.dr.ir. T.H.J.J. van der Hagen,
Chair of the Board for Doctorates
to be defended publicly on
Wednesday 4 May 2022 at 12:30 o'clock

by

Liangyuan WEI

Master of Engineering in Thermal Engineering,
Huazhong University of Science and Technology, China,
born in Huaihua, Hunan Province, China.

This dissertation has been approved by the promotors:
Prof. dr. ir. W. de Jong, Delft University of Technology, The Netherlands
Prof. dr. H. Grénman, Åbo Akademi University, Finland

Composition of the doctoral committee:

Rector Magnificus,	chairperson
Prof. dr. ir. W. de Jong	Delft University of Technology, promotor
Prof. dr. H. Grénman	Åbo Akademi University, copromotor

Independent members:

Prof. dr. A. Urakawa	Delft University of Technology
Prof. dr. ir. H.J. Heeres	University of Groningen
Prof. dr.-Ing. H. Spliethoff	Technical University of Munich, Germany
Prof. dr. ir. D.W.F. Brilman	Twente University
Prof. dr. J.J.C. Geerlings	Delft University of Technology, reserve member

Other member:

Dr. W. Haije	Delft University of Technology, supervisor

The research described in this thesis was conducted in the Large-Scale Energy Storage section of the Process and Energy Department, Faculty of Mechanical, Maritime and Materials Engineering (3mE) of the Delft University of Technology, and co-financed by the China Scholarship Council (CSC).

Keywords: Large scale energy storage, CO_2 methanation, zeolite, sorption enhanced
Printed by: Ipskamp Printing, The Netherlands

Copyright © 2022 by Liangyuan Wei
Cover design by Liangyuan Wei

ISBN 978-94-6421-730-8

An electronic version of this dissertation is available at
http://repository.tudelft.nl/.

格物致知 [1]

Explore the principles of things, gain wisdom and perception

Contents

Summary

Hydrogen produced by the electrolysis of water using sustainable electricity, will play an increasingly important role as an energy and a feedstock vector. Shifting from fossil to renewable resources means that new industrial platforms have to be set up to provide carbon-based fuels and bulk base chemicals to replace the current fossil resources based routes. The global demand cannot be met by indirect use of carbon dioxide via biomass necessitating the use from point sources or direct air capture, which changes the value of CO_2 from waste to commodity chemical. The production of chemicals by hydrogenation of CO_2 is typically hampered by the thermodynamic conversion being far from 100% under currently viable reaction conditions. The equilibrium can, however, be shifted to increase conversion by removing one of the reaction products, namely water, from the reaction mixture with sorbents like zeolites. Prerequisite to conversion enhancement and process intensification is the close proximity of sorption and catalytic sites. **Chapter 1** is the introduction, which presents the state of the art in synthesis and application of these, in fact, bi-functional materials.

In **Chapter 2**, zeolite 13X and 5A supported Ni catalysts were utilized, which synthesized for CO_2 methanation using the evaporation impregnation method. The influence of using different Ni precursors (nitrate, citrate, and acetate) as well as calcination temperatures on the catalyst properties and performance were investigated in this chapter. Using nickel citrate and acetate resulted in smaller NiO particle sizes compared to nitrate. STEM-EDX results showed that all the Ni-precursor complexes entered more efficiently the 13X zeolite structure, which is mainly due to steric hindrance resulting from the smaller pore size of 5A. Methanation experiments revealed that the 13X catalysts synthesized using nickel citrate displayed clearly higher activity, compared to the catalysts synthesized using nickel nitrate or nickel acetate. It can be concluded from this chapter, that the Ni precursor significantly influences the physico-chemical characteristics and catalytic properties of Ni 13X and Ni 5A zeolite catalysts in CO_2 methanation: complex size and pore size matter.

Chapter 3 describes zeolites 13X and 5A that were modified with nickel and/or ruthenium for CO_2 methanation, in order to study if the catalytic efficiency could be enhanced by introducing of ruthenium which is a commonly active metal towards hydrogenation. The physico-chemical characterization results showed that the zeolites structure did not change after the Ni, Ru modification. Ni was able to enter the pores of

13X, in the other cases an egg shell type structure was formed. Methanation experimental results showed that the mono-metallic catalysts outperformed the bi-metallic ones with Ni being the more active. One of the factors influencing the performance of the bi-metallic catalysts was that it was difficult to obtain good dispersion when both metals were present. Also, the morphology of the catalyst influenced significantly the selectivity. The catalysts with lower weak acidity displayed higher activity. The catalyst 2.5%Ru13X and 5%Ni13X showed good catalytic stability with around 97% CH_4 selectivity at 360 °C, with no catalyst deactivation during a 200 h catalyst stability test.

Chapter 4 deals with sub-nanometer zeolite 13X-supported Ni-ceria catalysts, which were synthesized for CO_2 methanation. XRD and SEM results showed that the structure and morphology of 13X zeolite did not change after impregnation and calcination. Ce loading affected the catalysts' metal dispersion, reducibility, basicity and acidity, and hence their activity and selectivity. STEM-EDX elemental mappings showed that Ce and Ni were predominantly highly dispersed. Ce had a positive effect on the reduction of NiO and lead to a relatively high number of medium basic sites with a low Ce loading. Highly stable 5%Ni2.5%Ce13X displayed high activity and nearly 100% CH_4 selectivity in CO_2 methanation at 360 °C, which was mainly attributed to the high dispersion of metals and relatively high amount of medium basic sites. It can be inferred from this chapter that this catalyst synthesis strategy has great potential for obtaining high metal dispersion, since metal uptake by the zeolite is selective for the metal citrate complexes in solution.

A highly dispersed and active Ce promoted Ni 13X zeolite bi-functional material was prepared by evaporation impregnation in **Chapter 5**. Methanation was in this chapter shown to be a durable large-scale option for CO_2 utilization, and it is one of the solutions for decreasing carbon emission and producing synthetic green methane. A long-term experimental study employing 5%Ni5A, 5%Ni13X, 5%NiL and 5%Ni2.5%Ce13X bifunctional materials with both catalytic and water adsorption properties was performed in a fixed bed reactor. The overall performance of the bifunctional materials decreased going from 5%Ni2.5%Ce13X, 5%Ni13X, 5%Ni5A, to 5% NiL. The highest obtained CO_2 conversion and CH_4 selectivity were close to 100 % during prolonged stability testing in 100 reactive adsorption – desorption cycles amounting to 203 hours in total with 5%Ni2.5%Ce13X. The catalytic activity remained stable and only a slight decrease in the water uptake capacity was observed at relatively low temperature.

Chapter 6 focuses on determining the kinetics of a nickel on zeolite 13X catalyst in comparison with a nickel catalyst on a meso-porous γ-Al_2O_3 support. In this chapter, the validity of the obtained rate equation is discussed. Both catalysts were prepared using incipient wetness impregnation. The results showed that 13X zeolite supported nickel catalyst was more active compared to the one supported on γ-Al_2O_3. This is mainly due to a better dispersion of nickel on the 13X zeolite catalyst. The results furthermore showed that there is no big difference between the two catalysts: the methane partial pressure has no influence on the CO_2 methanation kinetics, the most noticeable but small difference is in the water partial pressure exponent in the derived rate expressions.

Finally, **Chapter 7** provides the overall conclusions of the studies reported in this thesis. Recommendations for further research are also provided.

Samenvatting

Waterstof, geproduceerd door middel van elektrolyse van water, zal in toenemende mate een belangrijke rol spelen als energiedrager en voeding voor verdere conversie. De overgang van fossiele naar hernieuwbare grondstoffen impliceert dat nieuwe industriële platforms moeten worden opgezet voor de voorziening van op koolstof gebaseerde brandstoffen en bulk basischemicaliën ter vervanging van de huidige op fossiele grondstoffen gebaseerde routes. De mondiale vraag kan niet worden voorzien door indirect gebruik van koolstofdioxide via biomassa, waardoor het noodzakelijk is CO_2 te gebruiken uit puntbronnen of door vangst uit de lucht, hetgeen de waarde van CO_2 verandert van een afvalproduct in een gangbare chemische grondstof. De productie van chemicaliën door hydrogenering van CO_2 wordt normaalgesproken gelimiteerd door de conversie bij chemisch evenwicht, welke verre van 100% is onder de huidige toegepaste reactiecondities. Het evenwicht kan echter worden verschoven waarbij de conversie toeneemt door het verwijderen van één van de reactieproducten, water, uit het reactiemengsel met sorbentia zoals zeolieten. Voorwaarde voor deze conversieverbetering en de gerelateerde procesintensificatie is de dichte nabijheid van sorptie- en katalyseplaatsen. **Hoofdstuk 1** is de introductie, welke de “state of the art” in synthese en toepassing van deze feitelijk bi-functionele materialen weergeeft.

In **Hoofdstuk 2** zijn Nikkel op zeolieten 13X en 5A als drager toegepast, gesynthetiseerd voor CO_2 methanisatie gebruikmakend van de verdampingsimpregnatie (“evaporation impregnation”) methode. De invloed van het gebruik van verschillende Nikkel precursoren (nitraat, citraat en acetaat) alsmede calcineringstemperaturen op de katalysatoreigenschappen en –performance zijn in dit hoofdstuk nader bestudeerd. Het gebruik van Nikkelcitraat en –acetaat resulteerde in kleinere NiO deeltjesgroottes in vergelijking met nitraat. STEM-EDX resultaten tonen aan dat alle Ni-precursor complexen efficiënter de 13X zeolietstructuur binnendringen, hetgeen vooral het gevolg is van sterische hindering welke weer het gevolg is van de kleinere poriegrootte van 5A. Methaniseringsexperimenten tonen aan dat de 13X katalysatoren gesynthetiseerd op basis van Nikkelcitraat een duidelijk hogere activiteit hebben in vergelijking met de katalysatoren gesynthetiseerd met Nikkelnitraat en –acetaat. Uit dit hoofdstuk kan worden geconcludeerd, dat de Nikkelprecursor een significante invloed heeft op de fysisch-chemische en katalytische karakteristieken van Ni-13X en 5A zeoliet katalysatoren in CO_2 methanisering: grootte van het complex en poriegroottes zijn van belang.

Hoofdstuk 3 beschrijft de zeolieten 13X en 5A, gemodificeerd met Nikkel en/of Ruthenium voor CO_2 methanisering, met als doel te bestuderen of de katalytische efficiëntie kan worden verbeterd door introductie van Ruthenium, hetgeen een gebruikelijk actief metaal is voor hydrogeneringsreakties. De fysisch-chemische karakteriseringsresultaten tonen aan dat de zeolietstructuur niet verandert na de Ni, Ru modificatie. Ni is in staat om de poriën van 13X binnen te dringen; in de andere gevallen wordt een eierschaalstructuur gevormd. Experimentele methaniseringsresultaten tonen aan dat de mono-metallische katalysatoren beter zijn dan de bi-metallische, waarbij Ni het meer actieve materiaal is. Eén van de factoren die de performance van de bi-metallische katalysatoren beïnvloedt, is dat het lastig is om een goede dispersie te verkrijgen bij aanwezigheid van beide metalen. Ook heeft de morfologie een significante invloed op de selectiviteit. De katalysatoren met lagere zwakke zuurgraad vertonen een hogere activiteit. De katalysatoren 2.5%Ru13X en 5%Ni13X laten een goede katalytische stabiliteit zien met rond 97% CH_4 selectiviteit bij 360 °C zonder katalytische deactivering gedurende een 200 uur durende stabiliteitstest.

Hoofdstuk 4 behandelt de katalysatoren bestaande uit sub-nanometer Ni-Cerium op zeoliet 13X drager, welke zijn gesynthetiseerd voor CO_2 methanisering. XRD en SEM resultaten tonen aan dat de structuur en morfologie van 13X zeoliet niet verandert na impregnatie en calcinatie. Ce-belading beïnvloedt de katalysator metaaldispersie, reduceerbaarheid, basiciteit en zuurgraad, en daarom hun activiteit en selectiviteit. STEM-EDX met weergave van de verdeling van de elementen toont aan dat Ce en Ni vooral een hoge dispersiegraad hebben. Ce heeft een positief effect op de reductie van NiO en leidt tot een relatief hoog aantal van matig-basische “sites” met een lage Ce belading. 5%Ni2.5%Ce13X met hoge stabiliteit vertoont een hoge activiteit en bijna 100% CH_4 selectiviteit in CO_2 methanisering bij 360 °C, hetgeen vooral kan worden toegeschreven aan de hoge dispersie van metalen en de relatief grote hoeveelheid aan matig-basische “sites”. Uit dit hoofdstuk kan worden afgeleid dat deze synthese strategie voor de katalysator groot potentieel heeft voor het realiseren van een hoge metaaldispersie, aangezien metaalopname door het zeolietmateriaal selectief is voor de metaalcitraat complexen in oplossing.

Een actief Ce gepromoot Ni-13X zeoliet bi-functioneel materiaal met hoge dispersiegraad is gesynthetiseerd door verdampingsimpregnatie (“evaporation impregnation”) in **Hoofdstuk 5**. In dit hoofdstuk wordt aangetoond dat methanisering een duurzame, grootschalige optie is voor CO_2 gebruik, en het is één van de oplossingen voor het reduceren van koolstofemissies en het produceren van synthetische groene methaan. Een experimentele studie van lange duur, gebruikmakend van 5%Ni5A, 5%Ni13X, 5%NiL en 5%Ni2.5%Ce13X bi-functionele materialen met zowel katalytische als watersorptie eigenschappen is uitgevoerd in een vastbed reactor. De totale performance van de bi-functionele materialen neemt af in de volgorde 5%Ni2.5%Ce13X, 5%Ni13X, 5%Ni5A en 5% NiL. De maximaal verkregen CO_2 conversie en CH_4 selectiviteit benaderden 100 % gedurende een langdurige stabiliteitstest van 203 uren in totaal met 100 reactieve adsorptie – desorptie cycli met 5%Ni2.5%Ce13X. De katalytische activiteit bleef stabiel en enkel een geringe afname in de wateropname capaciteit is waargenomen bij een relatief lage temperatuur.

Hoofdstuk 6 richt de focus op de bepaling van de kinetiek van een Nikkel op zeoliet 13X katalysator in vergelijking met een Nikkel katalysator op een meso-poreuze γ-Al_2O_3 drager. In dit hoofdstuk wordt de validiteit van de verkregen reaktiesnelheidsvergelijking bediscussieerd. Beide katalysatoren zijn bereid op basis van de “incipient wetness” impregnatietechniek. De resultaten tonen aan dat de Nikkel katalysator op 13X zeoliet drager meer actief is in vergelijking met de katalysator op γ-Al_2O_3 drager. Dit is vooral het gevolg van een betere dispersie van Nikkel op de 13X zeoliet katalysator. Verder laten de resultaten zien, dat er geen groot verschil is tussen de twee katalysatoren: de partiaaldruk van methaan heeft geen invloed op de CO_2 methaniseringskinetiek; het meest in het oog springende maar kleine verschil is gelegen in de water partiaalspanningsexponent in de afgeleide reaktiesnelheidsvergelijkingen.

Tenslotte worden in **Hoofdstuk 7** de conclusies gepresenteerd van de studies die in dit proefschrift zijn gerapporteerd. Tevens worden in dit hoofdstuk de aanbevelingen gegeven voor verder onderzoek.

1

Introduction

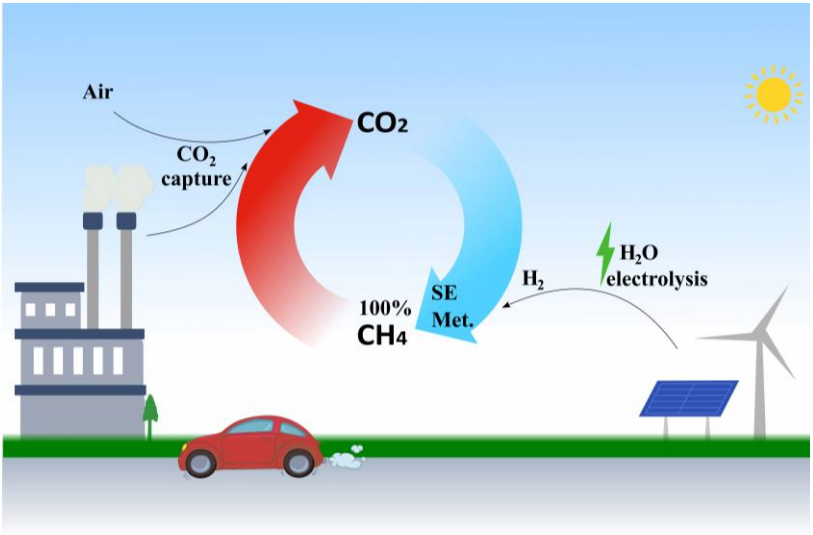

Keywords of this chapter:
Separation enhanced CO_2 hydrogenation,
zeolite catalyst,
bi-functional materials,
methane,
large scale green base chemicals.

This chapter is based on the following publication:
Liangyuan Wei, Wim Haije, Henrik Grénman, Wiebren de Jong, Sorption enhanced catalysis for CO_2 hydrogenation towards fuels and chemicals with focus on methanation (book chapter of Heterogeneous Catalysis: Materials and Applications), Elsevier (Accepted for publication).

1.1. Background

The combustion of fossil fuels is the major source of carbon emissions to the environment [2]. To achieve the goal of reducing carbon emissions according to the Paris agreement, the use of fossil fuels should be radically diminished as a source for energy and chemicals [3, 4]. This results in CO_2 and H_2 becoming increasingly important feedstock for the fuels and chemical industry, with hydrogen being produced by renewable electricity e.g. solar or wind power [5, 6].

Shifting from fossil to renewable resources means that a new industrial platform has to be developed to provide carbon-based fuels and large-scale base chemicals to replace the current petrochemical routes. The global demand cannot be met to a sufficient extent solely by indirect use of carbon dioxide via biomass, necessitating the direct use from point sources or direct air capture. This increases the value of CO_2 from waste to a commodity chemical. The production of chemicals by hydrogenation of CO_2 (Figure 1.1) is a promising way of CO_2 mitigation [7-10], and also a possible solution for large scale energy storage to cope with the intermittent nature of wind and solar sources as well as the energy demand fluctuations [7].

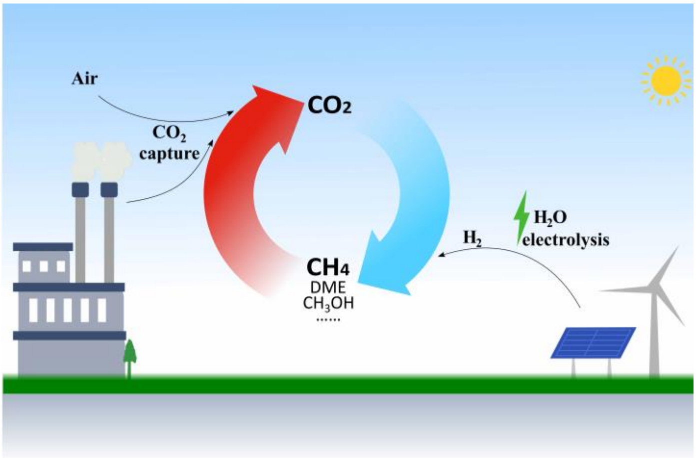

Figure 1.1: A schematic of carbon cycle with CO_2 utilization by hydrogenation, produce methane.

Several routes have been developed for CO_2 utilization through hydrogenation. Typical products include base and intermediary chemicals such as methane, methanol, formic acid, and dimethyl ether [2, 11, 12]. The current doctoral thesis mainly focused on CO_2 methanation, even though the developed technology can be applied also for other products, which is why also they are briefly mentioned.

Methanol is an important and widely used liquid fuel and base chemical, around 95 million tons of methanol was produced in the world in 2019 [13]. The methanol synthesis from CO_2 hydrogenation is thermodynamically limited and more favorable at high pressure [14-16]. Around 700000-800000 tons of formic acid is produced per year in the world, CO_2 hydrogenation to synthesize formic acid is an important route for formic acid production [17]. Dimethyl ether is an excellent fuel substituent for diesel and Liquefied Petroleum Gas [18] and the dimethyl ether global market was around 20 million tons in 2020 [19]. What is more, 3929.2 billion cubic metres methane (natural gas) was consumed in 2019 worldwide [20].

The CO_2 methanation reaction (Sabatier reaction (1-1)) was discovered in 1902 by Sabatier and Senderens [21]. CO_2 hydrogenation to produce methane (1-1) has great potential as energy carrier [9], which stems from the benefits of combining renewable hydrogen produced with wind or solar power, for instance with CO_2 from traditional stack emissions such as power plants, biomass conversion [22], or even air capture combined with the ease of distribution of the renewable methane in existing infrastructure. Moreover, CO_2 methanation has a higher energetic efficiency compared to producing e.g. methanol from CO_2 for energy storage, the exergy efficiency of methanation and methanol synthesis being 30.1% to 18.2%, respectively [23]. Today, the methane, methanol, formic acid and dimethyl ether are important chemicals used as fuels or raw materials in industry [11].

$$CO_2 + 4H_2 \leftrightarrow CH_4 + 2H_2O;\ \Delta H^0_{298} = \text{-165 kJ/mol} \tag{1-1}$$

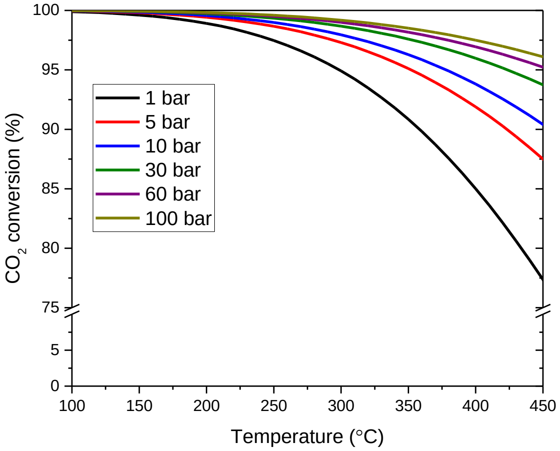

Figure 1.2: Thermodynamic equilibrium conversion for the stoichiometric feed gas composition of CO_2 methanation.

Methanation is typically hampered by the thermodynamic conversion being far from 100% under currently viable reaction conditions (Figure 1.2) [6, 11, 24]. According to Le Chatelier's principle [25], the equilibrium can, however, be shifted by removing one of the reaction side products, which in many reactions between CO_2 and H_2 is water. This can be efficiently achieved by sorbents like zeolites [26-30]. This process is called a sorption enhanced reaction [25]. In addition to a high-purity reaction product, the sorption enhanced CO_2 hydrogenation is also beneficial for high energy efficiency, lower temperature and pressure operation and process simplification intensification as less process steps and reactors are required [25]. Sorption enhanced CO_2 hydrogenation processes include sorption enhanced CO_2 methanation [27], methanol synthesis [28] and dimethyl ether synthesis [31, 32] to mention only a few. The current chapter mainly focused on sorption enhanced CO_2 methanation as a case exemplifying the typical challenges encountered in CO_2 hydrogenation as well as some solutions for tackling them.

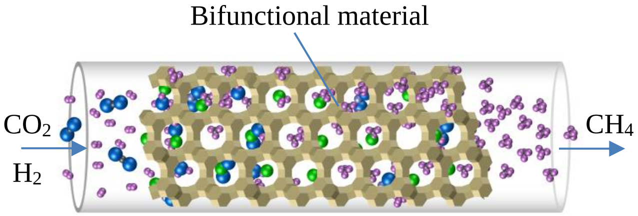

Figure 1.3: schematic of sorption enhanced CO_2 methanation.

Sorption enhanced CO_2 methanation (Figure 1.3) was developed to obtain close to 100% conversion and yield in the otherwise thermodynamically limited conditions [27, 33]. The water adsorbing capacity in the processes' operating window and catalytic performance are the critical material challenges in sorption enhanced CO_2 methanation. Even though novel catalysts, which are active at lower temperature than traditional catalysts are being developed, the water adsorbent still has to work at a relatively high temperature when thinking purely of adsorption, in order for reasonable reaction rates to be maintained. High temperature is not beneficial for water adsorption as high temperature rather enhances desorption. This emphasizes the importance of a proper material as the water adsorbent, which also acts as an efficient catalyst support (bi-functional material) in addition to developing low temperature activity.

Despite the importance of the topic for developing efficient large scale methanation processes, review publications on bi-functional materials synthesis and application for sorption enhanced CO_2 methanation are scarce. The current work presents the background and the state of the art in synthesis and application of these bi-functional materials and provides an outlook on future developments in sorption enhanced CO_2 methanation in particular and of sorption enhanced reactions in general.

This chapter presents the requirements and the state of the art in synthesis and application of these in fact bi-functional materials and gives an outlook to future developments in sorption enhanced CO_2 methanation.

1.2. Sorbent and catalytic metal

1.2.1. Sorbent choice

The requirement for a sorbent to be viable in sorption enhanced reactions is that the equilibrium vapour partial pressure is lower than that of the hydrogenation reaction. In the sorption enhanced CO_2 methanation, the water sorbent must be able to operate efficiently at a high temperature (> 200 °C) since the minimum working temperature of a conventional Ni based catalysts for example is well over 300 °C. Silica-gel cannot be used as its extremely low water capacity at the methanation reaction temperature [34]. Moreover, the water vapour partial pressure of silica gel is far too high to reach near 100% conversion. The most promising sorbent class for CO_2 methanation are zeolites [35], which provides high water absorption capacity and are stable under the reactor and regeneration conditions.

During the last decades, around 70 scientific papers have been published on CO_2 methanation with the help of a zeolite, and the number of publications has increased significantly during the last ten years (Figure 1.6). The FAU (X and Y type) and LTA framework zeolites are the most studied ones. The FAU and LTA zeolite frameworks can be found in Figure 1.4, more zeolite structure information can be found from reference [36]. Over 50% of the existing publications focused on utilizing FAU zeolite for CO_2 methanation. However, most publications mainly focus on the metal-zeolite catalysts preparation, characterization and the catalytic performance in CO_2 methanation, where the zeolite is merely a support disregarding the sorption effect.

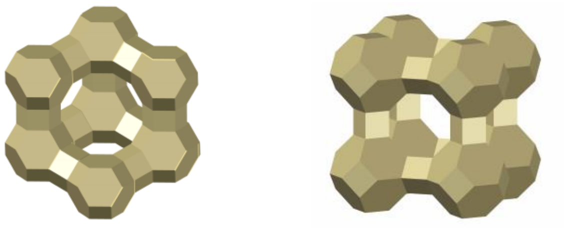

FAU LTA

Figure 1.4: The figurative construction of FAU and LTA zeolite frameworks that contain sodalite cages.

To investigate the sorption effect of Ni/5A zeolite catalysts in CO_2 methanation, Borgschulte et al. loaded Ni on 5A zeolite using the ion-exchange method. Their results show that Ni/zeolite 5A can be used as an efficient bi-functional catalyst [27]. Similar to 5A zeolite, 4A zeolite has a high water sorption capacity. In 2014, Walspurger et al. reported results using 4A zeolite (physically mixed with commercial Ni/Al_2O_3 catalyst): around 100% CO_2 conversion could be obtained in the temperature range 250-350 °C [33]. However, by comparing the kinetics of Ni/5A and Ni/3A bi-functional material, Borgschulte et al. found that the CH_4 selectivity was greatly enhanced when the zeolite's pore size is larger than 5Å [37], 5Å is large enough to allow the reactants (H_2 and CO_2) and the product (CH_4, CO) to enter and leave the zeolite.

A sorbent with a larger pore size should be beneficial for the rate diffusion of the reactants and products. Compared to LTA type zeolite (3A, 4A and 5A), zeolite 13X (FAU) not only has a bigger pore size but it also presents a higher water sorption capacity [38, 39]. It was reported that 5%Ni/13X (5% is the weight percentage of Ni on the catalyst) displayed nearly three-fold operation time compared to 5%Ni/5A in sorption enhanced CO_2 methanation, likely due to 13X having a higher water sorption capacity [26]. Even though the CO_2 conversion levels with both 5A and 13X zeolite catalyst were similar [26]. As can been seen from Figure 1.6 (b), zeolite Y (FAU type) is also widely used as the catalyst support for CO_2 methanation. However, the water sorption effect of Y zeolite has not been discussed in literature on CO_2 methanation [40-43].

1.2.2. Regeneration of sorbents

The sorbent regeneration i.e. the desorption of water is an essential step in the continuous operation of sorption enhanced CO_2 methanation. Sorbents have typically been regenerated under N_2, Air or H_2 atmosphere at 300- 500 °C [26, 33, 44]. According to the Van't Hoff equation (1-2), the water sorption capacity decreases significantly when sorption temperature increases from 200 to 300 °C as displayed in Figure 1.5, while the regeneration temperature does not have a large effect on the subsequent water uptake for 4A and 3A zeolite [33, 44]. Compared to H_2, air is a better carrier gas for the regeneration of the sorbent, since N_2 and O_2 have higher efficiency in carrying out water from the zeolite 5A and 13X due to oxygen and nitrogen molecules having sizes and weights that are comparable to the water molecule [26], but getting rid of the inert air constituents should be taken into consideration for the next cycle in practice operation.

$$\frac{d}{dT}\ln \mathrm{K}_{eq} = \frac{\Delta H^0}{RT^2} \tag{1-2}$$

Where K_{eq} is the adsorption equilibrium constant, T is adsorption temperature, ln denotes natural logarithm, R is the universal gas constant, ΔH^0 is the standard enthalpy change of the adsorption process [45].

Walspurger et al. reported the zeolite 4A water sorption capacity at 200, 250 and 300 °C under a water partial pressure of 0.039 bar. The water capacity ranged from 0.98-2.00 mmol/g, clearly dependent on the sorption temperature as described by a Van't Hoff plot [33]. Zeolite 3A showed similar water uptake capacity as zeolite 4A at sorption temperatures between 200-300 °C [44]. The mass transfer rate during adsorption on zeolite 3A can be described by a linear driving force approximation, as the mass transfer resistance is predominantly determined by micropore resistance, due to the cage aperture [46]. Zeolite 13X has a higher water uptake capacity compared to zeolite 3A, 4A and 5A in the temperature range 20-250 °C (Figure 1.5) [38].

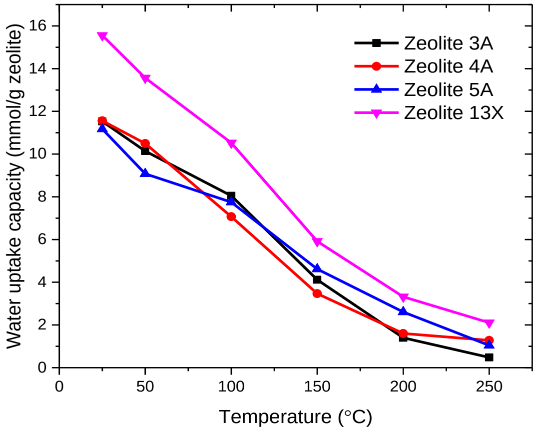

Figure 1.5: Water mass uptake capacity under an at 20 °C N_2 flow at different temperatures and 100 kPa total pressure for bead-shaped zeolites LTA-(3A, 4A, and 5A) and FAU-13X. Data from reference [38].

1.2.3. Other potential sorbents

Zeolites have been shown to be the most promising materials for in situ water removal in CO_2 methanation. The scientific articles published on CO_2 methanation with zeolites have mainly focused on FAU and LTA types zeolites, even though some other zeolites such as EMT and AFR could also be promising to be used for water removal [47]. Most work regarding the water sorption capacity for many typical zeolites has been performed at low temperature (<100 °C) (Figure 1.7) [39], however, the research on the water capacity of zeolites at high temperature (above 200 °C) under different water partial pressures (>16.4 kPa) is scarce [48]. Hardly any broad temperature and pressure range isosteres has been reported, even though the actual operational temperature in chemical processes is typically significantly above 100 °C. Further work needs to be performed regarding the zeolites that could be used in sorption enhanced CO_2 hydrogenation.

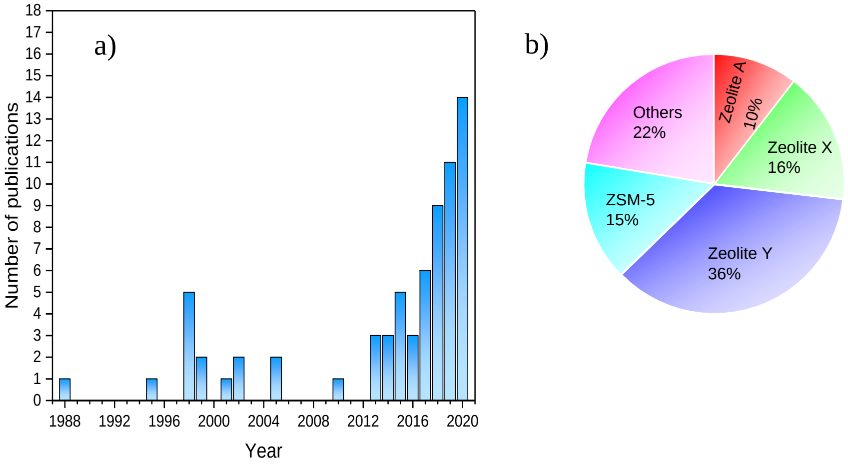

Figure 1.6: Publications analysis a) indexed topic as CO_2 methanation and zeolite/molecular sieve, b) percentage of zeolite/molecular sieve used in CO_2 methanation (source: web of science, range 1900-2020 3rd, Sep.).

Some new materials like MOF-74 and MOF-801 may also have the potential for water removal since they have a large water uptake capacity at room temperature [49], however, their thermal stability at higher temperatures, >200 °C is questionable. Furthermore, one drawback is that their ecological footprint is substantial due the organic precursors used in their manufacturing. Further study is needed for those materials.

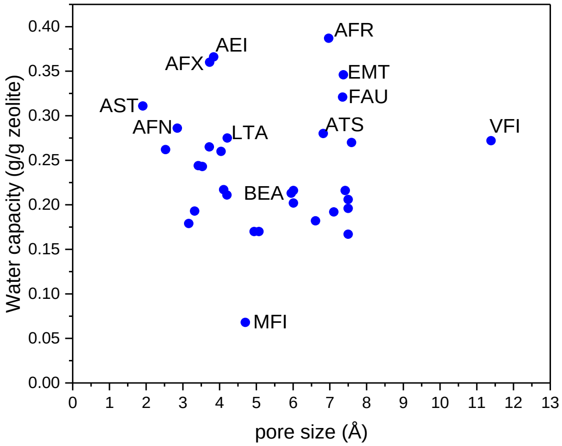

Figure 1.7: Water adsorption capacity of zeolite with respect to its pore size, water capacity data from reference [39], pore size data from IZA-SC (Copyright © 2017 Structure Commission of the International Zeolite Association).

1.2.4. Catalytically active metals

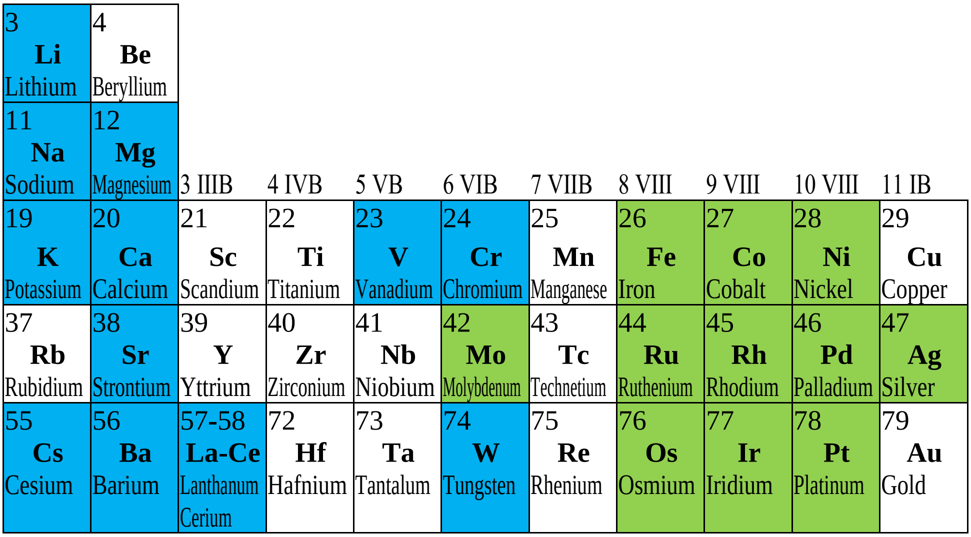

3 **Li** Lithium	4 **Be** Beryllium									
11 **Na** Sodium	12 **Mg** Magnesium	3 IIIB	4 IVB	5 VB	6 VIB	7 VIIB	8 VIII	9 VIII	10 VIII	11 IB
19 **K** Potassium	20 **Ca** Calcium	21 **Sc** Scandium	22 **Ti** Titanium	23 **V** Vanadium	24 **Cr** Chromium	25 **Mn** Manganese	26 **Fe** Iron	27 **Co** Cobalt	28 **Ni** Nickel	29 **Cu** Copper
37 **Rb** Rubidium	38 **Sr** Strontium	39 **Y** Yttrium	40 **Zr** Zirconium	41 **Nb** Niobium	42 **Mo** Molybdenum	43 **Tc** Technetium	44 **Ru** Ruthenium	45 **Rh** Rhodium	46 **Pd** Palladium	47 **Ag** Silver
55 **Cs** Cesium	56 **Ba** Barium	57-58 **La-Ce** Lanthanum Cerium	72 **Hf** Hafnium	73 **Ta** Tantalum	74 **W** Tungsten	75 **Re** Rhenium	76 **Os** Osmium	77 **Ir** Iridium	78 **Pt** Platinum	79 **Au** Gold

Figure 1.8: Active metals (marked in green) and promotional metals (marked in light blue) for CO_2 methanation, excerpt from the periodic Table of elements [6].

Active metals such as Ni, Co, Ru, Rh etc. have been studied for CO_2 methanation [5, 24, 50, 51], and in some studies metals like W, La and Ce, were used as promoters to enhance the catalytic metal dispersion increase, coke resistance and anti-CO-poisoning ability [50, 52]. The relevant active metals and promoters are displayed in Figure 1.8.

The observed order of activity and selectivity for the respective metal catalysts on CO_2 methanation is shown below [5, 6]. However, this order is only a generalized trend and sometimes differs depending on e.g. different metal-support interactions [5].

Activity: Ru > Fe > Ni > Co > Rh > Pd > Pt > Ir

Selectivity: Pd > Pt > Ir > Ni > Rh > Co > Fe > Ru

Nickel (Ni) is the most widely used active metal for conventional [6, 53-55] and sorption enhanced CO_2 methanation [26, 27, 33, 56], due to its rather high activity, CH_4 selectivity and low cost, which makes Ni an interesting active metal from a commercial perspective [57]. 5%Ni/SiO_2 catalyst has an approximate apparent activation energy of 84 kJ/mol in CO_2 methanation [58].

Cobalt (Co) catalysts exhibit a similar methanation activity and CH_4 selectivity comparable to Ni, the apparent activation energy of Co/MCF-17 in CO_2 methanation has been determined to be around 80 kJ/mol [59]. However, cobalt is not as widely used for commercial application since it is more expensive [50, 60]. Ashok et al. described that morphologies, surface orientations, catalyst supports and cluster size of metals are the key factors in Co catalyst performance in CO_2 methanation [24], like with other catalysts.

Iron (Fe) catalysts have been used for CO_2 reduction with H_2, and they exhibit a high activity, while showing low CH_4 selectivity, around 85% of the product gas is CO when using 5wt.%Fe/13X at 350 °C [61-63], which hindered its use even though Fe is cheaper and less toxic than Ni and Co, and much cheaper than noble metals (Rh, Ru, Pd, Pt). 15%Fe/SiO_2 displayed that 134 kJ/mol of apparent activation energy for CO_2 methanation at 253 to 299 °C .

Molybdenum (Mo) has a low activity in CO_2 methanation and the number of publications on Mo catalysts for CO_2 methanation is low. A special feature of Mo is that it has the highest Sulphur species tolerance [6]. The reported apparent activation energy of Mo based graphene catalysts for CO_2 methanation ranges between 62-115 kJ/mol [64].

As discussed above, the water adsorption capacity is higher at lower temperatures due to thermodynamics, therefore low temperature catalytic activity of the metals in the bi-functional materials in CO_2 methanation would be highly beneficial for the sorption enhanced CO_2 methanation.

Ruthenium (Ru) is known as one of the most active metals for CO_2 methanation even at lower temperatures [6], and thus it is an attractive alternative [24]. An apparent activation energy of 41 kJ/mol was obtained by researchers for Ru/MgO catalyst in CO_2 methanation which was measured at 80 to 180 °C [65]. Ru on NaY and 5A zeolite catalysts have been observed to yield high CH_4 selectivity [66], whereas 100% yield of CH_4 has been reported to be obtained at 160 °C using Ru/TiO_2 catalyst [67]. The dispersion of Ru on zeolite is important for the catalyst performance in CO_2 methanation and high dispersion of Ru has been obtained on FAU zeolite with the ion-exchange method [68, 69].

Rhodium (Rh) has been reported to be an active metal for CO_2 methanation at low temperatures [70], and its activation energy has been reported to be as low as 17.0 kJ/mol (3%Rh/TiO_2), and a turnover frequency of 0.524×10^2 (s^{-1}) in CO_2 methanation at 120 °C [71]. Rh could thus to be a promising active metal for sorption enhanced CO_2 methanation when loaded into zeolite. As the water uptake capacity of zeolites is increased dramatically at temperatures lower than 200 °C (Figure 1.5).

Platinum (Pt) modified ZSM-5 zeolite catalyst have displayed high catalytic activity and CH_4 selectivity even with 0.5% loading of Pt [72]. Pt can promote the activity of Co for CO_2 methanation [73]. The apparent activation energy has been reported to be 94 kJ/mol for Pt/Al_2O_3 in CO_2 methanation [74].

Luo et al. prepared highly dispersed palladium (Pd)/Fe catalyst, and the results showed that Pd promoted and stabilized the catalyst significantly [75]. 23.5 kJ/mol of apparent activation energy was measured at 250 to 350 °C for $Pd/\gamma\text{-}Al_2O_3$ in CO_2 methanation [76].

A summary of CO_2 methanation catalysts using different active metals can be found from Table 1.1.

Table 1.1: Summary of CO_2 methanation catalysts using different active metals.

Catalyst	m_{cat}^a g	$GHSV^b$ ml/g/h	H_2: CO_2 _	p^c (bar)	T^d (°C)	X_{CO_2} (%)	S_{CH_4} (%)	E_a^e (kJ/mol)	Ref.
5%Ni/SiO_2	0.200	50000	4:1	1	300	42.4	96.6	84	[58]
5.9%Ni/Al_2O_3	0.100	30000	4:1	1	250	2	98.1	92	[74]
4.9%Co/MCF-17	0.050	60000	3:1	6	250	5.1	58.8	80	[59]
15%Fe/SiO_2	0.39	1470^f	4:1	1	253	7.7	12.9	134	[77]
MoO_3-3/graphene	0.020	12000	3:1	10	400	21	100	79	[64]
MoS_2-3/graphene	0.020	60000	3:1	10	400	20	90	62	[64]
0.5%$Ru/\gamma\text{-}Al_2O_3$	0.375	5000	4:1	1	350	82	99.5	68.1	[78]
3%Rh/TiO_2	0.200	6000	4:1	1	120	0.65	100	17	[71]
2%$Rh/\gamma\text{-}Al_2O_3$	0.200	6000	4:1	1	200	6.2	100	16.4	[76]
19.5%Pt/Al_2O_3	0.100	30000	4:1	1	250	2	2	94	[59]
1.1%Pt/MCF-17	0.050	60000	3:1	6	250	1	98	_	[74]
5%$Pd/\gamma\text{-}Al_2O_3$	0.200	6000	4:1	1	300	4.3	100	23.5	[76]

m_{cat}^a: catalyst mass used in experiments; $GHSV^b$: gas hourly space velocity, ml/g_cat/h; p^c: reaction pressure; T^d: reaction temperature; X_{CO_2}: CO_2 conversion; S_{CH_4}: CH_4 selectivity; E_a^e: apparent activation energy; f: unit is /h.

1.2.5. Promoters

Promoters are used to improve the catalyst performance and their introduction may influence the catalyst properties such as the acidity, basicity, dispersion of the active metal etc., and as a result affect the activity, selectivity, and the resistance to coke deposition.

In addition to promoting the catalyst activity and stability, adding W in the Ni-

MgO_x catalyst can promote its anti-CO-poisoning ability and resistance against coke formation [52].

Na has been observed to have a negative effect on Na/Ni/CeO_2 catalysts performance on CO_2 methanation, even at low concentrations (0.1 wt.%). The adding of Na was reported to decrease the amount of chemisorbed CO_2 on Na/Ni/CeO_2 catalysts, and the CO_2 methanation activity of Na/Ni/CeO_2 decreased with Na content. A positive effect of Na was observed for CO_2 methanation over Na/Ni/SiO_2 catalysts in which the amount of chemisorbed CO_2 increases with Na content [79]. This was speculated to be related to the position on and interaction of Na with the support. The effect of alkali promoters (Li, Na, K, Cs) seems to depend also on the active metal, support, dispersion and loading [80].

The addition of lanthanum (La) in Ni/BETA zeolite catalyst can promote CO_2 conversion since La enhances the formation of surface hydroxyl groups greatly, which can interact with CO_2 and thus promote CO_2 conversion [81]. The increasing amount of CO_2 adsorbed by the catalyst as a result of the La_2O_3 was reported to lead to a higher CO_2 methanation activity and CH_4 selectivity [41]. Quindimil et al. reported that the Ni particle growth was influenced by La during catalyst calcination [41]. Cerium (Ce) is a typical metal used as a promoter. It has been reported that Ce can further improve the catalyst activity and selectivity, due to the ability to promote CO_2 dissociation [42, 43].

1.3. Preparation of the bi-functional material

In general, the catalyst activity and selectivity will be influenced by different preparation methods and different supports, since the active metal dispersion, particle size, and location [43], the acidity, and interaction with the Si-Al framework will be different. In order to remove the water produced during the CO_2 methanation, a zeolite should be used in preparing the bi-functional material, which sets certain requirements on the preparation. There are two types of routes for preparation of materials combining both catalytic and high water uptake capabilities: a) mixing and shaping (physical mixture) route; b) catalytic metal loading (chemical) route (Figure 1.9).

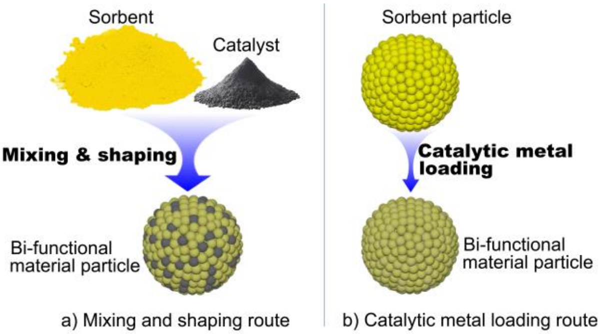

Figure 1.9: A schematic representation of bi-functional material preparation routes.

1.3.1. Mixing and shaping route

In the mixing and shaping route, the catalyst preparation process is separated from the synthesis of the sorbent. In this way, the bi-functional material preparation will not be limited by the sorbent structure and other properties, such as the pore size, the acid and basic sites etc. It is an easier way to prepare the bi-functional material compared to loading the metals directly on the sorbent, as all possible catalyst preparation methods can be utilized, such as impregnation, ion-exchange, deposition precipitation, chemical vapor deposition, atomic layer deposition, and co-precipitation [82, 83]. As long as a highly active catalyst can be obtained (even purchased from commercial companies), mixing the catalyst and sorbent can be performed. One of the few examples is from Walspurger et al.. They physically mixed a commercial Ni catalyst with 4A zeolite and pelletized the mixture for sorption enhanced CO_2 methanation and, around 100% CO_2 conversion was obtained at 250-350 °C [33]. However, the pelletizing is not always straight forward as mechanical stability many pose an issue. Moreover, pore blockage during pelletizing can significantly decrease the surface are of the material. This again results in significantly lower performance both in the catalysis as well as in the absorptive capacity and kinetics.

1.3.2. Catalytic metal loading route

Although the mixing and shaping route is very flexible, the distance between the sorbing and catalytic site would be in micro meter scale in these bi-functional materials. Terreni et al. reported that nano-structuring sorption enhanced catalysts to shorten the diffusion pathway is superior over physical mixtures of macroscopic sorbents and other catalysts which result in longer diffusion path lengths [84]. In other words, in sorption enhanced CO_2 methanation, close proximity of sorption and catalytic sites is a prerequisite to conversion enhancement and process intensification. Materials prepared by loading the active metals directly into the zeolite would therefore be preferable.

Ion-exchange is a typical method for catalyst preparation; the active metal, Ni for instance, can be loaded in the zeolite by exchanging it with the Na^+, K^+, Ca^{2+} from the zeolite framework [83]. Recent publications have used ion-exchange to prepare bi-functional materials with sorption enhancement [27, 37, 85]. In an ion-exchange process, a certain amount of metal salt (Ni precursor, e.g. nickel nitrate) is dissolved in distilled water. The sorbent, also acting as the catalyst support, is added into the solution and the mixture solution is stirred before filtering and washing with distilled water, after which the obtained solid sample is dried before calcination [27, 83]. The metal loading is limited by the amount of exchangeable ions in the zeolite, however, the method results in highly dispersed catalyst when successful.

Impregnation is another conventional way for catalyst preparation [83], in which a certain amount of distilled water is used to dissolve the metal precursor. The water amount exceeds the pore volume of the support in wet impregnation, while it is equal to the pore volume of the support in incipient wetness impregnation. The sorbent is added to the solution, and the water in the mixture solution is removed by filtering or evaporation after several hours stirring. The obtained solid is then dried further in an oven before calcination.

1.3.3. Other considerations for the bi-functional material preparation

Sub-nanometer or single-atom based materials are a desired option, as they typically display high activity and they should largely retain their water-adsorption capacity after metal loading as low loadings can be used due to the high dispersion and pore blockage should then be avoided due to the small cluster size. Several strategies exist for synthesizing sub-nano/single-atom catalysts [86, 87], of which mass-selected soft loading [88] and atomic layer deposition [89, 90] are limited by high cost and are complicated methods for large-scale catalyst production. In recent years, other synthesis strategies have emerged for single-atom catalyst preparation, such as defect engineering [91, 92], coordination pyrolysis [93-95], and gas migration using volatile metal complexes [96]. However, it is difficult to keep the material’s structure intact since the high calcination or pyrolysis temperatures needed are prone to damage the structure of the support irreversibly. Furthermore, there is the possibility of sintering of the metal (nano) particles. Additionally, these preparation routes are difficult to scale up because of the complicated and expensive methods involved. Nevertheless, if solutions can be found for the drawbacks mentioned above, it will be feasible to prepare an extremely highly dispersed (maybe down to single-atom) catalyst and combined with a sorbent for sorption enhanced CO_2 methanation. However, physical mixtures are mainly the possible option in many of the cases.

It is possible to prepare highly dispersed zeolite catalysts by a novel strategy or by modifying conventional methods [68, 97, 98]. Liu et al. reported a general strategy to prepare a highly dispersed (even single atom) Pt, Pd, Ru, Rh, Co, Ni and Cu on Y zeolite by adding ethylenediamine (EDA) as ligand to adjust the size the of precursors (Figure 1.10) [99].

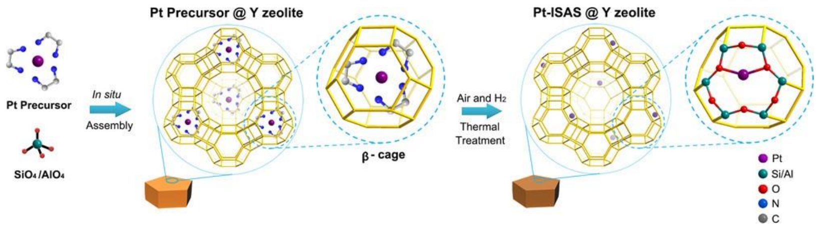

Figure 1.10: A schematic illustration of the in-situ separation and confinement of platinum precursor in β-cage followed by thermal treatments "Reprinted (adapted) with permission from [99]. Copyright (2019) American Chemical Society".

Moreover, the metal precursor has also been observed to play an important role in the metal dispersion during the catalyst preparation, which influences the catalyst performance in CO_2 methanation. Li et al. found that the performances of the NiLa/SiC catalysts prepared from nickel acetate were better than those of using nickel nitrate, due to the enhanced nickel dispersion and better reducibility of the catalyst from nickel acetate [100].

1.4. Characterization and performance of the material

1.4.1. Characterization of the material

Similar to conventional catalysts, the bi-functional material has some important properties which relate to its performance in CO_2 methanation, such as the crystal structure and size, the dispersion of the active metal, the actual loading of active and promoter metal, the cluster size of metal, the acidity and basicity of the material, the pore size, volume and surface area etc. Those properties can be characterized by conventional techniques such as X-ray powder diffraction (XRD) for crystal structure and size, scanning electron microscopy (SEM) with energy-dispersive X-ray spectroscopy (EDX) for material morphology and surface elemental content, transmission electron microscopy (TEM) for metal particle size on the support, scanning transmission electron microscopy equipped with energy-dispersive X-ray spectroscopy (STEM-EDX) for elemental distribution, X-ray photoelectron spectroscopy (XPS) for chemical valence states, hydrogen-temperature programmed reduction (H_2-TPR) for catalyst reduction behavior, CO_2-temperature programmed desorption (CO_2-TPD) for basicity, pyridine-FTIR for acidity distribution, and N_2 adsorption for pore size, volume and surface area, etc..

Single-atom catalyst is a challenging topic in the analysis, HAADF-STEM (High-angle annular dark-field - scanning transmission electron microscope) has in some cases been successfully used to characterize the single atoms catalyst to get direct evidence of metal dispersion [99].

For most single-atom catalyst, XANES (X-ray Absorption Near Edge Structure) and EXAFS (Extended X-Ray Absorption Fine Structure) are useful spectroscopic techniques to further determine the dispersion and coordination of the active metal in the zeolite [99].

1.4.2. Performance of the material

Around 100% CO_2 conversion and 100% CH_4 selectivity has been obtained by using bi-functional material 6%Ni/5A in sorption enhanced CO_2 methanation at temperatures lower than 200 °C [27], and 100% CH_4 selectivity was obtained using 5%Ni/5A and 5%Ni/13X under atmospheric pressure in fixed bed reactor [26]. These materials are easily regenerated under H_2 or air atmosphere at elevated temperatures [26, 33]. The results of the studies are summarized in Table 1.2.

Table 1.2: Performance of representative bi-functional materials for sorption enhanced CO_2 methanation.

Bi-functional Catalyst	Metal loading (wt.%)	Pressure (bar)	Temp. (°C)	X_{CO_2} (%)	S_{CH_4} (%)	Rege. T[a] (°C)	Ref.
Ni/5A	6	1.2	170	100	100	N.A.	[27]
Ni/Al_2O_3 mix 4A	N.A.	1	250-350	100	100	350-450	[33]
Ni/5A	5	1	300	100	100	300	[26]
Ni/13X	5	1	300	100	100	300	[26]

[a] Rege. T-regeneration temperature of bi-functional material; X_{CO_2}: CO_2 conversion; S_{CH_4}: CH_4 selectivity.

However, the number of publications on utilization of bi-functional materials for

CO_2 hydrogenation is low so far, and the published papers are mainly focused on nickel-based LTA and FAU (13X) zeolite. Another zeolite, USY has been widely studied for CO_2 methanation, however, the sorption effect of the USY has been ignored. Results found in literature are presented in Table 1.3. Other metals besides Ni have been explored in CO_2 methanation, with the aim of obtaining high low temperature activity.

Table 1.3: Performance of representative zeolite catalysts for conventional CO_2 methanation.

Zeolite catalyst	Metal loading (wt.%)	Prep. method[a]	Pressure (bar)	Temp. (°C)	X_{CO_2} (%)	S_{CH_4} (%)	Ref.
Ru/5A	2-5	Impregnation	23	320	92	99.5	[66]
Rh/Y	6	Ion-exchange	30	150	5.9	99.8	[101]
Ru/HZSM-5	2	Impregnation	1	350	20	99	[102]
Ru/Y	3	Ion-exchange	30	150	12.4	96	[69]
Ni/Beta	10	Impregnation	1	280	20	N.A.	[103]
Ni/HY	5	Impregnation	1	300	48.5	96.4	[58]
Ni/USY	5	IWI	1	400	24.7	61.4	[43]
Ni/USY	14	Impregnation	1	300	8	36	[104]
Ni/USY	4.8	IWI	1	300	10	95	[105]
Ni/HUSY	15	IWI	1	340	12	80	[106]
Ni/USY	5	IWI	1	350	12	72	[42]
Ni	15	IWI	1	337	12	80	[107]
Ni/Na-USY	15	IWI	1	305	14	95	[108]
Ni/USY	5	IWI	1	350	8	73	[109]
Ni/Na-Y	9.9	IWI	1	350	32	84	[41]
Ni/Na-USY	15	IWI	1	360	62	96	[110]
Ni/ZSM-5	5	Impregnation	N.A.	450	44	84	[111]
Rh/HZSM-5	0.42	Seed-directing	10	300	20	100	[112]
Ni/HZSM-5	10	IWI	1	400	68.4	94.8	[113]
Ni/X	10	IWI	1	470	49	96	[114]
Ni/ITQ-2	5	IWI	1	250	6	97	[115]
Fe/13X	5	Impregnation	1	350	13	11	[61]

[a] IWI-incipient wetness impregnation. X_{CO_2}: CO_2 conversion; S_{CH_4}: CH_4 selectivity.

A study has shown that there are at least three possible reaction pathways for CO_2 methanation, I) formate pathway; II) carbide pathway; III) carboxyl pathway (Figure 1.11). The water removal might influence the reaction pathway, therefore the reaction rate and product distribution could be different. The reaction mechanisms of sorption enhanced CO_2 methanation are not yet exhaustively studied, including the bifunctional catalysts with or without promoters. The presence of promoters such as Ce could change the reaction pathway of CO_2 methanation, and there exist reports that the detected intermediates were different when a promoter was added [42]. However, this has not been extensively studied for sorption enhanced CO_2 methanation.

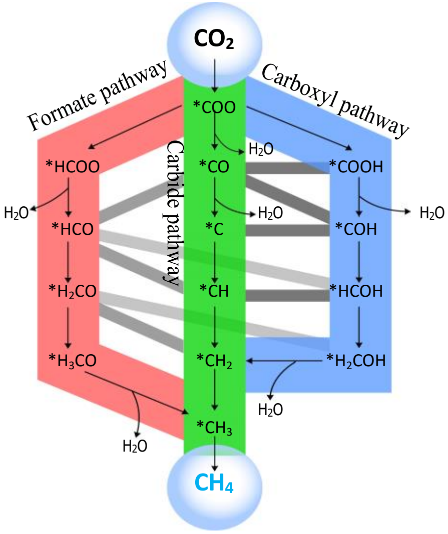

Figure 1.11: Possible reaction pathways for the methanation of CO_2 [116, 117]. I) formate pathway; II) carbide pathway; III) carboxyl pathway.

1.4.3. Stability of the material

The longevity and stability test of the catalyst/sorptive materials is extremely important for future commercial and large-scale projects on sorption enhanced CO_2 methanation.

The factors which influence the stability and performance of the materials include two main parts: the deactivation of the catalytic metal and the change in water uptake capacity of the sorbent. Compared to the conventional CO_2 methanation processes, the bi-functional sorption catalyst can work at relatively mild reaction conditions. The calculated results of equilibrium in CO_2 methanation reaction confirm the extremely low carbon depositions present, although water removal in sorption enhanced CO_2 methanation can result in significant carbon generation at high temperature (higher than 400 °C) [118, 119]. On the other hand, carbon formation can be avoided by supplying H_2 in slight excess [118], however, a balance should be achieved in getting a high quality product CH_4 with low H_2 concentration. Therefore, a good solution for avoiding carbon formation in bi-functional material is to operate the CO_2 methanation at low temperature. It has been shown that a CO_2 conversion of around 100% can be obtained at around 170 °C using Ni-5A zeolite bi-functional material [27], and it is also possible to obtain around full CO_2 conversion at 250-300 °C using physical mixtures (commercial Ni/Al_2O_3 catalyst with 4A zeolite) [33].

Moreover, some promoter metals such as Ce and La might also be an option for decreasing the carbon formation on the bi-functional materials in sorption enhanced CO_2 methanation. It would be necessary to further study the catalyst poisoning in practical operation of sorption enhanced CO_2 methanation, depending on the source, because some poisoning gases, H_2S for instance in biomass derived CO_2, would lead to the catalyst deactivation as in conventional catalysis.

A high water uptake capacity of the bi-functional material is vital in sorption enhanced CO_2 methanation. Delmelle et al. reported that no change in sorption performance was observed within 6 cycles of drying procedure for both 5Ni/5A and 5Ni/13X [26]. However, they found a degradation mechanism for Ni/5A specific to the sorption catalysis under cyclic methanation/drying periods, which affects water diffusion kinetics in the zeolite support and showed a decrease of water-diffusion coefficient during multiple cycling [120]. To understand the mechanism of decreased water sorption for different sorbents, further studies and many more operation cycles would be needed for further application of sorption enhanced CO_2 methanation.

1.5. Research systems and scale

Sorption enhanced CO_2 methanation is based on the conventional CO_2 methanation reaction (Sabatier reaction (1-1)). The CO_2 conversion values reported in literature (around 80%) [6, 24] are typically far from 100% under currently viable reaction conditions because conventional CO_2 methanation is hampered by thermodynamic limitations [6, 11, 24]. The sorption enhanced CO_2 methanation has the potential to provide high purity of CH_4 even meeting the requirements of the gas grid [33].

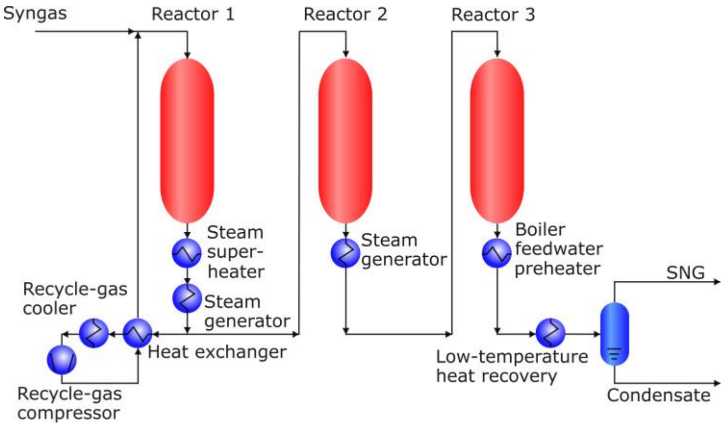

Figure 1.12: Exemplary fixed-bed methanation process configuration with intermediate cooling and gas recycle, adapted from reference [6].

To obtain high purity product gas in a conventional CO_2 methanation system (Figure 1.12), several consecutive reactors combined with water condensers are needed to be employed, and separation of CO_2 and CH_4 is typically also implemented on site (Figure 1.13) [23]. In conventional CO_2 methanation, a high operating pressure must be used for obtaining a high CO_2 conversion and CH_4 yield due to kinetics (Figure 1.2) [119]. The sorption enhanced CO_2 methanation route has the potential to produce high purity CH_4 with water removal in situ and it is operated at lower pressure as well as at relatively low temperatures. This provides an opportunity of process simplification and cost savings by decreasing the number of reactors needed and by elimination of the downstream separation steps [25]. The sorbent will be saturated after some time in operation, and need to be regenerated. There are two basic options for regeneration in a continuous process, which are adouble parallel fixed bed reactor system and circulating fluidized reactor system. A system which combines the fixed bed reactor, circulating fluidized reactor, and integrates the heat of reaction utilization is a promising solution for getting a high system energetic efficiency.

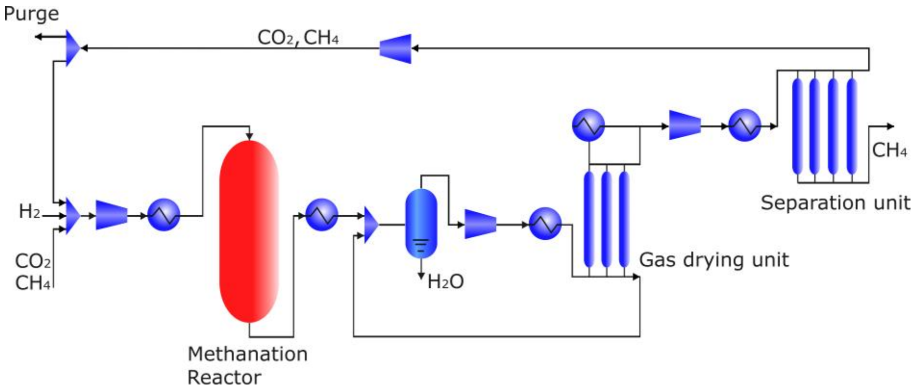

Figure 1.13 Schematic figure of the process configurations for CO_2 methanation with separation unit, adapted from reference [23].

1.5.1. Fixed bed reactor system

Sorption enhanced CO_2 methanation was first reported by Borgschulte et al. [29] in 2013 a study where, the experiments were performed in a lab scale stainless steel tubular fixed bed reactor system. Some publications on sorption enhanced CO_2 methanation have been published since then of which all are lab scale experimental research as commercial operation and review papers are scarce to date [35]. The utilization of zeolites as supports for CO_2 methanation catalysts was reported by Bacariza et al. [56], and Walspurger et al. described preliminary results from sorption enhanced CO_2 methanation experiment performed in a quartz reactor (inner diameter 10 mm) system in 2014 [33]. In 2015, Borgschulte et al. described the Sabatier reaction kinetics using Ni supported on zeolite 3A and 5A in a lab scale fixed bed reactor system [37].

A mechanistic study was performed by Borgschulte et al. in a lab scale fixed bed reactor system. They used time resolved neutron radiography on the reactor. Using this technique clearly showed that water accumulated in the reactor during the sorption enhanced methanation, and was released from the reactor inventory gradually in the regeneration process [85].

1.5.2. Fluidized bed reactor system

Compared to fixed bed reactor systems, fluidized bed reactor systems have advantages related to heat and mass transfer and they are favorable for integrating the sorbent regeneration involving large-scale operation of exothermic reactions [6]. Compared to fixed beds, the application of fluidized bed reactors can also lead to energy saving and favorable reaction conditions due to a much higher efficiency in heat exchange and the turbulent gas flow and rapid circulation [121]. However, the studies on sorption enhanced CO_2 methanation in fluidized bed reactor systems are scarce. Recently, Coppola et al. reported that they evaluated 3A zeolite and CaO for water removal in a lab-scale fluidized bed (40 mm inner diameter) system. They investigated the sorbents hydration in steam (balance air) at 200-300 °C and dehydration in air at 350-450 °C. The results show that zeolite 3A has a higher steam adsorption capacity compared to CaO, and that the capacity of CaO reduced as a result of the carbonation reaction [44]. However, the sorbents were not used in combination with CO_2 processing.

1.5.3. Other considerations and novel reactor systems

Compared to conventional CO_2 methanation, besides the advantage on methane yield and achieving zero CO_2 and CO outlet concentration, the operating temperature, pressure and CO_2/H_2 ratio range can also be extended significantly in sorption enhanced CO_2 methanation systems [27, 118, 119].

A membrane reactor can be used in CO_2 methanation to enhance the conversion of CO_2 by the removing H_2O from the product mixture [24, 122]. In other reaction setups, typically at least two reactors are needed for obtaining continuous operation, one is used for the sorption enhanced reaction, another is for the regeneration of the sorbent (Figure 1.14). However, the high cost of membrane reactors and operation costs due to the required high driving force (pressure) often out weigh the benefits of having a single reactor [119].

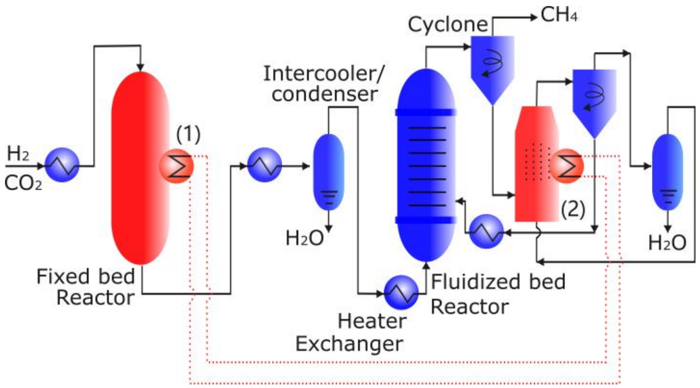

Figure 1.14: A schematic diagram of sorption enhanced CO_2 methanation with circulating fluidized bed reactor setup and heat utilization for sorbents regeneration. (1) Heater exchanger in reactor or regenerator, (2) Fluidized bed regenerator.

The Sabatier reaction (1-1) is highly exothermic, while the sorbent regeneration is endothermic, therefore the energy efficiency of the whole system can be improved by integrating the heat from the Sabatier reaction performed in a first stage reactor in relatively high temperature for sorbent regeneration. This would be beneficial for lowering the cost of a large scale commercial application of sorption enhanced CO_2 methanation. It is also beneficial to remove heat efficiently from the methanation reactor to avoid hotspots in the catalyst bed. One option would be to combine a circulating fluidized bed reactor with a fixed bed reactor according to the scheme presented in (Figure 1.14). The system integrates the heat utilization for obtaining a high system energetic efficiency.

In the proposed system, the conventional CO_2 methanation technologies can be used well on for the fixed bed reactor. The operating conditions such as the input ratio of H_2/CO_2, temperature and pressure of the fixed bed reactor could be regulated to optimize the output composition, which is then fed into the sorption enhanced fluidized bed reactor. For example, thermal oil could be cycled in the system for carrying the heat from the fixed bed reactor to the generator. The bi-functional material (sorptive catalyst) is cycled between the circulating fluidized bed and the regenerator. The removal of water from the methanation reactor results in the equilibrium shift for achieving high conversion of CO_2 and very pure CH_4.

The above-described sorption enhanced CO_2 methanation system is, not only beneficial for achieving 100% purity for CH_4, but it is also beneficial for lower temperature and pressure operation and process simplification. In addition to the application on earth, it may also have the potential for undertaking the role of H_2O and carbon cycle in space e.g. planet Mars (Figure 1.15) [116].

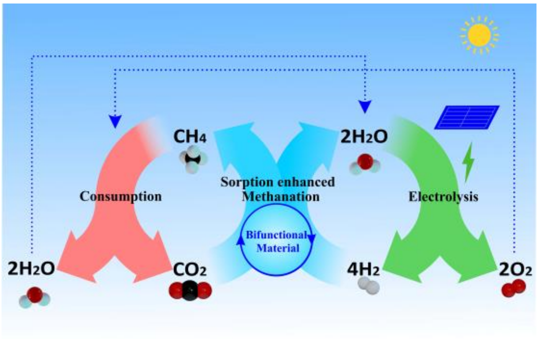

Figure 1.15: A schematic diagram of sorption enhanced CO_2 methanation system with carbon and hydrogen cycle.

1.6. Scope and outline of this thesis

1.6.1. Scope of this thesis

In summary, sorption enhanced CO_2 methanation has a great potential in the utilization of CO_2 and H_2 transfer for energy storage. In addition to the application on earth, it may also have the potential for undertaking the role of H_2O and carbon cycle in space [116]. Even though the basic concept has been presented previously, there are still many fundamental and practical aspects unclear and unresolved in sorption enhanced CO_2 methanation. Before the commercial application of sorption enhanced CO_2 methanation, further studies are needed, which include the structure and properties (pore size, acidity, basicity, metal dispersion, etc.) tuning of sorbent and catalyst, the possibility for long time and many regeneration cycles, bi-functional performance evaluation under operational practical operation conditions.

From literature study, it was found that the studies on the effect of different nickel precursors, active precious metal Ru, promoter, different zeolites for preparing zeolite supported catalysts (bifunctional materials) so far have been limited, especially related to sorption enhanced CO_2 methanation. What is more, the performance of Ni zeolite catalysts could be influenced by different nickel precursors, promoter, and thermal treatment steps, since the dispersion of the active phases and the reducibility of oxide precursors are dependent thereupon. Additionally, the kinetics behavior of Ni zeolite catalyst in CO_2 methanation is unclear.

The main focus of this study was to select a proper zeolite and modify the zeolite for sorption enhanced CO_2 methanation. Commercial zeolites 5A and 13X were used as the water sorbents, different Ni precursors were used for preparing the Ni modified zeolite catalysts. This study evaluated also the effect of using Ru for the bi-functional material Ni 13X and 5A zeolite catalysts, it also discusses the influence of Ce on Ni 13X zeolite catalysts for CO_2 methanation, investigated the performance of the Ce promoted Ni 13X zeolite material on sorption enhanced CO_2 methanation, and studied the kinetics of Ni 13X material for CO_2 methanation.

1.6.2. Outline of this thesis

The sequence of chapters in this thesis reflects that the investigation of catalyst and process development for sorption enhanced CO_2 methanation. Figure 1.16 provides the topics and keywords of the chapters.

- Chapter 2, the influence of Ni precursors on Ni zeolite 5A and 13X catalysts in CO_2 methanation was studied.
- Chapter 3, the effect of Ru for the bi-functional material Ni 13X and 5A zeolite catalysts for CO_2 methanation was studied.
- Chapter 4, different Ce loading Ni 13X bi-functional materials were prepared by evaporation impregnation, this chapter investigated the Ce-promoted Ni 13X zeolite catalysts for CO_2 methanation.
- Chapter 5, it is about the experimental study of sorption enhanced CO_2 methanation with highly active Ni 13X zeolite catalyst, it also contains part of characterizations of the reduced and cycled bi-functional material.
- Chapter 6, the kinetics study of CO_2 methanation over nickel zeolite 13X catalyst.
- Chapter 7, the conclusions and recommendations.

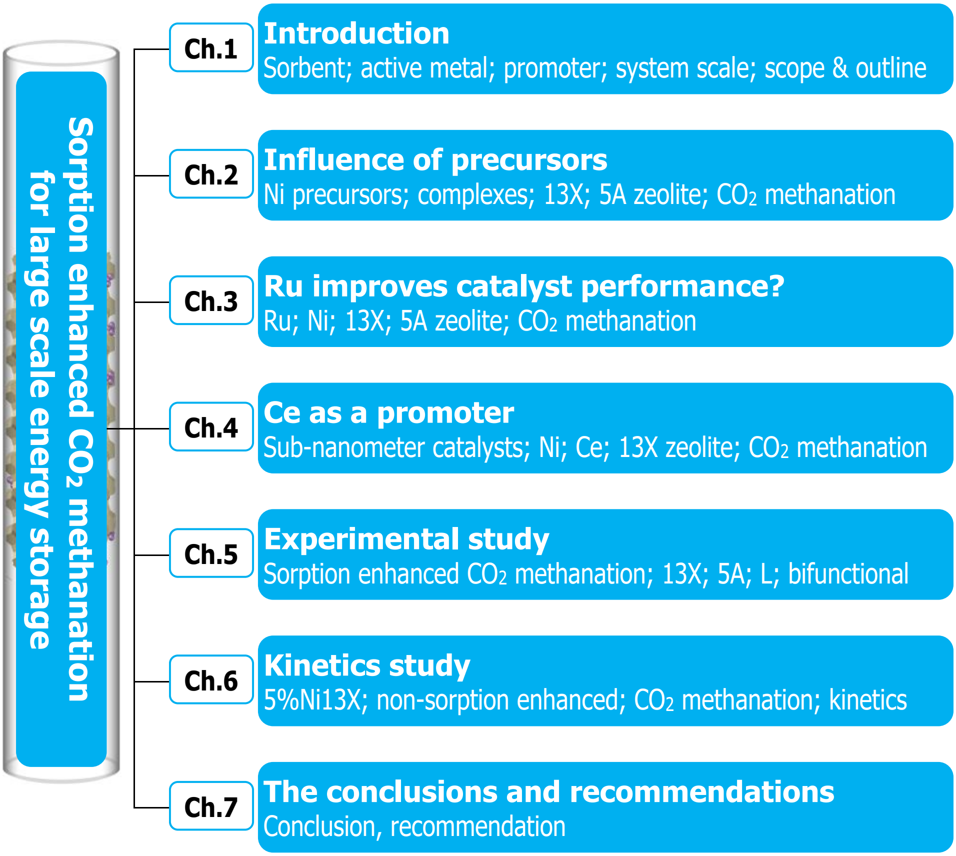

Figure 1.16: Scope of this thesis: topics and keywords of chapters.

2

Influence of Ni precursors on Ni zeolite 5A and 13X catalysts in CO_2 methanation

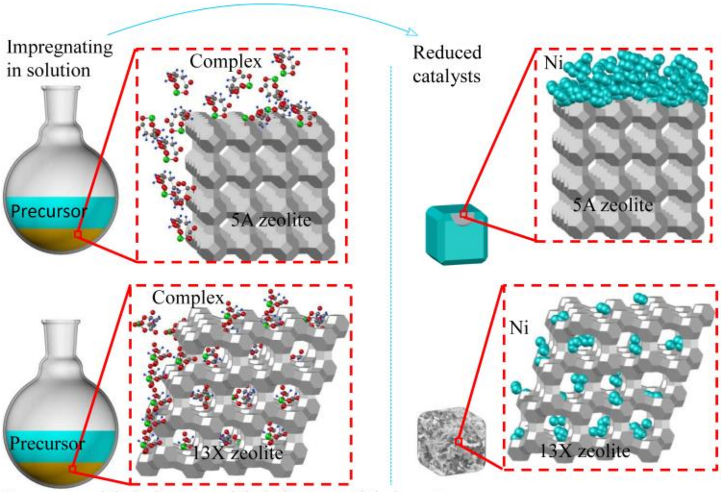

Precursor: nickel nitrate or nickel citrate or nickel acetate.

Keywords of this chapter:

Ni precursor salt anions,

13X zeolite,

5A zeolite,

CO_2 methanation catalyst,

material properties and catalytic performance.

This chapter is based on the following publication:
L. Wei, W. Haije, N. Kumar, J. Peltonen, M. Peurla, H. Grénman, W. de Jong, Influence of nickel precursors on the properties and performance of Ni impregnated zeolite 5A and 13X catalysts in CO_2 methanation. CATALYSIS TODAY, 2021. 362: p. 35-46. [123].

2.1. Introduction

Decreasing carbon dioxide emissions is a crucial task for all countries, in order to limit the severe challenges arising from global warming [124, 125]. Utilization of CO_2 to produce renewable energy carriers has attracted significant attention in the last few years. CO_2 can be converted to several synthetic fuels including methane (CH_4), methanol (CH_3OH) and further on to dimethyl ether (CH_3OCH_3) [126]. The availability of the raw materials CO_2 and H_2 in the future is a key factor in the large-scale production of synthetic fuel and chemicals. Large amounts of CO_2 can be currently obtained from industrial facilities such as, fossil fuel-burning power plants and plants with CCS technologies (like oxyfuel combustion, chemical-looping combustion and calcium looping) [126-128]. Technologies for capturing CO_2 directly from the air are being developed at an increasing pace [129]. Sustainable H_2 can be obtained from the splitting of water by electrolysis with sustainable electricity or from biomass gasification [130-132]. Hydrogen transport and storage are key factors for a H_2 based economy, especially for large scale industrial applications [133]. This chapter investigates the utilization of H_2 and CO_2 to produce CH_4 via the Sabatier (2-1), which is a promising method for storing energy in large scale in a form directly usable in already existing infrastructure [134]. It has the potential to provide a new way of obtaining renewable completely carbon neutral CH_4 for stabilizing energy demand, provided that CO_2 can be efficiently captured from biomass derived gas sources and air in the future [135, 136].

$$CO_2 + 4H_2 \leftrightarrow CH_4 + 2H_2O;\ \Delta H^0_{298} = -165\ \text{kJ/mol} \qquad (2\text{-}1)$$

The Sabatier reaction is limited by equilibrium. Sorption enhanced CO_2 methanation by removing water from the reaction mixture has received increasing attention during the last years, since it could be used to enhance the yield beyond equilibrium, according to Le Chatelier's principle [33, 137]. A CO_2 conversion of close to 100 % was obtained by Walspurger et al. by using a commercial Ni catalyst mixed with a 4A zeolite adsorbent in CO_2 methanation [33]. Borgschulte et al. observed that the selectivity to CH_4 was enhanced if the pore size of the support was larger than 5Å, and that the CO_2 overall conversion rate was reduced if the pore size was chosen to be smaller than 3Å, because the CH_4 produced inside the pores could not leave the crystal [37]. In a follow-up paper, Delmelle et al. developed new catalysts for sorption enhanced CO_2 methanation by loading Ni on a 13X zeolite using the wet impregnation method with nickel nitrate hexahydrate. They pointed out that 5wt % Ni/13X catalyst showed good performance and that it can be operated continuously two to three-fold longer than 5wt % Ni/5A in sorption enhanced CO_2 methanation [26]. Also these observations are prone to some serious doubt. The double peak in TPR can equally well be due to two different Ni species, those inside and those outside the zeolite structure. TPR on the 5A sample only exhibits the low temperature TPR peak presumably because these particles are all outside the zeolite structure, having a diameter of 20 nm on average.

For CO_2 methanation, nickel is the most widely used metal due to its high activity, high CH_4 selectivity, relatively abundant availability and low price [6, 138]. Nickel nitrate has an excellent solubility in water and it is easy to thermally decompose into NiO, which is why it is often used as the precursor for nickel catalysts [26, 137]. It has been reported that NiO and SiO_2 form nickel silicate like species that are stabilized by a nickel citrate precursor [139]. This effectively prevented the nickel particles from sintering at high reaction temperature [139]. He et al. found that the use of nickel citrate precursor, compared to nickel nitrate precursor, could significantly strengthen the NiO-support (SBA-15) interaction resulting in comparatively smaller nickel particles with high dispersion [140]. Citrate complex precursors have obtained much attention in the synthesis of nanomaterials, where similar methodology as used in catalyst preparation e.g. the amorphous citrate process has been employed [141-143]. Additionally, Li et al. observed that nickel acetate-derived Ni-Ac-La/SiC catalysts can obtain a small and narrow Ni particle size distribution [100].

The final aim of our approach to the Sabatier reaction is the envisioned sorption enhancement to 100% conversion using a molecular sieve supported catalysts. 13X and 5A zeolites with low Si/Al ratios have the right properties as adsorbent materials for gases and liquids. The adsorption of CO_2 and the hydrophilic properties in 13X and 5A zeolites are attributed to the presence of surface silanol (Si-OH) groups. The use of zeolites as catalyst support brings also challenges to the synthesis and the use of the catalyst due to the possible diffusion limitations caused by the microporous structure and the obtained benefits must be compared to the possible disadvantages. This is why focus is placed on obtaining insight in the actual location, size and dispersion of the Ni particles and how precursors play a role herein. Furthermore dispersion will evidently play a role in selectivity and activity. The performance of the zeolite supported catalyst is here investigated in the absence of the sorption enhancement (saturated with water) in order for the results to be comparable with catalysts not possessing this advantage. A follow-up study will report on the sorption aspects related to pore occupancy of impregnated material and sorption capacity. The performance of the catalyst with and without the benefit of sorption enhancement can in this way be clearly demonstrated and the benefit of using these zeolites to reach yields surpassing the thermodynamic limitations be verified. However, the basis for the catalyst development must be an active catalyst even without equilibrium shift.

Based on literature findings, apart from the common nitrates, nickel citrate and nickel acetate are promising nickel precursors for obtaining a high dispersion and small particle size. 13X (FAU) and 5A (LTA) zeolites are porous catalyst supports that have sodalite cages (β) and super cages (α) [36, 144-146]. Ni species can be located inside as well as outside these cages [43, 147], depending on their size. Studies on the effect of different nickel precursors for preparing zeolite supported catalysts have so far been limited, especially related to sorption enhanced CO_2 methanation. What is more, the performance of Ni zeolite catalysts could be influenced by different nickel precursors and thermal treatment steps, since the dispersion of the active phases and the reducibility of oxide precursors are dependent thereupon [140, 148, 149].

The current study focuses on the effect of preparation parameters of Ni modified 13X and 5A zeolite catalysts, using the evaporation impregnation method. Evaporation impregnation was chosen as it is a commonly used and easily operable synthesis method with high reproducibility. However, it offers also flexibility to the synthesis by varying different parameters such as temperature, impregnation concentration and time, evaporation rate and as in the current chapter, the choice of metal precursor [26]. Nickel nitrate (Nit), nickel citrate (Cit) and nickel acetate (Ace) were used as nickel precursors for the synthesis of catalysts: 5%Ni13X-Nit, 5%Ni13X-Cit, 5%Ni13X-Ace, 5%Ni5A-Nit, 5%Ni5A-Cit and 5%Ni5A-Ace. After calcination, crystal structure, morphology, NiO particle size, surface area and pore volume were characterized by XRD, SEM-EDX, TEM, STEM-EDX (elemental mapping), nitrogen physisorption, H_2-TPR, TG/DTA. Additionally, NH_3-TPD was used to determine the acidity of catalysts, relating to the catalyst performance in CO_2 methanation. The activity and selectivity tests of the catalysts were carried out using lab scale fixed bed flow reactor systems, where the product gas composition was analyzed online with a gas chromatograph.

2.2. Experimental section

2.2.1. Catalyst preparation

The Ni modified 13X and 5A zeolite supports were prepared using the evaporation impregnation method with different Ni precursors (nickel nitrate, nickel citrate and nickel acetate). A nominal Ni-metal loading of 5% by mass was aimed for in the preparation of the zeolite catalysts. Nickel (II) nitrate hexahydrate ($Ni(NO_3)_2{\bullet}6H_2O$, 99%, Merck Millipore), nickel (II) citrate hydrate ($Ni_3(C_6H_5O_7)_2{\bullet}xH_2O$, 98+%, Alfa

Aesar) and nickel(II) acetate tetrahydrate ($Ni(OCOCH_3)_2•4H_2O$, 98%, Sigma-Aldrich) were used as the three different Ni precursors. The nickel precursor was dissolved in 250 ml of distilled water in a flask. An equivalent of 5 g of 0.212-0.500 mm size (sieve fraction) 13X zeolite (Si/Al≈1.5 (Table S. 2.2, supplementary material)), Honeywell Fluka, The Netherlands) or 5A zeolite (Si/Al≈1.0 (Table S. 2.2, supplementary material)), Merck Millipore, The Netherlands) was dried at 100 °C overnight in an oven before it was added to the solution. The pH of the solution was measured by using a potentiometric pH meter during the process. It was observed that the pH of the solution decreased dramatically from 7.5 to 4.9 when nickel citrate hydrate dissolved in the solution, while it increased to 8.8 after 13X zeolite was mixed in the solution (Table S. 2.1, supplementary material). Meanwhile, the pH of other solutions with nickel nitrate and nickel acetate stayed around 7.3-7.4, and increased to 7.6-7.8 after the zeolite was mixed into the solution. The pH of the nickel citrate solution was around 5 due to the deprotonation of the hydroxyl group of the citrate ligand [150, 151]. The protons are taken up by basic sites in the zeolite leading to an increased pH eventually.

In order to avoid mechanical wear of the zeolite particle, the rotator-evaporator was operated at low rotational speed, 10 rpm, for 24 h at room temperature. After the 24 h of catalyst synthesis, evaporation of the aqueous solution was carried out in the rotator-evaporator at 50 °C using a water jet vacuum pump. The catalyst was then dried at 100 °C overnight before calcination in a muffle oven.

The calcination temperature should be higher than 300 °C since the decomposition temperature of nickel nitrate is around 280 °C [152]. The influence of the calcination temperatures 300 °C, 350 °C, 400 °C, 450 °C, for the 5%Ni13X-Nit catalyst was studied. The catalysts were calcined using a stepwise procedure [26]. They were put in a muffle furnace in air. The first heating step was to 250 °C with 4.5 °C/min and then temperature was kept constant for 40 minutes. Then the sample was heated to its target value with 2.5 °C/min and held there for 3 hours. The catalysts labelled as 5%Ni13X-Nit-300, 5%Ni13X-Nit-350 and 5%Ni13X-Nit-450, were calcined at the respective temperatures of 300 °C, 350 °C and 450 °C, respectively, all others only at 400 °C. Cooling down to room temperature took about 3 hours.

2.2.2. Catalyst characterization

The calcined catalysts were characterized before reduction by X-ray powder diffraction (XRD), scanning electron microscopy (SEM), energy dispersive X-ray spectroscopy (EDX), transmission electron microscopy (TEM), scanning transmission electron microscopy equipped with energy-dispersive X-ray spectroscopy (STEM-

EDX), nitrogen physisorption, hydrogen temperature programmed reduction (H_2-TPR), and temperature programmed ammonia desorption (NH_3-TPD).

A PANalytical Empyrean X-ray powder diffractometer was used in the XRD measurements. The diffractometer was operated in Bragg-Brentano diffraction mode, and the monochromatized Cu-Kα radiation (λ = 1.541874 Å) was generated with a voltage of 45 kV and a current of 40 mA. The scanning 2θ angle range was 3.0° to 80.0° using a step size of 0.013°, and counting time of 80 s /step. The measured XRD diffractograms were analyzed with Philips X'Pert HighScore (phase analysis refinement) and MAUD software programs (background subtraction).

Catalysts morphology, such as shape, size and size-distributions of crystals were studied using a LEO Gemini 1530 (LEO/ZEISS, Germany) Scanning electron microscope (SEM). The near surface elemental analysis was carried out by energy dispersive X-ray micro-analyses (EDX).

Transmission electron microscopy (TEM) was used to study the zeolite morphology and Ni- particle size distributions. The Ni-, particle size and the average particle size was calculated. The equipment used was JEM-1400(JEOL Ltd, Japan) with a maximum acceleration voltage of 120 kV.

To study the catalysts in more detail, scanning transmission electron microscopy equipped with an energy-dispersive X-ray spectroscopy (STEM-EDX) detector was used. The equipment used was a FEI Titan 80-300 electron microscope, the elemental mapping was investigated at a voltage of 300 kV with EDX. Specimen preparation consisted of immersing a carbon film supported on a copper grid into the catalysts powder, small particles adhering to the carbon film were measured.

The surface area and pore size of pristine 13X zeolite, Ni- modified 13X zeolite catalysts were measured using the nitrogen adsorption and similarly for the 5A counterpart. The instruments used were a Carlo Erba Sorptomatic, Sorptometer 1900 and Micromeretics, Tristar II. The catalysts were outgassed at 150 °C for 3 h at 8 mbar, prior to the surface area measurement. The calculation of surface area was carried out using the BET method.

Temperature programmed reduction (H_2-TPR) was carried out using a Micromeritics AutoChem 2910; The catalysts were dried at 250 °C for 1 h in a dry Ar atmosphere, then reduced by 5% H_2 (diluted by Ar) from room temperature to 900 °C with a 5 °C/min heating rate. A TCD detector was used to monitor the H_2 consumption.

Temperature programmed desorption of ammonia was carried out using a Micromeritics AutoChem 2910 for determining the acidic properties such as the amount of weak, medium, and strong acid sites and total amount of acid sites of the pristine forms of 13X, 5A and Ni-modified 13X and 5A zeolite catalysts. The samples were dried at 250 °C for 0.5 h in a dry He atmosphere before ammonia adsorption (5% NH_3 diluted by He) at room temperature, the desorption temperature ranged from 100 to 900 °C.

In order to investigate the catalysts calcination, thermogravimetric/differential thermal analyses (TG/DTA) were performed on SDT Q600 V20.9 Build 20 (TA Instruments) under 50 ml/min air atmosphere. The stepwise procedure of temperature in TG/DTA measurement was the same as the one for catalyst calcination above.

2.2.3. Catalysts test in fixed bed reactor

The catalysts' activity, selectivity and stability were tested using a fixed bed reactor made of quartz with an inner diameter of 10 mm. About 10 ml of silica beads (diameter around 1 mm) was placed in the reactor to support the catalyst bed. Then about 10 ml of silica beads was used to fill the upper part of the reactor. The reactor was heated by a vertical tube furnace equipped with a K-type thermocouple, while the temperature of the catalyst bed was monitored by another K-type thermocouple, which was inserted into the lower part of the catalyst bed and connected to a computer for data acquisition. A schematic representation of the fixed bed reactor system is displayed in Figure S. 2.1.

Before the experiments, around 0.9 g of the calcined catalyst was loaded into the reactor and reduced under 100 ml/min H_2 atmosphere at 500 °C for 4 hours. The reduction temperature was selected based on the results obtained with catalysts reduced at different temperatures. It was observed that catalysts reduced at 500 °C (100 ml/min H_2) were more active in CO_2 methanation compared to the ones calcined at lower or higher temperature (Figure S. 2.2, supplementary material). The catalysts activity tests were performed at temperatures between 240 °C and 440 °C with a gas hourly space velocity of 13333 ml/$g_{cat.}$/h. The feed mixture consisted of 40 ml/min H_2 and 10 ml/min CO_2 diluted by N_2 (150 ml/min). The product gas from the reactor was led through a cooling condenser and then analyzed using micro gas chromatography (GC). The GC (Varian, CP-4900 Micro-GC) equipped with HayeSep A, molecular sieve columns (Molsieve 5Å PLOT) and a thermal conductivity detector. Helium was used as the carrier gas.

The CO_2 conversion (2-2) and catalyst selectivity (2-3) forwards CH_4 were defined as [153, 154]:

$$X_{CO_2} = \frac{n_{CO_2,in} - n_{CO_2,out}}{n_{CO_2,in}} \tag{2-2}$$

$$S_{CH_4} = \frac{n_{CH_4,out}}{n_{CO_2,in} - n_{CO_2,out}} \tag{2-3}$$

where $n_{CO_2,in}$ is the input molar flow rate of CO_2 in the experiment, $n_{CO_2,out}$ and $n_{CH_4,out}$ are the molar flow rates of CO_2 and CH_4, respectively, calculated from GC results.

2.3. Results and discussion

2.3.1. Catalyst characterization

2.3.1.1. X-ray powder diffraction (XRD)

The XRD background corrected diffractograms for calcined Ni modified 13X and 5A zeolite catalysts with different Ni precursors are shown in Figure S. 2.3 (supplementary material). The XRD patterns indicate that the crystal structure of 13X (cubic Faujasite) zeolite is maintained after the modification by precursors nickel nitrate, nickel citrate and nickel acetate. Similarly, the crystal structure of 5A (cubic) zeolite did not change after the modification by nickel nitrate. The peaks for NiO cannot be distinguished in the XRD patterns. This could be due to a too low amount of NiO peaks overlapping with those from the zeolites, or the presence of NiO as amorphous or nano sized material leading to peak broadening [155].

2.3.1.2. Scanning electron microscopy (SEM) and Energy dispersive X-ray spectroscopy (EDX)

SEM was used to investigate the morphology of pristine (fresh) 13X and 5A zeolites and Ni modified 13X and 5A zeolite supported catalysts. Scanning electron micrographs of fresh 13X and 5A zeolites are shown in Figure **2.1**. The 13X zeolite showed relatively large agglomerates (around 2µm) which are composed of its characteristic smaller fibrous crystals [26], while 5A zeolite showed regular cubic crystals with more distinct edges. The crystal morphology of a spent sample, e.g. 5%Ni13X-Cit-Spent was also similar to that of fresh 5%Ni13X-Cit, clearly indicating that the CO_2 methanation reaction did not alter it.

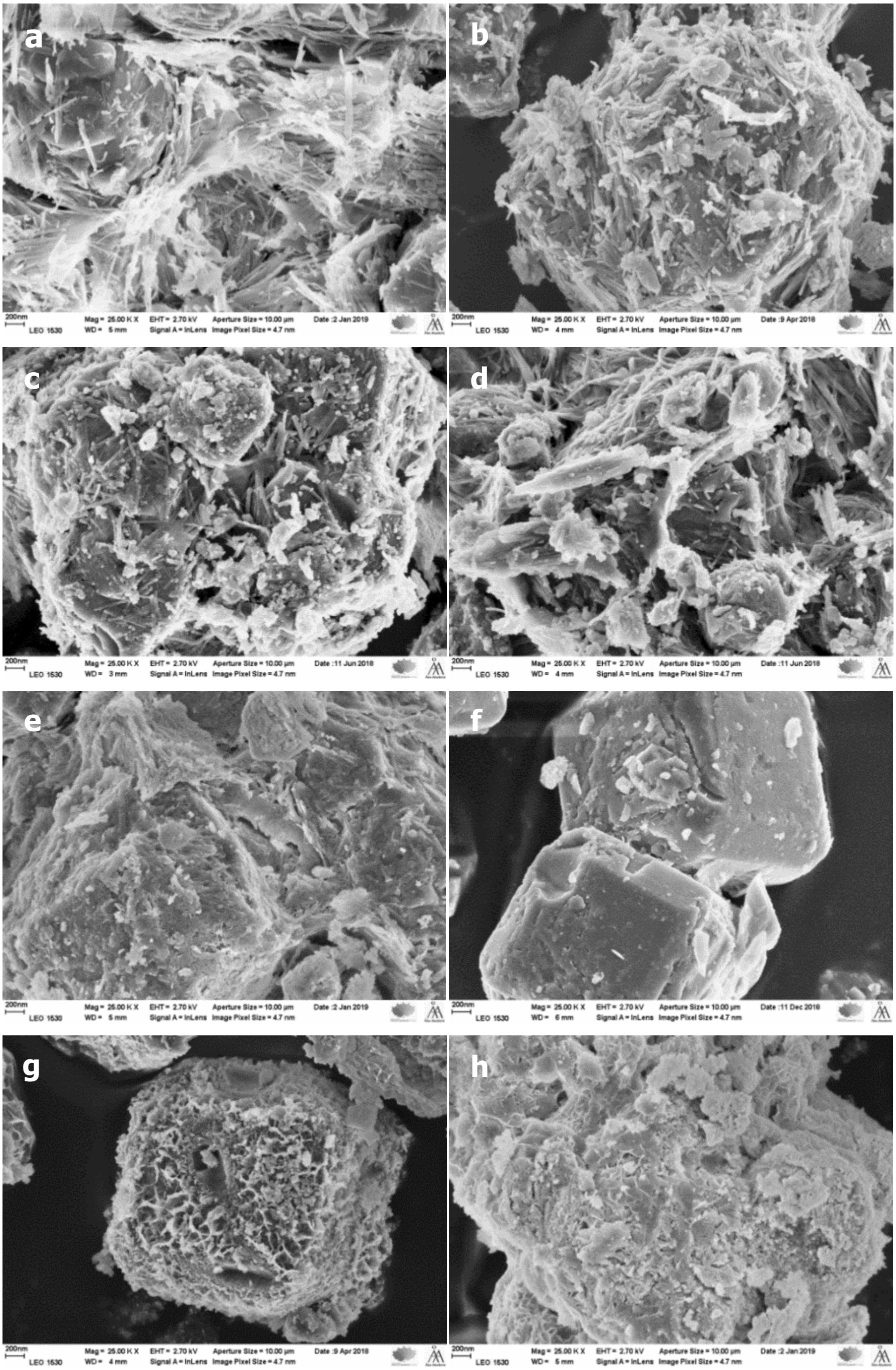

Figure 2.1: SEM images of a fresh 13X zeolite, b 5%Ni13X-Nit, c 5%Ni13X-Cit, d 5%Ni13X-Cit-Spent, e 5%Ni13X-Ace, f fresh 5A zeolite, g 5%Ni5A-Nit and h 5%Ni5A-Ace (25000×).

EDX results for catalysts are shown in Table S. 2.2 (supplementary material). It can be observed that the actual loading of Ni varies slightly for the different nickel precursors. The Ni content was 3.16% mass for the catalyst 5%Ni13X-Nit, and 3.52% mass for 5%Ni-13X-Cit. The Na and Ca content is very different for the fresh 13X and 5A zeolites which is reflected in the Ni modified 13X and 5A zeolite catalysts [156, 157]. The presence of Ca, Mg and Na in the fresh (pristine) 13X, 5A, Ni- modified 5A and 13X (Table S. 2.2) contributes to the formation of basic sites in line with the increase of the pH during the impregnation process.

2.3.1.3. Transmission electron microscopy (TEM)

TEM was used to investigate the NiO particle size distribution. Moreover, the textural properties of the fresh and calcined Ni modified 13X and 5A zeolites, their morphology and structure, were investigated. The TEM images of 5%Ni13X-Cit and 5%Ni5A-Cit prepared by nickel citrate are shown in Figure 2.2 (TEM figures for other catalysts can be found from Figure S. 2.4 (supplementary material)). The TEM images show the characteristic uniform structures of 13X and 5A zeolite, as well as the dispersed NiO particles on the external surface of 13X and 5A zeolite framework. It can again be observed from the TEM results that the Ni precursors (nickel nitrate, nickel citrate and nickel acetate) did not influence the morphology of 13X and 5A zeolite.

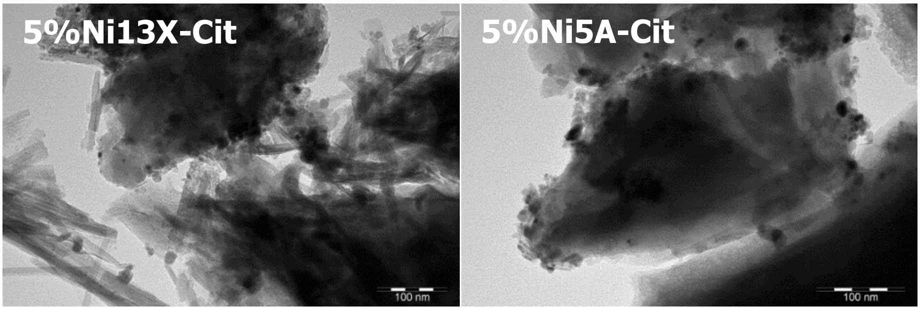

Figure 2.2: Transmission electron micrographs of calcined 5%Ni13X -Cit, 5%Ni5A-Cit catalysts with nickel citrate precursors.

There are clearly two different kinds of particles present in the sample, lumpy ones, presumably resulting from the precipitation during the drying step in the impregnation procedure, and very small and well dispersed ones aimed for by the impregnation process. The lumpy ones are too big, tens of nm, to fit inside the pores of the zeolites. The chelating capacity of citrate and acetate is probably leading to the smaller size as compared to nitrate [139, 158]. Furthermore, it has been reported that nickel citrate may leave a highly viscous, adhering film on the surface which breaks up and decomposes during calcination, resulting in a large amount of small NiO particles [155, 159].

2.3.1.4. STEM-EDX

The STEM micrographs depicted in Figure 2.3 show the NiO dispersion on and partly in the catalysts. The NiO dispersion is influenced by the properties of the support, e.g. the structure, pore size and crystal size of the zeolite and the precursor. Very small nano Ni (after reduction) particles (< 1-2 nm) are invisible in these TEM images, but still show high catalytic activity in reactions, due to their high surface free energy [160]. To further investigate the dispersion of the Ni (NiO) particles in 5A and 13X zeolite based catalysts, elemental mapping was carried out using STEM, equipped with EDX Micro -Analysis (STEM-EDX).

The STEM elemental mappings, Na (gold), Ca (blue) and Ni (red), of Ni-zeolite catalysts with different Ni precursors are shown in Figure 2.3. Ni is rather well dispersed on and in 13X zeolite for nickel nitrate, nickel citrate and nickel acetate precursors, however, the smallest Ni clusters can be clearly observed for the catalyst synthesized with the citrate precursor. The 5%Ni5A-Nit and 5%Ni5A-Cit catalyst, have predominantly Ni on the cubic crystal outside surface of 5A zeolite in an eggshell fashion (Figure 2.3), this “eggshell” could correspond to the smaller crystallites or particles observed from SEM results of Ni 5A catalysts (Figure 2.1). Clearly the precursors were too big to enter the 5A pores, as is further indicated by the deviating more homogeneous distribution of Ca and Na.

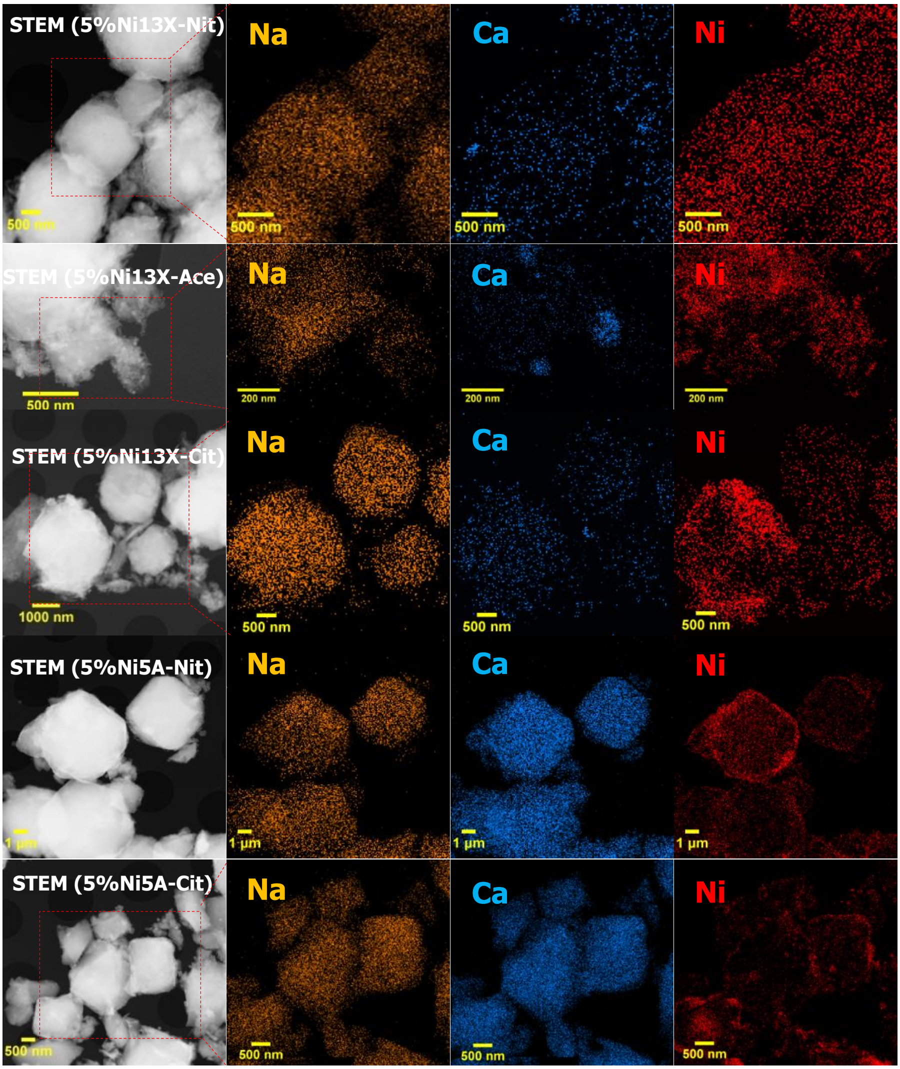

Figure 2.3: STEM images (left pictures), Na (gold), Ca (light blue) and Ni (red) maps of Ni-zeolite catalysts with different Ni precursors

2.3.1.5. Nitrogen physisorption

The specific surface area of fresh zeolites and catalysts was determined using nitrogen adsorption. The surface area of 13X and 5A was determined to be 685 m^2/g and 692 m^2/g, respectively. After the Ni modification, the catalysts had a lower surface area compared to the fresh 13X and 5A zeolites (See supplementary material Table S. 2.4). A plausible reason for decrease in the surface area is pore blocking. For the 13X based catalysts, it is especially noteworthy that the surface area decreased significantly less when the citrate precursor was used. For the more efficient 13X supported catalyst the surface area dropped from 685 m^2/g to 611 m^2/g with citrate precursor while 361 m^2/g was obtained with the nitrate precursor. The observed decrease in surface area was not as great with the 5A supported catalysts when nitrate was used, which supports the observation made with STEM-EDX that the nickel precursors did not penetrate the pores of the 5A efficiently. The external surface area of the parent zeolites was determined from the t-plots to be 44 m^2/g and 45 m^2/g for 13X and 5A, respectively. It can be concluded that external surface area does not explain the differences observed between the zeolites. The impregnation did not influence significantly the external surface area e.g. it decreased for the most efficient 5%Ni13X-cit from 44 to 40 m^2/g. The surface area measurements support the observations made with STEM-EDX. The Ni was deposited mainly on the external surface of 5A zeolite while for 13X, the nickel precursor is able to more efficiently penetrate into the pores of zeolite. Moreover, the use of nickel citrate seems to results in smaller clusters inside the pores of zeolite resulting in retaining a higher surface area.

2.3.1.6. H_2-Temperature programed reduction (TPR)

The TPR profiles of Ni-zeolite catalysts prepared by different Ni precursors and different calcination temperatures are displayed in Figure 2.4, and Figure 2.5. The reduction behavior of the catalyst and the relative H_2 consumption can be found in Table S. 2.5 (supplementary material). It can be seen that with increasing calcination temperature the TPR signal evolves from a quasi-single peak to a broad band of peaks extending to higher reduction temperature. For the catalysts prepared by different Ni precursors (Figure 2.4), 5%Ni13X-Nit shows a wide and intense peak at around 420 °C, while all the others have two peaks in the same temperature range, one appearing at around 330-350 °C and another at around 460-530 °C. This may indicate that different Ni precursors result in Ni oxides being formed at different reduction sites on or in the zeolite cages. The peak at 330-350 °C could correspond to NiO particles located outside of the zeolite cages and are more easily reduced, while the peak at 460-530 °C may correspond with NiO particles located within the zeolite super cages [43, 147, 161]. The reduction peaks of 5%Ni13X-Cit and 5%Ni5A-Cit at around 340 °C are strong, which indicates that more Ni oxides were located outside the 13X and 5A zeolite cages, compared to the catalysts prepared from nickel nitrate and nickel acetate.

The diameter of the $Ni^{2+}(H_2O)_x$ ion [162, 163] is similar or bigger than the pore diameter of 13X zeolite (7.4-11Å) [26, 164, 165] and 5A zeolite (4.3-5Å) [26, 165]. Nickel citrate and acetate complexes (especially the nickel citrate complexes) are both too big to enter zeolite 5A but may enter zeolite 13X during the catalyst preparation

[166]. This is also a plausible reason why Ni was predominantly found on the surface of 5A cubic crystals (Figure 2.3) as compared to the 13X particles.

The calcination temperature seems to influence the NiO reduction property significantly (Figure 2.5). A very sharp and strong reduction peak is observed for 5%Ni13X-Nit-300, which was calcined at 300 °C, while the catalysts calcined at higher temperature display a weaker and broader peak at around 400 °C and another at around 570 °C. Thus a higher calcination temperature results in clustered or sintered NiO particles located in the 13X cages.

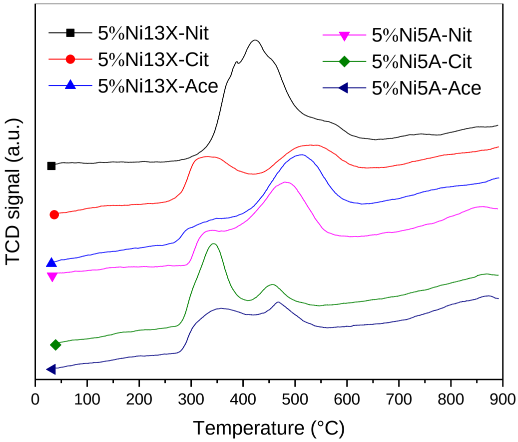

Figure 2.4: H_2-TPR profiles of Ni-zeolite catalysts with different Ni precursors

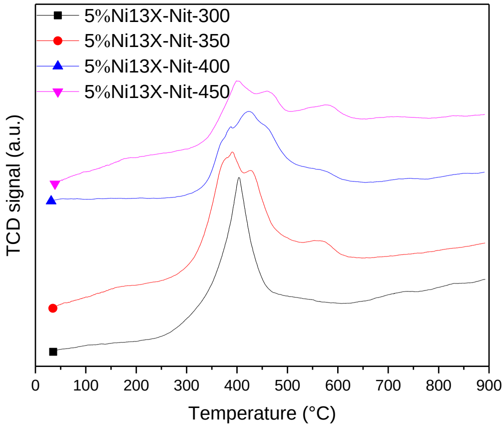

Figure 2.5: H_2-TPR profiles of Ni-zeolite catalysts with different calcination temperatures

2.3.1.7. Temperature programmed desorption of ammonia (NH_3-TPD)

The acidic properties of Ni-modified 13X and 5A zeolite catalysts were studied using temperature programmed desorption of NH_3-TPD. The comparisons of the pristine proton forms 13X and 5A zeolite supports were carried out with those of Ni-modified 13X and 5A zeolite catalysts. The most notable observation was that the total acidity only changed little, weak acidity is similar for all samples, medium acidity is virtually absent for the 13X series and the strong acidity is similar for all. On the whole, the 5A derived catalysts are more acidic than the 13X counterparts. The low temperature peaks are attributed to the Lewis acid sites and high temperature peaks (400-600 °C) are attributed to the Brønsted acid sites. Some peaks were also observed in the temperature range of 600-800 °C, these peaks are attributed to extra-framework aluminum species (Al-OH), $(Al\text{-}OH)_2$ and silanol groups (SiOH), $(SiOH)_2$. The extra-framework silanol groups are formed due to dehydroxylation reaction at high temperature (600-800 °C).

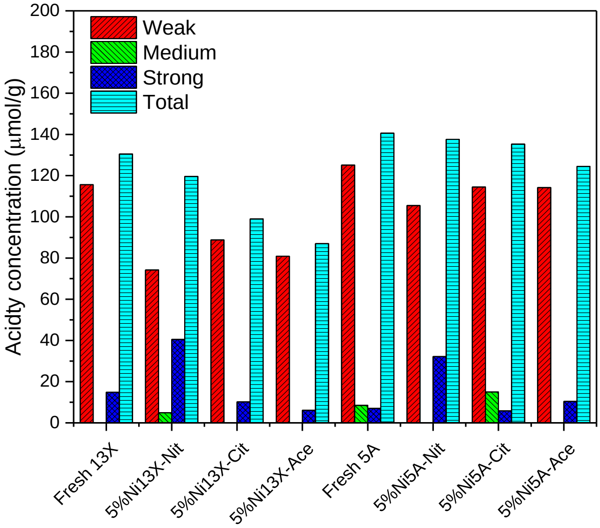

Figure 2.6: The catalyst acidity distribution calculated based on the results of NH_3-TPD

The catalyst acidity distribution calculated by the results of NH_3-TPD is shown in Figure 2.6 (NH_3-TPD profiles and detailed calculation results can be found from supplementary material Figure S. 2.5 and Table S. 2.6). The type of nickel precursor used for the synthesis of Ni modified 13X and 5A zeolite catalysts was observed to influence the total acidity only slightly, but there is a trend when looking in detail. The 5%Ni13X-Nit catalyst prepared using nickel nitrate aqueous solution exhibited highest total acidity. The total acidity of the Ni- modified catalysts followed the pattern: 5%Ni13X-Nit > 5%Ni13X-Cit > 5%Ni13X-Ace. The 5%Ni5A-Nit catalyst showed the highest total acid sites (137 µmol/g). The amount of total acid sites for Ni modified 5A zeolite catalyst followed the similar pattern as that of Ni modified 13X zeolite.

2.3.1.8. Thermogravimetric/differential thermal analyses (TG/DTA)

The TG/DTA was performed to investigate zeolite supported catalysts' calcination behavior, the results are shown in Figure 2.7. It can be observed that the mass of the samples is close to constant after 3 hours of calcination under air atmosphere at 400 °C. There are two main mass loss stages with the temperature increase. One is from room temperature to 250 °C, which corresponds to the desorption of water and other gases in zeolite 13X. This was followed by another main mass loss after 250 °C for the three samples, which corresponds to the decomposition of nickel nitrate [167], off-burning nickel citrate [168] and off-burning nickel acetate salt (or their intermediates) [169]. It was observed that the mass loss of Unc-5%Ni13X-Cit and 5%Ni13X-Ace in the second stage is much more severe than 5%Ni13X-Nit (Figure 2.7), and the mass loss of 5%Ni13X-Nit is less than the others (Table 2.1). This is due to the different decomposition reactions of the Ni precursors. The very sharp exothermic burning stage (second peak) of Unc-5%Ni13X-Cit and Unc-5%Ni13X-Ace can be observed from Figure 2.7, while Unc-5%Ni13X-Nit did not have the exothermic stage.

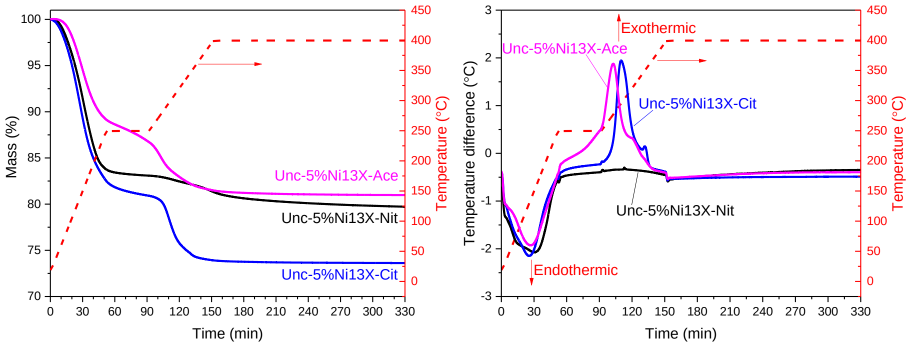

Figure 2.7: TG/DTA curves during thermal calcination under air for uncalcined Ni 13X samples prepared using nickel nitrate, nickel citrate and nickel acetate.

Table 2.1: Analysis summary of the TG/DTA results in Figure 2.7.

Sample	First mass loss[a]		Second mass loss[b]		Total mass loss
	Mass loss wt.%	Peak °C	Mass loss wt.%	Peak °C	wt.%
Unc-5%Ni13X-Nit	16.92	150	3.36	301	20.28
Unc-5%Ni13X-Cit	19.09	140	7.29	300	26.38
Unc-5%Ni13X-Ace	13.23	148	5.79	279	19.02

[a] Mass loss from room temperature to end of 250 °C; [b] Mass loss from 250 °C to end of 400 °C.

2.3.2. Experiments for catalysts performance on CO_2 methanation in a fixed bed reactor

2.3.2.1. Catalyst activity and selectivity

Ni- modified 13X and 5A zeolite catalysts activity and selectivity were tested in a lab scale fixed bed reactor system, and the results are shown in Figure 2.8 and Figure 2.9. The catalyst performance comparison with the results from literatures can be found in Table 2.2.

The CO_2 conversion at each temperature was the average value based on GC measurements for five times, which were stable after the zeolite absorbed some water under the experimental condition. The error bars in these figures show that all test results have a good reproducibility. As the catalyst was already saturated with water before activity and selectivity data was taken, adsorption enhancement can be excluded from the data. The thermodynamic equilibrium conversion of CO_2 was calculated to compare with the performance of the catalysts. It can be observed, that the CO_2 conversion is very close to the equilibrium value for most catalysts at 440 °C and for the most active catalysts rather close even at 320 °C. As the sorption enhancement effect of the zeolites was intentionally suppressed in this study to obtain comparable results with other catalysts, e.g. the conversion of the most active catalysts decreases after 320°C due to the thermodynamic limitations. Moreover, all the curves of CO_2 conversion in Figure 2.8 show a similar trend with increasing temperature, as the conversion increases dramatically from below 20% to near equilibrium followed by a decrease due to equilibrium limitations. The reaction is limited by kinetics at low temperature [137] and by thermodynamics at high temperatures [154].

Overall (Figure 2.8), the CO_2 conversion orders are 5%Ni13X-Cit > 5%Ni13X-Ace > 5%Ni13X-Nit, 5%Ni5A-Ace ≈ 5%Ni5A-Nit > 5%Ni5A-Cit. The CH_4 selectivity orders are 5%Ni13X-Cit > 5%Ni13X-Ace > 5%Ni13X-Nit, 5%Ni5A-Cit ≈ 5%Ni5A-Ace > 5%Ni5A-Nit. Ni13X zeolite catalysts made from nickel citrate and nickel acetate display a better conversion than all the other catalysts in the temperature range 240-440 °C. Even though most 5A zeolite supported catalysts display high CH_4 selectivity at low temperature (selectivity (100-x)% means x% CO is formed), the performance (conversion and selectivity) of the 5A zeolite supported catalysts are inferior to those of 5%Ni13X-Cit and 5%Ni13X-Ace, at temperatures around 320-360 °C. This may be attributed to a combination of acidity and particle size. Particles are formed inside the pores of 13X and they naturally possess a narrower particle size distribution compared to the particles, which are formed on the surface of the zeolite particles. Weak acidity inside 13X favors the interaction with CO_2. Additionally, according to the CO_2 methanation mechanism, more cations (e.g., Na^+, Mg^{2+}) in 13X zeolite may contribute the higher CO_2 adsorption thereby higher higher conversion during CO_2 methanation [40].

For Ni 5A zeolite catalysts, more Ni was located outside the 5A crystal surface and not homogenously distributed as with the Ni 13X zeolite catalysts (Figure 2.3). The small particles dispersed homogenously on zeolite are believed to be the most effective in CO_2 methanation. Additionally, the catalyst selectivity for CH_4 may be associated with the weak acidity of catalysts [170]. 5%Ni13X-Cit has the highest weak acidity, which may be one reason why it has the highest CH_4 selectivity among the Ni- 13X catalysts prepared with different Ni precursors. 5%Ni5A-Nit, 5%Ni5A-Cit and 5%Ni5A-Ace have a close value of weak acidity (Figure 2.6), which may result in the close CH_4 selectivity values.

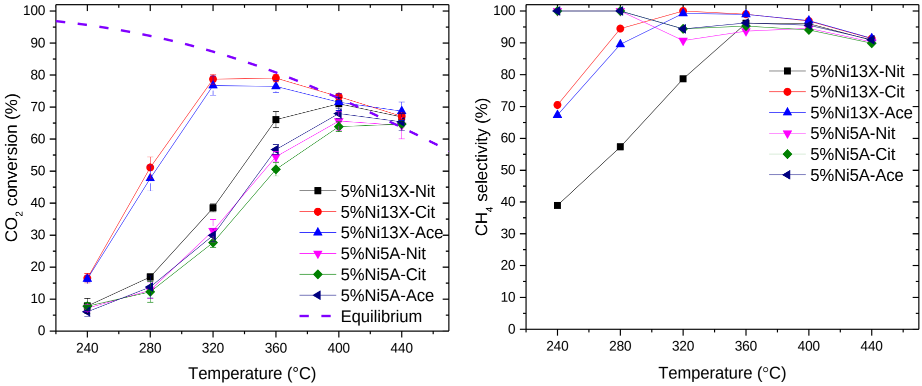

Figure 2.8: CO_2 conversion (left) and CH_4 selectivity (right) using catalysts with different Ni precursors (reduction at 500 °C, 4h), 0.9g, 150 ml/min N_2, 40 ml/min H_2, 10 ml/min CO_2.

In conclusion, nickel citrate is clearly an interesting Ni precursor for preparing

Ni13X zeolite catalysts with the evaporation impregnation method for CO_2 methanation.

The catalyst's calcination temperature is an important factor for catalyst activity, since the calcination procedure is a key factor for the growth of metal sites. Too high temperatures may lead to the sintering of the active metal and reduce the number of active sites. The calcination temperature influenced the conversion of CO_2 and selectivity towards CH_4. An optimum was found at 400 °C as displayed in Figure 2.9 as higher or lower temperature resulted in lowered activity and selectivity.

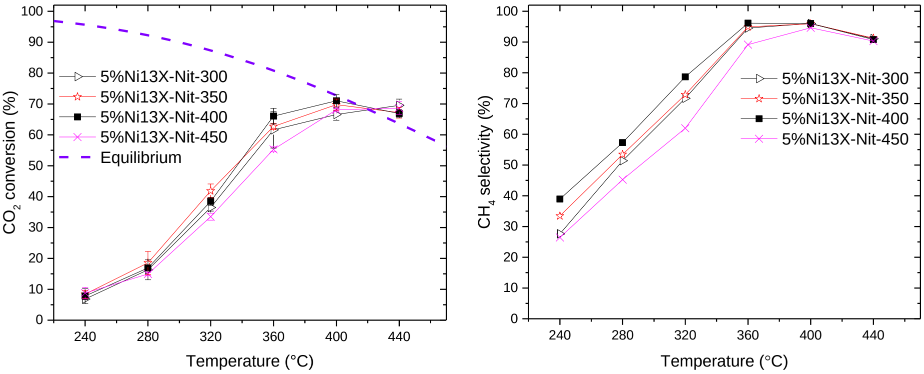

Figure 2.9: CO_2 conversion (left) and CH_4 selectivity (right) using catalysts with different calcination temperatures (reduction at 500 °C, 4h), 0.9g, 150 ml/min N_2, 40 ml/min H_2, 10 ml/min CO_2.

Table 2.2: Catalysts performance comparison with the results from literature sources.

Catalyst[a]	NiO or Ni particle size (nm)	Reactor ID (mm)	Catalyst size (mm)	Catalyst for test (g)	$H_2/CO_2/$ Inert gas ratio	Total flow (ml/min) (1 bar)	GHSV Or WHSV	CO_2 Conversion (%)	CH_4 Selectivity (%)	Rate ($mol\_CO_2/mol\_Ni/s$)[b]	Activation energy (kJ/mol)	Ref.
5%Ni13X-Nit	12.3	10	0.212-0.5	0.9	4:1:15	200	13333[w]	7.8, 240 °C 16.9, 280 °C	38.9, 240 °C 57.3, 280 °C	0.0030 0.0066	56[c]	This ch.
5%Ni13X-Cit	11.5	10	0.212-0.5	0.9	4:1:15	200	13333[w]	16.5, 240 °C 51.1, 280 °C	70.5, 240 °C 94.5, 280 °C	0.0064 0.0198	29[c]	This ch.
5%Ni13X-Ace	5.2	10	0.212-0.5	0.9	4:1:15	200	13333[w]	16.3, 240 °C 47.7, 280 °C	67.3, 240 °C 89.5, 280 °C	0.0063 0.0185	32[c]	This ch.
5%Ni5A-Nit	9.7	10	0.212-0.5	0.9	4:1:15	200	13333[w]	7.2, 240 °C 12.8, 280 °C	100, 240 °C 100, 280 °C	0.0028 0.0050	61[c]	This ch.
5%Ni5A-Cit	6.3	10	0.212-0.5	0.9	4:1:15	200	13333[w]	7.8, 240 °C 12.3, 280 °C	100, 240 °C 100, 280 °C	0.0030 0.0048	55[c]	This ch.
5%Ni5A-Ace	5.7	10	0.212-0.5	0.9	4:1:15	200	13333[w]	6.0, 240 °C 13.8, 280 °C	100, 240 °C 100, 280 °C	0.0023 0.0054	53[c]	This ch.
5%Ni13X-Nit-300	_	10	0.212-0.5	0.9	4:1:15	200	13333[w]	6.8, 240 °C 16.3, 280 °C	27.6, 240 °C 51.4, 280 °C	0.0026 0.0063	55[c]	This ch.
5%Ni13X-Nit-350	13.5	10	0.212-0.5	0.9	4:1:15	200	13333[w]	8.4, 240 °C 18.5, 280 °C	33.5, 240 °C 53.5, 280 °C	0.0033 0.0072	56[c]	This ch.
5%Ni13X-Nit-450	11.6	10	0.212-0.5	0.9	4:1:15	200	13333[w]	8.8, 240 °C 14.9, 280 °C	26.4, 240 °C 45.3, 280 °C	0.0034 0.0058	55[c]	This ch.
5%Ni/MSN	9.9	8	0.2-0.4	0.2	4:1:0	167	50000[w]	82, 350 °C	99.9, 350 °C	0.1196	76	[171]
5%NiUSY	-	-	-	-	36:9:10	250	43000/h	2.2, 250 °C 9.4, 300 °C	- -	0.0048	_	[40]
5%NiUSY	17-33	-	-	-	36:9:10	250	43000/h	2.1, 250 °C 6.7, 300 °C	99.4, 250 °C 93.1, 300 °C	0.0205	_	[43]
20%Ni/SiO_2	21.1	9	0.07-0.59	0.2	76:19:5	33	10000[w]	41, 350 °C	89, 350 °C	0.0046	_	[172]
5%NiMSN	9.9	8	0.02-0.04	0.2	4:1:0	167	50000[w]	64.1, 300 °C	99.9, 300 °C	0.0146	_	[58]
5%Ni/MCM-41	10.5	8	0.02-0.04	0.2	4:1:0	167	50000[w]	56.5, 300 °C	98.3, 300 °C	0.0030	_	[58]
5%Ni/HY	19.8	8	0.02-0.04	0.2	4:1:0	167	50000[w]	48.5, 300 °C	96.4(300 °C	0.0935	76	[58]
5%Ni/SiO_2	17.8	8	0.02-0.04	0.2	4:1:0	167	50000[w]	42.4, 300 °C	96.6, 300 °C	0.0824	78	[58]
5%Ni/γ-Al_2O_3	-	8	0.02-0.04	0.2	4:1:0	167	50000[w]	27.6, 300 °C	95.2, 300 °C	0.0707	81	[58]
20%Ni/Al_2O_3	>10	-	0.212-0.25	0.7	6:30:64	750	55000/h	20, 300 °C	99.8, 300 °C	0.0618	84	[173]
10%Ni/H-Y	17.0	9	0.3-0.5	0.5	4:1:1.25	250	10000/h	15, 350 °C	88, 350 °C	0.0403	103	[41]
10%Ni/Na-Y	19.8	9	0.3-0.5	0.5	4:1:1.25	250	10000/h	30, 350 °C	82, 350 °C	0.0094	_	[41]
10%Ni/H-BETA	19.1	9	0.3-0.5	0.5	4:1:1.25	250	10000/h	23, 350 °C	88, 350 °C	0.0066	_	[41]
10%Ni/Na-BETA	20.1	9	0.3-0.5	0.5	4:1:1.25	250	10000/h	33, 350 °C	88, 350 °C	0.0131	_	[41]

[a] HY or H-Y = protonated Y zeolite; USY=ultra-stable Y zeolite; H-BETA= protonated BETA zeolite. [b] Calculated under the specific temperature based on the total Ni metal in catalyst. [c] Calculated based on Arrhenius plots in the temperature range 553-593K. [w]-WHSV.

2.3.2.2. *Catalyst stability*

The catalyst stability in conversion and selectivity experiments were carried out in the same fixed bed reactor system. The CO_2 conversion and CH_4 selectivity of 5%Ni13X-Cit at 360 °C are shown in Figure 2.10 for two different catalyst loadings (0.2 g and 0.9 g). The experiment employing a lower catalyst amount was performed to decrease the conversion below the equilibrium. The results for conversion and selectivity are similar to its counterpart in Figure 2.8, taking into account that the temperature in Figure 2.10 is fixed. 5%Ni13X-Cit had an excellent stability at 360 °C and it displayed high CH_4 selectivity (above 96%).

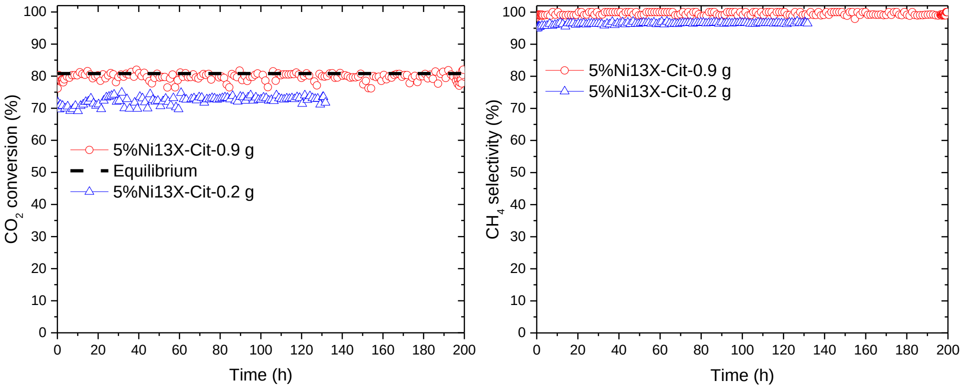

Figure 2.10: CO_2 conversion (left) and CH_4 selectivity (right) of 5%Ni13X-Cit at 360 °C with 150 ml/min N_2, 40 ml/min H_2, 10 ml/min CO_2.

2.4. Conclusions

Ni- modified 13X and 5A zeolite catalysts were synthesized using the evaporation impregnation method. The effect of Ni precursors and calcination temperature on the physico-chemical properties, and the catalytic performance in CO_2 methanation were investigated. The physico-chemical properties of the 13X and 5A zeolite, and Ni modified zeolite catalysts were characterized using XRD, SEM-EDX, TEM, STEM-EDX, N_2 physisorption, H_2-TPR and TPD-NH_3. The physico-chemical characterization results show that the crystal structure of 13X and 5A zeolites stays intact with all precursors. Nickel citrate combined with a rather low calcination temperature leads to Ni modified 13X and 5A zeolite catalysts which can be easily reduced at lower temperature compared to the other Ni 13X and 5A zeolite catalysts made with acetate and nitrate. The 13X supported catalysts outperformed the ones synthesized with 5A mainly due to the better penetration of the metal precursors into the zeolite structure. The nickel citrate precursor resulted in better dispersion compared to nitrate and acetate, which resulted also in better performance. 5%Ni13X-cit zeolite catalyst prepared with nickel citrate showed high activity and CH_4 selectivity in the Sabatier reaction at remarkably low temperatures and the catalyst displayed good stability. The current chapter clearly shows how the selection of precursor can influence the properties of a nickel modified catalyst.

2.5. Supplementary Material

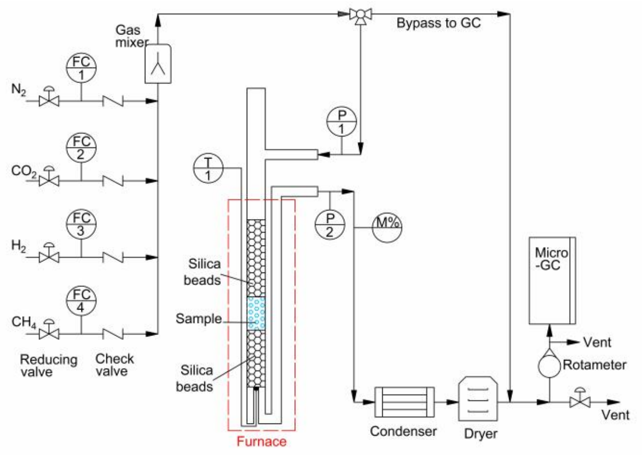

Figure S. 2.1: Scheme of the fixed bed reactor system, there is a thermocouple (T1) inserted into the lower part of the catalyst bed and connected to a computer for data acquisition).

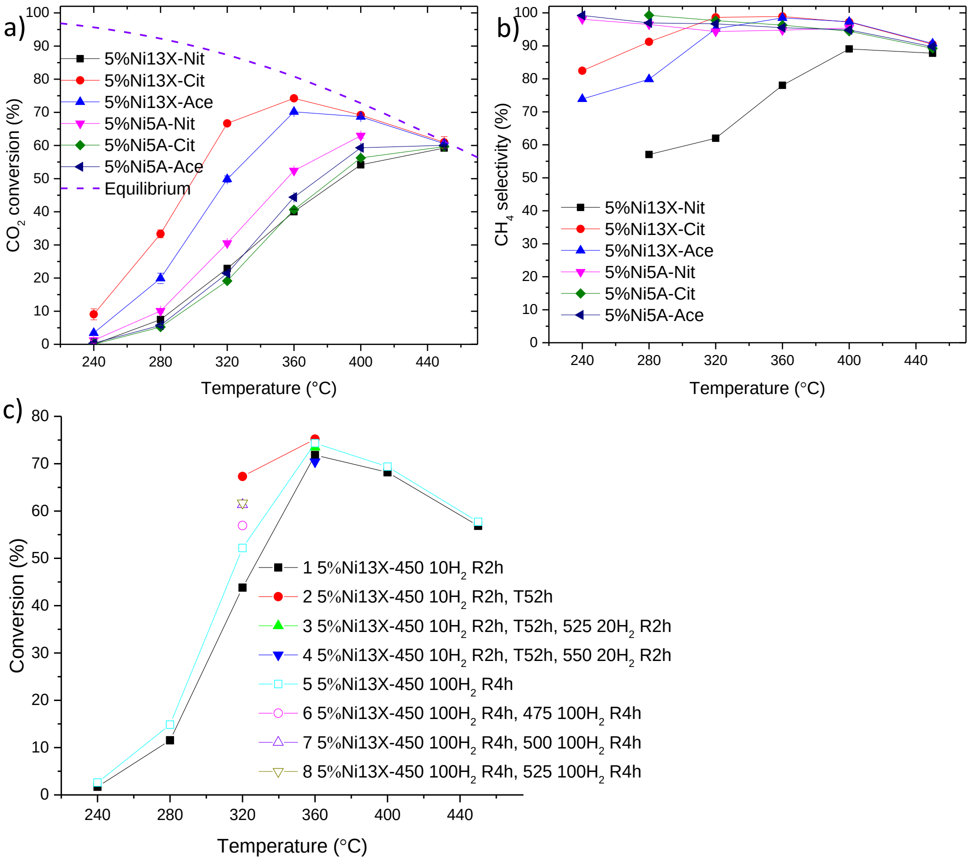

Figure S. 2.2: a) and b) CO_2 conversion using Ni 13X and Ni 5A catalysts with different Ni precursors (reduction at 450 °C, 10 ml/min H_2 diluted by 200 ml/min N_2, 2h), 0.9g, 150 ml/min He, 40 ml/min H_2, 10 ml/min CO_2.

c) H_2 conversion with 5%Ni13X (nickel nitrate, complexor), 0.9g, different reduction conditions:

1. 450 °C, under 200 N_2 and 10 ml/min H_2 2h;
2. 450 °C, under 200 N_2 and 10 ml/min H_2 2h + 52 hour of activity test;
3. 450 °C, under 200 N_2 and 10 ml/min H_2 2h + 52 hour of activity test + 525 °C, under 180 N_2 20 ml/min H_2 2h;
4. 450 °C, under 200 N_2 and 10 ml/min H_2 2h + 52 hour of activity test +525 °C, under 180 N_2 20 ml/min H_2 2h +550 °C, under 180 N_2 20 ml/min H_2 2h;
5. 450 °C, under 100 ml/min H_2 4h;(changed to a fresh catalyst from this experiment)
6. 450 °C, under 100 ml/min H_2 4h + 475 °C, under 100 ml/min H_2 4h;
7. 450 °C, under 100 ml/min H_2 4h + 475 °C, under 100 ml/min H_2 4h + 500 °C, under 100 ml/min H_2 4h;
8. 450 °C, under 100 ml/min H_2 4h + 475 °C, under 100 ml/min H_2 4h + 500 °C, under 100 ml/min H_2 4h + 525 °C, under 100 ml/min H_2 4h.

input gases for test:150 ml/min N_2, 40 ml/min H_2, 10 ml/min CO_2.

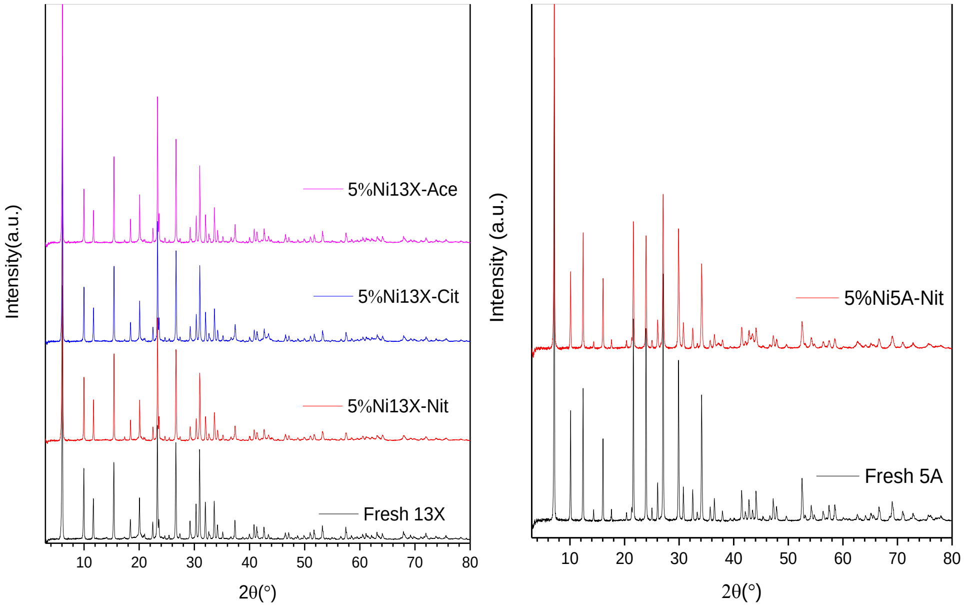

Figure S. 2.3: The XRD background corrected diffractograms for fresh zeolite 5A, 13X, Ni-zeolite 13X and 5A catalysts with different Ni precursors.

Table S. 2.1: The pH of solution during catalysts preparation**.**

Item	pH of distilled water	pH of Nickel salts solution	pH of salt solution with zeolite
5%Ni13X-Nit	_	7.4	7.7
5%Ni13X-Cit	7.5	4.9	8.8
5%Ni13X-Ace	7.4	7.4	7.8
5%Ni5A-Nit	_	7.3	7.7
5%Ni5A-Cit	7.3	4.7	8.5
5%Ni5A-Ace	7.3	7.3	7.6

Table S. 2.2: Summary of the EDX results for the catalysts and fresh zeolites**.**

Sample	Content (wt./wt.%)									
	O	Na	Mg	Al	Si	Cl	K	Ca	Fe	Ni
Fresh 13X	51.8 ±0.6	12.6 ±0.3	1.3 ±0.1	13.0 ±0.3	20.3 ±0.3	–	–	0.5 ±0.1	0.6 ±0.1	–
5%Ni13X-Nit	58.6 ±0.5	10.7 ±0.2	0.7 ±0.1	10.2 ±0.2	15.6 ±0.1	0.1 ±0.0	0.1 ±0.0	0.3 ±0.0	0.5 ±0.1	3.2 ±0.2
5%Ni13X-Cit	58.3 ±0.5	11.6 ±0.2	0.8 ±0.1	9.8 ±0.1	15.0 ±0.1	–	0.2 ±0.0	0.3 ±0.0	0.5 ±0.1	3.5 ±0.2
5%Ni13X-Cit-Spent	56.5 ±0.5	11.9 ±0.2	0.6 ±0.1	10.3 ±0.1	16.0 ±0.1	–	0.1 ±0.0	0.4 ±0.0	0.4 ±0.1	3.6 ±0.2
5%Ni13X-Ace	51.9 ±0.5	9.9 ±0.3	1.1 ±0.1	11.6 ±0.2	19.7 ±0.2	–	–	0.5 ±0.1	0.6 ±0.1	4.6 ±0.2
Fresh 5A	57.7 ±0.5	3.9 ±0.1	0.1 ±0.0	14.3 ±0.1	14.3 ±0.1	0.5 ±0.1	–	8.8 ±0.1	0.3 ±0.1	–
5%Ni5A-Nit	59.3 ±0.5	3.9 ±0.2	–	12.6 ±0.1	13.5 ±0.1	0.4 ±0.1	–	6.4 ±0.1	0.2 ±0.1	3.9 ±0.2
5%Ni5A-Cit	49.5 ±0.4	3.5 ±0.1	–	15.5 ±0.1	15.8 ±0.1	0.4 ±0.1	–	11.0 ±0.1	–	4.2 ±0.2
5%Ni5A-Ace	56.5 ±0.5	3.1 ±0.2	0.1 ±0.1	13.9 ±0.1	15.0 ±0.1	0.3 ±0.0	–	7.1 ±0.1	–	4.0 ±0.2

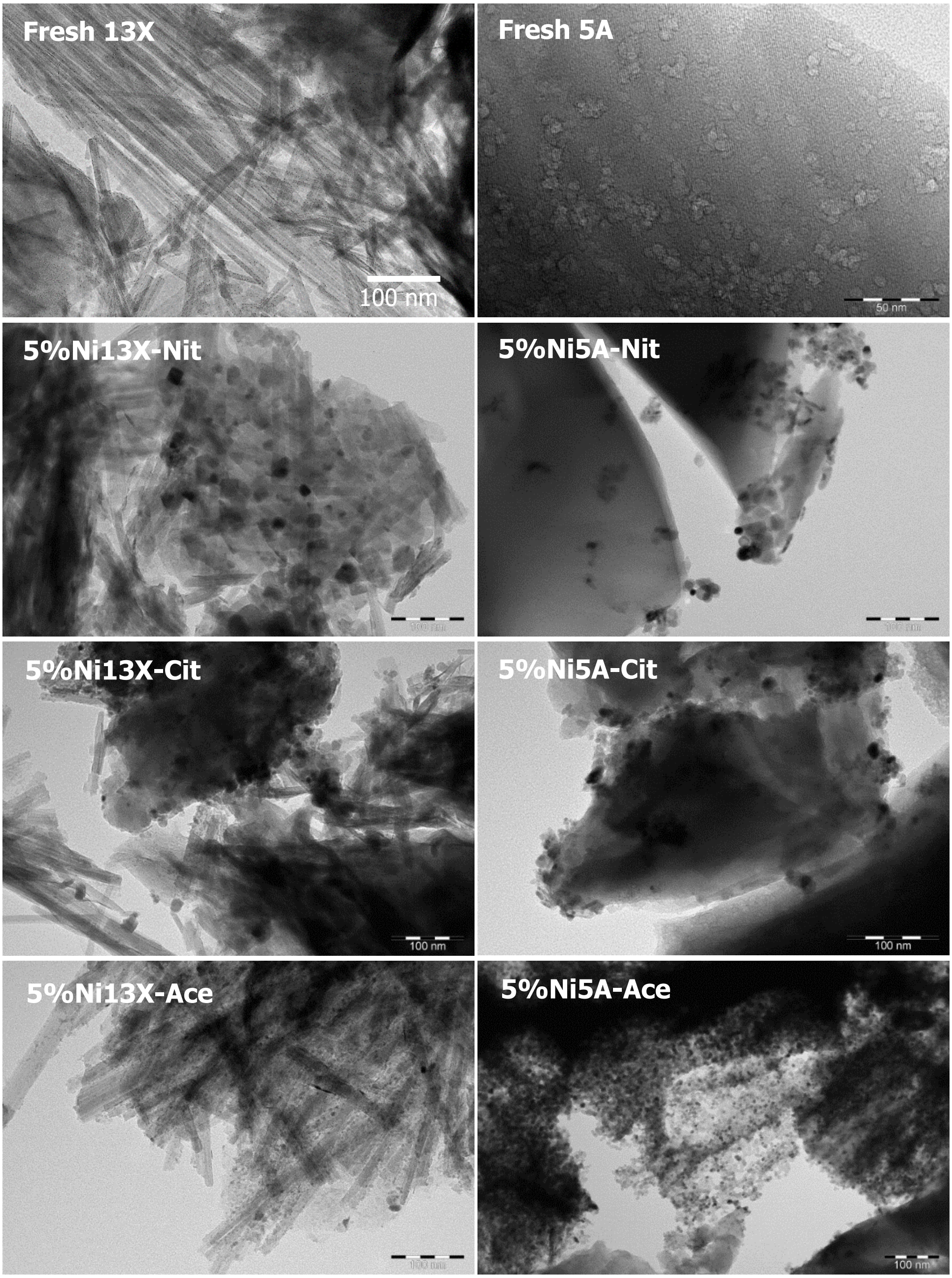

Figure S. 2.4: Transmission electron micrographs of fresh 13X, fresh 5A, 5%Ni13X-Nit, 5%Ni13X -Cit, 5%Ni13X -Ace, 5%Ni5A-Nit, 5%Ni5A-Cit, 5%Ni5A-Ace zeolite catalysts with nickel nitrate, nickel citrate and nickel acetate precursors

Table S. 2.3: The average particle size and particle size range of NiO on Ni modified catalysts (measured from TEM images using Image J software) These are of course the precipitates of the precursors after the evaporation treatment.

Catalyst	NiO particle size range (nm)	Average particle size of NiO (nm)
5%Ni13X-Nit	1.6-57.0	12.3
5%Ni13X-Cit	3.6-27.3	11.5
5%Ni13X-Ace	1.7-62.7	5.2
5%Ni5A-Nit	0.7-28.2	9.7
5%Ni5A-Cit	2.1-15.5	6.3
5%Ni5A-Ace	2.3-13.3	5.7
5%Ni13X-Nit-350	1.0-68.0	13.5
5%Ni13X-Nit-450	2.8-85.6	11.6

Table S. 2.4: The specific surface area and pore volumes of fresh zeolites and catalysts.

Sample	Specific surface area (m^2/g_{cat})	V_{tot} (cm^3/g_{cat})
13X zeolite	654.78	0.27
5%Ni13X-Nit	361.49	0.89
5A zeolite	592.52	0.25
5%Ni5A-Nit	454.14	1.01

Table S. 2.5: The peaks area and H_2 consumption calculated from TPR results.

Sample	Peak area 1	Peak area 2	Peak area 1/ Peak area 2	Total H_2 consumption ($mmol/g_{catalyst}$)[a]
5%Ni13X-Nit	31.6	8.0	3.9	0.59
5%Ni13X-Cit	9.6	12.3	0.8	0.33
5%Ni13X-Ace	4.8	19.6	0.2	0.37
5%Ni5A-Nit	6.2	20.0	0.3	0.39
5%Ni5A-Cit	13.1	5.6	2.3	0.28
5%Ni5A-Ace	9.1	8.9	1.0	0.27
5%Ni13X-Nit-300	13.6	29.6	0.5	0.65
5%Ni13X-Nit-350	51.7	5.4	9.6	0.85
5%Ni13X-Nit-400	31.6	8.0	3.9	0.59
5%Ni13X-Nit-450	21.6	15.7	1.4	0.56

[a] The total H_2 consumption is a relative value, it was calculated from the total peak area divided by theoretical area/($mmol/g_{catalyst}$), which assumed the biggest total peak area of catalysts is the theoretical area for 5wt.% Ni reduced from NiO.

The acidity of fresh zeolite and Ni-zeolite catalysts was determined by NH_3-TPD. The NH_3-TPD profiles of Ni-zeolite catalyst prepared with different Ni precursors are shown in Figure S. 2.5. The calculation results are shown in Table S. 2.6.

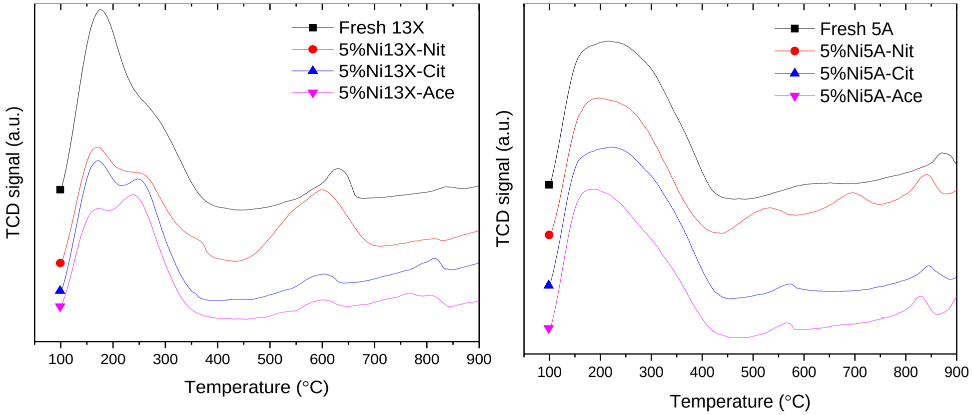

Figure S. 2.5: NH_3-TPD profiles of Ni-zeolite catalyst made from different Ni precursors.

Table S. 2.6: The catalyst acidity distribution calculated based on the results of NH_3-TPD [170].

Sample	Total acidity µmol/g	Weak acidity µmol/g (100-350 °C)	Medium acidity µmol/g (350-450 °C)	Strong acidity µmol/g (450-700 °C)
Fresh 13X	131	116	0	15
5%Ni13X-Nit	119	74	5	40
5%Ni13X-Cit	99	89	0	10
5%Ni13X-Ace	87	81	0	6
Fresh 5A	141	125	9	7
5%Ni5A-Nit	137	105	0	32
5%Ni5A-Cit	135	114	15	6
5%Ni5A-Ace	124	114	0	10

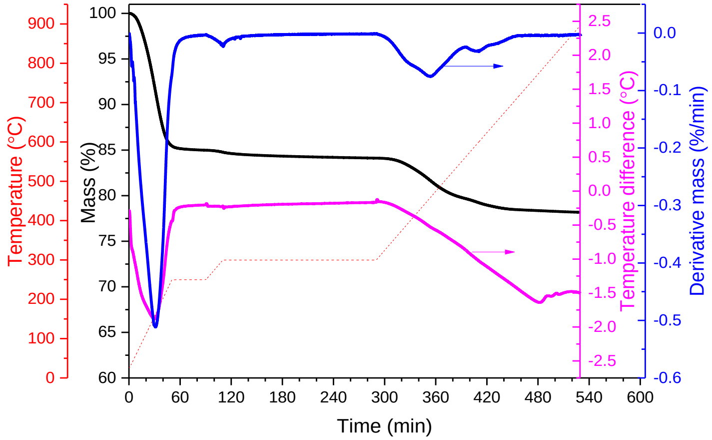

Figure S. 2.6: The TG/DTA curves for uncalcined unc-5%Ni13X-Nit (prepared using nickel nitrate). The sample was investigated using TG/DTA under 50 ml/min air atmosphere. The first heating step was to 250 °C with 4.5 °C/min and then kept constant for 40 minutes. Then the sample was heated to 300 °C with 2.5 °C/min and held there for 3 hours. Then, the sample was heated to 900 °C with 2.5 °C/min.

3

Can Ru improve Ni 13X and 5A zeolite catalysts for CO_2 methanation?

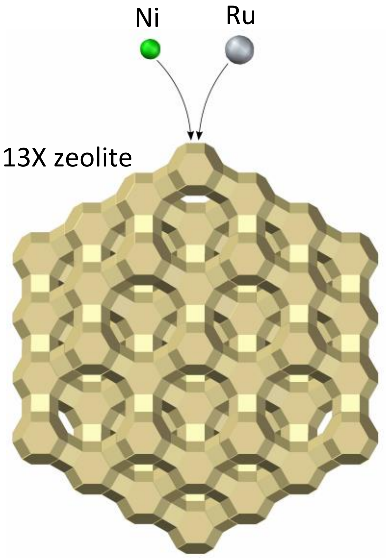

For $CO_2+4H_2\leftrightarrow 2H_2O+CH_4$?

Keywords of this chapter:

Ni and Ru,

13X and 5A zeolite catalysts,

CO_2 methanation.

This chapter is based on the following publication:
L. Wei, N. Kumar, W. Haije, J. Peltonen, M. Peurla, H. Grénman, W. de Jong, Can bi-functional nickel modified 13X and 5A zeolite catalysts for CO_2 methanation be improved by introducing ruthenium? Molecular Catalysis, 2020. 494: p. 111115. [174].

3.1. Introduction

Hydrogen energy is regarded as one of the most potential clean energy sources in 21st century. It can be produced from carbon fuels conversion like biomass gasification [130, 175], or made from electricity and water, however, it is difficult to store and dangerous to transport, especially on a large scale [133]. These challenges limit the transition to hydrogen economy [176]. Simultaneously, global warming is one of the most important environmental issues and the greatest challenges facing humanity today. Carbon dioxide is one of the most important greenhouse gases emitted in large scale from fossil fuel combustion processes. One of the methods for tackling these challenges is to capture CO_2 e.g. from stack sources and perform methanation with renewable H_2 via the Sabatier reaction ($CO_2 + 4H_2 \leftrightarrow CH_4 + 2H_2O$; ΔH^0_{298}= -165 kJ/mol) [135, 136, 177]. The product methane fits directly into existing energy infrastructure.

In order to meet the gas grid requirement for substitute gas high purity is required, however, this requires in practice efficient shift of the equilibrium (for high conversion) i.e. practically the removal of water [33, 178]. These results show that there is clear benefit to be gained by having the sorption properties in close vicinity of the active metals. This can be achieved by sequential reaction-separation steps in e.g. alternating fixed bed reactors [33].However, a more elegant and most probably economic alternative would be combining these functions, the catalytic and adsorptive, into a single bi-functional catalyst. Delmelle et al. studied the sorption enhanced methanation of CO_2 by loading Ni on zeolite 5A and 13X with wet impregnation and, they found that Ni/zeolite catalysts have a high activity and selectivity in CO_2 methanation [26]. Borgschulte et al. modified zeolite 5A by Ni, and observed a significant sorption enhanced effect in CO_2 methanation [137]. Methanation has been studied with different metals based catalysts, such as Ru, Ir, Rh and Ni [6, 135, 179-182]. Ni based catalysts is the most widely used due to its rather high activity, CH_4 selectivity and low cost [53, 54, 138, 178, 181]. Ru is known to be more active compared to Ni, with also high CH_4 selectivity and low coke forming properties [6, 183]. From the adsorption point of view, zeolites 13X and 5A are know for their high water-uptake properties [26, 47, 137].

The current project focuses on synthesis of bi-functional material possessing both catalytic and water adsorptive properties by depositing nickel and/or ruthenium on zeolites 13X and 5A using evaporation impregnation. The aim in the current chapter was the comparison of catalytic activities of the synthesized monometallic Ni and Ru catalysts with the bi-metallic Ni/Ru catalysts with varying proportions of the metals excluding the sorption enhancement. The The high activity of Ru at low temperature could be beneficial for the sorption enhanced CO_2 methanation. Surprisingly, the combination of Ru and Ni is hardly mentioned in sorption enhanced methanation literature, therefore, Ru combined with Ni on 13X and 5A zeolite were synthesized, characterized and tested for CO_2 methanation.

In this paper, 5%Ni13X, 1%Ru4%Ni13X, 2.5%Ru2.5%Ni13X, 2.5%Ru13X, 5%Ni5A, 1%Ru4%Ni5A, 2.5%Ru2.5%Ni5A, 2.5%Ru5A zeolite catalysts were prepared by evaporation impregnation. The pH of the solution during the preparation of each catalyst was monitored by pH meter. After the catalyst were prepared, XRD, SEM-EDX, TEM, STEM-EDX, nitrogen physisorption and H_2-TPR were used for physico-chemical characterization of crystal structure, morphology, NiO particle size, surface area and pore volume. Additionally, NH_3-TPD was used to determine the acidity of catalysts. The activity and selectivity test of catalysts were carried out in a laboratory scale fixed bed reactor system (Figure S. 2.1).

3.2. Experimental

3.2.1. Catalyst preparation using evaporation impregnation, deposition precipitation and ion-exchange methods

The catalyst 5%Ni13X, 1%Ru4%Ni13X, 2.5%Ru2.5%Ni13X, 2.5%Ru13X, 5%Ni5A, 1%Ru4%Ni5A, 2.5%Ru2.5%Ni5A and 2.5%Ru5A were prepared by evaporation impregnation method. A Ni-, Ru-, metal loading of 5% was targeted on the 13X and 5A zeolite supports. Nickel nitrate hexahydrate ($Ni(NO_3)_2{\cdot}6H_2O$, 99%, Merck Millipore) and Ruthenium (III)-chloride hydrate ($RuCl_3{\cdot}xH_2O$, 99%, Aldrich) were used as the Ni and Ru precursors. The metal precursors were dissolved in 250 ml of distilled water in a flask, and 5 g of 0.212-0.500 mm size (sieved fraction and dried at 100 °C overnight in an oven) 13X zeolite (Honeywell Fluka, The Netherlands) or 5A zeolite (Merck Millipore, The Netherlands) was added to the solution. The pH of the solution was measured by a pH meter during this process. In order to avoid the mechanical wear of zeolite, the rotator evaporator was operated at low rotation speed, 10 rpm, for 24 h at room temperature. After 24 h of catalyst synthesis, evaporation of the aqueous solution was carried out in the rotator evaporator at 50 °C using a water jet pump. The catalyst was dried at 100 °C overnight in an oven before calcination.

All catalysts were calcined in a muffle furnace using a step calcination procedure. In the stepwise calcination procedure, the heating rate from room temperature to 250 °C was 4.5 °C/min, where it was kept for 40 min, after which the temperature was increased to the target temperature (e.g. 400 °C) by 2.5 °C/min, where it was kept for 3 h and then cooled down to room temperature.

3.2.2. Catalyst characterization

The calcined catalysts were characterized before reduction by X-ray powder diffraction (XRD), scanning electron microscopy (SEM), transmission electron microscopy (TEM), scanning transmission electron microscopy equipped with an energy-dispersive X-ray spectroscopy (STEM-EDX), nitrogen physisorption, hydrogen temperature programed reduction (H_2-TPR), and temperature programmed ammonia desorption (NH_3-TPD).

The PANalytical Empyrean X-ray powder diffractometer was used in the XRD measurements. The diffractometer was operated in Bragg-Brentano diffraction mode, and the monochromatized Cu-*K*α radiation (λ = 1.541874 Å) was generated with a voltage of 45 kV and a current of 40 mA. The measured XRD diffractograms were analyzed with Philips X'Pert HighScore (phase analysis refinement) and MAUD programs (background subtraction), and the scanning 2θ angle range was 3.0° to 80.0° by step size of 0.013°, counting time 80 seconds/step.

Catalysts morphology, shape, size and distributions of crystals were studied by scanning electron microscopy (SEM) LEO Gemini 1530 (LEO/ZEISS, Germany). The catalyst elemental analysis was carried out by energy dispersive X-ray spectroscopy (EDX).

Transmission electron microscopy (TEM) was used to study the Ni-, Ru- particle size and distributions. The average RuO_2 or NiO particle size was calculated. Furthermore structure, textural properties of the pristine 13X and 5A zeolites and Ru-, Ni- modified 13X and 5A catalysts were also investigated using transmission electron microscopy. The equipment used was JEM-1400 (JEOL ltd, Japan) which maximum acceleration voltage is 120 kV.

To further study the composition and the nanoscale structure of the catalysts, scanning transmission electron microscopy equipped with an energy-dispersive X-ray spectroscopy (STEM-EDX) detector was used. The equipment used was FEI Titan 80-300 electron microscope, the elemental mapping was investigated at a voltage of 300 kV with EDX. Specimen preparation consisted of immersing a lacey carbon film supported on a copper grid into the catalysts powder, small particles adhering to the carbon film were measured.

The surface area, pore size and pore volume of pristine 13X and 5A zeolite, Ni-, Ru- modified 13 X and 5A zeolite catalysts were measured by nitrogen adsorption. The instrument used was 3Flex Physisorption (Micromeritics Instrument Corp.). The calculation of surface area was carried out using the BET method. The catalysts were outgassed at 350 °C for 3 h, prior to the surface area measurement.

H_2-TPR analysis was carried out in a Micromeritics AutoChem 2910. The catalysts were dried at 250 °C for 1 h with dry Ar atmosphere, then reduced by 5% H_2 (diluted by Ar) from room temperature to 900 °C with 5 °C/min heating rate, a TCD detector was used to monitor the H_2 consumption.

Temperature programmed desorption was carried out in Micromeritics AutoChem 2910 to investigate the acidity of the catalysts, the samples were dried at 250 °C for 0.5 h with dry He atmosphere before ammonia adsorption (5% NH_3 diluted by He) at room temperature, the desorption temperatures were from 100 to 900 °C.

3.2.3. Catalyst test

The prepared catalyst activity, selectivity and stability were tested in a fixed bed reactor system (Figure S. 2.1, supplementary material), made of quartz reactor with an inner diameter of 10 mm. Silica beads (around 10 ml) were placed in the lower part of the reactor to support the catalyst bed then, silica beads and the catalyst were layered by quartz wool, and silica beads (around 10 ml) were used again to fill the reactor. The reactor was heated by a vertical tube furnace equipped with a K-type thermocouple, while the temperature of the catalyst bed was monitored by another K-type thermocouple which was inserted into the bottom of catalyst bed and connected to the computer for recording and showing. A schematic of the fixed bed reactor system can be found in Figure S. 2.1.

In the catalyst test, 0.9 g of catalyst was loaded into the reactor and reduced under 100 ml/min H_2 atmosphere at 500 °C for 4 hours. Catalysts activity experiments were performed at 240 °C to 440 °C with a gas hourly space velocity of 13333 ml/g_cat/h, in reaction, 40 ml/min H_2 and 10 ml/min CO_2 diluted by N_2 (150 ml/min). The product gas from the reactor was lead through a cooling condenser and then analyzed by GC (Varian, CP-4900 Micro-GC). Helium was used as the carrier gas.

The CO_2 conversion (3-1) and catalyst selectivity (3-2) for CH_4 are defined as [153, 154]:

$$X_{CO_2} = \frac{n_{CO_2,in} - n_{CO_2,out}}{n_{CO_2,in}} \tag{3-1}$$

$$S_{CH_4} = \frac{n_{CH_{4,out}}}{n_{CO_2,in} - n_{CO_2,out}} \tag{3-2}$$

Where n_{CO_2} is the input molar flow rate of CO_2 in experiment, $n_{CO_2,out}$, $n_{CH_{4,out}}$ are the molar flow rate of CO_2 and CH_4 calculated from GC results, respectively (selectivity <100% means CO is formed).

3.3. Results and discussion

3.3.1. Catalyst characterization results

3.3.1.1. X-ray powder diffraction

The crystal structure of the Ni modified catalysts 5%Ni13X, 5%Ni5A, Ni and Ru modified 13X and 5A zeolite, fresh 13X and 5A zeolite were investigated by XRD measurement. As in Figure 3.1, the X-ray powder diffraction patterns indicated that catalyst preparation did not influence the crystal structure of 13X and 5A zeolites. Additionally, the peaks of RuO_2 for Ru modified 13X zeolite and 5A were observed from the XRD peaks, while the peaks for NiO could not be identified in the X-ray powder diffraction patterns (Figure 3.1). The plausible explanation for this observation could be the peak broadening due to lowered crystallinity as well as small nanoparticle size in the lower end of the particle size distribution (0.72- 28.23 nm) (Table S. 3.4).

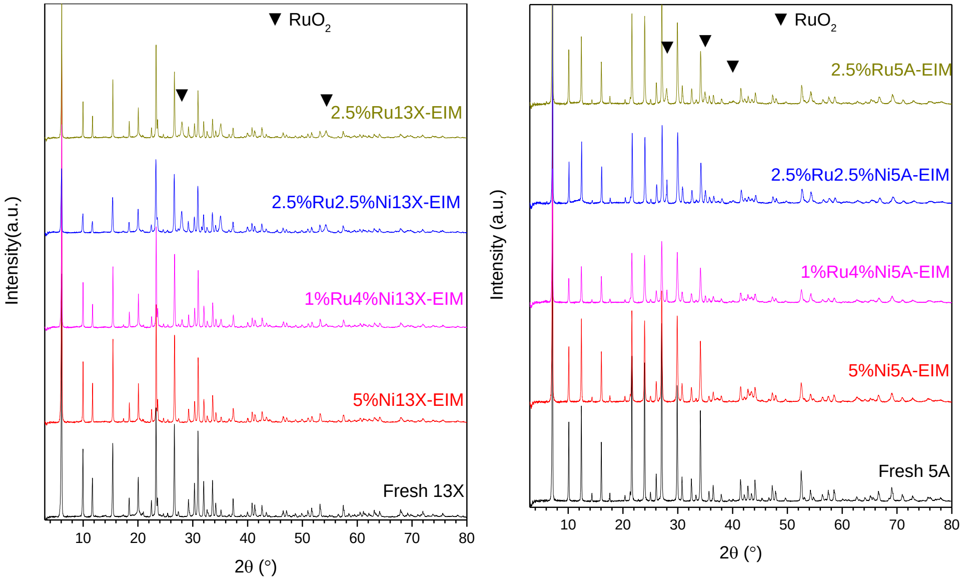

Figure 3.1: X-ray powder diffraction patterns for Ni or Ru13X and 5A zeolite catalysts, fresh 13X and 5A zeolite.

3.3.1.2. Scanning electron microscopy (SEM) and Energy dispersive X-ray spectroscopy (EDX)

The morphology of Ni and Ru modified catalysts were investigated by SEM, as shown in Figure 3.2. The 13X zeolite showed large crystals (around 2μm) composed of small fibrous crystals [26], less visible in 1%Ru4%Ni13X and 2.5%Ru2.5%Ni13X

(Figure 3.2). The small fibrous crystals of fresh 13X and 5%Ni13X are much more visible than in 1%Ru4%Ni13X and 2.5%Ru2.5%Ni13X. This may be due to change of fibrous crystals during the catalyst preparation, due to the acidic pH of Ruthenium (III)-chloride aqueous solution. The pH of the solution decreased dramatically from 6.69 to around 2.32 (Table S. 3.2, supplementary material), when ruthenium chloride was dissolved in the solution, while it increased to 4.13 after 13X zeolite was introduced. The increase in the pH of the ruthenium chloride solution after addition of 13X zeolite was attributed to the adsorption of ruthenium by 13X. The pH of solution was the lowest in the preparation of 2.5%Ru2.5%Ni13X and 2.5%Ru13X catalysts. By contrast, the pH of the solution was around 7.5 during the preparation of 5%Ni13X. The enhanced pH of the 5%Ni13X catalyst synthesis solution is attributed to the higher pH (7.4) of Ni $(NO_3)_2$ solution as compared to highly acidic pH (2.1) of $RuCl_3$ solution (Table S. 3.2).

Fresh 5A zeolite shows the smoothest crystal surface. The honeycomb type architecture of the 5A zeolite crystal surface could be NiO crystals, which displayed only on the Ni modified 5A zeolite surface.

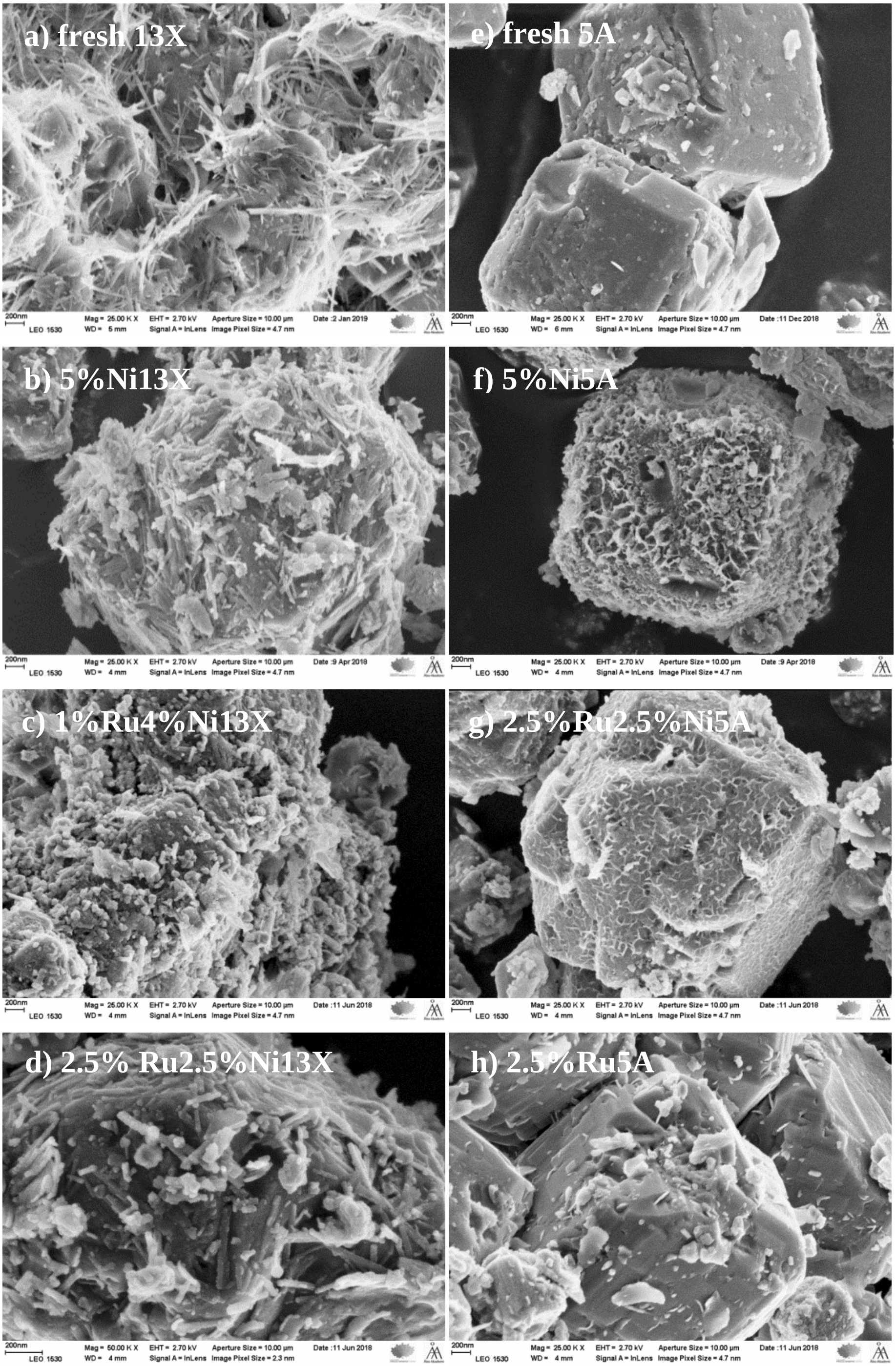

Figure 3.2: SEM images of fresh 13X zeolite, fresh 5A zeolite and calcined catalysts, a) fresh 13X zeolite, b) 5%Ni13X, c)1%Ru4%Ni13X, d) 2.5% Ru2.5%Ni13X, e) fresh 5A zeolite, f) 5%Ni5A, g) 2.5%Ru2.5%Ni5A h) 2.5%Ru5A.

In order to investigate the chemical composition of samples as well as the actual loading of Ni and Ru is in the Ni-, Ru-13X and 5A zeolite catalysts, SEM combined with EDX was employed. It was observed that Si to Al ratio in 13X and 5A zeolite did not change during the Ni, Ru modification (Table S. 3.3, supplementary material). This is consistent with the XRD results (Figure 3.1), which also show that the zeolite structure was maintained during modification.

3.3.1.3. Transmission electron microscopy (TEM)

The NiO particle size, distribution and morphology were analyzed with transmission electro micrographs (TEM). The images show the typical uniform porous structures of the 13X and 5A zeolite along with Ni and Ru nanoparticles. A small average NiO particle size around 10 nm can be observed for both 5%Ni13X and 5%Ni5A catalysts (Figure 3.3). However, the distribution of the particle size ranges from well below one nm upwards (Table S. 3.4) and the smallest particles are difficult to detect due to limitations of the analysis method. The results indicate that some of the Ni is located inside the pores of the 13X zeolite, however, the larger particles are clearly located on the external surface of the zeolite particles.

The RuO_2 was not well dispersed and displayed significantly larger average nanoparticle size and also the smallest detected particles were considerably larger than for Ni. RuO_2 appeared as big nanoparticles with a particle size range 7.3-97.7 nm (average 37.5 nm) for 2.5%Ru13X. The average RuO_2 particle size in 2.5%5A was around 44.9 nm (Table S. 3.4, supplementary material). These results clearly show that the majority of Ru is located on the external surface of the zeolite particles.

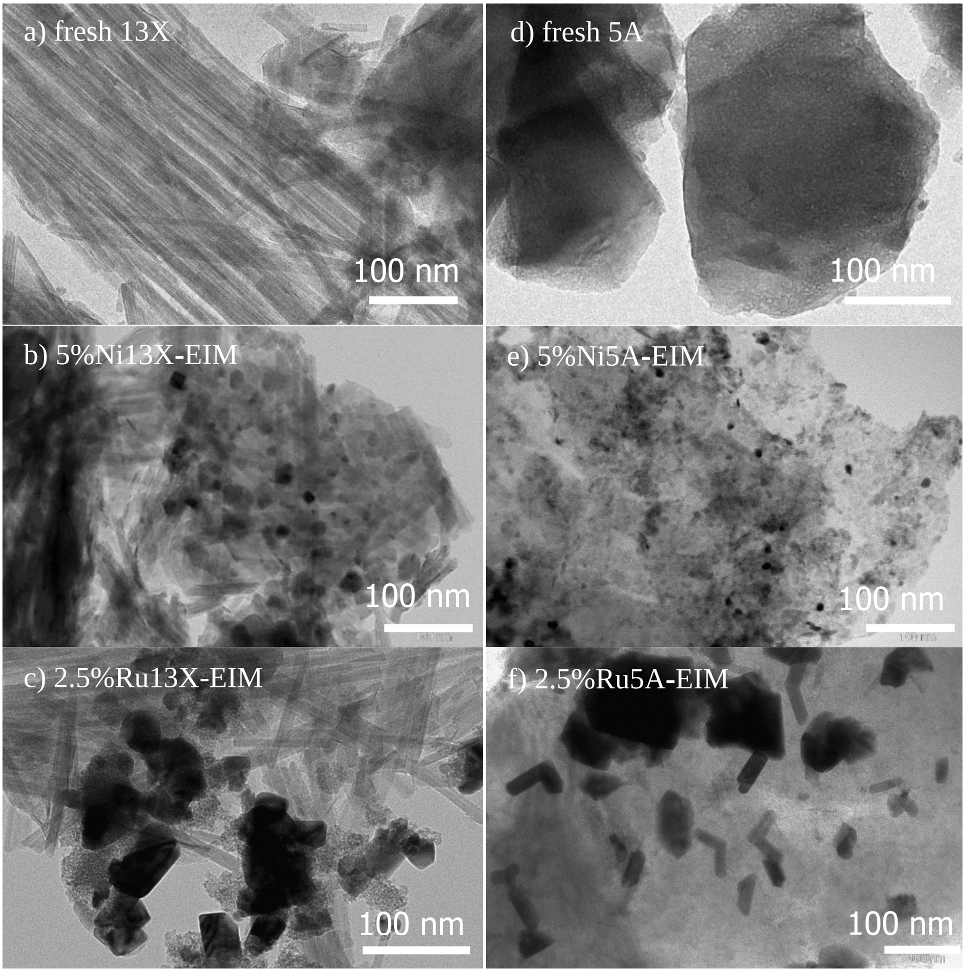

Figure 3.3: TEM images of a) fresh 13X, b) 5%Ni13X, c) 2.5%Ru13X, d) fresh 5A, e) 5%Ni5A and f) 2.5%Ru5A.

3.3.1.4. STEM-EDX

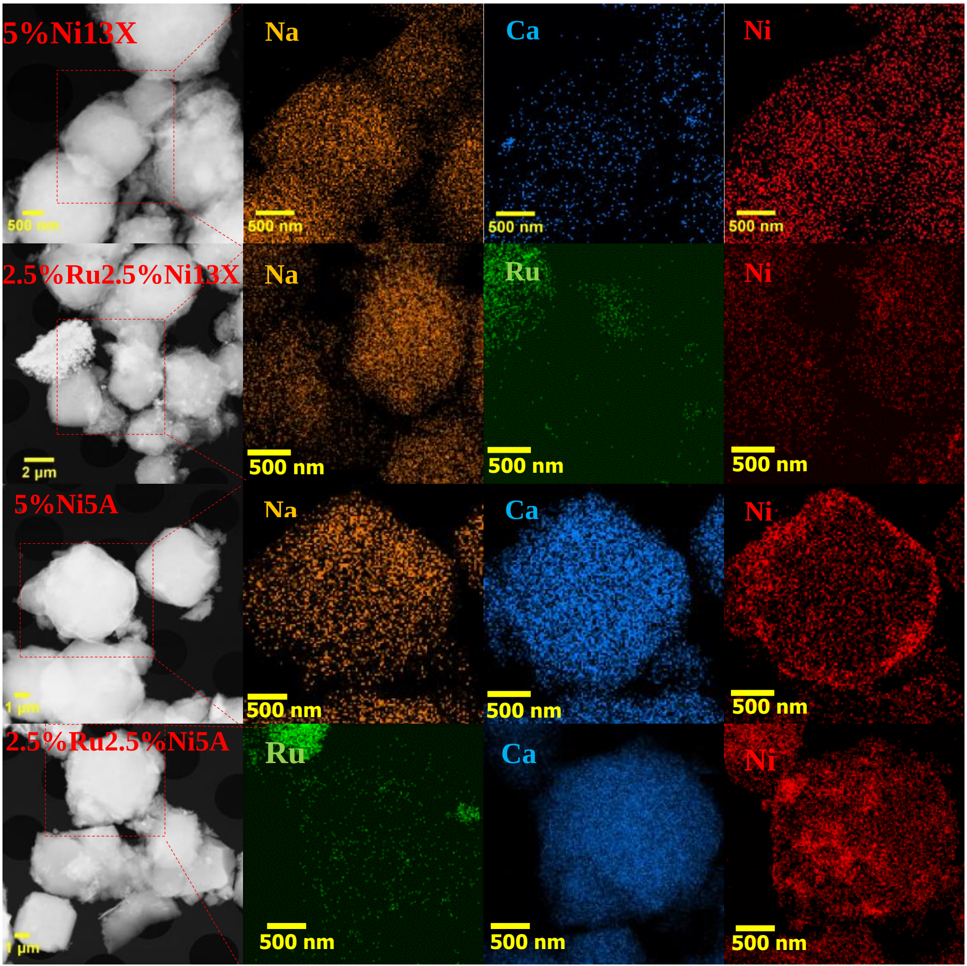

Figure 3.4: STEM images (first row), Na (gold), Ca (light blue), Ru(green) and Ni (red) maps of 5%Ni13X, 2.5%Ru2.5%Ni13X 5%Ni5A and 2.5%Ru2.5%Ni5A.

TEM is a good method for investigating nanoparticle size in mono-metallic catalysts, however, in bi-metallic catalysts, it is unable to distinguish between the metals. Moreover, some very small nano NiO (RuO_2) particles invisible in TEM pictures, while these metal sites are always with high activity in reaction since their high surface free energy [160]. For this purpose, STEM assisted with EDX was employed for studying the Ni-Ru catalysts.

The STEM images, Na (gold), Ca (blue), and Ni (red) maps of 5%Ni13X, 2.5%Ru2.5%Ni13X 5%Ni5A and 2.5%Ru2.5%Ni5A are shown in Figure 3.4. As can be seen from the images, Ni dispersed well on 13X zeolite even on the bi-metallic catalysts prepared by evaporation impregnation. However, Ni appeared to form a type of egg shell coating on zeolite 5A instead of penetrating evenly into the particles, and similar phenomenon can be seen when both Ru and Ni were loaded on 5A zeolite (2.5%Ru2.5%Ni5A). For the catalysts 2.5%Ru2.5%Ni13X and 2.5%Ru2.5%Ni5A, Ru nanoparticles are much bigger than Ni Similarly to the mono-metallic Ru catalysts, the presence of both metal precursors in the solution does not seem to enhance the dispersion of the metals (Ru-, Ni-) based on STEM-EDX.

3.3.1.5. Nitrogen physisorption

Nitrogen adsorption-desorption was used to determine the specific surface area and pore volume of fresh zeolite and the impregnated catalysts (Table S. 3.5, supplementary material).

Fresh 13X zeolite has the highest surface area 655 m^2/g, which is followed by 1%Ru4%Ni13X (640 m^2/g). The surface area decreased after the Ni modification for both 5%Ni13X and 5%Ni5A. Also, the micro-pore volume changed after the Ni loading on the 13X and 5A zeolite, and 5%Ni13X catalyst has the lowest micro-pore volume. The plausible reason for the decreasing of surface area and micropore volume is the blocking of micropores with NiO particles during the calcination step.

3.3.1.6. Temperature programed reduction

The H_2-Temperature programed reduction (H_2-TPR) profiles are shown in Figure 3.5 for 13X, 5%Ni13X, 1%Ru4%Ni13X, 2.5%Ru2.5%Ni13X, 2.5%Ru13X, fresh 5A zeolite, 5%Ni5A, 1%Ru4%Ni5A, 2.5%Ru2.5%Ni5A and 2.5%Ru5A.

As can be seen from Figure 3.5, a strong and broad peak can be observed at around 420 °C for the catalyst 5%Ni13X, which should correspond to the NiO particles in the super cages or on the surface of 13X zeolite [43, 147]. Some nickel hydroxyaqua complexes may also be generated in the solution during catalysts preparation [184-186], which do not penetrate the pores of 13X zeolite as sufficiently leaving some of the NiO on or close to the surface of the particles. By contrast, two obvious peaks (at around 325 °C and 475 °C) were observed for 5%Ni5A, which should correspond to the NiO particles on the 5A zeolite surface and in the super cages, respectively.

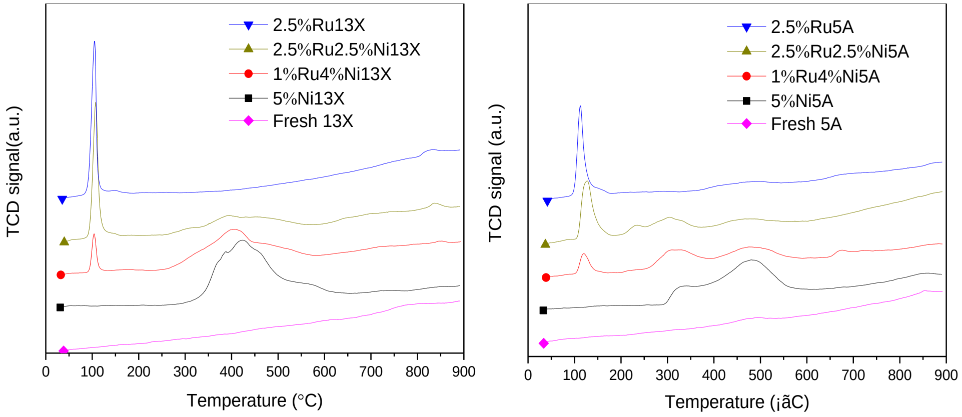

Figure 3.5: H_2-TPR profiles of fresh 13X zeolite, 5%Ni13X, 1%Ru4%Ni13X, 2.5%Ru2.5%Ni13X, 2.5%Ru13X, fresh 5A zeolite, 5%Ni5A, 1%Ru4%Ni5A, 2.5%Ru2.5%Ni5A, 2.5%Ru5A.

After the introduction of Ru, a strong and sharp reduction peak could be observed at around 100 °C, Since NiO was reduced around 420 °C for 5%Ni13X as seen in Figure 3.5, it can be deduced that ruthenium oxide on or in 13X zeolite with a low reduction temperature (around 100 °C). Moreover, NiO reducibility seemed to be enhanced by Ru oxide as the NiO reduction peaks can be observed to be shifted to lower temperatures in Figure 3.5, when Ru was introduced. This shows clear interaction between the two metal phases directly or via the support [187, 188]. Similarly, a sharp and strong RuO_2 reduction peak can be observed at around 120 °C for 1%Ru4%Ni5A, 2.5%Ru2.5%Ni5A and 2.5%Ru5A zeolite catalysts. The H_2-TPR results provided important information of catalyst reduction temperature before using them in experiments.

3.3.1.7. Temperature programmed desorption of ammonia (NH_3-TPD)

NH_3-TPD was used to determine the acidic properties (weak, mild, strong) of 13X, 5A zeolite and Ru, Ni modified catalysts. For fresh 13X zeolite, peaks at around 175 °C and 625 °C can be found, which correspond to the weak (175 °C) and strong (625 °C) acidity, respectively [189-191]. With the ruthenium catalysts, a very sharp peak could be observed at around 290 °C. The introduction of Ni broadened the peak between 200 °C - 400 °C and additional, peaks were observed at higher temperatures between 500 °C - 600 °C, which indicate the presence of strong acid sites. However, the peaks at the higher temperatures were observed by the introduction of Ru, which indicates interaction between the metals and the support in the formation of acid sites into the catalyst. The ratio of O:Al:Si was, however, kept constant as displayed in the EDX results in Table S. 3.3 (supplementary material).

The catalyst acidity distribution is shown in Figure 3.6. With 13X zeolite, the introduction of Ni resulted in a clear increase in strong acid sites. In the bi-metallic catalysts, increasing amounts of Ru decreased both the concentration of strong acid sites and total acidity. The mono-metallic Ru catalyst displayed the lowest overall and strong acidity.

With 5A zeolite, the introduction of Ni resulted in a clear increase in strong acid sites, just as with 13X. The introduction of Ru decreased again the concentration of strong acid sites, however, the trend in the total acidity was not as clear as with 13X, as ruthenium seemed to increase the concentration of weak acid sites.

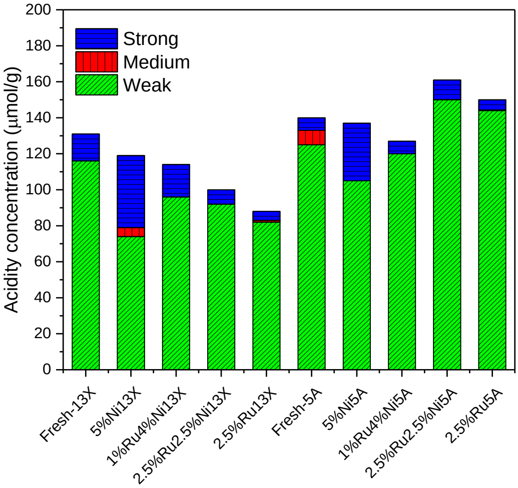

Figure 3.6: The catalyst acidity distribution calculated based on the results of NH_3-TPD.

3.3.2. Results of CO_2 methanation reaction in a fixed bed reactor

3.3.2.1. Catalyst activity and selectivity

The catalyst activity and selectivity test were carried out in a lab scale fixed bed reactor system. The CO_2 conversion curves along with the selectivities towards CH_4 are shown in Figure 3.7 and Figure 3.8. Because the zeolites were already saturated with water at steady state condition when activity and selectivity data was recorded, adsorption enhancement can be excluded. It can be seen that conversion curves show similar trend, which increases strongly with increasing temperature to reach equilibrium values at the highest temperature. The results show that the choice of catalyst amount and GHSV was successful as a broad range of conversions was obtained, which enables good comparison of the catalysts performance.

Interestingly, the performance of the catalysts on the different zeolites was rather different. With 13X, the highest conversion were obtained with the mono-metallic Ni and Ru catalysts, with Ni out performing Ru at the lower temperatures. The bi-metallic catalysts did not perform as well, especially at the higher temperatures. The highest CH_4 selectivity was obtained with the mono-metallic Ru catalyst, while pure Ni on 13X as well as the bi-metallic catalyst displayed significantly lower selectivity, especially at the lower temperatures. The selectivities increased with temperature.

With 5A, the highest conversions were obtained with Ni on 5A, the conversions decrease with increasing loading of Ru. The selectivities of the 5A supported catalysts displayed almost opposite behaviors compared to the 13X supported catalysts. The lowest selectivity was obtained with Ru on 5A and selectivity increased with a decrease in Ru concentration and an increase in Ni concentration. Moreover, the highest selectivities were obtained at the lowest temperatures.

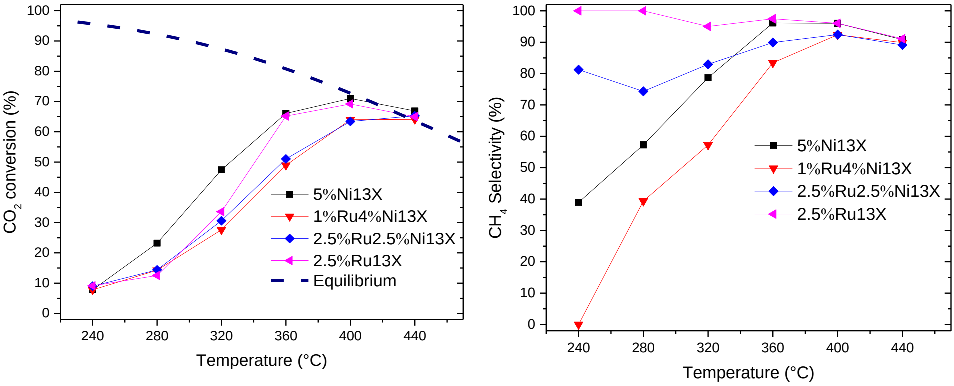

Figure 3.7: CO_2 conversion and CH_4 selectivity with catalyst 5%Ni13X, 1%Ru4%Ni13X, 2.5%Ru2.5%Ni13X and 2.5%Ru13X (reduction at 500 °C, 4 h) 0.9 g, 150 ml/min He, 40 ml/min H_2, 10 ml/min CO_2.

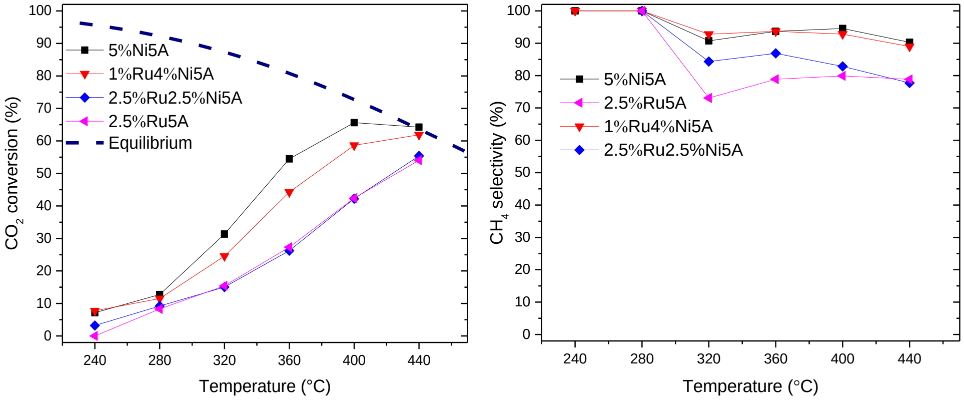

Figure 3.8: CO_2 conversion and CH_4 selectivity with 1%Ru4%Ni5A, 2.5%Ru2.5%Ni5A and 2.5%Ru5A (reduction at 500 °C, 4h) 0.9g, 150 ml/min N_2, 40 ml/min H_2, 10 ml/min CO_2

The differences in the behavior of the catalyst depending on the zeolites and the deposited metals are very interesting, as is the fact that the deposition of Ru did not increase the activity of the catalysts as expected (Figure 3.7, Figure 3.8). Catalyst behavior and as a result also the formed reaction intermediates can vary depending not only on the type of the metal but also on the metal/support ratio and interaction as well as reaction conditions and catalyst morphology. The reaction conditions were identical for all the tested catalysts. The activity on 13X follows the trends in the changes in weak acidity based on loading (Figure 3.6) and the same can be observed for 5A supported catalysts. However, the significant variations especially in the selectivity are most likely not dependent on the variations in acidity. The possible and plausible influence of the different factors explaining the observed results are presented below.

The differences in the behavior of the catalyst depending on the zeolites and the deposited metals are very interesting, as is the fact that the deposition of Ru did not increase the activity of the catalysts as expected (Figure 3.7, Figure 3.8). Catalyst behavior and as a result also the formed reaction intermediates can vary depending not only on the type of the metal but also on the metal/support ratio and interaction as well as reaction conditions and catalyst morphology. The reaction conditions were identical for all the tested catalysts. The activity on 13X follows the trends in the changes in weak acidity based on loading (Figure 3.6) and the same can be observed for 5A supported catalysts. However, the significant variations especially in the selectivity are most likely not dependent on the variations in acidity. The possible and plausible influence of the different factors explaining the observed results are presented below.

3.3.2.2. Reaction mechanisms of CO_2 hydrogenation on Ni and Ru

The reaction pathways of CO_2 methanation are divided into two main categories. The first one proposes the conversion of CO_2 to CO through reactive CO_2 adsorption via the reverse water gas shift reaction, and its subsequent reaction to methane through the same pathway as CO methanation [192, 193]. The second pathway proposes dissociative adsorption of CO_2 followed by direct methanation [194, 195]. Nowadays, it is generally accepted for most catalysts that in CO_2 methanation, CO is the main intermediate. The different reaction pathways also result in different rate limiting steps.

When evaluating the possible reaction mechanism depending on the metal, the probability of dissociative chemisorption on the surface is in key role as the second mechanism is based on it. The dissociative chemisorption energy of CO_2 on various metals was thoroughly described by T. Bligaard et al. [196]. The results show that dissociative chemisorbed of CO_2 occurs spontaneously on Ru with an energy of -0.77 eV. A value of 0.17 eV was obtained for the adsorption of CO_2 on Ni, which clearly shows that this pathway is not favorable and the first mechanism seems more likely.

Westermann et al. [40] studied the reaction mechanism of CO_2 methanation using nickel impregnated on ultra stable Y zeolite with IR measurements. They detected both carbonate and formate species on the Ni, but concluded that the CO_2 methanation pathway does not proceed through carbonate formation but through formate dissociation on Ni, leading to the formation of adsorbed CO. They concluded that CO is the main intermediate and its dissociation is the rate determining step of CO_2 methanation. The reaction pathway via formate formation was also recently reported by Dongapure et al. for Ni/Al_2O_3 [197]. Detailed studies regarding the interaction of CO_2 with Ni(110) via high pressure TPR (Temperature Programed Reactions) experiments were carried out by Vesselli et al. [198]. They reported that CO_2 chemisorbed on Ni(110) is negatively charged and that it is mainly bonded via the carbon atom. The molecule binds to the surface with a resulting energy barrier for its hydrogenation smaller than the energy barrier for CO_2 desorption or that for dissociation into COad and Oad. The presence of adsorbed and dissociated hydrogen Had leads to the formation of formate intermediates which subsequently react to provide methane.

They also performed ultrahigh vacuum (UHV) low temperature experiments and DFT calculations, which indicated that CO + OH is generated from CO_2 hydrogenation via a type of Eley-Rideal mechanism [198, 199].

Based on the finding presented above, the CO_2 methanation on Ni is proposed to follow the following mechanism, where ad represents a surface cite/adsorbed species:

$H_2(g) + 2ad \leftrightarrow 2Had$ (3-3)

$CO_2(g) + Had \leftrightarrow HCOOad$ (3-4)

$HCOOad + Had \leftrightarrow H_2Oad + COad$ (3-5)

$COad \leftrightarrow Cad + Oad$ (rate limiting step) (3-6)

$Cad + Had \leftrightarrow CHad$ (3-7)

$CHad + Had \leftrightarrow CH_2ad$ (3-8)

$CH_2ad + Had \leftrightarrow CH_3ad$ (3-9)

$CH_3ad + Had \leftrightarrow CH_4ad$ (3-10)

$CH_4ad \leftrightarrow CH_4(g)$ (3-11)

$Oad + Had \leftrightarrow OHad$ (3-12)

$OHad + Had \leftrightarrow H_2Oad$ (3-13)

$H_2Oad \leftrightarrow H_2Og$ (3-14)

Reaction intermediates in CO_2 methanation when using ruthenium supported on alumina (Ru/γ-Al_2O_3) as catalysts were investigated by [192] Eckle et al., 2011. The intermediates were investigated by steady state isotopic transient kinetic analysis coupled with DRIFT experiments. Formate mechanism was considered as highly unlikely to be the dominant rate determining reaction. It was proposed that on a Ru catalyst, CO_2 methanation proceeds via dissociative adsorption (3-15) forming COad and Oad, which is the rate determining reaction of the process. Based of the results presented above, the reaction mechanism can be presented as

$CO_2 \leftrightarrow COad + Oad$ (rate determining step) (3-15)

$COad \leftrightarrow Cad + Oad$ (rapid) (3-16)

followed by reactions (3-7) to (3-14).

Based on the reaction mechanisms and the literature data presented above, it could be argued that the higher selectivity achieved with Ru is due to the efficient CO dissociation which minimized the desorption of CO. However, the reaction mechanisms cannot explain the very significant increase of selectivity observed with increasing temperature and conversion for Ni on 13X and the opposite behavior for Ni and Ru on 5A (Figure 3.7 & Figure 3.8). Catalyst behavior and as a result also the formed reaction intermediates can vary depending not only on the type of the metal but also other factors and partly contradicting observations have been reported in literature.

3.3.2.3. Differences in characteristics of the support

Both zeolites were primarily chosen for their large water adsorption capacity in order obtain the bi-functional catalytic and water adsorptive capabilities of the catalysts. However, there exists some differences between them. Zeolite 13X has a higher water adsorption compared to 5A. When increasing the experimental temperature towards 400 °C, the water is mostly desorbed from both [34]. The zeolites adsorb also efficiently CO_2 and the capacity of 5A is higher compared to 13X. Both zeolites also adsorb rather efficiently CH_4 and CO [34, 200].

The adsorption of the different compound is at least partly competitive and e.g. a lower amount of water enables the increased loading of CO_2. It has been reported that an increased amount of methane decreases the CO_2 uptake for 5A, whereas 13 would not be so significantly influenced [34, 201].

The high concentration of the reactant CO_2 on the zeolite and close to the reactive sites is logically beneficial for the reaction, whereas the high concentration of the final product CH_4 could have a negative effect on the reaction rate as well as promote side product (CO) formation. This could contribute to the decreasing selectivity of the ruthenium catalysts on both zeolites with increasing conversion.

3.3.2.4. Morphology of the catalyst

The pore size of zeolite 5A is about 5 Å whereas the pore size of 13 X is about 10 Å [27]. As described previously in the results part, the nanoparticle size of Ru was much larger compared to Ni in both the mono- and bi-metallic catalysts. The Ni nanoparticle size was significantly smaller compared to Ru in all the catalysts. Well below one nm particles were observed for Ni, while the Ru nanoparticles were much larger (Table S. 3.4) also in average size. When considering the pore sizes of the zeolites, it is evident that the ruthenium was deposited on both zeolites as an eggshell structure, as was the nickel on zeolite 5A. However, a part of the nickel was able to penetrate the pores of the zeolite forming highly active sub-nano sized nanoparticles. This was displayed in the nitrogen physisorption results (Table S. 3.5), as the total surface area and total pore volume of 5%Ni13X were about 45% lower compared to pristine 13X, while the values did not change significantly for the Ru containing catalysts compared to the pristine zeolites. As described previously in the experimental section, the zeolites were saturated with water during the steady state experiments. This leads to the fact that the concentration of water inside the pores of the zeolites was very high at the lower experimental temperatures, whereas, at the higher temperatures, the majority of water was desorbed. The high concentration of water promoted the formation of the intermediary product CO decreasing the selectivity according to the overall reaction (3-14) [27]. With 13X zeolite, the highest conversions were obtained with the   This explains why the Ni / 13X catalysts where the most active sub-nano sized nanoparticles were inside the pores of the zeolite, where the water also was, displayed increasing selectivity with temperature. On the contrary, the ruthenium was located on the outer surface of the zeolite 13X, which is why the active external sites were not influenced by the water retained inside the zeolite and high selectivity was observed even at lower temperature. With zeolite 5 A, both Ni and Ru displayed high selectivity at lower temperature as both formed an eggshell structure.

The intended advantage of obtaining close proximity of the reactive sites on the sub-nano Ni nanoparticles with the water adsorbing sites inside 13 X acts as a disadvantage in steady state experiments in decreased selectivity, even though high activity is maintained. The more robust eggshell structure, where the reactive sites are located further from the water adsorbing sites located inside the zeolites do not suffer as much from this disadvantage. However, it must be pointed out that this applies to steady state conditions and not the dynamic conditions the bi-functional catalyst is intended to be operated in.

3.3.2.5. Catalyst stability

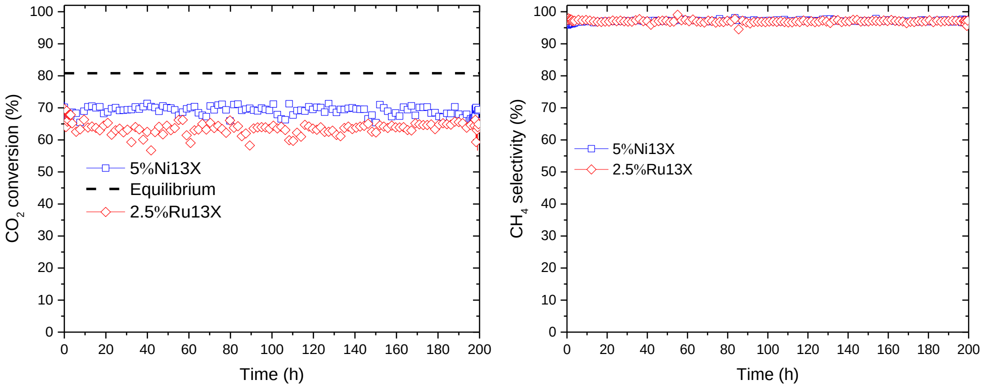

Figure 3.9: CO_2 conversion and CH_4 selectivity with catalyst 5%Ni13X and 2.5%Ru13X (reduction at 500 °C, 4 h), 0.9 g, 150 ml/min N_2, 40 ml/min H_2, 360 °C, 10 ml/min CO_2 during 200 h experiments.

The catalyst stability test was carried out at 360 °C for 200 hours, and the catalysts were reduced at 500 °C for 4 hours prior to performing the catalyst evaluation experiments. The CO_2 conversions are shown in Figure 3.9. Very stable performance can be observed for both catalysts. It can be concluded that the stability of the catalysts was excellent with time on stream and no indications of deactivation could be observed.

3.4. Conclusions

Nickel-ruthenium modified mono- and bi-metallic catalysts were synthesized on zeolite 13X and 5A using evaporation impregnation. The physico-chemical properties of the pristine and modified catalysts were characterized using XRD, SEM-EDX, TEM, STEM-EDX, N_2 physisorption and TPD-NH_3. The catalysts were tested for CO_2 methanation in a fixed bed reactor system in the temperature interval 240-440 °C.

The surface area and, micro-pore volume decreased after Ni modification of 13X zeolite, however, no significant influence was observed with 5A. A significantly smaller cluster size was obtained for Ni while Ru formed large nanoparticles. The same observation was valid for both mono- and bi-metallic catalysts. The metal modification clearly influenced the acidity of the catalysts with Ni promoting strong acidity.

The 13X supported catalyst outperformed in general the 5A supported ones, when considering conversion. Interestingly, the conversion and selectivity depended significantly on the zeolite. With 13X, the highest conversions were obtained with the mono-metallic catalysts, while with 5A, the conversion decreased with increasing Ru loading. With 13X, the highest selectivity was obtained with pure Ru catalyst, while with 5A, the result was opposite. Moreover, with 13X the selectivity increased with temperature, while with 5A, it was the opposite.

The selectivity was clearly influenced by the fact that Ni was able to penetrate the pores of the 13X catalyst, while the Ru nanoparticles were formed on the surface of the particles. This was also the case with both Ni and Ru on 5A. This resulted in the active Ni clusters inside 13X being influenced by the high concentration of water inside the zeolite at lower temperatures, while at higher temperature, water was desorbed from the catalyst which resulted in increased selectivity. With the egg shell type structure for Ru/13X and Ni/Ru/5A, the water adsorbed by the zeolite did not influence selectivity as it was not in such close proximity to the active sites. Moreover, the selectivity was most probably influenced by the competitive adsorption of CO_2 and methane in 5A as well as the different reaction mechanisms of the methanation on the Ni and Ru metals. The catalysts exhibited good stability and CH_4 selectivity during 200 hours.

It can be concluded that the conversion of CO_2 methanation by Ni based catalysts cannot be improved by adding Ru. However, the selectivity can be significantly influenced depending on the properties of 13X and 5A zeolites.

3.5. Supplementary Material

Table S. 3.1: The molar ratio of Ni to Ru in catalysts.

Catalyst	Ni:Ru mol ratio
5%Ni13X	1:0
1.0%Ru4.0%Ni13X	6.9:1
2.5%Ru2.5%Ni13X	1.7:1
2.5%Ru13X	0:1
5%Ni5A	1:0
1.0%Ru4.0%Ni5A	6.9:1
2.5%Ru2.5%Ni5A	1.7:1
2.5%Ru5A	0:1

Table S. 3.2: The pH of the catalyst synthesis solutions during Ru, Ni modifications of 13 X and 5 A zeolites.

Item	pH of distilled water	pH of Nickel Nitrate salts solution	pH of Ruthenium(III)-chloride solution	pH of Nickel Nitrate and Ruthenium chloride salt solution	pH of salt solution with zeolite
5%Ni13X	_	7.4	_	_	7.7
1%Ru4%Ni13X	7.0	6.7	_	2.3	4.1
2.5%Ru2.5%Ni13X	7.0	6.9	_	2.0	3.3
2.5%Ru13X	7.5		2.1	_	3.4
5%Ni5A	_	7.3	_	_	7.7
1%Ru4%Ni5A	7.6	6.9	_	2.3	3.5
2.5%Ru2.5%Ni5A	7.5	7.0	_	2.1	3.3
2.5%Ru5A	7.6	_	2.2	_	3.7

Table S. 3.3: Summary of the elemental analyses using energy dispersive X-ray microanalyses for fresh 13X, 5A zeolite, the Ni-, Ru- modified 13X and 5A zeolite catalysts using evaporation impregnation method.

Sample	Content (wt./wt.%)										
	O	Na	Mg	Al	Si	Cl	K	Ca	Fe	Ni	Ru
Fresh 13X	51.8	12.5	1.3	13.0	20.3	_	_	0.5	0.6	_	_
5%Ni13X	58.6	10.7	0.7	10.2	15.6	0.1	0.1	0.3	0.5	3.2	_
1%Ru4%Ni13X	59.3	9.9	0.8	10.0	15.1	0.4	0.1	0.4	0.4	2.49	1.0
2.5%Ru2.5%Ni13X	60.3	8.6	0.8	9.9	14.5	0.9	_	0.4	0.5	1.50	2.6
Fresh 5A	57.68	3.93	0.08	14.31	14.34	0.52	_	8.83	0.32	_	_
5%Ni5A	59.27	3.85	_	12.55	13.51	0.36	_	6.37	0.16	3.93	_
2.5%Ru2.5%Ni5A	58.57	3.32	0.12	12.55	12.66	1.64	_	6.43	0.23	1.95	2.53
2.5%Ru5A	60.54	3.29	0.07	12.90	13.11	1.15	_	6.62	_	_	2.32

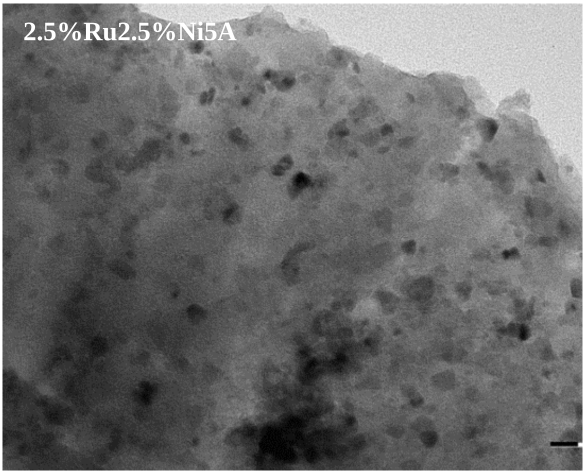

Figure S. 3.1: Transmission electron micrographs of 2.5%Ru2.5%Ni5A catalyst.

Table S. 3.4: The average particle size and range of NiO (RuO_2) on Ni (Ru) modified catalysts (calculated from TEM results).

Catalyst	NiO (RuO_2) particle size range (nm)	Average particle size of NiO (RuO_2) (nm)
5%Ni13X	1.56-56.98	12.32
2.5%Ru13X	7.26-97.65	37.46
5%Ni5A-EIM	0.72- 28.23	9.71
2.5%Ru2.5%Ni5A	2.27- 27.57	8.87
2.5%Ru5A	2.97- 120.45	44.93

Table S. 3.5: Specific surface area and pore volumes of fresh zeolite and catalysts.

Sample	Specific surface area (m^2/g_{cat})	V_{total} (cm^3/g_{cat})
13X zeolite	654.78	0.23
5%Ni13X	361.49	0.13
1%Ru4%Ni13X	640.07	0.23
2.5%Ru2.5%Ni13X	591.17	0.21
2.5%Ru13X	629.44	0.23
5A zeolite	592.52	0.21
5%Ni5A	454.14	0.16
1%Ru4%Ni5A	546.01	0.20

Table S. 3.6: The weak, medium and strong acid sites calculated using NH_3-TPD.

Sample	Total acidity µmol/g	Weak acidity µmol/g 100-350°C	Medium acidity µmol/g 350-450°C	Strong acidity µmol/g 450-700°C
Fresh-13X	130	116	0	15
5%Ni13X	120	74	5	40
1%Ru4%Ni13X	115	96	0	18
2.5%Ru2.5%Ni13X	100	92	0	8
2.5%Ru13X	87	82	1	5
Fresh-5A	141	125	8	7
5%Ni5A	138	105	0	32
1%Ru4%Ni5A	128	120	0	7
2.5%Ru2.5%Ni5A	161	150	0	11
2.5%Ru5A	150	144	0	6

4

Ce-promoted Ni 13X zeolite catalysts for CO_2 methanation

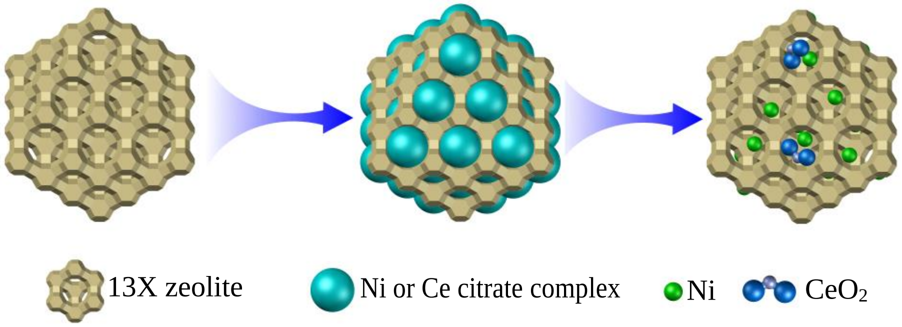

Keywords of this chapter:

Sub-nanometer nickel-ceria on zeolite 13X,

citrate complexes,

nickel citrate,

cerium citrate,

CO_2 methanation.

This chapter is based on the following publication:
L. Wei, H. Grénman, W. Haije, N. Kumar, A. Aho, K. Eränen, L. Wei, W. de Jong, Sub-nanometer ceria-promoted Ni 13X zeolite catalyst for CO_2 methanation. Applied Catalysis A: General, 2021. 612: p. 118012. [202].

4.1. Introduction

Sorption-enhanced CO_2 methanation has attracted significant attention from researchers in recent years due to its potential in future processes for energy storage and use [27, 33]. Water-adsorbing zeolite-supported catalysts were used for the Sabatier reaction [116] ($CO_2 + 4H_2 \leftrightarrow CH_4 + 2H_2O$; ΔH^0_{298} = -165 kJ/mol) in our work to enhance the yield beyond equilibrium according to Le Chatelier's principle and in this way limiting downstream cumbersome separations. When traditional methods are used to prepare catalysts [26, 27, 33], the dispersion of Ni on zeolite is typically far from single-atom or sub-nanometer. This decreases the activity of the active metal, and increases its inventory. Water-absorption properties of the support have not traditionally been a research focus. Obtaining high metal dispersion on a highly water-adsorbing support is a key area of our research. The great potential stems from combining renewable hydrogen (produced with biomass gasification [130], solar and wind power) with CO_2 from stack emissions and eventually Direct Air Capture (DAC), and the distribution and use of the renewable methane in the existing infrastructure.

The main challenge in the Sabatier reaction is that rather high temperatures, around 400 °C, are needed for reasonable reaction rates, while thermodynamically conversion is favored at lower temperatures. When the reaction does not proceed to completion, costly separation of the products and reactants is needed, which prohibits the economic viability of the process. There are two ways to tackle this problem: i) developing active catalysts for lower temperatures and ii) removing one of the products, namely water, from the gas mixture to shift the equilibrium to the product side. We seek synergistic effects by using both options, through catalyst development. This enables practical application in for example circulating fluidized bed reactors to end up with a continuous process.

Studies on preparing single Ni-atom zeolite catalysts for sorption-enhanced CO_2 methanation are scarce in the literature. Single-atom catalysts are considered ideal catalysts for many reactions, because of the remarkable efficiency of the active metals and excellent activity [86, 160, 203-206]. Few or single-atom based bi-functional materials, *i.e.* having catalytic plus sorption properties, are a promising option (Figure 4.1), because they have high activity and should largely retain their water-adsorption capacity by loading only a very limited amount of metal in the support material. Several strategies exist for synthesizing single-atom catalysts [86, 87], of which mass-selected soft loading [88] and atomic layer deposition [89, 90] are limited by high cost and are complicated methods for large-scale catalyst production. In recent years, other synthetic strategies have emerged for single-atom catalyst preparation, such as defect engineering [91, 92], coordination pyrolysis [93-95], and gas migration using volatile metal complexes [96]. However, it is difficult to keep the material's structure intact since the high calcination or pyrolysis temperatures will damage the structure of the support irreversibly. Furthermore, there is the possibility of sintering of the metal (nano) particles. Additionally, these preparation routes are difficult to scale up because of the complicated methods involved.

We describe a facile metal-complex precursor strategy to prepare sub-nanometer (possibly in single sites) Ni clusters to be used in conjunction with the bi-functional material with great potential for heterogeneous catalysis. A schematic representation of the preparation route is shown in Figure 4.2: 13X zeolite was used as the catalyst support as well as the water sorbent for sorption-enhanced CO_2 methanation. Nickel citrate hydrate and cerium nitrate were dissolved in water, and both metal ions compete to form citrate complexes. The size selectivity of the zeolites limits the number of metal complexes that can enter the zeolite and therefore holds the promise of having very limited Ni and Ce content inside. After calcination, Ni and Ce citrate complexes are decomposed to their respective oxides where CeO_2 particles could act as a separator for Ni species in the 13X super cages. We investigated the Ni/Ce ratio effect for Ni:Ce 13X zeolite catalysts with Ce loading varying from 0 to 10 wt.% and Ni loading fixed at 5 wt.% (throughout the paper reference is made to the metal weight percentage). This chapter focused on the complexation strategy for atomically dispersed Cerium doped Ni-catalyst preparation and characterization. Sorption-enhanced experiments are explicitly not included yet.

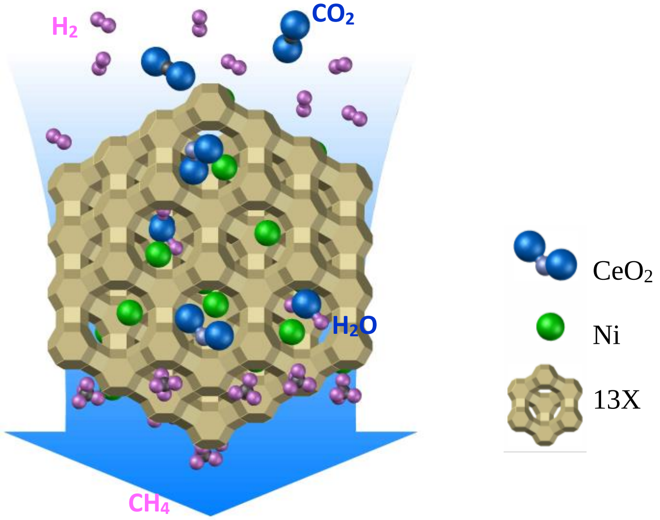

Figure 4.1: Schematic representation of sorption-enhanced CO_2 methanation.

4.2. Experimental section

4.2.1. Catalyst preparation

The catalysts 5%Ni13X, 5%Ni1%Ce13X, 5%Ni2.5%Ce13X, 5%Ni5%Ce13X and 5%Ni10%Ce13X (metal weight percentages) were prepared by the evaporation impregnation method [207]. A nominal Ni- metal loading of 5% weight was targeted in all 13X zeolite catalysts. Nickel citrate hydrate ($Ni_3(C_6H_5O_7)_2 \cdot xH_2O$, 98+%, Alfa Aesar) and $Ce(NO_3)_3 \cdot 6H_2O$ (Sigma Aldrich, 99.0%) were used as the Ni and Ce precursors. Ni-metal precursors were dissolved in 250 mL of distilled water in a flask, and 5 g of 0.212–0.500 mm size (sieve fraction dried at 100 °C overnight in an oven) 13X zeolite (Honeywell Fluka, The Netherlands) was added to the solution. The 13X zeolite particles used for Ni- and Ce-modification were no longer spherical after treatment in a mortar but had irregular shapes. To prevent mechanical wear of the zeolite particles, the rotary evaporator was operated at low rotation speed, 10 rpm, for 24 h at room temperature. Subsequently the aqueous solution was evaporated in the same at 50 °C using a water jet pump to reduce the pressure. The catalyst was then dried at 100 °C overnight before calcination.

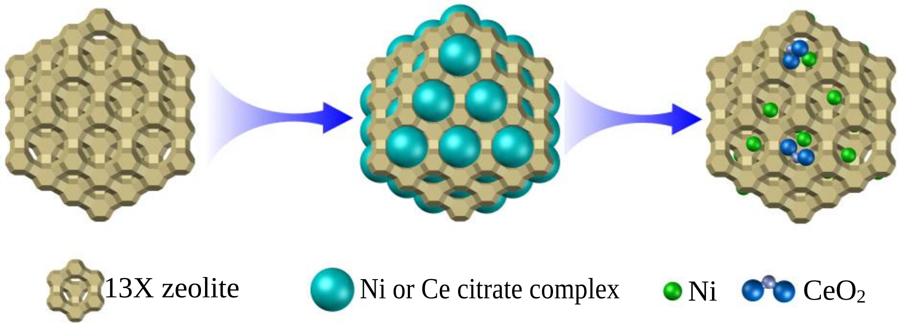

Figure 4.2: Schematic representation of catalyst synthesis.

All catalysts were calcined in air in a muffle furnace using a stepwise calcination procedure. In the stepwise procedure, the heating rate from room temperature to 250 °C was 4.5 °C/min and the temperature was kept there for 40 min; then it was increased to the target temperature 400 °C by 2.5 °C/min, and kept there for 3 h, then cooled to room temperature.

4.2.2. Catalyst characterization

The calcined catalysts (before reduction) were characterized by X-ray powder diffraction (XRD), scanning electron microscopy (SEM) with energy-dispersive X-ray spectroscopy (EDX), transmission electron microscopy (TEM), scanning transmission electron microscopy equipped with energy-dispersive X-ray spectroscopy (STEM-EDX), X-ray photoelectron spectroscopy (XPS), hydrogen-temperature programmed reduction (H_2-TPR), Fourier transform infrared (FT-IR), CO_2-temperature programmed desorption (CO_2-TPD), and pyridine-FTIR. Additionally, the reduced catalysts were characterized by N_2 adsorption at 77 K.

A Bruker D8 advance diffractometer and Lynxeye position sensitive detector were used in the XRD measurements. The diffractometer was operated in Bragg-Brentano diffraction mode, and the Cu-*K*α radiation was generated with a voltage of 45 kV and a current of 40 mA. The scanning 2θ angle range in 0D mode was 10.0° to 100.0° using a step size of 0.026°, counting time 2 seconds/step. The measured XRD diffractograms were analyzed with Bruker software DiffracSuite EVA vs 5.0.

Catalyst morphology, shape, size and crystallite distribution were studied by scanning electron microscopy (SEM) JEOL JSM 6500F (JEOL Ltd., Japan). The imaging modes used were secondary electron imaging (SEI) and back-scattered electron imaging (BEI). Energy dispersive spectroscopy (EDS) was performed with a Thermo Fisher-Noran Ultradry silicon drift detector (SDD) and operated and analyzed with the Noran System Seven (NSS) ™ software package (version 2.3).

Transmission electron microscopy (TEM) was used to study the Ni- and Ce-particle size and distribution. The equipment used was JEM-1400 (JEOL Ltd, Japan) with a maximum acceleration voltage of 120 kV.

To further study the nanoscale of catalysts, scanning transmission electron microscopy (STEM) equipped with an energy-dispersive X-ray spectroscopy (EDX) detector was used. The equipment used was FEI Titan 80-300 electron microscope. Elemental mapping was investigated at 300 kV with EDX. Specimen preparation consisted of immersing a lacey carbon film supported on a copper grid into the catalyst powder and small particles adhering to the carbon film were measured.

The chemical states of Ce-promoted Ni 13X catalysts were determined using X-ray photoelectron spectroscopy (XPS). A Perkin-Elmer PHI 5400 spectrometer with an Mg K&#945 X-ray source operated at 14 kV and 200 W was used in the XPS analysis of the samples. The pass energy of the analyzer was 35.5 eV and the energy step 0.1 eV. Peak fitting was performed with the program XPS Peak 4.1. The background was corrected with the Shirley function. Charge compensation was done with the Si 2p peak of the support. A pure 5wt% Ni13X sample was used as a reference.

H_2-TPR analysis was carried out in a Micromeritics AutoChem 2910. Catalysts were dried at 250 °C for 1 h in a dry Ar atmosphere, then reduced by 5% H_2 (diluted by Ar) from room temperature to 900 °C with 5 °C/min heating rate. A TCD detector was used to monitor the H_2 consumption.

Fourier transform infrared (FTIR) analysis was performed to investigate the metal complexes in solutions during catalyst preparation. The equipment was a Thermo Scientific Nicolet iS50 FTIR spectrometer with an attenuated total reflectance (ATR) accessory.

CO_2-TPD was performed in a Micromeritics AutoChem II 2920 to investigate the catalyst basic sites. Catalysts were reduced in situ at 450 °C for 2 h with 10% H_2 (diluted by Ar) before CO_2 adsorption (10% CO_2 in He) at 50 °C for 1 h. After waiting 30 min for a stable baseline, the CO_2-TPD experiment was carried out from 50 to 750 °C with a heating rate of 10 °C/min under a 50 mL/min He flow.

A pyridine (Sigma-Aldrich, >99.5%) adsorption/desorption study with FTIR was used to investigate the Brønsted or Lewis acid sites of catalysts. An ATI Mattson instrument was used with molar extinction coefficients from Emeis [208].

The surface area and pore volume of fresh 13X, reduced Ni-modified and Ce-promoted Ni zeolite 13X catalysts were measured using nitrogen adsorption. The instrument used was a Micromeritics TriStar II 3020. The fresh 13X and catalysts were outgassed at 350 °C overnight, prior to the surface area measurement. The calculation of surface area was carried out using the BET method.

4.2.3. Evaluation of catalytic properties for the methanation reaction in a fixed-bed reactor

The catalyst activity, selectivity and stability were tested in a quartz fixed-bed reactor with an inner diameter 10 mm. The reactor was filled with silica beads (diameter around 2 mm, around 10 mL) to support the catalyst bed. The silica beads and catalyst were layered by silica wool, and silica beads (around 10 mL) were used to fill the upper part of the reactor (around 12 mm high). The reactor was heated by a vertical tube furnace equipped with a K-type thermocouple, while the temperature of the catalyst bed was monitored by another K-type thermocouple inserted into the bottom of the catalyst bed and connected to a computer. A schematic representation of the fixed-bed reactor system can be found in Figure S. 2.1.

Before the testing, around 0.9 g of calcined catalyst was loaded in the reactor and reduced under 100 mL/min H_2 at 500 °C for 4 hours. It was shown that the catalysts reduced at 500 °C had better performance on CO_2 methanation (Figure S. 2.2). Catalyst activity experiments were carried out at 240 °C to 400 °C with a gas hourly space velocity of around 13,333 mL/$g_{cat.}$/h, in a reaction mixture of 40 mL/min H_2 and 10 mL/min CO_2 diluted by N_2 (150 mL/min). The gas produced from the reactor went through a cooling condenser and was analyzed by GC (Varian, CP-4900 Micro-GC) equipped with HayeSep A, molecular sieve columns (Molsieve 5 Å PLOT) and a thermal conductivity detector. Helium was used as the carrier gas.

The CO_2 conversion (4-1) and catalyst selectivity (4-2) for CH_4 are defined as [153, 209]:

$$X_{CO_2} = \frac{n_{CO_{2,in}} - n_{CO_{2,out}}}{n_{CO_{2,in}}} \tag{4-1}$$

$$S_{CH_4} = \frac{n_{CH_{4,out}}}{n_{CO_{2,in}} - n_{CO_{2,out}}} \tag{4-2}$$

Where $n_{CO_{2,in}}$ is the input molar flow rate of CO_2 in the experiment, $n_{CO_{2,out}}$ and $n_{CH_{4,out}}$ are the molar flow rate of CO_2 and CH_4 calculated from GC results respectively (selectivity <100% means CO is formed).

4.3. Results and discussion

4.3.1. Catalyst structure and surface properties

4.3.1.1. X-ray powder diffraction (XRD)

The XRD results for Ce-promoted Ni 13X catalysts are presented in Figure 4.3. The XRD patterns showed no visible peaks for NiO and CeO_2 for any of the samples, which we attribute to the size of NiO particles in the Ni 13X catalysts being too small, < 3 nm, and most probably not well crystallized at the low calcination temperature, leading to significant peak broadening [210]. Similar reasoning applies to CeO_2: the CeO_2 peaks could not be identified even for the 5%Ni10%Ce13X. Small particles are due to the synthesis in which the citrate chelated form of Ni and Ce were the precursor species in solution. This procedure has been shown to produce small well dispersed particles [123]. The XRD patterns indicated that the crystal structure of 13X zeolite had not changed after the Ni/Ce impregnation using citrate as a complexing agent and calcination treatment. The fresh 13X zeolite patterns were similar to those of the calcined 5%Ni10%Ce13X, 5%Ni5%Ce13X, 5%Ni2,5%Ce13X, 5%Ni1%Ce13X, 5%Ni13X catalysts (Figure 4.3).

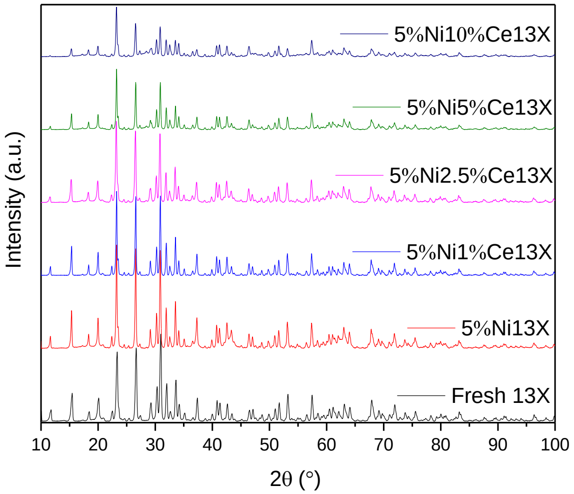

Figure 4.3: The XRD patterns for calcined fresh 13X, 5%Ni13X, 5%Ni1%Ce13X, 5%Ni2.5%Ce13X, 5%Ni5%Ce13X and 5%Ni10%Ce13X catalysts.

4.3.1.2. Scanning electron microscopy (SEM)

The scanning electron micrographs (Figure 4.4) showed that the fresh 13X, Ni-modified and Ce-promoted Ni zeolite 13X catalysts were composed of the characteristic fibrous crystals. It was inferred from the morphological studies that the Ni- and Ce-promoted complex strategy did not change the zeolite 13X fibrous morphology. This is in accordance with XRD where no obvious change in habitus was observed, induced by a change in preferred orientation. On the other hand, according to the EDX results (Table S. 4.2, supplementary material), the Al and Si ratios as well as the charge neutralizing cations' quantities in the modified catalysts, were close to fresh 13X zeolite, which again showed that the 13X zeolite composition did not significantly change after Ni (Ce) modification procedures.

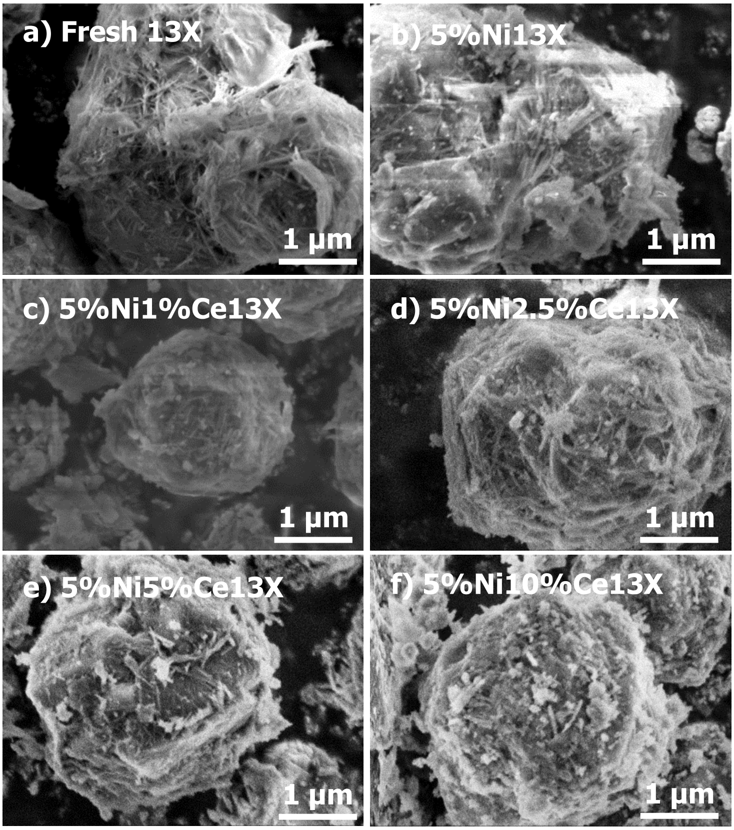

Figure 4.4: SEM images of a) fresh 13X, b) 5%Ni13X, c) 5%Ni1%Ce13X, d) 5%Ni2.5%Ce13X, e) 5%Ni5%Ce13X and f) 5%Ni10%Ce13X catalyst.

4.3.1.3. Transmission electron microscopy (TEM)

TEM was used to investigate the NiO and CeO_2 particle size distribution. The TEM images of the Ce-promoted Ni catalysts are shown in Figure 4.5. Nano particles are observed in all impregnated samples. The ones in the 5 and 10% Ce are clearly much bigger (tens of nm) than the highly dispersed ones in the 1 and 2,5% Ce samples, which are of the order of 1 nm. The characteristic 13X channels can be seen clearly. Indeed, some NiO clusters could be observed in 5%Ni13X, in which a possible dispersion effect of Ce could not be active. However, the larger particles were observed in the catalysts with higher Ce loading (5%Ni5%Ce13X and 5%Ni10%Ce13X). The possible explanation here is that Ce promoted the Ni dispersion during the catalyst preparation, but the excess Ce formed 3D clusters when the Ce loading was higher than 5 wt.% mostly outside the zeolite confinement. The characterization of the textural properties of the 13X zeolite as fresh, 5%Ni13X, 5%Ni1%Ce13X, 5%Ni2.5%Ce13X, 5%Ni5%Ce13X, 5%Ni10%Ce13X catalysts using transmission electron microscopy clearly showed the characteristic fibrous structure, as well as the ordered uniform pores and channel systems (Figure 4.5).

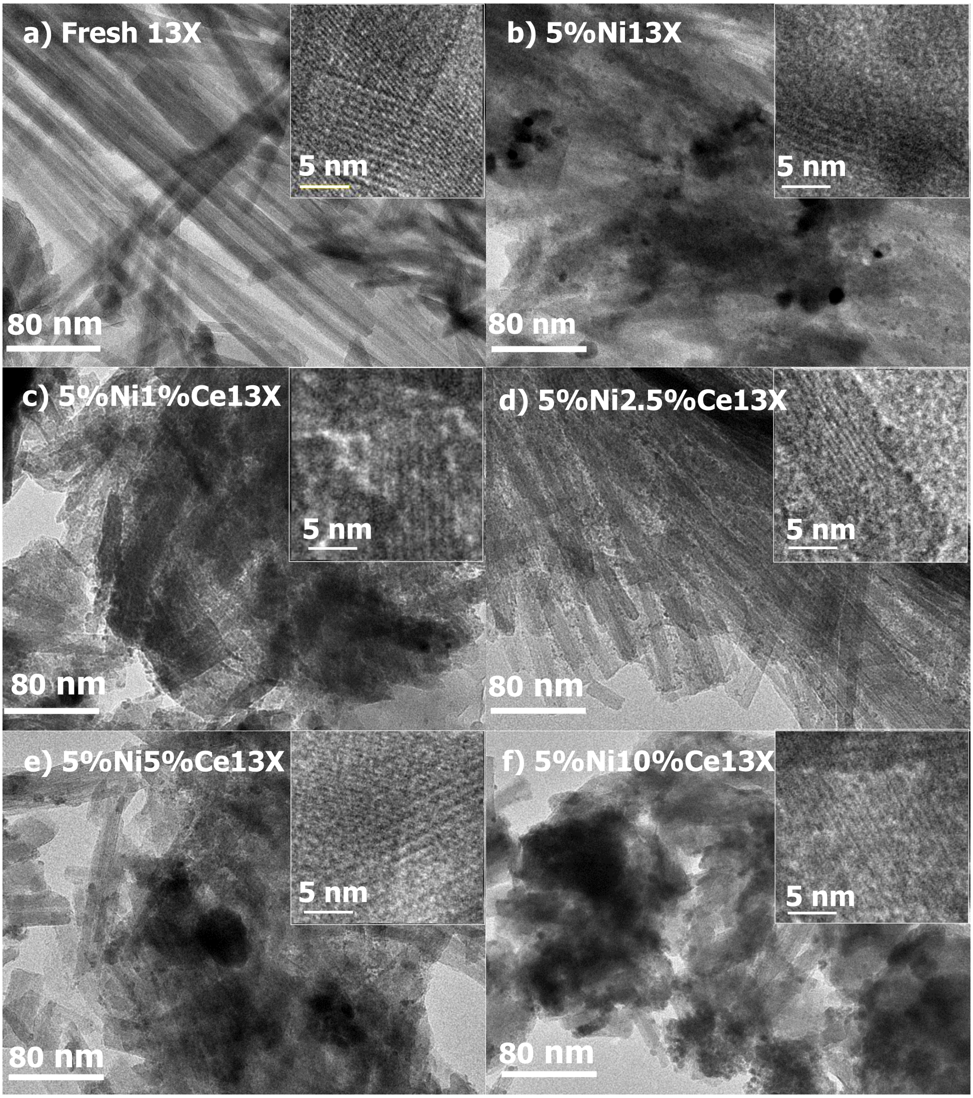

Figure 4.5: TEM images of a) fresh 13X, b) 5%Ni13X, c) 5%Ni1%Ce13X, d) 5%Ni2.5%Ce13X, e) 5%Ni5%Ce13X and f) 5%Ni10%Ce13X catalyst.

Due to limitations of the TEM used we cannot distinguish between Ce or Ni containing particles. That is why elemental mapping was used in Figure 4.6. In Figure 4.5, it is clear that pristine zeolite does not contain particles and samples where Ni is diluted with Ce show the best dispersed, small, particles, as substantiated in the mappings (Figure 4.6).

4.3.1.4. Elemental mapping

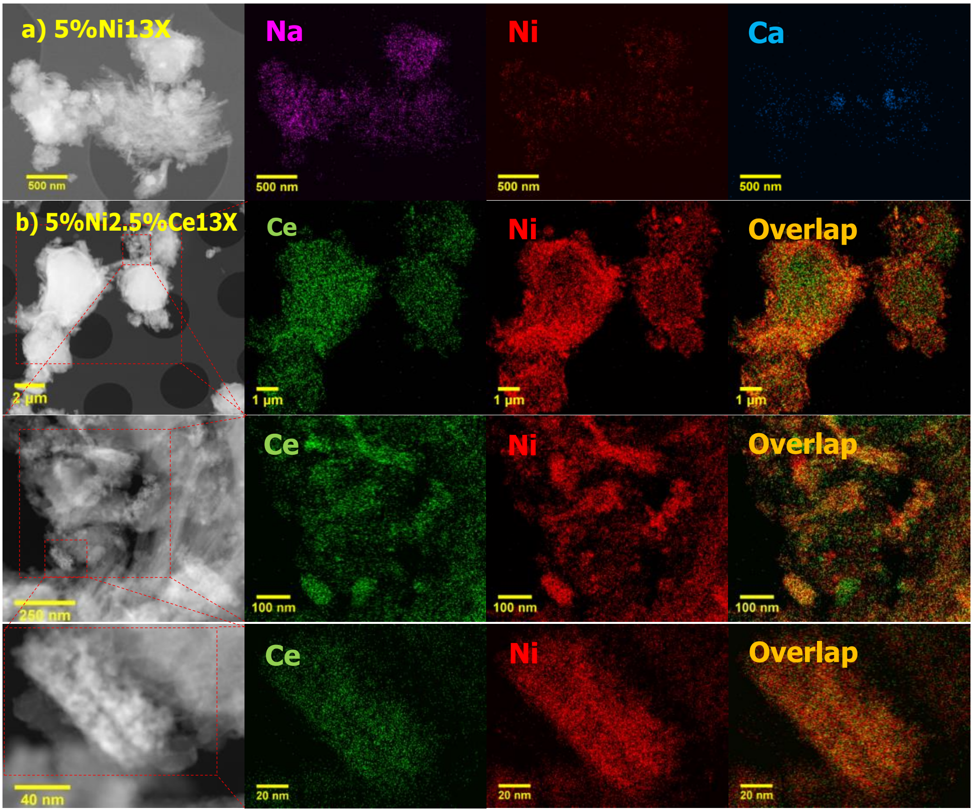

Figure 4.6: STEM images (first row), Na (pink), Ni (red), Ca (light blue), Ce (green) and Ce Ni overlap (yellow) maps of a) 5%Ni13X and b) 5%Ni2.5%Ce13X.

A closer study of the dispersion of Ni and Ce on or in the 13X zeolite, and the determination of the relative distribution of Ni and Ce, was carried out through an elemental mapping with STEM-EDX (Figure 4.6). Ni is dispersed well on both 5%Ni2.5%Ce13X and 5%Ni13X, and the Ce also shows a good dispersion on 5%Ni2.5%Ce13X. In Figure 4.6 (20 nm scale bar) we see that Ni and Ce are highly dispersed and may be present even as single atoms in 5%Ni2.5%Ce13X. Since the diameter of 13X zeolite pores is around 7.4 Å [36], while CeO_2 is between 5.5–7.5 Å, and NiO is around 3.24 Å [211], it is possible for one or a pair of NiO and/or CeO_2 to exist in a zeolite super-cage. Additionally, it is obvious that the Ni and Ce are overlapping in 5%Ni2.5%Ce13X (Figure 4.6, yellow). The lowest row in Figure 4.6 clearly shows high dispersion of both Ce and Ni and very small sub-nano cluster size. This implies that Ni atoms in the reduced state are isolated by surrounding Ceria if space permits, or are just by themselves. This substantiates the close proximity of Ni and Ce.

4.3.1.5. H_2-Temperature programmed reduction (H_2-TPR)

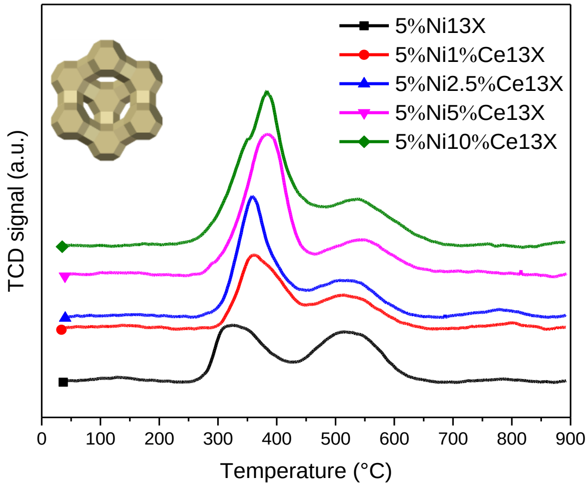

Figure 4.7: H_2-TPR profiles of 5%Ni13X, 5%Ni1%Ce13X, 5%Ni2.5%Ce13X, 5%Ni5%Ce13X and 5%Ni10%Ce13X catalysts (same scale for all traces).

The H_2-TPR profiles of Ni- and Ce-promoted Ni 13X catalysts are shown in Figure 4.7. Two major peaks were observed for all catalysts. It has been reported that the first reduction peak corresponds to NiO particles outside the zeolite or in super-cages and the second peak to NiO particles in sodalite cages [212, 213]. It is noticeable that the intensity of the TCD signal in the second peak became weaker with increased loading of Ce, and that the ratio of the first peak to the second peak increased with increasing Ce loading, which might indicate that less NiO appeared in sodalite cages. Efforts to quantify the hydrogen amount consumed in the reduction led to values in excess of the theoretical amount of NiO present in the samples. Table 4.1 displays the amount of catalyst analyzed (m_cat (g)), the amounts of Ni and Ce, the consumed amount of hydrogen as well as the ratio of consumed hydrogen and the amount of nickel (n_H_2/n_Ni). As can be seen from the values, the amount of consumed hydrogen exceeds the theoretical amount of Ni present in the samples and the ratio increases with increasing ceria content. This is most probably a result of both spill-over from the Ni to the support as well as reduction of the ceria [214].

Table 4.1: Temperature programmed reduction of the catalysts.

Catalyst	m_cat (g)	Ni %	Ce %	n_Ni (mmol)	n_Ce (mmol)	V_H_2 (ml)	n_H_2 (mmol)	n_H_2/n_Ni
5%Ni13X	0.2013	5.00	0.00	0.1715	0.0000	16.89	0.6905	4.03
5%Ni1%Ce13X	0.1934	5.00	1.00	0.1648	0.0138	19.41	0.7935	4.82
5%Ni2.5%Ce13X	0.1977	5.00	2.50	0.1684	0.0353	18.05	0.7379	4.38
5%Ni5%Ce13X	0.2071	5.00	5.00	0.1764	0.0739	24.14	0.9869	5.59
5%Ni10%Ce13X	0.1893	5.00	10.00	0.1613	0.1351	31.43	1.2849	7.97

In contrast, the first reduction peak of Ce-promoted Ni 13X catalysts became stronger with increasing Ce loading. This may result from the improved dispersion of Ni species [215] and the partial reduction of CeO_2 [216]. Additionally, the two reduction peaks of the catalyst were shifted slightly to a higher temperature upon increasing Ce loading. For 5%Ni13X, the first peak appeared at around 325 °C and a second reduction peak at around 545 °C. After the Ce loading, the first reduction peak shifted to around 360 °C for 5%Ni1%Ce13X, even to 380 °C for 5%Ni10%Ce13X. It has been reported that the reduction peaks of Ce-promoted Ni/γ-Al_2O_3 catalysts shifted to a lower temperature, since the Ce^{4+}/Ce^{3+} redox couple created surface and bulk oxygen vacancies [217]. This could be due to the CeO_2 which on the surface or in super-cages of 13X limited the H_2 reaching NiO, due to the size of CeO_2 [211] (5.5–7.5 Å) and pore size of 13X (7.4 Å) [36]. The highly dispersed NiO (possibly in single sites, sub-nanometer at least) and CeO_2 could result from the size exclusion of 13X zeolite for Ni and Ce citrate complexes during catalyst preparation.

In relation to the seemingly deviating trend of the 5%Ni5%Ce13X the following can be argued. The general trend is a shift to higher T for both distinct peaks (in fact envelopes). The samples are quite inhomogeneous in nature so it is not clear if the Ni/Ce ratio inside and outside the particles is always the same and that will certainly give rise to different reduction behavior. Furthermore, the accuracy of the temperature inside the sample can cause the observed, seemingly, deviating behavior.

4.3.1.6. Fourier transform infrared spectrometry

ATR-FTIR was used to investigate the Ni and Ce complexes during catalyst preparation, to determine the coordination shell of the metals in solution, which may determine how metals disperse in catalysts. The FTIR spectra of the solutions are shown in Figure 4.8, and Table S. 4.3 (supplementary material) shows the adsorption band assignments. Citric acid, nickel nitrate, cerium nitrate and nickel citrate mixed with nickel nitrate solution were the references.

Overall, the ATR-FTIR spectra of solutions e, f and i are much different to free Ce solutions (Figure 4.8). For nickel citrate mixed with cerium nitrate solution, the bands at 1607 cm^{-1} disappeared and a strong band was observed at 1542 cm^{-1}. These two ν_{as} carboxylate stretch-associated bands' changes may result from the new complex (e.g. $[Ce(HCit)(Cit)]^{2-}$), which has a longer bond length than $[Ni(HCit)(Cit)]^{3-}$, eventually leading to the band shifting to a lower wavenumber and 1607 cm^{-1} disappearing [218-220]. The band at 1434 cm^{-1} is also more obviously visible than free cerium solutions, and two new bands at 1298 and 1265 cm^{-1} were observed for citric acid mixed with nickel nitrate solution and nickel citrate mixed with cerium nitrate solution. Other right-shift bands are found at 1249, 1178 and 1141 cm^{-1} for cerium solutions. These differences could be contributed by the ν_s carboxylate stretch in the Ce citrate complexes [218, 219, 221]. In summary, the FTIR spectra show that Cerium ions also complexate with citrate in competition the nickel citrate complexes. The competition is shown to prove that both Ce and Ni are available to the zeolite as citrate complexes, thereby excluding large amounts to penetrate the pores because of the complex' size. This adds to the final conclusion of the presence of very small Ni-Ce clusters, if not even 'single atom' ones.

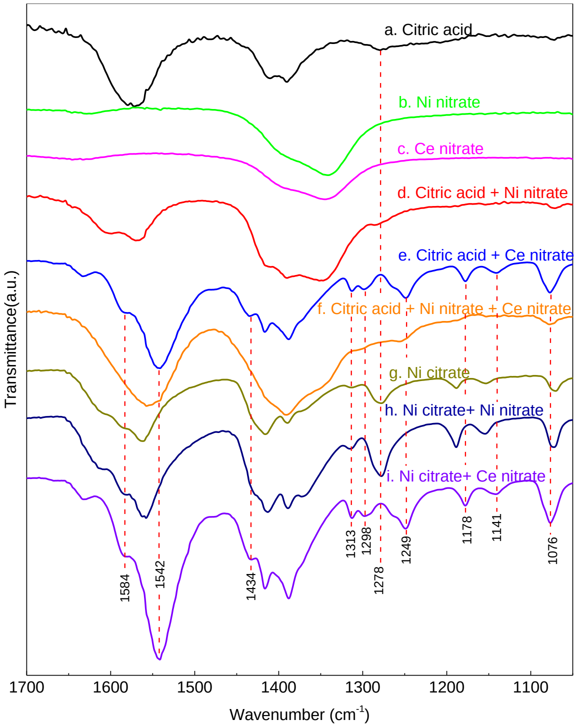

Figure 4.8: ATR-FTIR spectra for aqueous solutions: a) citric acid, b) nickel nitrate, c) cerium nitrate, d) citric acid mixed with nickel nitrate, e) citric acid mixed with cerium nitrate, f) citric acid mixed with nickel nitrate and cerium nitrate, g) nickel citrate, h) nickel citrate mixed with nickel nitrate and i) nickel citrate mixed cerium nitrate. Solutions d, e and f were prepared with stoichiometric ratios. In solution f the molar ratio of Ni:Ce is 1:1, in solution h the molar ratio of nickel citrate to nickel nitrate was 0.83, and in solution i the molar ratio of nickel citrate to cerium nitrate was 0.83. The pH of solutions a, d, e and f were adjusted using 3.4M KOH solution to around 4.5.

4.3.1.7. X-ray photoelectron spectroscopy (XPS)

The chemical valence states of the Ni and Ce in samples were investigated using X-ray photoelectron spectroscopy (Figure 4.9 and supplementary Figure S. 4.1). In Figure 4.9b, a peak observed in the Ni $2p_{3/2}$ at 856.1 eV is assigned to Ni^{2+}; it was accompanied by satellite peaks at around 861.6 eV [222]. Because the $NiSiO_3$ and $NiAl_2O_4$ peaks are at 856.1eV and 855.8 eV, respectively, this indicates that the Ni particles interacted strongly with zeolite 13X via Ni-O-Si(Al) bonding [223]. It could be inferred that the Ni particles in 5%Ni5%Ce13X show similar behavior to 5%Ni2.5%Ce13X, due to their closely resembling spectra (Figure 4.9b and Figure

4.9d). The XPS spectra of Ce 3d (Figure 4.9a and Figure 4.9c) were fitted to several peaks corresponding to Ce $3d_{5/2}$ (v, 898.0 eV) and Ce $3d_{3/2}$ (u_0, 898.7 eV; u, 901.3 eV; u_1, 902.2 eV; u_2, 908.2 eV; u_3, 916.7 eV). The u_0 and u_3 are attributed to Ce^{3+} species, and the remaining peaks (v, u, u_1, u_2) are Ce^{4+} species [224].

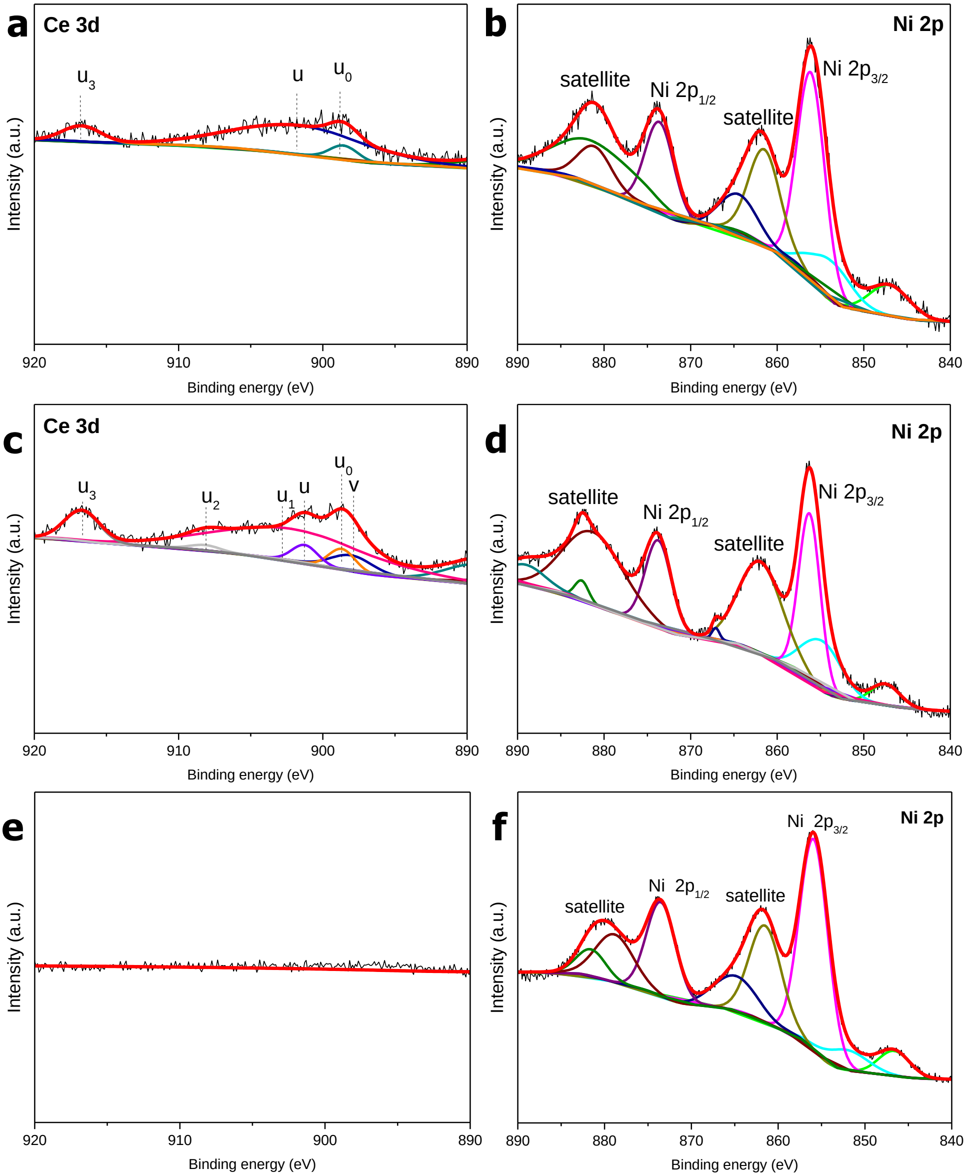

Figure 4.9: (a) Ce 3d XPS spectra in 5%Ni2.5%Ce13X; (b) Ni 2p XPS spectra in 5%Ni2.5%Ce13X; (c) Ce 3d XPS spectra in 5%Ni5%Ce13X; (d) Ni 2p XPS spectra in 5%Ni5%Ce13X ; (e) Ce 3d spectra in 5%Ni13X., (f) Ni 2p XPS spectra in 5%Ni13X.

The X-ray photoelectron spectroscopy of the 5wt % Ni-13 X catalyst has been included for reference in Figure 4.9 (e) and (f). Taking into consideration that the catalyst is monometallic i.e, Ni modified 13 X zeolite without Ce, XPS spectra did not exhibit the presence of Ce^{3+} or Ce^{4+} peaks at binding energies 890-920 eV. The peaks attributed to Ni $^{2+}$ (856.1 eV) and a satellite peak (861.6 eV) were observed at binding energies 840-890 eV.

4.3.1.8. CO_2-temperature programmed desorption (CO_2-TPD)

Figure 4.10 shows the CO_2-TPD profiles of fresh 13X and modified catalysts. The calculated basic site distribution is shown in Figure 4.11 (for detailed information, see supplementary material Table S. 4.5). Most of the samples have three peaks at around 50–150 °C, 250–450 °C and 450–750 °C, which correspond to weak, medium and strong basic sites, respectively [225]. These three basic sites are assigned to surface hydroxyl groups, metal-oxygen pairs and low-coordination oxygen anions, respectively [226]. Overall, the fresh 13X has the most weak, medium and strong basic sites (213 μmol/g). The reason for formation of basic sites is the chemical composition of 13X zeolite (Table S. 4.2). The presence of large amounts of basic sites can be attributed to the presence of alkaline metal oxides: Na (11.2 wt.%), Mg (1.3 wt.%), Ca (0.3 wt.%), K (0.3 wt.%) in the fresh 13X zeolite (Table S. 4.2). The largest amount of total basic sites among the impregnated catalysts was (122 μmol/g) obtained for 5%Ni10%Ce13X (Figure 4.11).

The basicity decreased significantly after modification, which can only be partly be attributed to the removal of Na, Ca, K, Mg from 13X zeolite by ion exchange. Compared to 5%Ni13X, with only nickel, the basicity decreased when Ce was increased up to loading of 2.5 wt.%. When the Ce loading was further increased, the total basicity increased again. It has been reported that Ce^{3+} can act as Lewis base adsorbing CO_2 [227, 228]. A reasonable explanation could be that at low Ce loadings the Ce^{3+} is the dominant charge in the smaller Ni/Ce particles, whereas bulkier particles that are also mainly outside the zeolitic framework contain more Ce^{4+}, causing an increase in basicity again [229].

Furthermore, the basicity of 5%Ni2.5%Ce13X was very similar to 5%Ni2.5%Ce13X-3 h, which was reduced in situ for 3 h at 450 °C instead of 2 h. This shows that the basicity of catalysts is stable after 2 h of reduction before the catalyst test experiments.

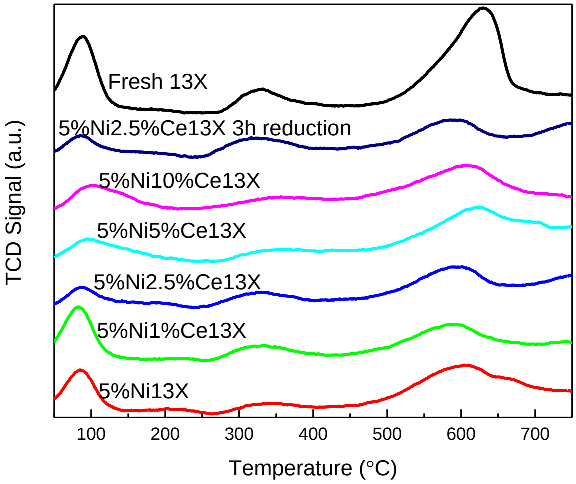

Figure 4.10: CO_2-TPD profiles of fresh 13X, 5%Ni13X, 5%Ni1%Ce13X, 5%Ni2.5%Ce13X, 5%Ni5%Ce13X and 5%Ni10%Ce13X catalyst.

4.3.1.9. Measurement of Brønsted and Lewis acid sites by FTIR using pyridine as probe molecule

The concentration of Brønsted acid sites (BAS) and Lewis acid sites (LAS) in the pristine and titrated zeolites was determined with FTIR using pyridine as a probe molecule method [208, 230-232]. The results are shown in Figure 4.12 (for detailed information, see supplementary material Table S. 4.6).

Overall, compared to fresh 13X, the catalysts' total acidity decreased after the Ni modification promoted by Ce. The lowest total acidity of 427 μmol/g was measured for 5%Ni2.5%Ce13X among 13X catalysts, which is much lower than the other Ce-promoted Ni 13X catalysts. With increasing Ce amount, the acidic sites could be shielded or blocked by the higher Ce loading in the catalysts [232]. It should be noted, however, that Brønsted acid sites and Lewis acid sites in the catalysts changed significantly after the Ce-promoted Ni modification. The Lewis acid sites decreased from 545 μmol/g to 196 μmol/g (250 °C), while the Brønsted acid sites increased dramatically from 12 μmol/g to 282 μmol/g (250 °C), then decreased to 122 μmol/g for 5%Ni2.5%Ce13X, and increased again with the increasing Ce loading. It can be concluded that Ni introduction increased the amount of Brønsted acid sites for 13X zeolite catalysts, where relatively low Ce loading decreases it (Table S. 4.6, supplementary material). The presence and amount of Brønsted acid sites in the 13X fresh zeolite, Ni- and Ce- modified 13X catalysts can be in large part attributed to the Al species in the tetrahedral coordination. Although we do not have Al-NMR results for the coordination (tetra-, penta-, hexa-, hepta-, octa-) of Al species, the quantitative amount of Al measured using energy dispersive X-ray analyses can give some indication regarding the amount of Brønsted acid sites in these catalysts (Figure 4.12). The largest amount of total acid sites (764 µmol/g) was measured for 13X zeolite fresh (Al 13.7 wt.%), the smallest amount of total acid sites (427 µmol/g) was measured for 5%Ni2.5%Ce13X catalyst (Al 12.2 wt.%) with the larger contribution by the Lewis weak acid sites.

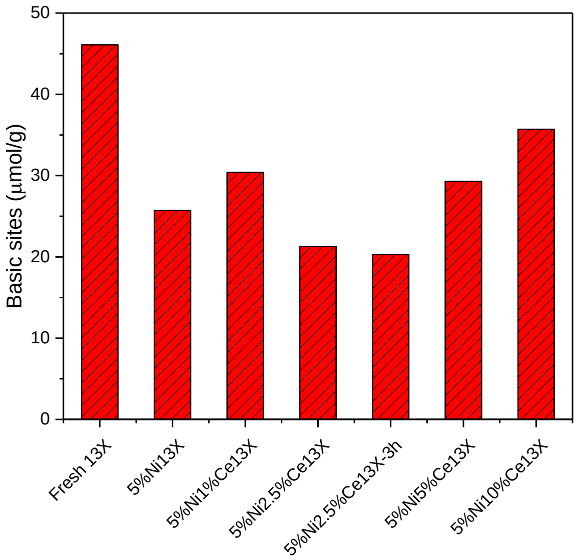

Figure 4.11: Catalyst basic site distribution, calculated based on the results of CO_2-TPD.

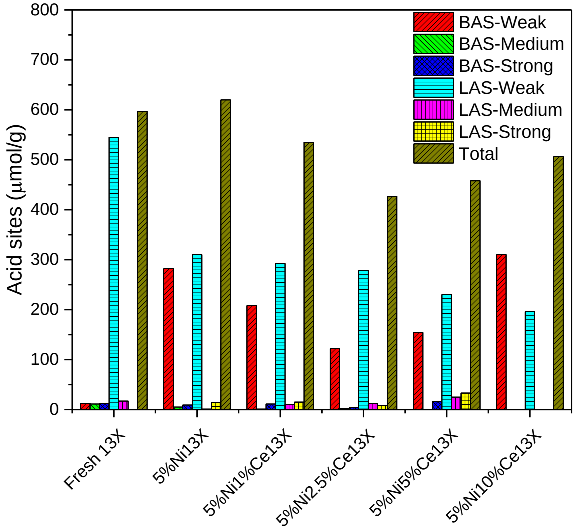

Figure 4.12: Concentrations of Brønsted acid sites (BAS) and Lewis acid sites (LAS) determined with FTIR-pyridine method for fresh 13X, 5%Ni13X, 5%Ni1%Ce13X, 5%Ni2.5%Ce13X, 5%Ni5%Ce13X and 5%Ni10%Ce13X.

4.3.2. Evaluation of catalytic properties in methanation using a fixed-bed reactor

4.3.2.1. Catalyst activity and selectivity

Catalyst activity and selectivity were investigated on a lab-scale fixed-bed reactor system. Details about experimental conditions and settings are in the experimental section. The results are shown in Figure 4.13. A comparison of catalyst performance with literature results can be found in Table S. 4.7 (supplementary material). The CO_2 conversion at each temperature was the average value based on GC measurements of five consecutive stable measurements, after the zeolite 13X adsorbed water under experimental conditions. The adsorption enhancement can be excluded from the data.

Overall, it can be observed from Figure 4.13 that the catalyst around the minima in Figure 4.11 and Figure 4.12, 5%Ni1%Ce13X, 5%Ni2.5%Ce13X and 5%Ni5%Ce13X, performed best. In other words, neither the acidity nor basicity should be too strong, but a balanced amount of both are needed. Furthermore, Lewis acidity is not as influential as Brønsted acidity and the basic sites should clearly not be too strong [233]. The activation energy is rather high and we observed the largest conversion gain compared with the literature at between 280 and 320 °C (Table S. 4.7, supplementary material). 5%Ni2.5%Ce13X and 5%Ni1%Ce13X are really highly active catalysts and display the highest reported low temperature (below 300 °C) activity with industrially relevant catalyst particle sizes.

Ce has a significant influence on the catalyst performance for CO_2 conversion. It has been reported that the oxygen vacancy resulting from Ce could contribute to the catalyst activity [227], but in the 5%Ni5%Ce13X and 5%Ni2.5%Ce13X the Ce^{3+}/Ce^{4+} ratios are equal. It must therefore rather be ascribed to the basicity of ceria which is stronger in the 2.5–5% case. Even though both the weak and medium basic sites are beneficial for CO_2 activation [234] and Ce-promoted catalysts have more weak and medium basic sites than 5%Ni13X (Figure 4.11), the pores blocked by excess Ce oxides counteract this effect at higher loadings. The theoretical maximum Ce loading is around 3.4 wt.% for the case that Ce only located in 13X super cages, which was calculated based on the crystal structure of 13X zeolite. The catalysts surface area and pore volume can be found from supplementary material Table S. 4.8) or too strong adsorption of CO_2 to the strong sites could also account for the lower 5%Ni5%Ce13X and 5%Ni10%Ce13X activities.

The role of the acidic sites is explained in the following. CO_2 methanation on Ni is proposed to proceed via dissociative adsorption of hydrogen followed by a reactive adsorption of CO_2 forming a formate intermediate. The formate then reacts with an additional hydrogen to form water and CO. The rate limiting step of the overall reaction is the dissociation of CO to form adsorbed carbon and oxygen intermediates [174]. It is proposed that the acid base balance of the support influences the dissociation of CO on the Ni surface, especially at lower temperatures. This is reflected in the activity of the catalyst as it is the rate limiting step as well as in the selectivity towards CH_4. Higher activity is thus directly correlated with higher selectivity as displayed in Figure 13. The selectivity is decreased when CO is partly desorbed before it is dissociated.

$$H_2(g) + 2ad \leftrightarrow 2Had \tag{4-3}$$

$$CO_2(g) + Had \leftrightarrow HCOOad \tag{4-4}$$

$$HCOOad + Had \leftrightarrow H_2Oad + COad \tag{4-5}$$

$$COad \leftrightarrow Cad + Oad \text{ (rate limiting step)} \tag{4-6}$$

In general, all catalysts show good CH_4 selectivities, especially for 5%Ni1%Ce13X and 5%Ni2.5%Ce13X, which show CH_4 selectivity higher than 95% at 280–400 °C. Figure 4.13 shows that Ce is not always beneficial to CH_4 selectivity when the Ce loading is higher than 2.5%. This could again be attributed to the influence of Ce on catalysts' basic sites, pore blockage (Table S. 4.8, supplementary material) and acidity (Figure 4.11, Figure 4.12).

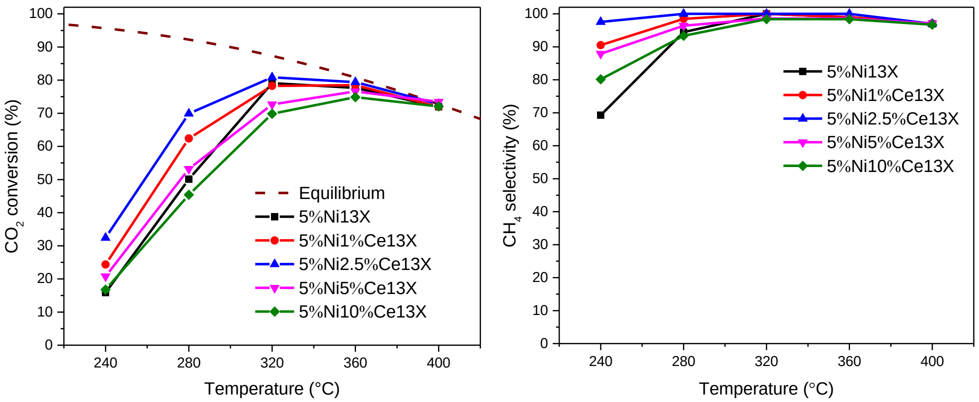

Figure 4.13: CO_2 conversion and CH_4 selectivity with 5%Ni13X, 5%Ni1%Ce13X, 5%Ni2.5%Ce13X, 5%Ni5%Ce13X and 5%Ni10%Ce13X catalyst (reduction at 500 °C, 4 h), 0.9 g, 150 mL/min N_2, 40 mL/min H_2, 10 mL/min CO_2.

4.3.2.2. Catalyst stability and selectivity

The catalyst stability test results (Figure 4.14) show that 5%Ni2.5%Ce13X and 5%Ni13X perform very stably during 200-hour experiments, and they have excellent (high and stable) CH_4 selectivity. The catalyst stability tests were carried out in the lab-scale fixed-bed reactor system at 360 °C; other conditions for evaluation of catalytic properties in the methanation reactions were described in the experimental section above. The conversions are in full agreement with Figure 4.13. It can be concluded that the "sub-nanometer Ni atoms" Ce-promoted 13X catalyst is stable for the CO_2 methanation at a high temperature for 200 hours on stream. The fact that no severe deactivation occurs even at this higher temperature, makes it very unlikely that it would occur at lower temperature.

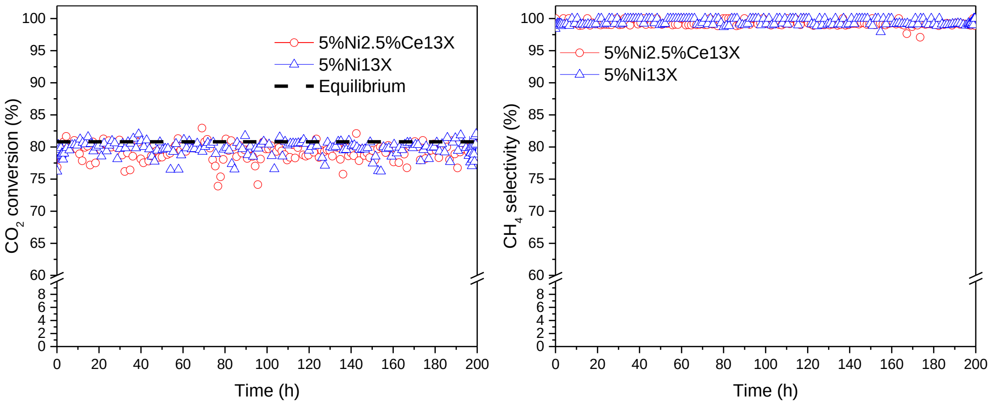

Figure 4.14: CO_2 conversion and CH_4 selectivity of 5%Ni2.5%Ce13X and 5%Ni13X at 360 °C (reduction at 500 °C, 4 h), 0.9 g, 150 mL/min N_2, 40 mL/min H_2, 10 mL/min CO_2.

4.4. Conclusions

Active functional ceria-promoted Ni 13X zeolite catalysts were synthesized using a citrate complexation strategy for CO_2 methanation. The influence of Ce loading on catalyst properties and the catalysts' performance were investigated. The results showed that the loading of Ce affected the catalysts' metal dispersion, reducibility, basicity and acidity, and as a consequence their activity and selectivity. Activity increase is most pronounced at lower temperatures, below 280°C, selectivity is satisfactory from this temperature upward. XRD and SEM results showed that the structure of 13X zeolite did not change after citrates' impregnation and calcination. TEM and STEM-EDX mappings showed that most Ce and Ni were highly dispersed as sub-nanometer. Ce and Ni ions were chelated by citrate and as such diffused in the zeolite structure. It was shown that there was a strong correlation between acidity, basicity and conversion: neither should be too strong and a balance should prevail. The basicity should not be too high to result in too strong bonding of CO_2 and the acidity should not be too high to allow for interaction with CO_2. The catalysts' stability test results showed that the highly active catalyst 5%Ni2.5%Ce13X had a very stable performance on CO_2 methanation and high CH_4 selectivity for a 200-hour timescale.

In summary, using Ni and Ce citrate complexes is a very promising strategy to prepare highly dispersed (sub-nanometer) ceria-promoted Ni zeolite 13X catalysts. The metal precursors in solution both exist as citrate complexes and the catalyst supports are selective to these complexes' size and geometry. It can be inferred that this strategy has significant potential for the preparation of highly active sub-nanometer even single-atom catalysts.

4.5. Supplementary Material

Table S. 4.1: The molar ratio of Ni to Ce in Catalysts.

Catalyst	Ni:Ce mol ratio
5%Ni13X	1:0
5%Ni1%Ce13X	1:0.08
5%Ni2.5%Ce13X	1:0.21
5%Ni5%Ce13X	1:0.42
5%Ni10%Ce13X	1:0.84

Table S. 4.2: Summary of the EDX results for fresh 13X, 5%Ni13X, 5%Ni1%Ce13X, 5%Ni2.5%Ce13X, 5%Ni5%Ce13X and 5%Ni10%Ce13X.

Sample	Content (wt./wt.%)									
	O	Na	Mg	Al	Si	Cl	K	Ca	Fe	Ni	Ce
Fresh 13X	49.6 ±0.7	11.2 ±0.3	1.3 ±0.2	13.7 ±0.3	22.5 ±0.3	0.2 ±0.1	0.3 ±0.1	0.4 ±0.1	0.9 ±0.2	–	–
5%Ni13X	48.2 ±0.9	11.4 ±0.4	0.7 ±0.2	11.9 ±0.3	19.4 ±0.4	–	0.2 ±0.1	0.3 ±0.1	1.1 ±0.2	6.7 ±0.8	–
5%Ni1%Ce13X	46.2 ±0.6	9.3 ±0.2	1.2 ±0.2	13.5 ±0.3	22.0 ±0.3	0.1 ±0.1	0.2 ±0.1	0.8 ±0.1	0.8 ±0.2	4.7 ±0.5	1.1 ±0.2
5%Ni2.5%Ce13X	46.7 ±0.6	10.2 ±0.3	1.7 ±0.2	12.2 ±0.3	19.4 ±0.3	0.1 ±0.1	0.2 ±0.1	0.5 ±0.1	0.3 ±0.2	6.2 ±0.3	2.6 ±0.2
5%Ni5%Ce13X	44.6 ±0.6	9.0 ±0.3	1.5 ±0.2	12.1 ±0.3	19.9 ±0.3	–	0.2 ±0.1	0.5 ±0.1	0.9 ±0.2	5.9 ±0.5	5.5 ±0.5
5%Ni10%Ce13X	43.9 ±0.5	7.7 ±0.3	0.7 ±0.1	11.9 ±0.2	19.6 ±0.3	–	0.1 ±0.1	0.3 ±0.1	0.2 ±0.2	5.0 ±0.5	10.4 ±0.4

Table S. 4.3: Infrared absorption bands assignments for aqueous solutions: a) citric acid, b) nickel nitrate, c) cerium nitrate, d) citric acid mixed with nickel nitrate, e) citric acid mixed with cerium nitrate, f) citric acid mixed with nickel nitrate and cerium nitrate, g) nickel citrate, h) nickel citrate mixed with nickel nitrate and i) nickel citrate mixed cerium nitrate. The solution d, e and f were prepared by stoichiometric, the pH of solution a, d, e and f were adjusted using 3.4M KOH solution to around 4.5.

Solution	Species [235, 236]	Absorption (cm^{-1})	Assignment [211, 218, 235, 236]
Citric acid	Water	1632	$\delta(H_2O)$
	$[(HCit)(Cit)]^{5-}$	1567	$\nu_{as}(COO^-)$
	$(HCit)^{2-}$	1410	$\nu_s(COO^-)$
	Cit^{3-}	1391	$\nu_s(COO^-)$
	$[H_2Cit]^-$	1278	$\nu_s(C\text{-}O)$
	-COOH (monomer)	1073	$\nu_s(C\text{-}O)$
Ni nitrate	Water	1632	$\delta(H_2O)$
	NO_3^-	1386	$\nu\ (NO_3^-)$
	NO_3^-	1343	$\nu\ (NO_3^-)$
Ce nitrate	Water	1632	$\delta(H_2O)$
	NO_3^-	1386	$\nu\ (NO_3^-)$
	NO_3^-	1343	$\nu\ (NO_3^-)$
Citric acid + Ni nitrate	Water	1632	$\delta(H_2O)$
	$Ni[(HCit)(Cit)]^{3-}$	1602, 1567	$\nu_{as}(COO^-)$
	$[Ni(HCit)]$	1415	$\nu_s(COO^-)$
	$[Ni(Cit)_2]^{4-}$	1390	$\nu_s(COO^-)$
	NO_3^-	1345	$\nu\ (NO_3^-)$
	$[NiH_2Cit]^+$	1284	$\nu_s\ (C\text{-}O)$
	-COOH (monomer)	1072	$\nu_s\ (C\text{-}O)$
Citric acid + Ce nitrate	Water	1632	$\delta(H_2O)$
	$[Ce(HCit)(Cit)]^{2-}$	1584, 1542	$\nu_{as}(COO^-)$
	$[Ce(HCit)]^+$	1434	$\nu_s(COO^-)$
	$[Ce(HCit)]^+$	1416	$\nu_s(COO^-)$
	[CeCit]	1388	$\nu_s(COO^-)$
	$[CeH_2Cit]^{2+}$	1313, 1298	$\nu_s(C\text{-}O)$
	CeCit	1249	$\nu_s(C\text{-}O)$
	COOH (monomer)	1178, 1141, 1076	$\nu_s(C\text{-}O)$
Citric acid + Ni nitrate+ Ce nitrate	Water	1632	$\delta(H_2O)$
	$[Ni(HCit)(Cit)]^{3-}$	1557	$\nu_{as}(COO^-)$
	$[Ni(HCit)]$	1416	$\nu_s(COO^-)$
	$[Ni(Cit)_2]^{4-}$ or	1391	$\nu_s(COO^-)$
	$[Ce(Cit)_2]^{3-}$	1345	$\nu(NO_3^-)$
	NO_3^-	1298	$\nu_s(C\text{-}O)$
	$[CeH_2Cit]^{2+}$	1256	$\nu_s(C\text{-}O)$
	CeCit	1076	$\nu_s(C\text{-}O)$
	-COOH (monomer)		
Ni citrate	Water	1632	$\delta(H_2O)$
	$[Ni(HCit)(Cit)]^{3-}$	1607, 1584,1561	$\nu_{as}(COO^-)$
	$[Ni(HCit)]$	1416	$\nu_s(COO^-)$
	$[Ni(Cit)_2]^{4-}$	1389	$\nu_s(COO^-)$
	$[NiH_2Cit]^+$		$\nu_s(C\text{-}O)$

	-COOH (monomer)	1313, 1278, 1188, 1154,1073	ν_s(C-O)
Ni citrate + Ni nitrate	Water	1632	$\delta(H_2O)$
	$[Ni(HCit)(Cit)]^{3-}$	1607, 1584,1561	$\nu_{as}(COO^-)$
	[Ni(HCit)]	1416	$\nu_s(COO^-)$
	$[Ni(Cit)_2]^{4-}$	1389	$\nu_s(COO^-)$
	$[NiH_2Cit]^+$	1313, 1278, 1188,	ν_s(C-O)
	-COOH (monomer)	1154, 1073	ν_s(C-O)
Ni citrate + Ce nitrate	Water	1632	$\delta(H_2O)$
	$[Ce(HCit)(Cit)]^{2-}$	1584, 1542	$\nu_{as}(COO^-)$
	$[Ce(HCit)]^+$	1434	$\nu_s(COO^-)$
	[Ni(HCit)]	1416	$\nu_s(COO^-)$
	$[Ce(Cit)_2]^{3-}$	1388	$\nu_s(COO^-)$
	$[CeH_2Cit]^{2+}$	1313, 1298	ν_s(C-O)
	CeCit	1249	ν_s(C-O)
	-COOH (monomer)	1178, 1141, 1076	ν_s(C-O)

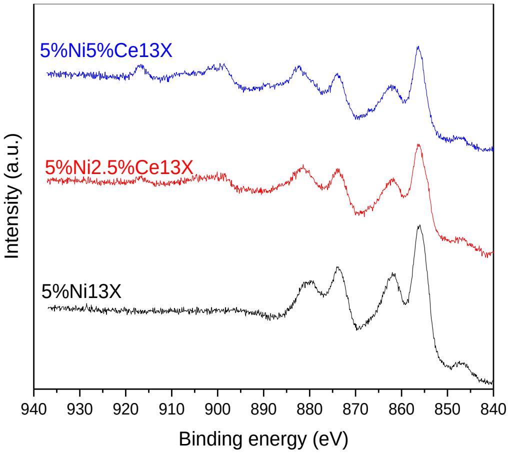

Figure S. 4.1: XPS spectra in 5%Ni13X, 5%Ni2.5%Ce13X and 5%Ni5%Ce13X.

The Figure S. 4.1 shows the binding energies of each peak from XPS results, the ratio of Ce^{3+}/Ce^{4+} in each catalyst. The u_0 and u_3 are attributed to Ce^{3+} species, and the remaining peaks (v, u, u_1, u_2) are Ce^{4+} species [237].

Table S. 4.4: XPS results of Ce 3d in catalysts.

Peak	Binding energy (eV)	5%Ni2.5%Ce13X area	5%Ni5%Ce13X area
u_3	916.7	2397.8	4415.4
u_2	908.2	_	661.8
u_1	902.2	_	21144.4
u	901.3	15803.5	1931.1
u_0	898.7	1627.2	2280.9
v	898.0	_	2781.6
	Ce^{3+}	4025.0	6696.3
	Ce^{4+}	15803.5	26518.9
	Ce^{3+}/Ce^{4+}	0.255	0.253

Table S. 4.5: The catalyst basic sites distribution calculated based on the results of CO_2-TPD.

Sample	Distribution of basic sites (µmol/g)					
	Weak	Medium	Strong	Weak +Medium	Medium +Strong	Total
Fresh 13X	46.1	27.4	140	73.5	167.4	213.5
5%Ni13X	25.7	10.1	75.2	35.8	85.3	111
5%Ni1%Ce13X	30.4	20.1	48.2	50.5	68.3	98.7
5%Ni2.5%Ce13X	21.3	17.8	39.2	39.1	57	78.3
5%Ni2.5%Ce13X- 3h reduction	20.3	26.5	34.4	46.8	60.9	81.2
5%Ni5%Ce13X	29.3	13.7	61.5	43	75.2	104.5
5%Ni10%Ce13X	35.7	11	75.5	46.7	86.5	122.2

Table S. 4.6: Concentrations of Brønsted acid sites (BAS) and Lewis acid sites (LAS) determined with FTIR-pyridine method for fresh 13X, 5%Ni13X, 5%Ni1%Ce13X, 5%Ni2.5%Ce13X, 5%Ni5%Ce13X and 5%Ni10%Ce13X.

Sample	C_{BAS} (µmol/g)			C_{LAS} (µmol/g)			Total (µmol/g)
	250 °C	350 °C	450 °C	250 °C	350 °C	450 °C	
fresh 13X	12	11	12	545	17	166	764
5%Ni13X	282	5	9	310	1	14	620
5%Ni1%Ce13X	208	1	11	292	10	15	535
5%Ni2.5%Ce13X	122	2	4	278	12	8	427
5%Ni5%Ce13X	154	0	16	230	25	33	458
5%Ni10%Ce13X	310	0	0	196	0	0	506

Table S. 4.7: Catalysts performance comparison with the results from literature.

Catalyst[a]	NiO or Ni particle size (nm)	Reactor diameter (mm)	Cat. size (mm)	m_Cat. for test (g)	H_2/CO_2/Inert gas ratio	Total flow rate_input (ml/min) (exp. pressure)	GHSV or WHSV	CO_2 Conversion (%)	CH_4 Selectivity (%)	Rate (mol_CO_2/mol_Ni/s)[b]	Activation energy (kJ/mol)	Ref.
5%Ni13X	11.5	10	0.212-0.5	0.9	4:1:15	200 (1 bar)	13333 ml/g/h	15.9 (240 °C) 50.1 (280 °C) 79.1 (320 °C)	69.3 (240 °C) 94.5 (280 °C) 100 (320 °C)	0.0062 0.0194 0.0307	68[c]	This chapter
5%Ni1%Ce 13X	sub-nano	10	0.212-0.5	0.9	4:1:15	200 (1 bar)	13333 ml/g/h	24.4 (240 °C) 62.4 (280 °C) 78.3 (320 °C)	90.5 (240 °C) 98.5 (280 °C) 100 (320 °C)	0.0096 0.0242 0.0304	55[c]	This chapter
5%Ni2.5%Ce13X	sub-nano	10	0.212-0.5	0.9	4:1:15	200 (1 bar)	13333 ml/g/h	32.4 (240 °C) 69.9 (280 °C) 80.9 (320 °C)	97.6 (240 °C) 100 (280 °C) 100 (320 °C)	0.0126 0.0271 0.0314	45[c]	This chapter
5%Ni/MSN	9.9	8	0.2-0.4	0.2	4:1:0	167 (1 bar)	50000 ml/g/h	82 (350 °C)	99.9 (350 °C)	0.1196	76	Ref.[171]
20%Ni/SiO_2	21.1	9	0.07-0.59	0.2	76:19:5	33 (1 bar)	10000 ml/g/h	41 (350 °C)	89 (350 °C)	0.0030	_	Ref.[172]
20%Ni/Al_2O_3	>10	-	0.212-0.25	0.7	30:6:64	750 (1 bar)	55000/h	20 (300 °C)	99.8 (300 °C)	0.0078	_	Ref.[173]
5%NiUSY	-	-	-	-	36:9:10	250 (1 bar)	43000/h	9.4 (300 °C)	-	0.0205	_	Ref.[40]
5%NiUSY	17-33	-	-	-	36:9:10	250 (1 bar)	43000/h	6.7 (300 °C)	93.1 (300 °C)	0.0146	_	Ref.[43]
4%Ni3%Ce USY	17-33	-	-	-	36:9:10	250 (1 bar)	43000/h	3.0 (300 °C)	84 (300 °C)	0.0082	_	Ref.[43]
5%NiMSN	9.9	8	0.02-0.04	0.2	4:1:0	167 (1 bar)	50000 ml/g/h	64.1 (300 °C)	99.9 (300 °C)	0.0935	76	Ref.[58]
5%Ni/MCM-41	10.5	8	0.02-0.04	0.2	4:1:0	167 (1 bar)	50000 ml/g/h	56.5 (300 °C)	98.3 (300 °C)	0.0824	78	Ref.[58]
5%Ni/HY	19.8	8	0.02-0.04	0.2	4:1:0	167 (1 bar)	50000 ml/g/h	48.5 (300 °C)	96.4(300 °C)	0.0707	81	Ref.[58]
5%Ni/SiO_2	17.8	8	0.02-0.04	0.2	4:1:0	167 (1 bar)	50000 ml/g/h	42.4 (300 °C)	96.6 (300 °C)	0.0618	84	Ref.[58]
5%Ni/γ-Al_2O_3	-	8	0.02-0.04	0.2	4:1:0	167 (1 bar)	50000 ml/g/h	27.6 (300 °C)	95.2 (300 °C)	0.0403	103	Ref.[58]
10%Ni/H-Y	17.0	9	0.3-0.5	0.5	4:1:1.25	250 (1 bar)	10000/h	15 (350 °C)	88 (350 °C)	0.0066	_	Ref.[41]
10%Ni/Na-Y	19.8	9	0.3-0.5	0.5	4:1:1.25	250 (1 bar)	10000/h	30 (350 °C)	82 (350 °C)	0.0131	_	Ref.[41]
10%Ni/H-BETA	19.1	9	0.3-0.5	0.5	4:1:1.25	250 (1 bar)	10000/h	23 (350 °C)	88 (350 °C)	0.0100	_	Ref.[41]
10%Ni/Na-BETA	20.1	9	0.3-0.5	0.5	4:1:1.25	250 (1 bar)	10000/h	33 (350 °C)	88 (350 °C)	0.0144	_	Ref.[41]
10%Ni5%La_2O_3/Na-BETA	12.5	9	0.3-0.5	0.5	4:1:1.25	250 (1 bar)	10000/h	58.5 (350 °C)	-	0.0255	_	Ref.[41]
5%Ni3%Ce/Na-USY	2.4	-	-	-	36:9:10	250 (1bar)	-	23 (350 °C)	82 (350 °C)	0.0502	_	Ref.[109]

[a] HY or H-Y = protonated Y zeolite; USY=ultra-stable Y zeolite; H-BETA= protonated BETA zeolite. [b] Calculated under the specific temperature based on the total Ni metal in catalyst. [c] Calculated based on Arrhenius plots in the temperature range 513-553K.

Table S. 4.8: The specific surface area and pore volumes of fresh zeolites and catalysts

Sample	Specific surface area (m^2/g_{cat})	V_{total} (cm^3/g_{cat})
13X zeolite	685	0.24
5%Ni13X	612	0.21
5%Ni1%Ce13X	628	0.22
5%Ni2.5%Ce13X	611	0.21
5%Ni5%Ce13X	573	0.20
5%Ni10%Ce13X	539	0.19

5

Sorption enhanced CO_2 methanation with highly active Ni 13X zeolite catalyst

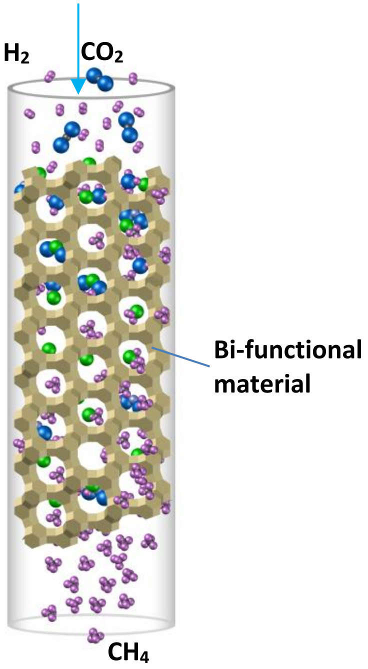

Keywords of this chapter:

sorption enhanced,

zeolites,

bifunctional materials,

water removal,

CO_2 methanation.

This chapter is based on the following publication:
L. Wei, H. Azad, W. Haije, H. Grénman, and W. de Jong, Pure methane from CO_2 hydrogenation using a sorption enhanced process with catalyst/zeolite bifunctional materials. Applied Catalysis B: Environmental, 2021. 297: p. 120399. [238].

5.1. Introduction

Converting CO_2 to chemicals and fuels is one of the potential routes for achieving the goal of reducing carbon emission as agreed on in the Paris agreement [3, 4]. This makes CO_2 and H_2 from renewable sources, e.g. biomass, wind or solar energy, increasingly important as feedstocks for the chemical industry [5, 6, 130, 131]. Methanation via the Sabatier Reaction **(5-1)** is an exemplary method for CO_2 utilization within the context of large-scale energy storage based on power to gas [7, 78], which is aimed at carbon neutrality [239, 240]. It is also a promising method for upgrading the biomass thermochemical conversion product gases which contain CO_2 and H_2 [22].

$$CO_2 + 4H_2 \leftrightarrow CH_4 + 2H_2O;\ \ \Delta H^0_{298} = -165 \text{ kJ/mol} \qquad (5\text{-}1)$$

One important advantage in methanation is that existing infrastructure can be used for the product’s transportation and storage, which has great potential for industrial and transport applications. The Sabatier reaction is limited by equilibrium, so, in order to reach high yields, it has to be performed at very high pressures (Figure 5.1), or costly separations must be performed to obtain a pure enough product.

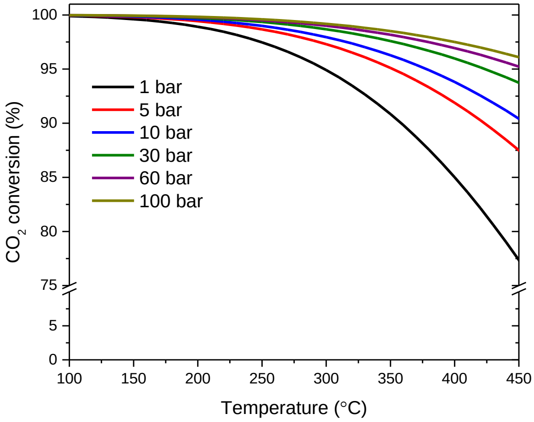

Figure 5.1: Thermodynamic equilibrium conversion for the stoichiometric feed gas composition of CO_2 methanation. The equilibrium constant K_{eq} was retrieved from the database of Factsage^{TM} software for the reaction of CO_2 methanation $4H_2+CO_2 \leftrightarrow CH_4+2H_2O$ at different pressures and temperatures. More information concerning the calculation procedure can be found in the supplementary material.

The CO_2 methanation reaction equilibrium **(5-1)** can, however, be shifted towards the products according to Le Chatelier’s principle [25] by removing water from the reaction mixture by sorbents like zeolites [27]. The resulting methane-rich product gas can then even easily meet the gas grid feed requirement. There are many publications about CO_2 methanation using zeolite as the catalyst support, but the research on sorption enhanced CO_2 methanation is scarce [40, 41, 113]. LTA zeolites (3A, 4A and 5A) and zeolite13X have been used by researchers in the sorption enhanced CO_2 methanation during the past several years [27, 33, 37]. Borgschulte et al. found that the CH_4 selectivity was greatly enhanced by the zeolite pore size if it is larger than 5Å [37]. Zeolite 13X is well known for its high water uptake capacity and hence a potential candidate in sorption enhanced CO_2 methanation [123, 174]. It was reported by Delmelle et al. that a Ni/13X catalyst allows for a longer operation time compared to Ni/5A catalyst, since zeolite 13X has a significantly higher water sorption capacity [26].

Terreni et al. [84] reported that nano-structured sorption enhanced catalysts with short diffusion pathways are advantageous over physical mixtures of sorbents and catalysts which result in long diffusion path lengths. In other words, bifunctional materials which contain both catalytic and adsorption sites in close proximity are needed. Low temperature promotes high equilibrium CO_2 conversion (Figure 5.1), while temperatures above 280 °C are typically required to obtain reasonable CO_2 conversion kinetics and resulting in far from 100% equilibrium conversion values. Bifunctional materials should thus have high activity and selectivity below 280 °C, as well as high water adsorption capacity for obtaining high CO_2 conversion, which can also prevent carbon formation and lead to efficient operation of the CO_2 methanation in a fluidized-bed reactor [118]. Bifunctional materials prepared by loading catalytically active metal directly into the zeolite have therefore been identified as a promising solution. A schematic of such bifunctional materials is shown in (Figure 5.2).

Recently, three papers were published by the current authors on the aforementioned bifunctional materials, detailing synthesis options, catalyst material, catalyst metal concentration and promoters in conjunction with their performance and material characterization details [123, 174, 202].

The current chapter focuses on the combined sorption enhancement and catalytic properties of the following impregnated zeolite bifunctional materials: 5%Ni5A, 5%Ni13X, 5%NiL and 5%Ni2.5%Ce13X. The previous publications focused only on preparation, characterization, conversion and selectivity of the non-enhanced process. The bifunctional material 5%NiL, though, has not been described in the earlier mentioned publications. It was included to provide a second larger pore zeolite in addition to zeolite 13X.

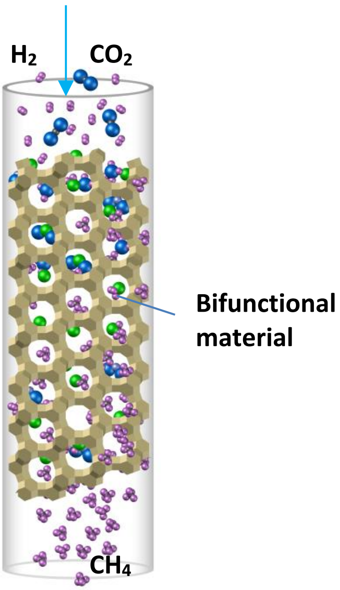

Figure 5.2. Schematic of sorption enhanced CO_2 methanation.

5.2. Experimental section

5.2.1. Catalyst preparation and characterization

The 5%Ni5A, 5%Ni13X, 5%NiL and 5%Ni2.5%Ce13X were prepared by evaporation impregnation and characterized thoroughly by e.g. STEM-EDX, TEM, N_2 physisorption, XRD, XPS and chemisorption as described in our previous work [123, 174]. The zeolite L was prepared as the references [241, 242], the zeolite L based bifunctional material was synthesized by evaporation impregnation according to the description in references [123, 174] and the characterization details can be found in the Supplementary Material.

5.2.2. Sorption enhanced CO_2 methanation in a fixed-bed reactor

The catalyst activity, selectivity, and sorption enhancement capacity, as well as prolonged stability experiments were performed in a quartz fixed-bed reactor described in our previous work [202]. The input gases in experiments were controlled by mass flow controllers, which had output pressure of 1-1.3 bar. All flow rate unit refers to under normal condition (20 °C, 1bar).

Before the experiment, 6.5 g of calcined catalyst 5%Ni2.5%Ce13X was loaded in the reactor and reduced under 100 ml/min H_2 at 500 °C for 2 h. The 5%Ni13X, 5%Ni5A and 5%NiL samples were tested in the same reactor system with a 8.4 g loading. The catalyst activity determination experiments were carried out between 180 °C to 360 °C with a gas hourly space velocity (GHSV) of 923 ml/$g_{cat.}$/h, in a reaction mixture of H_2, CO_2, CH_4 and N_2, where N_2 was used as balance gas. The total input volumetric gas flow rate was 100 ml/min. Additionally, different GHSV values were applied. The gas produced from the reactor flowed through a cooling condenser and was analyzed by GC (Varian, CP-4900 Micro-GC) equipped with HayeSep A, molecular sieve columns (Molsieve 5 Å PLOT) and a thermal conductivity detector. Helium was used as the carrier gas.

The CO_2 conversion (5-2) and catalyst selectivity (5-3) for CH_4 are defined as [153, 154]:

$$X_{CO_2} = \frac{n_{CO_{2,in}} - n_{CO_{2,out}}}{n_{CO_{2,in}}} \tag{5-2}$$

$$S_{CH_4} = \frac{n_{CH_{4,out}}}{n_{CO_{2,in}} - n_{CO_{2,out}}} \tag{5-3}$$

Where $n_{CO_{2,in}}$ is the input molar flow rate of CO_2 in the experiment, $n_{CO_{2,out}}$ and $n_{CH_{4,out}}$ are the molar flow rate of CO_2 and CH_4 calculated from GC results respectively (selectivity <100% means CO is formed).

The water breakthrough capacity of bifunctional materials was calculated using equation:

$$C_{wb} = t_{wb} \cdot S_{wp} \tag{5-4}$$

where, C_{wb} is the water breakthrough capacity of the bifunctional material, having the unit mmol/g (per gram bifunctional material), t_{wb} (min) is the time it takes to for the bifunctional material to be saturated with water, it starts from the beginning of the reaction to water exiting the catalyst bed and being detected by the humidity detector, and S_{wp} is the rate of water production in the catalyst bed (mmol/min/g). The conversion was calculated based on the GC analysis results.

5.3. Results and discussion

5.3.1. Sorption enhanced and non-sorption enhanced experiments using a fixed-bed reactor

Sorption enhanced and non-sorption enhanced CO_2 methanation experiments using 5%Ni2.5%Ce13X were carried out at the same experimental conditions for comparison.

Before the non-sorption enhanced CO_2 methanation was performed, the bifunctional material was utilized in an experiment at 180 °C to saturate it with water, then the furnace temperature was increased to investigate the catalyst performance. The sorption enhanced experiments were carried out with a completely dry sorbent.

The bifunctional material was regenerated at 300 °C under 90 ml/min N_2 and 10 ml/min H_2 for 1 hour before each sorption enhanced CO_2 methanation. Each sorption enhanced CO_2 methanation experiment was carried out for 55 min until water exited the system i.e. the breakthrough capacity was reached. The experimental results are shown in Figure 5.3 and Figure 5.4.

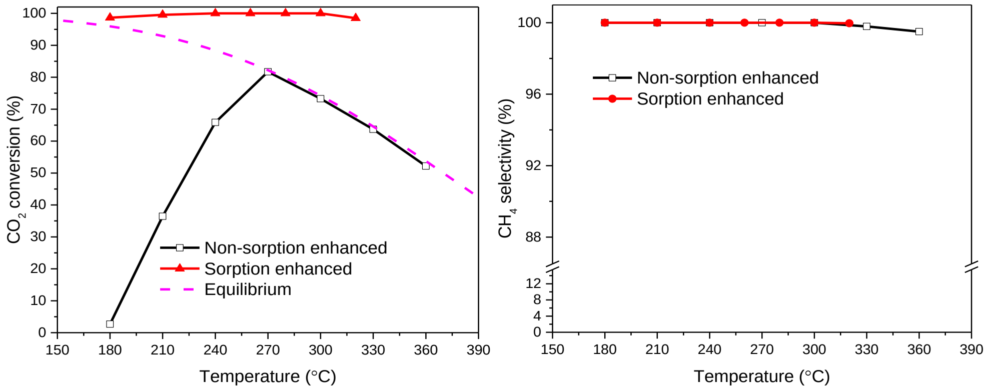

Figure 5.3: CO_2 conversion and CH_4 selectivity of 5%Ni2.5%Ce13X at non-sorption enhanced and sorption enhanced CO_2 methanation. Inlet gas composition (volumetric basis): 6% N_2, 10% H_2, 2.5% CO_2, 81.5% CH_4, 100 ml/min in total (GHSV= 923 ml/g_{cat}/h). 6.5 g catalyst was reduced at 500 °C under 100 ml/min H_2 for 2 h.

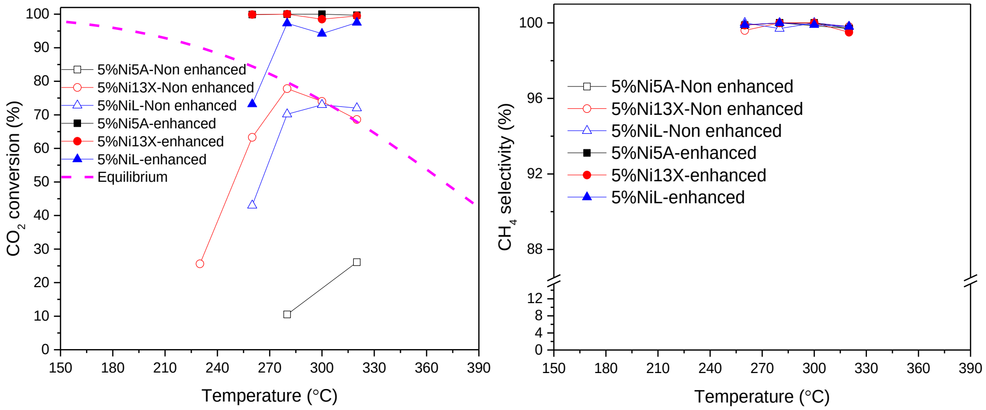

Figure 5.4: CO_2 conversion and CH_4 selectivity of 3 different bifunctional materials at non-sorption enhanced and sorption enhanced CO_2 methanation. Inlet gas composition (volumetric basis): 9.9% H_2, 2.5% CO_2, 81.6% CH_4, 6.0% N_2, 100 ml/min in total (GHSV=714 ml/g_{cat}/h). The bifunctional material of 8.4 g was reduced by a 100 ml/min H_2 for 2h at 450 °C before testing.

For the non-sorption enhanced CO_2 methanation, displayed in Figure 5.3 the catalyst activity seems to be severely diffusion limited by the presence of water at lower temperatures [123]. The CO_2 conversion reached equilibrium (82%) at 270 °C and it decreased to 52% at 360 °C as conversion was limited by thermodynamics [33]. It can be clearly seen, that the CO_2 conversion reaches practically thermodynamic equilibrium at the high temperature. However, a close to complete CO_2 conversion can be obtained at temperatures between 180 to 320 °C with the sorption enhanced CO_2 methanation conditions. A slight decrease in CO_2 conversion was observed when the temperature was increased to 320 °C, which results from the thermodynamics of the methanation equilibrium as well as the water uptake capacity of the zeolite: both are reduced at high temperature. Slightly lower CO_2 conversion (98.6%) was obtained at 180 °C, which is due to decreased Sabatier reaction rates at low temperature. The sorption enhanced CO_2 methanation resulted in a significant increase in the conversion % (up to 84%) which shows the very high impact of water removal by the bifunctional material 5%Ni2.5%Ce13X.

Around 100% CH_4 selectivity was obtained from both non-sorption and sorption enhanced CO_2 methanation using 5%Ni2.5%Ce13X within the temperature range of 180 to 330 °C, although a slight decrease at 360 °C can be observed. This shows that the sorption enhancement has no significant effect on the CH_4 selectivity. Our previous article showed that a proper acid-base balance is beneficial for non-sorption enhanced CO_2 methanation of 5%Ni2.5%Ce13X [202] concerning zeolite material acidity as Lewis acidity is not as influential as Brønsted acidity and the basic sites should clearly not be too strong [233]. The evidence is lacking for a changing reaction path of CO_2 methanation in this chapter, even though the presence of CeO_2 often leads to a carbide pathway to produce *CO [43]. The strong water removal by the bifunctional material would be beneficial for cutting short reaction steps in the carbide pathway [116], since it enables water removal in time. The CO_2 conversion is still around 100% under sorption enhanced condition at 180 °C, even though the catalyst catalytic activity is low at 180 °C. This can also be ascribed to the strong water removal effect by the bifunctional material. Additionally, the CO_2 conversion and CH_4 selectivity clearly results from the highly dispersed subnanometer Ni particles of the bifunctional material [202].

A high CH_4 selectivity around 100% was also obtained from all bifunctional materials without Ce promotion (Figure 5.4), while the CO_2 conversions are different especially in non-sorption enhanced CO_2 methanation [243]. The dispersion of Ni on 13X was higher than on 5A zeolite due to the fact that 13X zeolite has a larger pore size, which resulted in a higher activity of 5%Ni13X [123]. The zeolite L also has larger pores compared to 5A zeolite. Around 100% CO_2 conversion could be obtained with 5%Ni5A and 5%Ni13X bifunctional materials even without Ce promotion which has been shown to increase activity, while the water vapor breakthrough time of 5%Ni13X was longer compared to 5%Ni5A (Figure 5.5). The higher water uptake capacity of zeolite 13X [38] promoted the sorption enhanced methanation. The influence of sorption enhancement could also be seen when using 5%NiL in CO_2 methanation, but the water vapor breakthrough time was only some minutes when using 8.4 g of catalyst indicating considerably lower water uptake capacity compared to zeolite 13X [243].

The water breakthrough capacities of all the catalysts investigated are displayed in Figure 5.5.

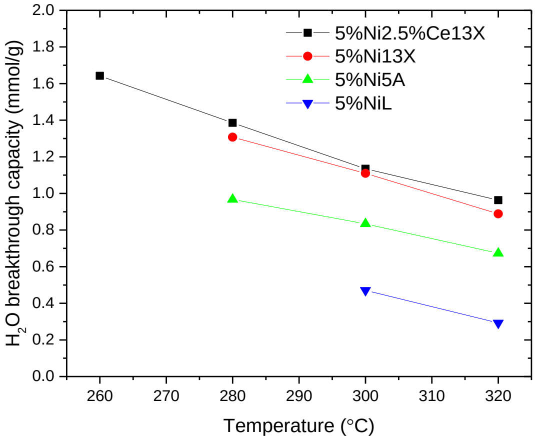

Figure 5.5: H_2O breakthrough capacities of 5%Ni2.5%Ce13X, 5%Ni13X, 5%Ni5A and 5%NiL calculated from sorption enhanced CO_2 methanation experiments (GHSV = 923 ml/$g_{cat.}$/h).

Table 5.1 summarizes the performance of representative bifunctional materials for sorption enhanced CO_2 methanation found in literature. The comparison reveals that the 5%Ni2.5%Ce13X has an excellent activity and performance in the sorption enhanced CO_2 methanation at 1 bar total pressure and that both 5%Ni13X and 5%Ni5A are promising bifunctional materials.

Table 5.1: Performance of representative bifunctional materials for sorption enhanced CO_2 methanation.

Bifunctional Catalyst	Metal loading (wt.%)	Feed gases H_2: CO_2: N_2: CH_4	GHSV	Mass^a (g)	P (bar)	T (°C)	X_{CO2} (%)	S_{CH4} (%)	T_{reg}^b (°C)	Ref.
Ni/5A	6	400: 50: 0: 0	1000 /h	13	1.2	170	100	100	N.A.	[27]
Ni/Al_2O_3 mix 4A	N.A.	9.9: 2.5: 6: 81.6	2500 ml/g_{cat}/h	3.6	1	250-350	100	100	350-450	[33]
Ni/5A	5	4.05: 1: 0: 0	92 /h	250	1	300	100	100	300	[26]
Ni/13X	5	4.05: 1: 0: 0	92 /h	250	1	300	100	100	300	[26]
5%Ni2.5%Ce13X	5	10: 2.5: 6: 81.5	923 ml/$g_{cat.}$/h	6.5	1	180-320	100	100	300	This ch.
5%Ni13X	5	9.9: 2.5: 6: 81.6	714 ml/g_{cat}/h	8.4	1	260-320	100	100	450	This ch.
5%Ni5A	5	9.9: 2.5: 6: 81.6	714 ml/g_{cat}/h	8.4	1	260-320	100	100	450	This ch.
5%NiL	5	9.9: 2.5: 6: 81.6	714 ml/g_{cat}/h	8.4	1	260-320	98	100	450	This ch.

Mass^a -Mass of bifunctional material.

^{a} $T_{reg.}$-regeneration temperature of bifunctional material.

5.3.2. Effect of CH_4 partial pressure

In a practical large-scale two step CO_2 methanation, a considerable amount of CH_4 will be fed to the sorption enhanced second step for maximizing the CH_4 content in the final product [33]. In an industrial methanation plant, the process will be divided into at least two different consecutive reactors, in which the first one(s) operate at higher temperature bringing the conversion to equilibrium, which would be at around 80% [33]. In order to avoid the costly separation of H_2 from CO_2 and CH_4, a sorption enhanced reactor is required to bring the conversion close to 100%. Thus, in the current study, methane corresponding to practical operational conditions was co-fed into the reactor to investigate and demonstrate operation.

The effect of the CH_4 partial pressure on sorption enhanced CO_2 methanation was investigated in a lab scale fixed bed reactor system. The bifunctional material was regenerated at 300 °C under 90 ml/min N_2 and 10 ml/min H_2 for 1 hour before each sorption enhanced CO_2 methanation experiment.

Different CH_4 partial pressures were employed for sorption enhanced CO_2 methanation at 210 - 300 °C. The water breakthrough capacities of the bifunctional material are shown in Figure 5.6. A 100% CO_2 conversion was observed in the experiments with varying CH_4 partial pressures. The water breakthrough time was observed to occur around 21.4 min during experiments at 300 °C and extended to 47 min during experiments at 210 °C (Table S. 5.1). The water breakthrough capacities (Figure 5.6) were calculated from sorption enhanced CO_2 methanation experiments. Inlet gas composition: y% N_2, 10% H_2, 2.5% CO_2, x% CH_4, 100 ml/min in total, x from 0-81.5, y from 87.5-6.0. An amount of 6.5 g catalyst was reduced at 500 °C under 100 ml/min H_2 for 2 h. It is shown that there is no significant difference for different CH_4 partial pressures (Figure 5.6) especially at temperatures in the range of 270 to 300 °C. It can therefore be concluded that the CH_4 partial pressure has no significant effect on sorption enhanced CO_2 methanation with 5%Ni2.5%Ce13X bifunctional material (i.e. zeroth order in methane partial pressure), which may result from the low competitive adsorption of CH_4 (CH_4 capacity) on the bifunctional 5%Ni2.5%Ce13X.

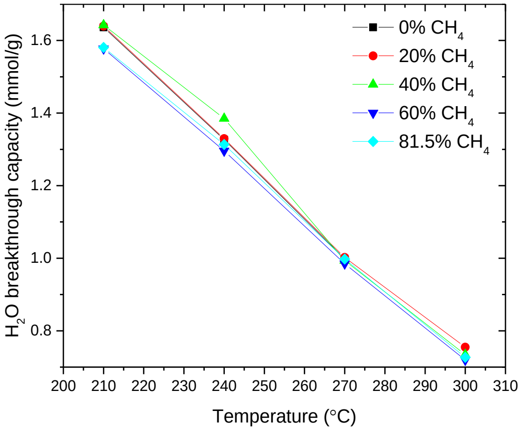

Figure 5.6: H_2O breakthrough capacities of 5%Ni2.5%Ce13X under different CH_4 partial pressures (GHSV= 923 ml/g_{cat}/h).

5.3.3. Effect of regeneration temperature

The regeneration is performed to retain the water uptake capacity of the bifunctional material. The effect of the regeneration temperature on sorption enhanced CO_2 methanation was investigated in a lab scale fixed bed reactor system.

It was found, that the regeneration temperature has a significant effect on restoring the water uptake capacity i.e. desorbing water, which was also visible in the water breakthrough experiments (Figure 5.7). When comparing the different regeneration temperatures it can be noticed that, in general, the water uptake capacities are larger at low temperatures, which should be reflected in a practical operation. The water breakthrough time can be found in the supplementary material (Table S. 5.2)). Even though a higher water breakthrough capacity can be obtained through more efficient desorption of water at higher regeneration temperature, the associated heat loss and higher operation costs should be taken into account in practical sorption enhanced CO_2 methanation. A too high regeneration temperature could also lead to a collapse of the structure of the bifunctional material, which is not beneficial for a long-term operation.

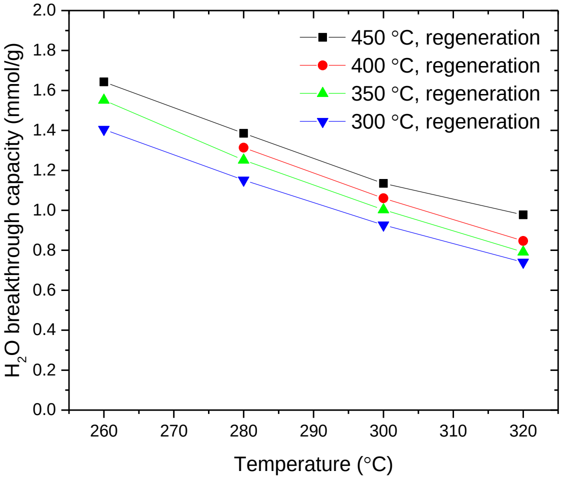

Figure 5.7: Water breakthrough capacities of 5%Ni2.5%Ce13X at different regeneration temperatures (1 h regeneration), calculated from sorption enhanced CO_2 methanation experiments. Inlet gas composition (volumetric basis): 6% N_2, 10% H_2, 2.5% CO_2, 81.5% CH_4, total flow rate 100 ml/min (GHSV= 923 ml/g_{cat}/h). 6.5 g catalyst was reduced at 500 °C under 100 ml/min H_2 for 2 h.

5.3.4. Effect of gas hourly space velocity (GHSV)

Gas hourly space velocity (GHSV) determines the reactants residence time in the catalyst bed and influences the reactants conversion. The effect of GHSV on sorption enhanced CO_2 methanation was investigated using bifunctional material 5%Ni2.5%Ce13X in a lab scale fixed bed reactor system. The results are displayed in Figure 5.8 and Table S. 5.3 (supplementary material). The bifunctional material was regenerated at 300 °C under 90 ml/min N_2 and 10 ml/min H_2 for 1 hour before each sorption enhanced CO_2 methanation.

It can be seen in Figure 5.8, that the H_2O breakthrough capacity at different GHSV values show a similar trend and magnitude, decreasing with an increase of the reaction temperature due to the lower temperature being advantageous for water adsorption on zeolite. The differences between the H_2O breakthrough capacities are different at different temperatures; the lower the reaction temperature the larger the H_2O breakthrough capacity. This is due to the rapid increase of water capacity of zeolite 13X with a decreasing temperature.

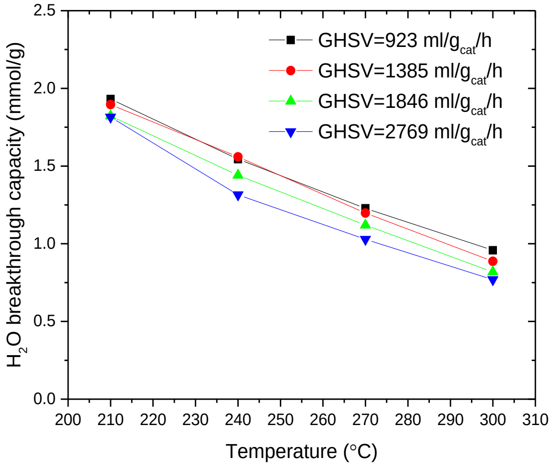

Figure 5.8: H_2O adsorption capacities of 5%Ni2.5%Ce13X at different GHSV values (ml/g_{cat}/h), calculated from sorption enhanced CO_2 methanation experiments. Inlet gas composition (volumetric basis): 6% N_2, 10% H_2, 2.5% CO_2, 81.5% CH_4, total flow rate 100, 150, 200 and 300 ml/min. 6.5 g catalyst was reduced at 500 °C under 100 ml/min H_2 for 2 h.

5.3.5. Performance stability

To investigate the catalyst stability and the regenerability of water breakthrough capacity of the bifunctional 5%Ni2.5%Ce13X, sorption enhanced CO_2 methanation was performed until the water breakthrough point and regeneration was performed during 100 cycles. The results are shown in Figure 5.9 and a typical water breakthrough capacity and duration of an absorption cycle of bifunctional catalyst 5%Ni2.5%Ce13X is shown in Figure 5.10.

Overall, the 5%Ni2.5%Ce13X shows very good stability for the long-term sorption enhanced CO_2 methanation (Figure 5.9). The CO_2 conversion and CH_4 selectivity were around 100% during the 100 cycles test, and only a slight decreasing of the water uptake capacity was observed. Both the experiments performed at 240 and 300 °C show a similar behavior during the methanation. No significant change of the crystal structure (Figure S. 5.5, supplementary material) and surface properties (Table S. 5.5, supplementary material) was observed during the experiment. No carbon deposition was either detected in the thermo-gravimetric analysis (TGA) results (Figure S. 5.6, supplementary material), which were performed on the spent 5%Ni2.5%Ce13X in an air atmosphere. This was compared to the mass loss behavior to fresh 13X zeolite and reduced 5%Ni2.5%Ce13X. The low reaction temperature enabled by the active catalyst and removing H_2O by sorbent in the sorption enhanced CO_2 methanation most probably contributed to avoiding carbon deposition on the catalysts [118]. In addition, the TEM result shows that the spent 5%Ni2.5%Ce13X maintained very good metal dispersion (Figure S. 5.7, supplementary material). However, an observation of some particles formation (TEM, Figure S. 5.7) in the prolonged 100 cycle experiments caused possibly by limited sintering of Ni or the formation of some carbonaceous deposits on the surface of the particles could be a possible reason for the slight deactivation observed for the bifunctional materials. Another possible reason for the slight decrease of the micropore surface area and the water uptake capacity is the CO_2 and H_2O co-adsorption on the zeolite 13X [146, 244].

It can be concluded that the bifunctional material had a high catalytic performance for CO_2 methanation; the extremely low water partial pressure which resulted from the sorption effect of the zeolite 13X did not lead to a rapid degradation of the bifunctional material in 100 cycles test (over 223 hours on stream).

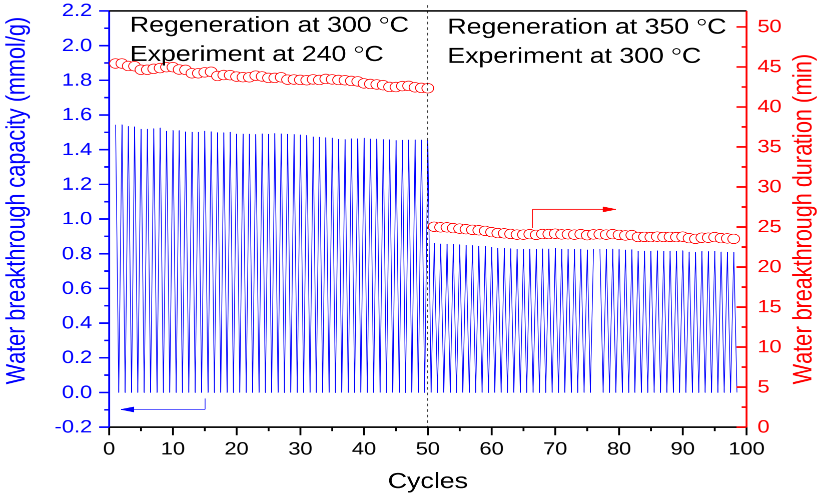

Figure 5.9: Water breakthrough capacity and stability of bifunctional catalyst 5%Ni2.5%Ce13X. Cycles 1-50: regeneration at 300 °C, experiment at 240 °C; 51-100 cycles: regeneration at 300 °C, experiment at 240 °C. Regeneration under 90 ml/min N_2 and 10 ml/min H_2 for 1 hour, each sorption enhanced experiment was run around 52 min with input gases 10 ml/min H_2, 2.5 ml/min CO_2, 81.5 ml/min CH_4 and 6 ml/min N_2; GHSV=923 ml/g_{cat}/h. Total time was around 223 hours for 100 cycles.

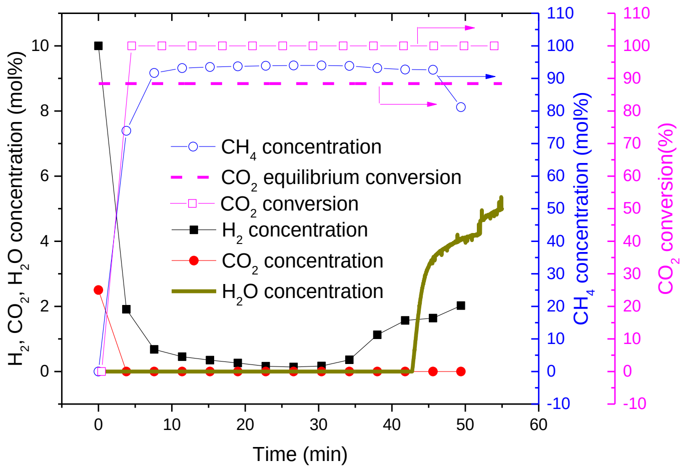

Figure 5.10: Typical water breakthrough capacity and duration of bifunctional catalyst-sorbent 5%Ni2.5%Ce13X. Regeneration at 300 °C, experiment at 240 °C; Regeneration under 90 ml/min N_2 and 10 ml/min H_2 for 1 hour, each sorption enhanced experiment was run with input gases 10 ml/min H_2, 2.5 ml/min CO_2, 81.5 ml/min CH_4 and 6 ml/min N_2 (GHSV= 923 ml/g_{cat}/h). No CO was detected by the GC. A CH_4 concentration of 94% means full conversion of CO_2 (N_2 dilution).

5.4. Conclusions

In this chapter, four different bifunctional catalyst-sorbent materials (5%Ni2.5%Ce13X, 5%Ni13X, 5%Ni5A and 5%NiL) were tested in atmospheric CO_2 methanation with a stoichiometric feed ratio of $4H_2 : 1CO_2$. All the materials showed high water capacity and very high selectivity towards methanation. Their high catalytic activity and sorption enhancement significantly increased the low temperature yields, which was observed during non-sorption enhancement experiments with the same materials. The best performing material appeared to be 5%Ni2.5%Ce13X, which was further subjected to long term testing with 100 adsorption-desorption cycles where also the catalyst stability was examined. The conversion was shown to be independent of the methane partial pressure under the reaction conditions. The material shows 100% CO_2 conversion and practically 100% selectivity for CH_4 formation at temperatures as low as 180 ^{o}C.

5.5. Supplementary Material

Figure 5.1 was simulated by the authors using the following equation:

$$X_{CO_2} = \frac{n_{CO_{2,in}} - n_{CO_{2,eq}}}{n_{CO_{2,in}}},$$

where $n_{CO_{2,in}}$ is the input/initial molar mass of CO_2 in the experiment, $n_{CO_{2,eq}}$ is the equilibrium molar mass of CO_2 calculated from the following equation:

$$K_{eq} = \frac{P_{CH_4} \cdot P_{H_2O}^2}{P_{CO_2} \cdot P_{H_2}^4} \cdot \left(\frac{P_{total}}{P_{ref}}\right)^{-2},$$

where, K_{eq} was retrieved from the database of Factsage software for the reaction of CO_2 methanation $4H_2+CO_2 \leftrightarrow CH_4+2H_2O$ at different pressures and temperatures. P_{CH_4}, P_{H_2O}, P_{CO_2} and P_{H_2} are the partial pressure of gases CH_4, H_2O, CO_2 and H_2, respectively. P_{total} is the total pressure of the reaction performed which we assumed to be 1, 5, 10 bar etc. P_{ref} is the reference pressure which was 1 bar. The CO_2 equilibrium conversion at different pressures and temperatures can be obtained as a provided reactant input if we got the equilibrium molar mass (concentration) of CO_2 from this simulation.

Table S. 5.1: H_2O adsorption capacities of 5%Ni2.5%Ce13X under different CH_4 partial pressure, calculated from sorption enhanced CO_2 methanation experiments, regenerate at 300 °C 1 hour under 90 ml/min N_2 and 10 ml/min H_2, at a total pressure of 1 bar.

CH_4 input concentration (%)	Sorption enhanced experiment temperature (°C)	H_2O breakthrough duration (min)	H_2O adsorption capacity (mmol/g_cat)
0	300	_	_
0	270	29.07	0.998
0	240	38.63	1.327
0	210	47.65	1.636
20	300	21.98	0.755
20	270	29.18	1.002
20	240	38.72	1.330
20	210	47.75	1.640
40	300	21.38	0.734
40	270	28.93	0.994
40	240	40.95	1.406
40	210	47.83	1.643
60	300	20.95	0.719
60	270	28.68	0.985
60	240	37.73	1.296
60	210	45.93	1.577
81.5	300	21.17	0.727
81.5	270	29.05	0.998
81.5	240	38.25	1.314
81.5	210	46.03	1.581

Table S. 5.2: H_2O adsorption capacities of 5%Ni2.5%Ce13X under different regeneration temperatures, calculated from sorption enhanced CO_2 methanation experiments, at a total pressure of 1 bar.

Regeneration temperature (°C)	Sorption enhanced experiment temperature (°C)	H_2O breakthrough duration (min)	H_2O adsorption capacity (mmol/g_cat)
450	320	28.47	0.978
450	300	33.05	1.135
450	280	40.35	1.386
450	260	47.83	1.643
400	320	24.65	0.846
400	300	30.88	1.061
400	280	38.25	1.314
400	260	_	_
350	320	23.03	0.791
350	300	29.20	1.003
350	280	36.43	1.251
350	260	45.17	1.551
300	320	21.55	0.740
300	300	26.98	0.927
300	280	33.52	1.151
300	260	40.92	1.405

Table S. 5.3: H_2O adsorption capacities of 5%Ni2.5%Ce13X under different GHSV, calculated from sorption enhanced CO_2 methanation experiments, regenerate at 300 °C 1 hour under 90 ml/min N_2 and 10 ml/min H_2, at a total pressure of 1 bar.

GHSV (ml/g_cat/h)	Total flow rate (ml/min)	Sorption enhanced experiment temperature (°C)	H_2O breakthrough duration (min)	H_2O adsorption capacity (mmol/g_cat)
923	100	300	27.88	0.958
923	100	270	35.77	1.228
923	100	240	44.97	1.544
923	100	210	52.75	1.931
1385	150	300	17.22	0.887
1385	150	270	23.25	1.198
1385	150	240	30.27	1.559
1385	150	210	36.80	1.896
1846	200	300	11.92	0.818
1846	200	270	16.30	1.120
1846	200	240	20.98	1.441
1846	200	210	26.53	1.822
2769	300	300	7.47	0.769
2769	300	270	9.98	1.029
2769	300	240	12.77	1.315
2769	300	210	17.62	1.815

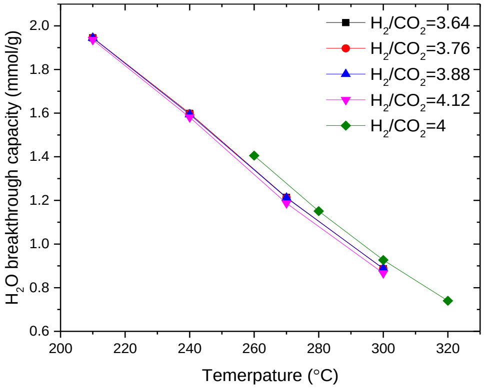

Figure S. 5.1: H_2O adsorption capacities of 5%Ni2.5%Ce13X under different ratios of H_2/CO_2 (ml/g_cat/h), calculated from sorption enhanced CO_2 methanation experiments. Inlet gas composition: 6% N_2, H_2/CO_2 from 3.64-4.12, 81.5% CH_4, 100 ml/min in total. 6.5 g catalyst was reduced at 500 °C under 100 ml/min H_2 for 2 hours.

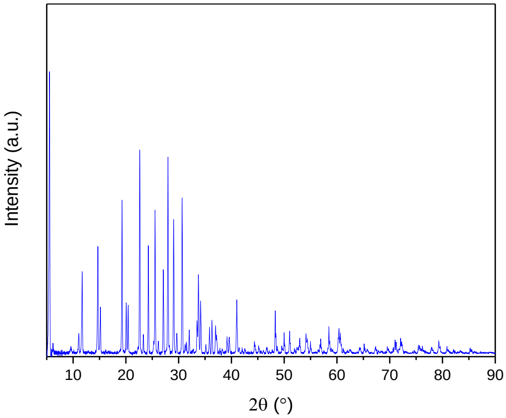

Figure S. 5.2: The XRD pattern for 5%NiL**.**

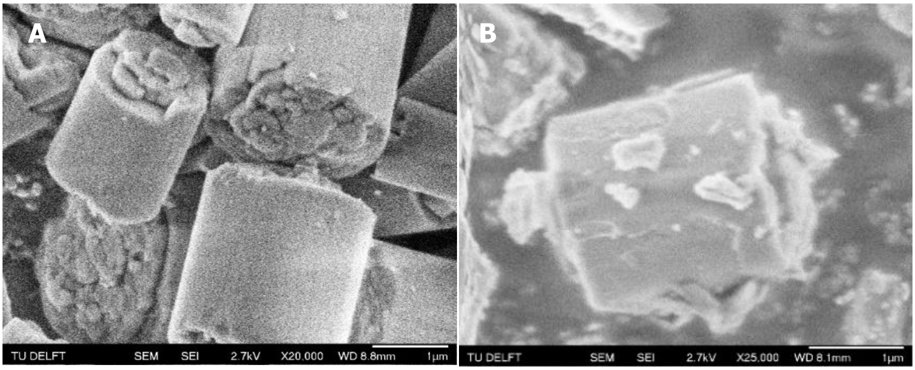

Figure S. 5.3: SEM images of fresh zeolite L (A) and 5%NiL (B).

Table S. 5.4: EDX results of fresh L zeolite and 5%NiL.

Sample	Content (wt./wt.%)				
	O	Al	Si	K	Ni
Fresh L	47.04	9.24	29.80	13.94	-
5%NiL	46.74	8.88	27.49	11.74	5.18

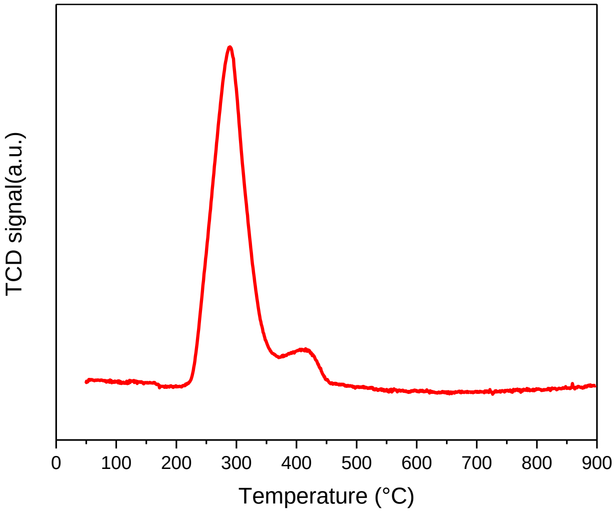

Figure S. 5.4: The H_2-TPR pattern for 5%NiL.

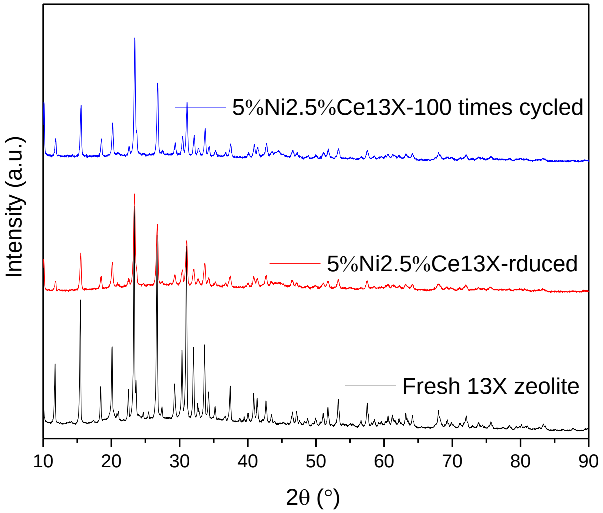

Figure S. 5.5: The XRD patterns for fresh 13X zeolite, reduced 5%Ni2.5%Ce13X and 100 times cycled 5%Ni2.5%Ce13X.

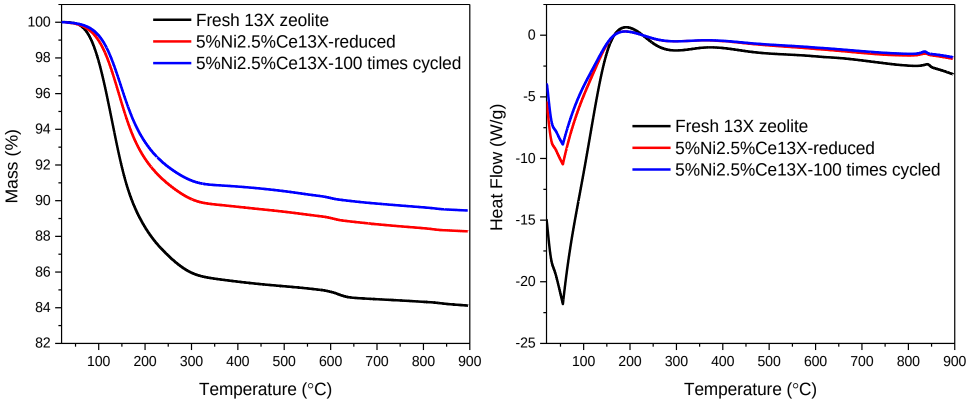

Figure S. 5.6: TG/DTA curves during thermal calcination under air for fresh 13X zeolite, reduced 5%Ni2.5%Ce13X and 100 times cycled 5%Ni2.5%Ce13X.

Table S. 5.5: The specific surface area and pore volumes of fresh zeolites and catalysts.

Sample	Specific surface area (m^2/g_{cat})			V_{total} (cm^3/g_{cat})
	Total	Micro	external	
Fresh 13X zeolite	685	641	44	0.24
5%Ni2.5%Ce13X-	611	565	46	0.21
5%Ni2.5%Ce13X-100	579	529	50	0.20

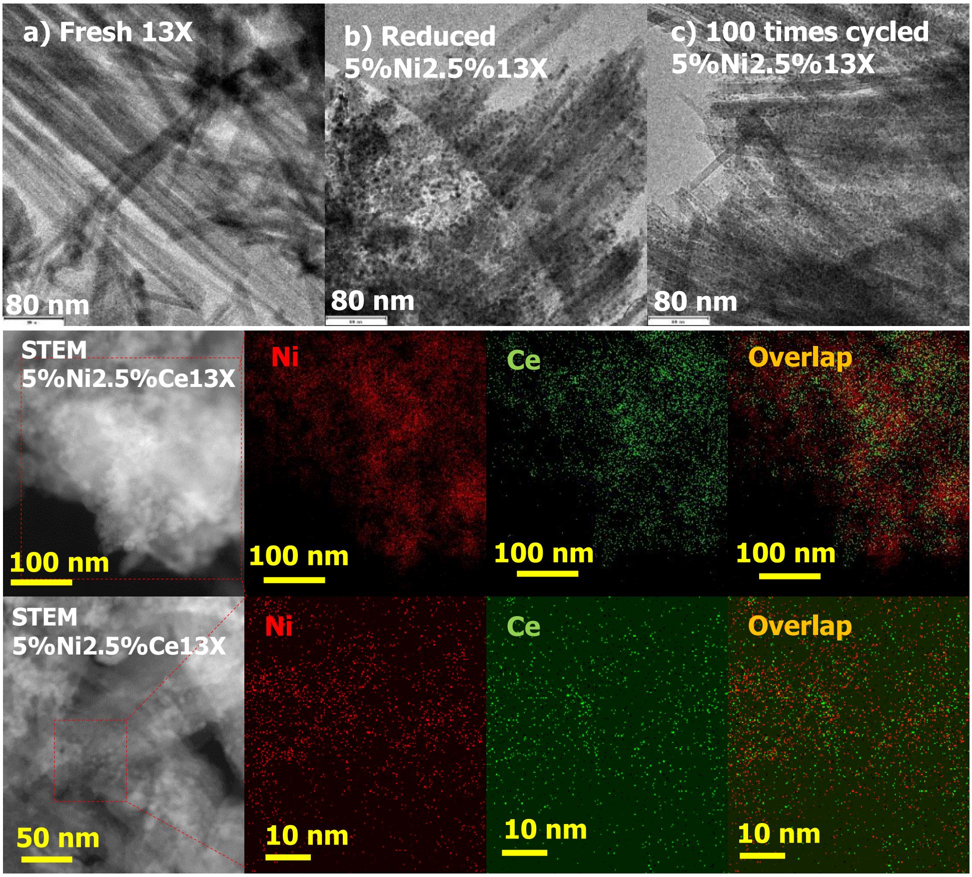

Figure S. 5.7: TEM pictures of a) fresh 13X zeolite, b) reduced 5%Ni2.5%Ce13X, c) 100 times cycled 5%Ni2.5%Ce13X; STEM image, Ni (red), Ce (green) and Ce Ni overlap (yellow) maps of calcined 5%Ni2.5%Ce13X.

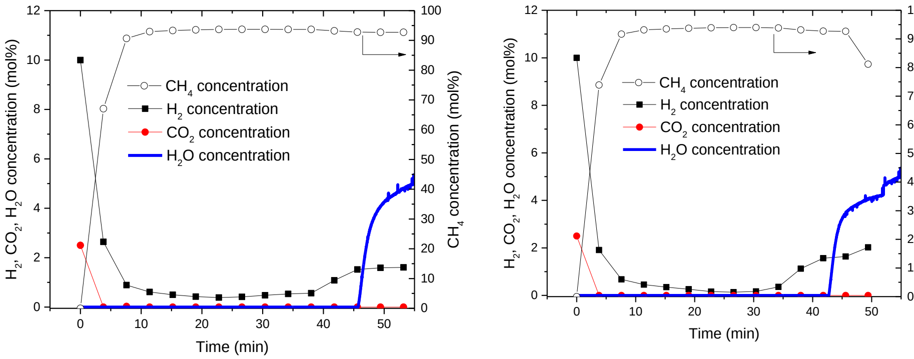

Figure S. 5.8: Water breakthrough capacity and duration of bifunctional catalyst 5%Ni2.5%Ce13X (left-Cycle 1, right-Cycle 50). Cycles 1-50: regeneration at 300 °C, experiment at 240 °C; Regeneration under 90 ml/min N_2 and 10 ml/min H_2 for 1 hour, each sorption enhanced experiment was run with input gases 10 ml/min H_2, 2.5 ml/min CO_2, 81.5 ml/min and 6 ml/min N_2.

6

Kinetics study of CO_2 methanation over nickel zeolite 13X catalyst

$$r = \underbrace{k_0 \cdot exp\left(-\frac{E_a}{R} \cdot \left(\frac{1}{T} - \frac{1}{T_{ref}}\right)\right)}_{\text{Temperature dependence}} \cdot \underbrace{p_{CO_2}^{n_{CO_2}} \cdot p_{H_2}^{n_{H_2}} \cdot p_{CH_4}^{n_{CH_4}} \cdot p_{H_2O}^{n_{H_2O}}}_{\text{Component dependence}}$$

$$\downarrow$$

$$r = (3.4 \times 10^2 \pm 4 \times 10^1) \cdot exp\left(-\frac{(65.2 \pm 2.2)}{R} \cdot \left(\frac{1}{T} - \frac{1}{T_{ref}}\right)\right) \cdot p_{CO_2}^{(0.1 \pm 0.003)} \cdot p_{H_2}^{(0.51 \pm 0.017)} \cdot p_{CH_4}^{(0.016 \pm 0.0008)} \cdot p_{H_2O}^{(0.06 \pm 0.03)}$$

Keywords of this chapter:
nickel 13X zeolite catalyst,
CO_2 methanation,
kinetics,
γ-Al_2O_3,
renewable energy,
energy storage.

This chapter is based on the following publication:
Daniël van den Berg, Liangyuan Wei, Wiebren de Jong, Wim Haije. Kinetics study of CO_2 methanation over nickel zeolite 13X catalyst (In preparation).

6.1. Introduction

Methane production through the Sabatier reaction (6-1) is an important conversion route for CO_2 utilization in energy storage and green chemicals production. Renewable H_2 can be produced by water electrolysis using sustainable electricity or from biomass gasification [130, 131]. CO_2 has a wide range of sources ranging from CO_2 capture in industry, fossil fuel combustion and, most importantly, capture from the air [245].

$$CO_2 + 4H_2 \leftrightarrow CH_4 + 2H_2O;\ \Delta H^0_{298} = -165\ \text{kJ/mol} \tag{6-1}$$

Full conversion of CO_2 is preferred but cannot be reached under industrial conditions, as thermodynamics of CO_2 conversion are favoured at a lower temperature, where again the reaction kinetics is show. Alternatively, the driving force behind the reaction can be kept up if the reaction products are continuously removed, following Le Châtelier's principle [27, 33]. This strategy is applied in adsorption enhanced CO_2 methanation [246]. This technique is applied by adding a sorbent, often zeolites, to adsorb the water that is formed during the reaction so that the equilibrium can be shifted towards full conversion. Walspurger et al. reported on the possibility of producing high grade methane at operational pressures below 10 bar using a nickel based catalyst mixed with 4A type zeolite adsorbent [33]. Borgschulte et al. obtained reaction yields up to 100% using nickel on a 5A-type zeolite, with catalytic activity surpassing that of commercially available non-adsorbing catalysts [27]. A short diffusion distance between the adsorption and catalytic sites in the bi-functional material enhances the conversion rate even further [84]. Therefore, in this work, the nickel was placed directly on the zeolite in an attempt to minimize this distance.

However, besides the thermodynamic limits of the reaction, the zeolite could also influence the CO_2 methanation reaction rate and even the reaction mechanism through the adsorption of any of the reactants or products involved. In the current work, the kinetics of a Ni/13X zeolite catalyst is examined and modeled to evaluate the influence of the zeolite and reaction conditions on the kinetics of the CO_2 methanation reaction. Zeolite 13X was chosen as support, since it has been shown to have better performance than e.g. 5%Ni/5A zeolite catalyst in CO_2 methanation, due to the larger pore size [26, 123]. Full CO_2 conversion can be obtained using the bifunctional material 5%Ni/13X under sorption enhancement [238]. 5% nickel on γ-Alumina was used as a reference.

6.2. Experimental section

6.2.1. Catalyst preparation

Incipient Wetness Impregnation (IWI) was used for the preparation of 5%Ni/13X zeolite and 5%Ni/ γ-Al_2O_3 catalysts [247]. The zeolite 13X (Honeywell Fluka, The Netherlands), γ-Al_2O_3 (Alfa Aesar, Germany) were crushed to 0.5-1 mm. $Ni(NO_3)_2{\cdot}6H_2O$ (Merck KGaA, 99%) was used as the nickel precursor and dissolved in deionized water. Here 5% Ni means 5 weight percent Ni metal on the support. The volume of the nickel precursor solution was close to the volume of the pores of the 13X or γ-Al_2O_3 support. This solution was added dropwise to the zeolite under continuous stirring to ensure homogeneous deposition. After impregnation, the catalysts were dried at 80 °C for approximately 18 hours. The dried catalyst was subsequently calcined at 400 °C for 6 hours using a heating ramp of 2 °C/min.

6.2.2. Catalyst characterization

The catalysts characterization results employing XRD, SEM, EDX, TEM, N_2 adsorption and H_2-TPR can be found in the supplementary material.

6.2.3. Catalysts test

All experimental data was acquired using a 10 mm (inner diameter) quartz fixed-bed reactor system, please see section 1 of the supplementary material for more details. The experimental conditions covered are given in Table 6.1. N_2 was used as an inert balance gas. A narrow range of low CO_2 concentrations was chosen since high concentrations of CO_2 would speed up the reaction rate, thereby generating a lot of heat. This could lead to a local temperature rise on the catalyst in case of heat transfer limitations. Furthermore, instead of choosing a set of low and high points for the hydrogen and methane concentration, it was instead opted to set certain low, centre and high ratios of H_2: CO_2 and CH_4: CO_2, in order to keep these ratios constant between the different experiments. The temperature range for each catalyst was chosen between temperatures where the activity of the catalysts became measurable and where mass transfer limitations began to play a role. All experimental data points were also validated using the intrinsic validation criteria formulated by Kapteijn and Moulijn [248]. No external or internal mass or heat-transfer limitations were observed for the used experimental data. As the catalyst was already saturated with water before kinetic data was taken, adsorption enhancement can be neglected in these experiments.

Table 6.1 Experimental matrix.

Parameter	Value		
CO_2 (vol.%)	3,	4,	5
H_2: CO_2	4,	5,	6
CH_4: CO_2	0,	1,	2
N_2	Balance		
Total flow (ml/min)	250		
T_5%Ni13X (°C)	240, 250, 260, 270, 280, 300 ($T_{ref} = 266$)		
T_5%Ni/Al_2O_3 (°C)	325, 350, 375, 400 ($T_{ref} = 361$)		

The simplest model study of CO_2 methanation is a power law solely considering the reaction orders of H_2 and CO_2 [249, 250]:

$$r = k \cdot p_{CO_2}^{n_{CO_2}} \cdot p_{H_2}^{n_{H_2}} \cdot (1 - \beta_{METH}) \qquad (6\text{-}2)$$

$$\beta_{METH} = \frac{p_{CH_4} \cdot p_{H_2O}^2}{K_{eq} \cdot p_{CO_2} \cdot p_{H_2}^4} \qquad (6\text{-}3)$$

To minimize the correlation between pre-exponential factor and activation energy, the pre-exponential factor k in equation (6-2) was expressed as:

$$k = k_0 \cdot \exp\left(-\frac{E_a}{R} \cdot \left(\frac{1}{T} - \frac{1}{T_{ref}}\right)\right) \qquad (6\text{-}4)$$

The data was fitted to the following power-law rate equation, which also includes CH_4 and H_2O concentrations:

$$r = \underbrace{k_0 \cdot \exp\left(-\frac{E_a}{R} \cdot \left(\frac{1}{T} - \frac{1}{T_{ref}}\right)\right)}_{\text{A = Temperature dependence}} \cdot \underbrace{p_{CO_2}^{n_{CO_2}} \cdot p_{H_2}^{n_{H_2}} \cdot p_{CH_4}^{n_{CH_4}} \cdot p_{H_2O}^{n_{H_2O}}}_{\text{B = Component dependence}} \cdot \underbrace{(1 - \beta_{METH})}_{\text{C = Equilibrium dependence}}$$

(6-5)

In the rate equation, k_0 denotes the pre-exponential factor; E_a, the activation energy, n_{CO_2}, n_{H_2}, n_{CH_4} and n_{H_2O}, are the apparent reaction orders and K_{eq} is the equilibrium constant of CO_2 methanation.

This power law equation constitutes of three separate parts. First, the Arrhenius equation (A) is to take into account the temperature dependency of the reaction rate. The reference temperature is calculated as the inverse of the average of the inverse temperatures used. This is done following Boon et al. [251]. The middle part (B) contains the power-law concentration dependencies of the reaction components. The final part (C) of the equation, the equilibrium factor, is added to take the reverse reaction rate into account. The partial pressures of the different gases were calculated using the following equation (6-6), where X is the conversion of CO_2 to methane, which was calculated using the experimental methane yield [238]. $F_{CO_2,0}$ is the initial CO_2 molar flow, $F_{i,0}$ is the initial molar flow rate of the component, $F_{tot,0}$ is the initial molar flow rate of all components, $P_{tot,0}$ is 1 bar, v_i is the stoichiometric number.

$$p_i = \frac{F_{CO_2,0} \cdot \left(\frac{F_{i,0}}{F_{CO_2,0}} + v_i \cdot X\right)}{F_{tot,0} - 2 \cdot X \cdot F_{CO_2,0}} \cdot P_{tot} \tag{6-6}$$

Since the rate cannot be directly measured, the rate equation was entered into the following conversion model (6-7), which was subsequently integrated and fitted to the experimental data. Where, W_{cat} is the catalyst weight has unit g, y_i is the gaseous mole fraction of each reaction compound, ζ is the dimensionless length over the reactor.

$$\frac{d(X)}{d\zeta} = \frac{W_{cat} \cdot r\left(T, P(P_{tot}, y_i)\right)}{F_{CO_2,0}} \tag{6-7}$$

The experimental methane yield was used instead of the overall conversion of CO_2 or H_2 to avoid a mix-up with any side reactions (Reverse Water Gas Shift e.g.).

6.3. Results and discussion

6.3.1. Data fitting

6.3.1.1. Influence of equilibrium factor

The two catalysts 5%Ni/13X and 5%Ni/Al_2O_3 were tested in the lab scale fixed-bed reactor system under the conditions listed in Table 6.1. Both catalysts showed high selectivity for CH_4 (~80 %), the other side product being CO, which is consistent with our previous report [123]. The experimental data was fitted to the kinetic model, in which equation (6-7) and (6-8) were implemented in Matlab.

During the first iterations of the model, the equilibrium factor overestimated the reverse reaction rate leading to inconsistent results. Different forms of the equilibrium factor were tried, but eventually the influence of the reverse reaction under these conditions was concluded to be negligible, see section 2 of the supplementary material. Therefore, the equilibrium factor is henceforth omitted from the rate equation and Equation (6-5) will be rewritten as equation (6-8) given below.

$$r = \underbrace{k_0 \cdot exp\left(-\frac{E_a}{R} \cdot \left(\frac{1}{T} - \frac{1}{T_{ref}}\right)\right)} \cdot \underbrace{p_{CO_2}^{n_{CO_2}} \cdot p_{H_2}^{n_{H_2}} \cdot p_{CH_4}^{n_{CH_4}} \cdot p_{H_2O}^{n_{H_2O}}} \qquad (6\text{-}8)$$

A= Temperature dependence B= Component dependence

6.3.1.2. Stability of the solution

It was further noticed that the calculated values strongly depended on the initial value of the activation energy used in the fitting of the model. Hence, the activation energy was first estimated separately from Arrhenius plots of each set of experimental conditions in order to obtain good initial values for the estimation. As the activation energy is assumed to be independent of the initial gas composition, the values of this parameter from the different experiments are assumed to be normally distributed around the true activation energy. Thus, the value of the activation energy and its 95% confidence interval were calculated by taking the average of these values and using the t-distribution respectively, the results can be seen from Table S. 6.3, supplementary material. Next, the obtained average activation energy was fixed prior to the optimization. Now, all initial estimates converged to the same minimum showing that this is the global minimum for that specific activation energy. Next, the data was fitted to the five remaining parameters n_{CO_2}, n_{H_2}, n_{CH_4}, n_{H_2O} and k_0. The results can be found in (Table 6.2). From these estimations, parity plots were obtained, which are given in the Figure 6.1 and showing the quality of fit.

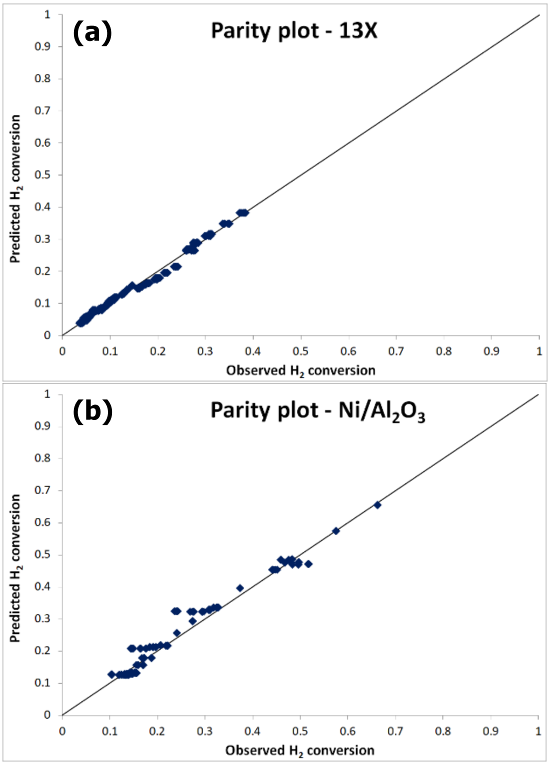

Figure 6.1: Parity plots of the fits of all investigated catalysts (a) 5%Ni/13X (b) 5%Ni/Al_2O_3.

Table 6.2: Parameter estimations using the conversion rate of CH_4.

	5%Ni/13X		5%Ni/ γ-Al_2O_3	
	Estimate	Estimated error (95%)	Estimate	Estimated error (95%)
n_{CO_2} (-)	0.10	0.003	0.08	0.004
n_{H_2} (-)	0.51	0.017	0.59	0.030
n_{CH_4} (-)	0.016	0.0008	0.022	0.002
n_{H_2O} (-)	0.06	0.03	0.17	0.050
E_a (kJ mol^{-1})	65.2	2.2	49.5	3.2
k_0 (mol $min^{-1}g^{-1}$)	3.4×10^2	4×10^1	9.39	1
SSE (-)		0.062		0.304
χ^2 (-)		5488		27645

6.3.2. Comparison of the kinetics of the catalysts

Two rate equations have been deduced from kinetics measurements of the two catalysts: 5%Ni on zeolite13X (6-9) and on γ-Alumina (6-10).

$$r = (3.4 \times 10^2 \pm 4 \times 10^1) \cdot exp\left(-\frac{(65.2 \pm 2.2)}{R} \cdot \left(\frac{1}{T} - \frac{1}{T_{ref}}\right)\right) \cdot p_{CO_2}^{(0.1 \pm 0.003)} \cdot p_{H_2}^{(0.51 \pm 0.017)} \cdot p_{CH_4}^{(0.016 \pm 0.0008)} \cdot p_{H_2O}^{(0.06 \pm 0.03)} \left[\frac{mol}{g \cdot min}\right] \tag{6-9}$$

$$r = (9.39 \pm 1) \cdot exp\left(-\frac{(49.5 \pm 3.2)}{R} \cdot \left(\frac{1}{T} - \frac{1}{T_{ref}}\right)\right) \cdot p_{CO_2}^{(0.08 \pm 0.004)} \cdot p_{H_2}^{(0.59 \pm 0.03)} \cdot p_{CH_4}^{(0.022 \pm 0.002)} \cdot p_{H_2O}^{(0.17 \pm 0.05)} \left[\frac{mol}{g \cdot min}\right] \tag{6-10}$$

What was observed is quite as expected: there is not much difference because the sorption properties were not included since the supports were in fact saturated with water. Then for the hydrogen exponent the usual exponent of 0.5 is found, typical for the H_2 dissociation reaction, CO_2 has in both cases an exponent of about 0.1, methane zero in both cases and only water has two distinct exponents. This is probably due to the fact that the mesoporous γ-Alumina has still unfilled pores and a non zero exponent is found whereas for 13X the degree of saturation is constant and complete leading to a zero exponent.

Then there is k_0 the pre-exponential factor being indicative of the amount of active catalytic sites which is indeed, as proven with TEM significantly higher than for γ-Alumina Figure 6.2. Last but not least, the activation energy is also clearly larger for the 13X support.

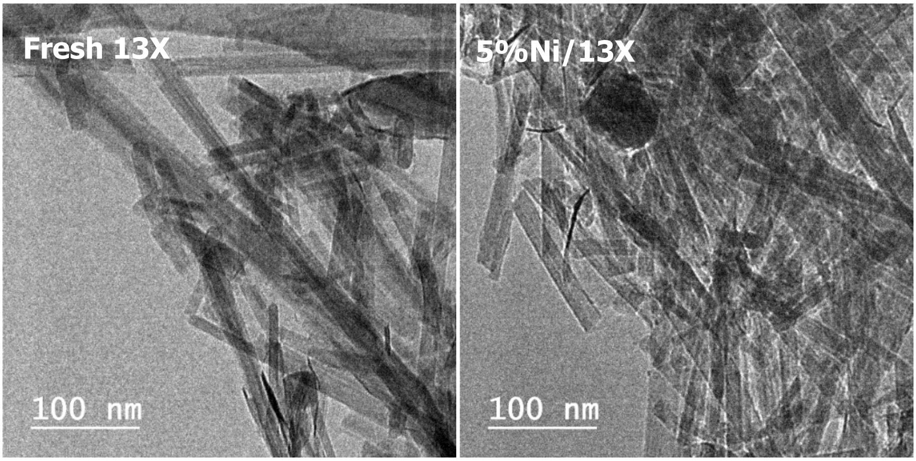

Figure 6.2: TEM pictures of Fresh 13X zeolite, 5%Ni/13X catalyst.

It was observed from rate equation (6-9) and (6-10) that the effect of methane is negligible for the two catalysts, showing that there is no product inhibition on the catalysts, which is to be expected as CH_4 is a neutral, nonpolar molecule and hence will not adsorb strongly to the nickel. It is consistent with our previous report that CH_4 did not significantly influence the sorption enhanced CO_2 methanation using nickel zeolite 13X bifunctional material [238]. Also the pore sizes of the two supports do not hamper this product to get out since they are larger than 5 Å [37].

The difference in CO_2 exponent is small yet significant, which may be explained by the difference of basic sites between zeolite 13X and gamma γ-Alumina. The CO_2 capacity could be decreased during the reaction with a saturated zeolite 13X due to the competitive adsorption of H_2O and CO_2 on 13X [146].

From all fits of experimental results, the 5%Ni/13X was found to be more active than the 5%Ni/Al_2O_3, which is due to a better dispersion of nickel on zeolite 13X, which is reflected in a much larger pre-exponential factor: sticking probability. The TEM results (Figure 6.2) showed that nickel particles are highly dispersed on 13X zeolite with a nickel particle size of less than 5 nm, while the γ-Alumina catalyst 5%Ni/Al_2O_3 was reported to have a nickel particle size was around 13.3 nm when prepared using wetness impregnation [252]. Our former reports also showed that a better dispersion of nickel particles on zeolite 13X was beneficial for a higher activity in CO_2 methanation [123, 174, 202]. The improved dispersion is also related to the higher surface area (Table 6.3) of zeolite 13X (685 m^2/g_{cat}) compared to that of γ-Al_2O_3 which has a surface area lower than 300 m^2/g_{cat} [253].

Table 6.3: N_2 adsorption results of catalysts.

Sample	Specific surface area (m^2/g_{cat})			Pore volume (cm^3/g_{cat})		
	Total	Micropore	External	Total	Micropore	1.7-300nm
Fresh 13X	685	641	44	0.40	0.24	0.16
5%Ni/13X	290	252	38	0.22	0.10	0.12

There are at least three possible reaction pathways for CO_2 methanation according to literatures, I) formate pathway; II) carbide pathway; III) carboxyl pathway (Figure 6.3) [116, 117]. These pathways are linked [117]: the step of H_2O dissociation can result from each of the three pathways. It is unclear whether the adsorption of H_2O promoted the methanation reaction using 5%Ni/13X, even though we found the effects of partial vapour pressure were significantly different for 5%Ni/13X and 5%Ni/γ-Al_2O_3. (Table

6.2).

The higher activity of 5%Ni/13X might possibly benefit from the larger number of basic sites 13X zeolite has. The adsorption of CO_2 on the catalyst is a prerequisite for all pathways, while CO_2 adsorption is influenced by the catalyst basic sites due to interaction with cations (Na^+) [40, 254]. It was reported that Ni alumina catalyst had more basic sites when Ca was introduced [255]. Our previous report found that zeolite 13X contained around 14 wt.% metals (Na, Mg, Ca) which contribute to the basicity [123].

The estimated activation energy of 5%Ni/13X was higher than 5%Ni/Al_2O_3 (Table S. 6.3, supplementary material), while the 5%Ni/13X had a higher activity.

The experimental results showed that around 20% of CO was formed during the reaction using either of the two catalysts. This could mean that the pathway which contains the step of CO production is active in CO_2 methanation: the carbide pathway with the *CO dissociation, since the reverse water gas shift is highly limited by the thermodynamics at temperature lower than 400 °C [256]. Meanwhile, it was shown that the carbide pathway has the lowest energy among the three pathways by comparing their potential energy diagrams [117], the rate-determining step of CO_2 methanation being *H assisted *CO dissociation [257, 258]. This could be an explanation that CO_2 methanation mainly followed the carbide pathway when using 5%Ni/γ-Al_2O_3 with a lower activation energy, and the catalyst activity was limited by the step of *CO dissociation. Therefore, formate and carboxyl were the main pathways of CO_2 methanation when using 5%Ni/13X.

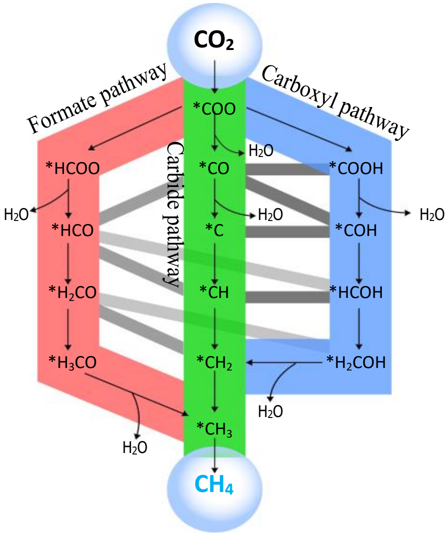

Figure 6.3: Possible reaction pathways for the methanation of CO_2, adapted from literature [117]..

6.4. Conclusions

The main goal of the current chapter was to obtain a kinetic rate expression for a nickel impregnated zeolite catalyst for the CO_2 methanation. A rate model was developed to model the kinetics of this 5%Ni/13X catalyst. The kinetic behaviour of the two catalysts was determined: adsorbing catalyst (5%Ni/13X) and non-adsorbing catalyst (5%Ni/γ-Al_2O_3). As the adsorbing catalyst was already saturated with water before kinetic data was taken, adsorption enhancement was ruled out.

The 5%Ni/13X was found to be more active than the 5%Ni/γ-Al_2O_3, accounted to a better distribution of nickel The rate equations for both catalysts are very similar. The effect of methane was negligible for the two catalysts, showing that there was no product inhibition on the catalysts. The reverse reaction rate (methane steam reforming) was negligible for all covered conditions and its contribution was taken out of the original conversion model. Finally, the general CO_2 methanation rate equation using 5%Ni/13X can be written as follows:

$$r = (3.4 \times 10^2 \pm 4 \times 10^1) \cdot exp\left(-\frac{(65.2 \pm 2.2)}{R} \cdot \left(\frac{1}{T} - \frac{1}{T_{ref}}\right)\right) \cdot p_{CO_2}^{(0.1\pm0.003)} \cdot p_{H_2}^{(0.51\pm0.017)} \cdot p_{CH_4}^{(0.016\pm0.0008)} \cdot p_{H_2O}^{(0.06\pm0.03)}$$

6.5. Supplementary Material

The experimental setup

The bulk of the experimental data was acquired in a quartz fixed-bed reactor system (Figure S. 6.1). The setup has five gas inlets, for N_2, CO_2, H_2, CH_4 and CO, which are supplied by Linde. The gas flow of each inlet is controlled by a flow-controller (Bronkhorst). which is designed up to 150 ml/ min for the CO_2 flow and 250 ml/ min for the other gas streams. The flow rate unit refers to the flow rate under normal conditions (20 °C, 1bar). The quartz tube reactor is heated by a furnace (Eva 12/300B, Carbolite Gero). The pressure drop over the reactor was monitored using two Cerabar T PMC131 pressure indicators (P1 and P2). These pressure sensors have a range from vacuum up to 40 bar and accuracy of 0.05 bar. Inside the tube reactor the catalyst is held in place by a quartz grid. The temperature of the furnace is controlled using a temperature controller (TC) (RKC RB100) with a range of 0 °C - 600 °C and accuracy of 1.0 °C. The temperature of the bed was measured using a separate thermocouple (T1, type K) with a range of –270 °C to 1260 °C and accuracy of 2.2 °C.

The reactor effluent first flows through a relative humidity detector (accuracy of 2% and 1.1 °C for the relative humidity and temperature sensor, respectively) and then into a condenser where gaseous water is condensed. The condenser serves to get the main part of the water out of the reactor effluent. The gas is then run through a vessel containing silica gel (SiO_2) to get rid of the last amount of water in the gas mixture to protect the micro GC. Finally, part of gas flow is diverted to the gas chromatograph (Agilent 490 micro GC, column type COX^H) and the rest is vented. In the gas chromatograph, argon gas is used as a carrier gas and the different gas fractions are separated from one another.

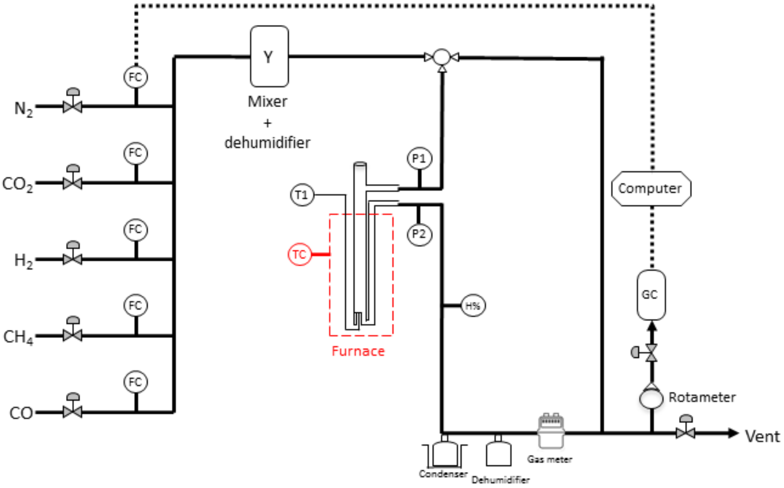

Figure S. 6.1: Piping and instrumentation diagram of the CO_2 methanation setup. FC = Flow Controller, T = Thermocouple, P = Pressure sensor, H% = Humidity Detector, GC = Gas Chromatograph

The quartz tube reactor had an inner diameter of 10 mm. The maximal allowable pressure drop over the catalyst bed was set at 0.01 bar. A Gas Hourly Space Velocity (GHSV) of 100 min^{-1} was maintained consistent with previous work [259]. From the set volumetric flowrate and GHSV, the intrinsic gas velocity could be determined using $u = \frac{\phi}{\varepsilon \cdot A_\perp}$,where $A_\perp$ is the area of the cross section of the reactor pipe. The catalyst bed volume was calculated using the definition of the gas hourly space velocity ($GHSV = \frac{\phi}{V}$).

To determine the bed height and particle diameter several constraints were set. First of all, it was of utmost importance that the reactor bed showed plug-flow behaviour to ensure that all reactants had the same retention time in the reactor. This can be described using the Péclet number $Pe = \frac{L_b \cdot u}{D_{ax}}$. Ideal plug-flow behaviour would be obtained when $Pe \to \infty$. However, the flow behaviour would already be adequate when Péclet approaches a certain value. According to Gierman [260], this value depends on the conversion and reaction order of the reaction that is occurring:

$$Pe > 8 \cdot n \cdot ln\left(\frac{1}{1-X}\right) \qquad \text{(S6-1)}$$

Here, the Péclet number can be rewritten as the Bodenstein number $Bo = \frac{d_p \cdot u}{D_{ax}}$:

$$\frac{L_b}{d_p} > \frac{8 \cdot n}{Bo} \cdot ln\left(\frac{1}{1-X}\right) \tag{S6-2}$$

This gives us a value for the ratio between the bed height and the particle diameter. The value for Bo was calculated using the intrinsic velocity and estimating the axial diffusion coefficient by taking the diffusion coefficient of CO_2 through N_2, since this is the limiting reactant at room temperature and then extrapolating the value to obtain the diffusion coefficient at 350 °C, as the diffusion coefficient scales with ~ $T^{1.5}$ according to the Chapman–Enskog theory [261]. For the conversion (X) 99 % was taken, since this leads to the most stringent constraints. For the reaction order, n, the value 1 was taken as a first assumption.

However, not only the axial direction can give discrepancies from ideal plug-flow behavior, also the radial distance can have an influence. Over the diameter of the reactor, the packing density varies due to the disruption of the flat wall surface. When the packing density is lower, this means that there is more voidage for the flow to go through and therefore higher local velocities. Chu et al. give the following condition to avoid this [262]:

$$\frac{d_b}{d_p} > 10 \tag{S6-3}$$

Finally, due to the strong influence of pressure on the reaction kinetics, it is important that the pressure drop over the bed is kept as low as possible. The pressure drop over a packed bed can be calculated using the Ergun equation [263]:

$$\Delta P = \frac{150 \cdot \mu_f \cdot \nu \cdot L_b(1-\varepsilon)^2}{d_p^2 \cdot \varepsilon^3} + \frac{1.75 \cdot \rho_f \cdot \nu^2 \cdot L_b \cdot (1-\varepsilon)}{d_p \cdot \varepsilon^3} \tag{S6-4}$$

The gas properties (μ_f and ρ_f) of the gas mixture was estimated to be similar to the values of the parameters of pure N_2 at 350 °C. The void fraction was calculated using a correlation from Dixon [264] and using the formula $u = \frac{\phi}{A_\perp}$. These conditions were plotted for a range of values for the particle diameter (1 − 0.1mm) and bed height (100 − 50 mm). The results can be found from Figure S. 6.2 and Figure S. 6.3 (supplementary material). In Figure S. 6.2, one can see that if the particle diameter stays below 0.2 mm, the pressure drop does not go above the set 0.01 bar pressure drop for any given bed height. In Fig. S. 2, we can see that for any given particle diameter, Gierman's condition is met if the bed height does not drop below 70 mm. Therefore, in order to make sure both conditions were met taking into account some leeway for any made assumptions, the bed height was set at 100 mm and the particle diameter range was taken between 1 and 0.5 mm. The bed volume of the catalyst particles was however already set at 2.5 ml to meet the specified GHSV which results in a catalyst bed height of 3 mm. Therefore, inert borosilicate spheres (1 mm in diameter) were used to fill up the rest of the bed. This also aided in the heat transfer of the catalyst bed and leads to a more homogeneous temperature distribution. In Table S. 6.1, a summary of reactor characteristics is given.

Table S. 6.1: Reactor characteristics

Characteristic	Value	Unit
Bed length (L_b)	100	mm
Bed diameter (d_b)	10	mm
Catalyst particle diameter (d_p)	1 - 0.5	mm
Pressure drop (Δp)	0.01	bar
Gas Hourly Space Velocity ($GHSV$)	100	min ^{1}
Flow rate (ϕ)	250	mlmin ^{1}
Catalyst bed volume (V)	2.5	ml

Table S. 6.2: Overview of the performed kinetic experiments.

No.	N_2 (vol%)	CO_2 (vol%)	H_2 (vol%)	CH_4 (vol%)
1	75%	5%	20%	0%
2	70%	5%	20%	5%
3	65%	5%	20%	10%
4	40%	4%	16%	0%
5	76%	4%	16%	4%
6	72%	4%	16%	8%
7	85%	3%	12%	0%
8	82%	3%	15%	0%
9	79%	3%	18%	0%
10	82%	3%	12%	3%
11	79%	3%	12%	6%

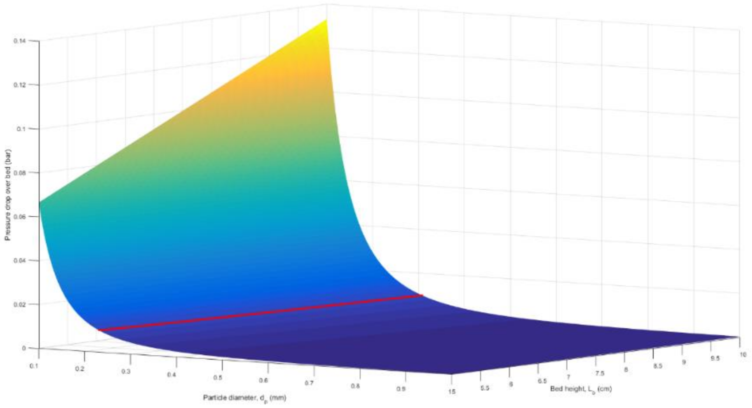

Figure S. 6.2: Pressure drop over the reactor according to the Ergun equation for different bed heights and catalyst diameters.

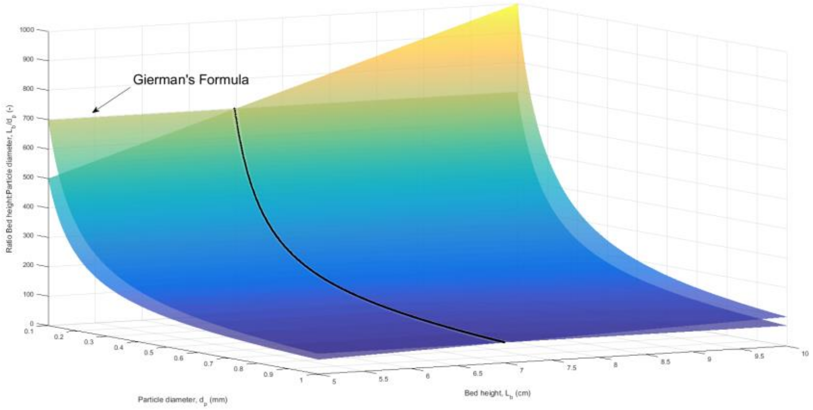

Figure S. 6.3: Comparison between the bed height and the catalyst diameter constraint according to Gierman (equation 3 for different bed heights and catalyst diameters.

Data fitting

There were six different parameters that needed to be fitted: $k_{T_{ref}}$, which will henceforth be referred to as the pre-exponential factor, E_a, the activation energy, and n_{CO_2}, n_{H_2}, n_{CH_4} and n_{H_2O}, which will be referred to as the exponent of the respective gas.

$$r = \underbrace{k_0 \cdot exp\left(-\frac{E_a}{R}\cdot\left(\frac{1}{T}-\frac{1}{T_{ref}}\right)\right)}_{\text{A= Temperature dependence}} \cdot \underbrace{p_{CO_2}^{n_{CO_2}} \cdot p_{H_2}^{n_{H_2}} \cdot p_{CH_4}^{n_{CH_4}} \cdot p_{H_2O}^{n_{H_2O}}}_{\text{B= Component dependence}} \cdot \underbrace{(1-\beta_{METH})}_{\text{C=Equilibrium dependence}} \tag{S6-5}$$

$$\beta_{METH} = \frac{p_{CH_4} \cdot p_{H_2O}^2}{K_{eq} \cdot p_{CO_2} \cdot p_{H_2}^4} \tag{S6-6}$$

$$p_i = \frac{F_{CO_2,0} \cdot \left(\frac{F_{i,0}}{F_{CO_2,0}} + v_i \cdot X\right)}{F_{tot,0} - 2 \cdot X \cdot F_{CO_2,0}} \cdot P_{tot} \tag{S6-7}$$

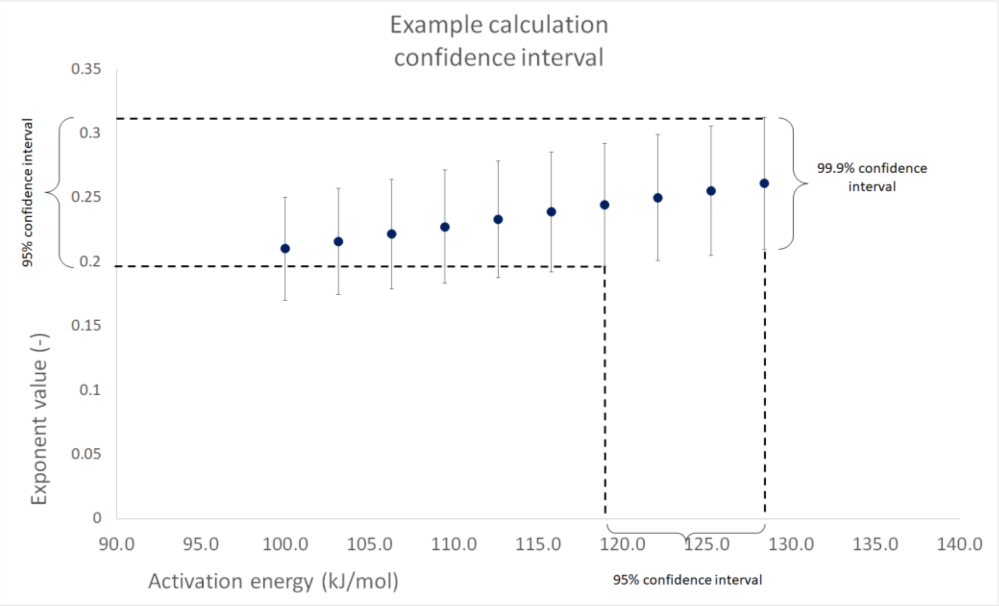

Figure S. 6.4: Indication how the confidence interval for the parameters over the activation energy interval was calculated.

Table S. 6.3**:** Overview of the activation energies that were obtained from all eleven different experiments.

Activation energy (kJ/mol)		CO_2 : H_2 : CH_4 (vol%: vol%: vol%)
5%Ni/13X	5%Ni/Al_2O_3	
82.4	62.0	5:20:0
80.7	59.1	5:20:5
77.1	55.8	5:20:10
84.0	57.2	4:16:0
81.8	55.2	4:16:4
79.5	53.5	4:16:8
82.1	52.5	3:12:0
85.3	56.1	3:15:0
87.1	58.5	3:18:0
81.3	50.0	3:12:3
79.4	48.4	3:12:6
81.9	55.3	Average

The final results for all parameter estimations are given in Table S. 6.4.

Table S. 6.4**:** Parameter estimations using the conversion rate of H_2

	5%Ni/13X		5%Ni/Al_2O_3	
	Estimate	Estimated error (95%)	Estimate	Estimated error (95%)
n_{CO_2} (-)	0.16	0.07	0.15	0.07
n_{H_2} (-)	0.48	0.08	0.61	0.10
n_{CH_4} (-)	0.01	0.01	-0.001	0.011
n_{H_2O} (-)	-0.003	0.04	0.16	0.06
$k_{T_{ref}}$ (mol min^{-1} g^{-1})	1.1×10^{-4}	3×10^{-5}	8.3×10^{-4}	2.5×10^{-4}
E_a (kJ mol^{-1})	81.9	1.8	55.3	2.6
k_0 (mol min^{-1}g^{-1})	9.4×10^{3}	2.4×10^{3}	2.9×10^{1}	9
SSE (-)		0.045		0.170
χ^2 (-)		15055		35876

Catalyst characterization

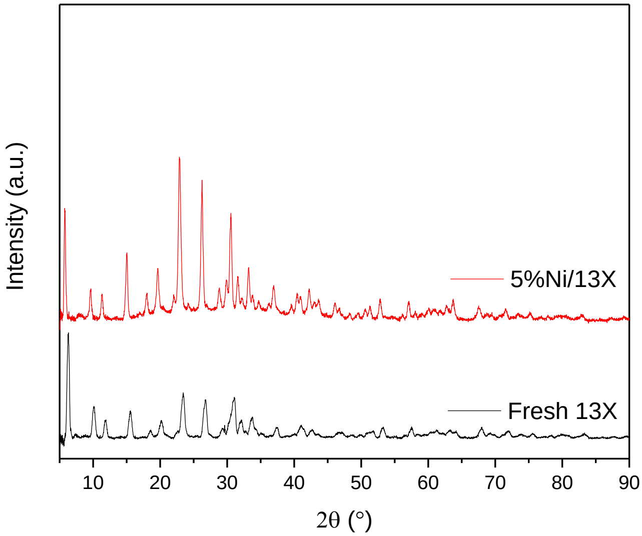

Figure S. 6.5: The XRD patterns for fresh 13X zeolite and prepared 5%Ni/13X catalyst.

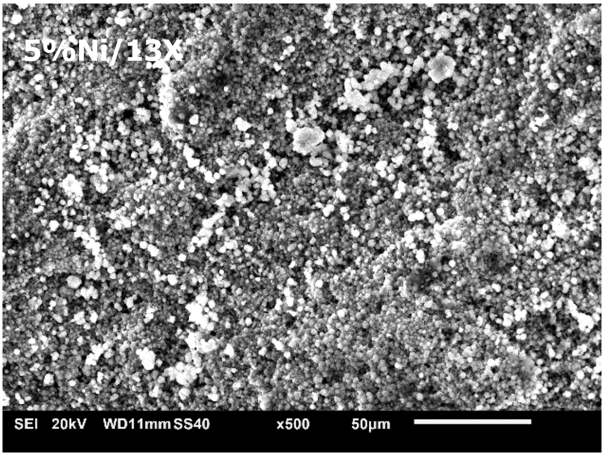

Figure S. 6.6: SEM picture of 5%Ni/13Xcatalyst.

Table S. 6.5: SEM-EDX results of catalyst 5%Ni/13X.

Sample	Content (wt./wt.%)										
	O	Na	Mg	Al	Si	K	Cl	Ca	Fe	Ni	Total
5%Ni/13X	49.9	9.8	1.6	12.1	20.7	_	_	0.5	0.6	4.9	100.0

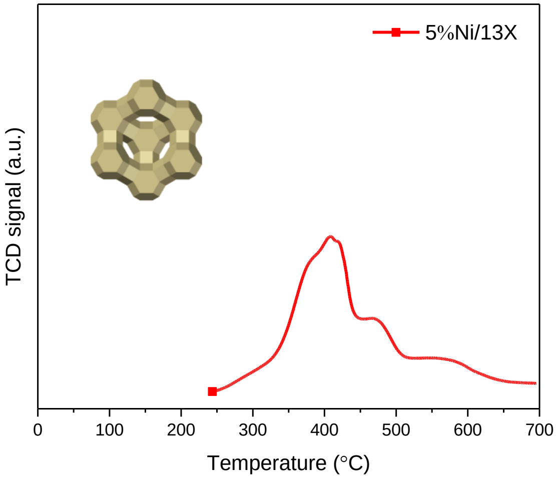

Figure S. 6.7: H_2-TPR profile of 5%Ni/13X.

7

Conclusions and recommendations

7.1. Conclusions

Different zeolites were selected/prepared as the bifunctional materials' support in this study concerning the Sabatier reaction. The bifunctional materials were prepared by impregnation with active metal (nickel, ruthenium) for sorption enhanced CO_2 methanation. Commercial zeolites 5A, 13X and an own synthesized zeolite L were used as the water sorbents, and three different Ni precursors were used for preparing the Ni modified zeolite catalysts. This study evaluated the effect of Ru loaded bi-functional material Ni 13X and 5A zeolite catalysts, it also discussed the influence of Ce on Ni 13X zeolite catalysts for CO_2 methanation, and investigated the performance of the Ce promoted Ni 13X zeolite material on sorption enhanced CO_2 methanation. Finally, in this thesis the kinetics of Ni 13X material was studied for non-sorption enhanced CO_2 methanation.

The physico-chemical characterization results show that the crystal structure of 13X and 5A zeolites stays intact with all precursors. Nickel citrate combined with a rather low calcination temperature leads to Ni modified 13X and 5A zeolite catalysts which can be easily reduced at lower temperature compared to the other Ni 13X and 5A zeolite catalysts made using acetate and nitrate. The 13X supported catalysts outperformed the ones synthesized with 5A mainly due to the better penetration of the metal precursors into the zeolite structure. The nickel citrate precursor resulted in better dispersion compared to nitrate and acetate, which resulted also in better performance. 5%Ni13X-cit zeolite catalyst prepared with nickel citrate showed high activity and CH_4 selectivity in the Sabatier reaction at remarkably low temperatures and the catalyst displayed good stability. The current work clearly shows how the selection of precursor can influence the properties of a nickel modified catalyst.

The surface area and, micro-pore volume decreased after Ni modification of 13X zeolite, however, no significant influence was observed with 5A. A significantly smaller cluster size was obtained for Ni while Ru formed comparatively large nanoparticles. The same observation was valid for both mono- and bi-metallic catalysts. The metal modification clearly influenced the acidity of the catalysts with Ni promoting strong acidity. The 13X supported catalyst outperformed in general the 5A supported ones, when considering conversion. Interestingly, the conversion and selectivity depended significantly on the zeolite type. With 13X, the highest conversions were obtained with the mono-metallic catalysts, while with 5A, the conversion decreased with increasing Ru loading. Regarding zeolite 13X, the highest selectivity was obtained with pure Ru catalyst, while with 5A, the result was opposite. Moreover, with 13X the selectivity increased with temperature, while with 5A, it was the opposite. Moreover, the selectivity was most probably influenced by the competitive adsorption of CO_2 and methane in 5A as well as the different reaction mechanisms of the methanation on the Ni and Ru metals. The catalysts exhibited good stability and CH_4 selectivity during a 200 hours test. It can be concluded that the conversion of CO_2 methanation by Ni based catalysts cannot be improved by adding Ru. However, the selectivity can be significantly influenced depending on the properties of 13X and 5A zeolites.

The influence of Ce loading on catalyst properties and the catalysts' performance were investigated in this study. The results showed that the loading of Ce affected the catalysts' metal dispersion, reducibility, basicity and acidity, and as a consequence their activity and selectivity. Activity increase is most pronounced at lower temperatures, below 280 ^{o}C, selectivity is satisfactory from this temperature upward. XRD and SEM results showed that the structure of 13X zeolite did not change after citrates' impregnation and calcination. TEM and STEM-EDX mappings showed that most Ce and Ni were highly dispersed as sub-nanometer clusters. Ce and Ni ions were chelated by citrate and as such diffused into the zeolite structure. It was shown that there was a strong correlation between acidity, basicity and conversion: neither should be too strong and a balance should prevail. The basicity should not be too high to result in too strong bonding of CO_2 and the acidity should not be too high to allow for interaction with CO_2. The catalysts' stability test results showed that the highly active catalyst 5%Ni2.5%Ce13X had a very stable performance on CO_2 methanation and high CH_4 selectivity for a 200-hour timescale.

A high CO_2 conversion around 100% can be obtained from the temperature range 180 to 320 °C under sorption enhanced CO_2 methanation conditions using bi-functional material 5%Ni2.5%Ce13X. The characterization results showed that the crystal structure of zeolite was not changed after 100 times cycle in fixed bed reactor. While a decrease was found from their pore volume and surface area, and the water breakthrough capacity decreased with the cycle time increasing from 1 to 100. It could be due to the carbon deposition or metal sintering in the zeolite 13X.

The 5%Ni/13X was found to be more active than the 5%Ni/γ-Al_2O_3 in non-sorption enhanced CO_2 methanation, accounted to a better distribution of nickel. The rate equations for both catalysts are very similar. The effect of methane was negligible for the two catalysts, showing that there was no product inhibition on the catalysts. The reverse reaction rate (methane steam reforming) was negligible for all covered conditions and its contribution was taken out of the original conversion model. Finally, the general CO_2 methanation rate equation using 5%Ni/13X can be written as follows:

$$r = (3.4 \times 10^{2} \pm 4 \times 10^{1}) \cdot exp\left(-\frac{(65.2 \pm 2.2)}{R} \cdot \left(\frac{1}{T} - \frac{1}{T_{ref}}\right)\right) \cdot p_{CO_2}^{(0.1 \pm 0.003)} \cdot p_{H_2}^{(0.51 \pm 0.017)} \cdot p_{CH_4}^{(0.016 \pm 0.0008)} \cdot p_{H_2O}^{(0.06 \pm 0.03)}$$

In summary, sorption enhanced CO_2 methanation has a great potential in the application of CO_2 utilization and H_2 transfer for energy storage. It is possible to obtain full CO_2 conversion and high purity of CH_4 in sorption enhanced CO_2 methanation. Ni citrate is beneficial to obtain better performance Ni 13X and 5A catalysts, Ni and Ce citrate complexes utilization is a very promising strategy to prepare highly dispersed (sub-nanometer) ceria-promoted Ni zeolite 13X catalysts, while adding Ru cannot improve the conversion of CO_2 methanation by Ni based catalysts. The zeolite 5A and 13X are good support for CO_2 methanation, while in most cases, 13X zeolite supported catalysts show a better performance on CO_2 methanation. The effect of methane was negligible for the 5%Ni/13X and 5%Ni/γ-Al_2O_3 catalysts, showing that there was no product inhibition on the catalysts.

7.2. Recommendations

Before the industrial application of the sorption enhanced CO_2 methanation bi-functional materials, many scientific and practical challenges have to be addressed. Based on the study of this topic, the author believes the following issues are necessary to be studied:

- To investigate water adsorption behavior of 13X, 5A zeolite and Ni/Ce modified bi-functional materials under different water partial pressures at temperatures in the range of 100-350 °C.
- To select a proper zeolite, or tune the zeolite property or synthesize a new zeolite for sorption enhanced CO_2 methanation.
- To develop a bi-functional catalyst which can work at a low temperature would be interesting for a future sorption enhanced CO_2 methanation application. This kind of bi-functional material would have a high dispersion of catalytic metal and low activation energy. The loading of the catalytic metal would also have limited effect on the sorption capacity of the sorbent.
- Some harsh conditions with poisoning gases such as CO and sulphur compounds are needed for further study in sorption enhanced CO_2 methanation, which is an important issue for avoiding the catalyst poisoning and water capacity decreasing for the bi-functional material.
- Further study on more cycles for different sorbents (bi-functional materials) on sorption enhanced CO_2 methanation is needed before these can be applied commercially. It is to investigate the deactivation of water-adsorbing and catalytic performance of the bi-functional materials.
- It would be worth to study sorption enhanced CO_2 methanation with a process system design which considers the heat utilization and mass cycle, as well as the considerations on systematic scale up for sorption enhanced CO_2 methanation by process (-heat) integration.
- The kinetics behavior and related mechanism of sorption enhanced CO_2 methanation needs further study.

Appendix

The code of CO_2 equilibrium conversion calculation:

	initial	final		mole fraction
H_2	3.916667	3.916667	-4x	0.094
CO_2	1	1	-x	0.024
CH_4	32.41667	32.41667	x	0.778
H_2O	1.958333	1.958333	2x	0.047
N_2	2.333333	2.333333		0.056
Total	41.625	41.625-2x		

```
clear all
T = 100:10:500;
P_total = [1]; % bar
K = [1.04E+14 2.51E+13 6.49E+12 1.79E+12 5.21E+11 1.61E+11 5.22E+10
1.78E+10 6.33E+09 2.35E+09 9.08E+08 3.64E+08 1.51E+08 6.47E+07 2.86E+07
1.30E+07 6.10E+06 2.93E+06 1.44E+06 7.28E+05 3.75E+05 1.98E+05 1.06E+05
5.82E+04 3.25E+04 1.85E+04 1.07E+04 6.25E+03 3.72E+03 2.25E+03 1.38E+03
8.58E+02 5.40E+02 3.44E+02 2.22E+02 1.45E+02 9.53E+01 6.35E+01 4.27E+01
2.90E+01 1.99E+01]; %K is from Factsage software
Conversion = zeros(numel(P_total), numel(T)); %name matrix of Conversion
 for j = 1:numel(P_total)
    for i = 1:numel(T)
    Fun = @(x) (32.41667+x)*(1.95833+2*x)^2*(41.625 - 2*x)^2  -  P_total(j)^2 *
K(i) * (1 - x) * (3.91667 - 4*x)^4;
     Conversion(j, i) = fzero(Fun,1);
    end
    plot(T,Conversion(j,:))
    hold on
    grid on
% y axis
    ylabel('CO_Conversion(%)');
% x axis
    xlabel('Temperature(0C)');
```

```
% legend
    legend('1 bar'),
        'Location', 'SouthWest')
 end
```

Conversion

Acknowledgements

I would like to thank many people who helped, encouraged or supported me during my PhD study in the Netherlands.

My first great thankfulness goes to my really nice and easy-going prof. Wiebren de Jong. You gave me the chance to study in TU Delft, you are my promoter and supervisor. Thank you very much for your nice and patient care, supporting and supervision during my PhD. I am lucky that I can join your group. I was influenced by your attitude for science and technology. To be honest, I was motivated much to do my study by your passion for work and your knowledge. I am very grateful to you for your kind and open mind for the training of young generation, like supporting me without hesitation to take the DFT calculation training when I tell you my idea. My study went well cannot without your practical suggestions, timely remaindering of deadlines. You provided me chances of attending conferences, trainings all over the world, although you are not a fan of conference, I was fortunately involved in the international network of energy and chemical engineering.

Thank you, my friendly and easy-going daily supervisor dr. Wim Haije, one of the most important persons for my PhD journey. It seems happened yesterday that you came to me to tell me do not call you professor. You are an approachable gentleman, thank you for your patient explaining when we have different ideas, especially in the cases I were wrong. Thank you to make my daily study relax, like our progress meeting always started with a joke, although I cannot get the point of most jokes. Your open mind helped me to put my study forward well, we rebuild our smaller setup which carried out all experiments of Daniel, Hamza and me. We have the "Taiwu" appointment for delicious Chinese foods, since our first publication and the bet of who find out the reference paper we were looking for.

I am very grateful to Henrik Grénman (my co-promoter) for your nice help in the testing of the old Sabatier setup and the construction of the new small-scale experimental setup. Thanks for inviting and supporting me to visit Johan Gadolin Process Chemistry Centre, Åbo Akademi University. It is a hard experience but we had much great outputs, I learned much during this period. You and dr. Narendra Kumar helped me to solved many problems in time. Thank you so much for your critical and timely ideas, comments, suggestions for improving our manuscripts after I returned to Delft, especially during my difficult time. I would like to give my many thanks to dr. Atte Aho, Kari Eränen and Ekaterina Kholkina, you trained me and helped me to use

the machines for catalysts characterization. Thank prof. Dmitry Murzin, prof. Tapio Salmi, Sodabeh Saeed, Nemanja Vucetic, dr. Zuzanna Siky Vajglova and dr. Ayat Nuri etc. at Johan Gadolin Process Chemistry Centre, I had a nice journey at Turku. Meanwhile, for my really friendly roommates Maxine Mattsson, Linda Kuhlberg, I cannot forget the pizza and other foods you shared me when I arrived at Turku at the first cold day at temperature around minus 10 degrees, thank you for letting me have a good memory about Turku.

Thanks to Leon Rohrbach at University of Groningen for the TPD and TPR characterization. Thank Dr. Wiel H. Evers at the Department of Chemical Engineering of TU Delft for the TEM analysis; Thanks very much to Willy Rook and prof. Freek Kapteijn for your kind help on the nitrogen adsorption training and test. Moreover, I am appreciate to have a chance to visit your lab for MOF preparation by the help from dr. Xiaohui Sun and Willy Rook. Thanks to dr. Mengyue Wu for the STEM-EDX analysis. Thanks to Ruud Hendrikx for the XRD analysis, and Wim Sloof and Kees Kwakernaak at the Department of Materials Science and Engineering of TU Delft for my training of SEM analysis.

Thank Martijn Karsten and Daniel van Baarle in constructing and modifying the Sabatier setup. To Michel van den Brink and Jaap van Raamt, thank you very much for your nice help and solving the problems during my daily work. Thanks to Jan Graafland for the problem solving of Labview. Thanks for the help and assistance in the daily work from Eveline van der Veer, Rob van den Boogaard, Leslie van Leeuwen, Hilma etc.

Many thanks to our group members in large scale energy storage. Thanks to Mara del Grosso and Andrea Mangel Raventos for the TGA and FTIR training and analysis, thanks to Shilong Fu for the XRD, nitrogen adsorption and other help for my study. Thank you all for your assistance, encouragement and help during my PhD: Christos Tsekos, dr. Ruud Kortlever, dr. Mahinder Ramdin, dr. Andrew Morrison, dr. Elyas Moghaddam, Boaz Izelaar, Daniël van den Berg, Min Wang, Chengkun Long, Jingjing Xu, Jiaoyi Wu, Lize Zhao, Hamza Azad, Hamid Gilvari, Luis Cutz, Marilia Moura de Salles Pupo, Ming Li, Mohammed Majied, Nandalal Girichandran, Simone Asperti etc.

Thanks for the great working atomsphere since our nice office member Pengjie Fang, Anna, Frechesca, Hansa, Johan Stimi, Fatma Ibis, dr. Iman Ataei Dadavi, dr. Hadi Rajaei, dr. Bin Chen, dr. Peng Yan, Rumen Georgiev, Aviral Rajora, Stephan Smit, Jay Pee Ona etc. I like the delicious international food party with our office members.

Thank you for your kind help, encouragement and assistance from my good

friends dr. Ran Shang, Hongxiao Guo, dr. Xuedong Zhang, dr. Yu Tao, dr. Yanxiang Deng, dr. Junhao Hu, Rujie Liu, Guangyuan Huang, dr. Biao Liu, dr. Jun Zou, dr. Wei Yang, dr. Xiong Zhang, dr. Zixiang Ma, Long Hu, Dingan Liu, Chunyao Huang, Neng Yang and other bachelor classmates, dr. Nan Jiang, dr. Peng Wei, dr. Jiecui Feng, dr. Jingyi Hu, dr. Feifei Wang, prof. Bin Li, prof. Haiping Yang, dr. Jingai Shao, dr. Xianhua Wang, dr. Yingquan Chen, Xiang Tang, Fan Li, dr. Hesheng Bao, dr. Zhu Cheng, dr. Meixia Shan, Zerui Zhang, Zhe Deng, Bin Lin, Junhua He, Li Shu, Haijun Zhang, Hualin Zeng, dr. Cong Xiao, Wensen Li.

I will never forget the happy time I had with Dr. Xu Huang, dr. Meng Wang, dr. Peng Yan, dr. Mengmeng Ren, dr. Bin Chen, dr. Jie Ren, dr. Zhenming Li, dr. Weiwei Li, dr. Zhiyuan Chen, dr. Xiangmei Meng, dr. Xuan Tao, Rong Fan, dr. Zhichao Zhang, Mengmeng Zhang, Fan Liu, Shilong Fu, dr. Wenze Guo, Haoyu Li, Heng Li, Qi An. Additionally, thanks to my football mates dr. Riming Wang, dr. Bowen Fan, dr. Yong Zhang, dr. Wei Fang, dr. Bensheng Su, Zheyi Zeng, dr. Meng Zhao, dr. Cong Xiao, Yanggu Zheng.

My most sincere thanks to my family. Thanks to my mother and father for your unconditional support and endless love since I was born. Thanks to my twin brother dr. Liangfu Wei for your accompany, care and concern. My older brother Liangwang, my sister Siyue, Qiuyue, Dongyue and Shengyue, brothers-in-law and sister-in-law, thanks for your love, care, help, support and encouragement, especially during the difficult time I was sick.

Many thanks to my best friend, Yanhong. Thank you for your listening, support, encouragement and help, which has made me confident in my study and life.

My sincere gratitude goes to all of you.

Liangyuan WEI
Delft, The Netherland

Curriculum Vitæ

Liangyuan WEI
魏良元

Born in Huaihua of Hunan, China, 22-02-1987

Email:weilyon@foxmail.com

Education

PhD. Delft University of Technology 2016-
Department: Process and Energy
Graduation Thesis: Sorption enhanced CO_2 methanation for large scale energy storage
Supervisor: Dr. Wim Haije; Promoters: Prof. Wiebren de Jong. Prof. Henrik Grénman (Åbo Akademi University)

M.E. Huazhong University of Science and Technology 2011-2014
Major: Thermal Engineering
Graduation Thesis: Study on calcium base catalytic gasification of biomass for hydrogen production
Supervisor: Prof. Haiping Yang, Prof. Hanping Chen

B.E. Changsha University of Science and Technology 2006-2010
Major: Thermal Process Automation
Graduation Thesis: Database design of power plant bidding decision support system
Supervisor: Prof. Zhisheng Chen

Experience

Visiting PhD student Mar.2018-Jul.2018
Åbo Akademi University
Supervisors: Prof. Henrik Grénman, Dr. Narendra Kumar

Assistant Engineer 2014- 2015
Hunan Electric Power Design Institute of China Energy Engineering Group
Thermal Process Automation Department

List of Publications

1. **L. Wei**, W. Haije, N. Kumar, J. Peltonen, M. Peurla, H. Grénman, and W. de Jong, Influence of nickel precursors on the properties and performance of Ni impregnated zeolite 5A and 13X catalysts in CO_2 methanation. CATALYSIS TODAY, 2021. 362: p. 35-46.
2. **L. Wei**, N. Kumar, W. Haije, J. Peltonen, M. Peurla, H. Grénman, and W. de Jong, Can bi-functional nickel modified 13X and 5A zeolite catalysts for CO_2 methanation be improved by introducing ruthenium? Molecular Catalysis, 2020. 494: p. 111115.
3. **Liangyuan Wei**, Henrik Grénman, Wim Haije, Narendra Kumar, Atte Aho, Kari Eränen, Liangfu Wei, Wiebren de Jong. Sub-nanometer ceria-promoted Ni 13X zeolite catalyst for CO_2 methanation. Applied Catalysis A: General, 2021: p. 118012.
4. **L. Wei**, H. Azad, W. Haije, H. Grénman, W. de Jong, Pure methane from CO_2 hydrogenation using a sorption enhanced process with catalyst/zeolite bifunctional materials, Applied Catalysis B: Environmental, 297 (2021) 120399.doi:10.1016/j.apcatb.2021.120399.
5. **Liangyuan Wei**, Narendra Kumar, Wim Haije, Janne Peltonen, Markus Peurla, Henrik Grénman, Wiebren de Jong. A comparison of synthesis methods for Ni 13X and 5A zeolite catalysts for CO_2 methanation (In preparation).
6. **Liangyuan Wei**, Wim Haije, Henrik Grénman, Wiebren de Jong, Sorption enhanced catalysis for CO_2 hydrogenation towards fuels and chemicals with focus on methanation (book chapter of Heterogeneous Catalysis: Materials and Applications), Elsevier, 2022 (Accepted).
7. Daniël van den Berg, **Liangyuan Wei**, Wiebren de Jong, Wim Haije. Kinetics study of CO_2 methanation over nickel zeolite 13X catalyst (In preparation).
8. **L. Wei**, H. Yang, B. Li, X. Wei, L. Chen, J. Shao, and H. Chen, Absorption-enhanced steam gasification of biomass for hydrogen production: Effect of calcium oxide addition on steam gasification of pyrolytic volatiles. INTERNATIONAL JOURNAL OF HYDROGEN ENERGY, 2014. 39(28): p. 15416-15423.
9. B. Li, **L. Wei**, H. Yang, X. Wang, H. Chen, The enhancing mechanism of calcium oxide on water gas shift reaction for hydrogen production, Energy, 68 (2014) 248-254.
10. Bin Li, Haiping Yang, Biao Liu, **Liangyuan Wei,** Jingai Shao, Hanping Chen. (2017). Influence of high amount of calcium oxide addition on the yields of pyrolysis products and non-condensable gas evolving during corn stalk pyrolysis. Energy & Fuels. 31. 10.1021/acs.energyfuels.7b02516.
11. Bin Li, Haiping Yang, **Liangyuan Wei**, Jingai Shao, Xianhua Wang, Hanping Chen. (2017). Absorption-enhanced steam gasification of biomass for hydrogen production: Effects of calcium-based absorbents and NiO-based catalysts on corn stalk pyrolysis-gasification. International Journal of Hydrogen Energy. 42. 10.1016/j.ijhydene.2016.12.031.
12. Bin Li, Haiping Yang, **Liangyuan Wei**, Jingai Shao, Xianhua Wang, Hanping Chen. (2017). Hydrogen production from agricultural biomass wastes gasification in a fluidized bed with calcium oxide enhancing. International Journal of Hydrogen Energy. 42. 10.1016/j.ijhydene.2017.01.138.

13. B. Li, X. Han, Y. Chen, L. Wei, H. Yang, H. Chen, Effects of different calcium-based absorbents on hydrogen production of corn stalk pyrolysis-gasification, Kezaisheng Nengyuan / Renewable Energy Resources, 35 (2017) 502-507.
14. **Liangyuan Wei**, Henrik Grénman, Wim Haije, Narendra Kumar, Liangfu Wei, Wiebren de Jong. Sub-nanometer ceria-promoted Ni 13X zeolite catalyst for CO_2 methanation, NCCC, 2020.03 (Poster).
15. **Liangyuan Wei**, Wim Haije, Narendra Kumar, Janne Peltonen, Markus Peurla, Henrik Grénman, Wiebren de Jong, Physico-chemical and catalytic properties of Ni- modified 13X and 5A zeolite catalysts for sorption enhanced CO_2 methanation: Influence of nickel precursors, 18th Oct. UCRA2019, Zaragoza, Spain (Oral).

References

[1]. Zengzi, *Great Learning*.

[2]. Modak, A., P. Bhanja, S. Dutta, B. Chowdhury, and A. Bhaumik, *Catalytic reduction of CO_2 into fuels and fine chemicals.* GREEN CHEMISTRY, 2020. **22**(13): p. 4002-4033.

[3]. UNFCCC, *Adoption of the Paris agreement.* 2015.

[4]. Rogelj, J., M. den Elzen, N. Hohne, T. Fransen, H. Fekete, H. Winkler, R. Schaeffer, F. Sha, K. Riahi, and M. Meinshausen, *Paris Agreement climate proposals need a boost to keep warming well below 2 degrees C.* NATURE, 2016. **534**(7609): p. 631-9.

[5]. Lee, W.J., C. Li, H. Prajitno, J. Yoo, J. Patel, Y. Yang, and S. Lim, *Recent trend in thermal catalytic low temperature CO_2 methanation: A critical review.* Catalysis Today, 2020.

[6]. Rönsch, S., J. Schneider, S. Matthischke, M. Schlüter, M. Götz, J. Lefebvre, P. Prabhakaran, and S. Bajohr, *Review on methanation – From fundamentals to current projects.* FUEL, 2016. **166**: p. 276-296.

[7]. Bailera, M., P. Lisbona, L.M. Romeo, and S. Espatolero, *Power to Gas projects review: Lab, pilot and demo plants for storing renewable energy and CO_2.* Renewable and Sustainable Energy Reviews, 2017. **69**: p. 292-312.

[8]. Rahman, F.A., M.M.A. Aziz, R. Saidur, W.A.W.A. Bakar, M. Hainin, R. Putrajaya, N.A.J.R. Hassan, and S.E. Reviews, *Pollution to solution: Capture and sequestration of carbon dioxide (CO_2) and its utilization as a renewable energy source for a sustainable future.* 2017. **71**: p. 112-126.

[9]. Thomas, J.M. and K.D.M. Harris, *Some of tomorrow's catalysts for processing renewable and non-renewable feedstocks, diminishing anthropogenic carbon dioxide and increasing the production of energy.* Energy & Environmental Science, 2016. **9**(3): p. 687-708.

[10]. Artz, J., T.E. Muller, K. Thenert, J. Kleinekorte, R. Meys, A. Sternberg, A. Bardow, and W. Leitner, *Sustainable Conversion of Carbon Dioxide: An Integrated Review of Catalysis and Life Cycle Assessment.* CHEMICAL REVIEWS, 2018. **118**(2): p. 434-504.

[11]. Alvarez, A., A. Bansode, A. Urakawa, A.V. Bavykina, T.A. Wezendonk, M. Makkee, J. Gascon, and F. Kapteijn, *Challenges in the Greener Production of Formates/Formic Acid, Methanol, and DME by Heterogeneously Catalyzed CO_2 Hydrogenation Processes.* CHEMICAL REVIEWS, 2017. **117**(14): p. 9804-9838.

[12]. Saeidi, S., N.A.S. Amin, and M.R. Rahimpour, *Hydrogenation of CO_2 to value-added products—A review and potential future developments.* Journal of CO_2 Utilization, 2014. **5**: p. 66-81.

[13]. Bazaluk, O., V. Havrysh, V. Nitsenko, T. Baležentis, D. Streimikiene, and E.A. Tarkhanova, *Assessment of Green Methanol Production Potential and Related Economic and Environmental Benefits: The Case of China.* 2020. **13**(12): p. 3113.

[14]. Din, I.U., M.S. Shaharun, M.A. Alotaibi, A.I. Alharthi, and A. Naeem, *Recent developments on heterogeneous catalytic CO_2 reduction to methanol.* Journal of CO_2 Utilization, 2019. **34**: p. 20-33.

[15]. Xie, S., W. Zhang, X. Lan, and H. Lin, *CO_2 Reduction to Methanol in the Liquid Phase: A Review.* ChemSusChem, 2020. **13**(23): p. 6141-6159.

[16]. Dang, S., H. Yang, P. Gao, H. Wang, X. Li, W. Wei, and Y. Sun, *A review of research*

progress on heterogeneous catalysts for methanol synthesis from carbon dioxide hydrogenation. CATALYSIS TODAY, 2019. **330**: p. 61-75.

[17]. Bulushev, D.A. and J.R.H. Ross, *Heterogeneous catalysts for hydrogenation of* CO_2 *and bicarbonates to formic acid and formates.* Catalysis Reviews, 2018. **60**(4): p. 566-593.

[18]. Roy, S., A. Cherevotan, and S.C. Peter, *Thermochemical* CO_2 *Hydrogenation to Single Carbon Products: Scientific and Technological Challenges.* ACS Energy Letters, 2018. **3**(8): p. 1938-1966.

[19]. Nakyai, T. and D.J.J.o.C.P. Saebea, *Exergoeconomic comparison of syngas production from biomass, coal, and natural gas for dimethyl ether synthesis in single-step and two-step processes.* 2019. **241**: p. 118334.

[20]. p.l.c., b., *bp Statistical Review of World Energy June 2020.* 2020.

[21]. Sabatier, P. and J.J.P.I.G.-V. Senderens, *Comptes Rendus Des Séances De L'Académie Des Sciences, Section VI–Chimie.* 1902.

[22]. Li, B., H. Yang, B. Liu, L. Wei, J. Shao, and H. Chen, *Influence of Addition of a High Amount of Calcium Oxide on the Yields of Pyrolysis Products and Noncondensable Gas Evolving during Corn Stalk Pyrolysis.* ENERGY & FUELS, 2017. **31**(12): p. 13705-13712.

[23]. Uebbing, J., L.K. Rihko-Struckmann, and K. Sundmacher, *Exergetic assessment of* CO_2 *methanation processes for the chemical storage of renewable energies.* APPLIED ENERGY, 2019. **233-234**: p. 271-282.

[24]. Ashok, J., S. Pati, P. Hongmanorom, Z. Tianxi, C. Junmei, and S. Kawi, *A review of recent catalyst advances in* CO_2 *methanation processes.* CATALYSIS TODAY, 2020. **356**: p. 471-489.

[25]. Carvill, B.T., J.R. Hufton, M. Anand, and S. Sircar, *Sorption-enhanced reaction process.* AICHE JOURNAL, 1996. **42**(10): p. 2765-2772.

[26]. Delmelle, R., R.B. Duarte, T. Franken, D. Burnat, L. Holzer, A. Borgschulte, and A. Heel, *Development of improved nickel catalysts for sorption enhanced* CO_2 *methanation.* INTERNATIONAL JOURNAL OF HYDROGEN ENERGY, 2016. **41**(44): p. 20185-20191.

[27]. Borgschulte, A., N. Gallandat, B. Probst, R. Suter, E. Callini, D. Ferri, Y. Arroyo, R. Erni, H. Geerlings, and A. Zuttel, *Sorption enhanced* CO_2 *methanation.* PHYSICAL CHEMISTRY CHEMICAL PHYSICS, 2013. **15**(24): p. 9620-5.

[28]. Terreni, J., M. Trottmann, T. Franken, A. Heel, and A. Borgschulte, *Sorption-Enhanced Methanol Synthesis.* Energy Technology, 2019. **7**(4): p. 9.

[29]. Haije, W. and H. Geerlings, *Efficient production of solar fuel using existing large scale production technologies.* ENVIRONMENTAL SCIENCE & TECHNOLOGY, 2011. **45**(20): p. 8609-10.

[30]. VAN BERKEL, F.P.F., H.A.J. VAN DIJK, P.D. Cobden, W.G. Haije, and J.F. Vente, *Process and system for producing dimethyl ether*. 2020, Google Patents.

[31]. Guffanti, S., C.G. Visconti, J. van Kampen, J. Boon, and G. Groppi, *Reactor modelling and design for sorption enhanced dimethyl ether synthesis.* CHEMICAL ENGINEERING JOURNAL, 2021. **404**: p. 126573.

[32]. van Kampen, J., J. Boon, J. Vente, and M.J.J.o.C.U. van Sint Annaland, *Sorption enhanced dimethyl ether synthesis for high efficiency carbon conversion: Modelling and cycle design.* 2020. **37**: p. 295-308.

[33]. Walspurger, S., G.D. Elzinga, J.W. Dijkstra, M. Sarić, and W.G. Haije, *Sorption enhanced methanation for substitute natural gas production: Experimental results and thermodynamic considerations.* CHEMICAL ENGINEERING JOURNAL, 2014. **242**: p. 379-386.

[34]. Wang, Y. and M.D. LeVan, *Adsorption Equilibrium of Carbon Dioxide and Water Vapor on Zeolites 5A and 13X and Silica Gel: Pure Components.* Journal of Chemical & Engineering Data, 2009. **54**(10): p. 2839-2844.

[35]. van Kampen, J., J. Boon, F. van Berkel, J. Vente, and M. van Sint Annaland, *Steam separation enhanced reactions: Review and outlook.* CHEMICAL ENGINEERING JOURNAL, 2019. **374**: p. 1286-1303.

[36]. Newsam, J.M., *The zeolite cage structure.* SCIENCE, 1986. **231**(4742): p. 1093-9.

[37]. Borgschulte, A., E. Callini, N. Stadie, Y. Arroyo, M.D. Rossell, R. Erni, H. Geerlings, A. Züttel, and D. Ferri, *Manipulating the reaction path of the* CO_2 *hydrogenation reaction in molecular sieves.* Catalysis Science & Technology, 2015. **5**(9): p. 4613-4621.

[38]. Ghodhbene, M., F. Bougie, P. Fongarland, and M.C. Iliuta, *Hydrophilic zeolite sorbents for In-situ water removal in high temperature processes.* The Canadian Journal of Chemical Engineering, 2017. **95**(10): p. 1842-1849.

[39]. Tatlier, M., G. Munz, and S.K. Henninger, *Relation of water adsorption capacities of zeolites with their structural properties.* MICROPOROUS AND MESOPOROUS MATERIALS, 2018. **264**: p. 70-75.

[40]. Westermann, A., B. Azambre, M.C. Bacariza, I. Graça, M.F. Ribeiro, J.M. Lopes, and C. Henriques, *Insight into* CO_2 *methanation mechanism over NiUSY zeolites: An operando IR study.* Applied Catalysis B: Environmental, 2015. **174-175**: p. 120-125.

[41]. Quindimil, A., U. De-La-Torre, B. Pereda-Ayo, J.A. González-Marcos, and J.R. González-Velasco, *Ni catalysts with La as promoter supported over Y- and BETA- zeolites for* CO_2 *methanation.* Applied Catalysis B: Environmental, 2018. **238**: p. 393-403.

[42]. Westermann, A., B. Azambre, M.C. Bacariza, I. Graça, M.F. Ribeiro, J.M. Lopes, and C. Henriques, *The promoting effect of Ce in the* CO_2 *methanation performances on NiUSY zeolite: A FTIR In Situ/Operando study.* CATALYSIS TODAY, 2017. **283**: p. 74-81.

[43]. Graça, I., L.V. González, M.C. Bacariza, A. Fernandes, C. Henriques, J.M. Lopes, and M.F. Ribeiro, CO_2 *hydrogenation into* CH_4 *on NiHNaUSY zeolites.* Applied Catalysis B: Environmental, 2014. **147**(Supplement C): p. 101-110.

[44]. Coppola, A., F. Massa, P. Salatino, and F. Scala, *Evaluation of two sorbents for the sorption-enhanced methanation in a dual fluidized bed system.* Biomass Conversion and Biorefinery, 2020. **11**(1): p. 111-119.

[45]. Asnin, L.D. and M.V. Stepanova, *Van't Hoff analysis in chiral chromatography.* JOURNAL OF SEPARATION SCIENCE, 2018. **41**(6): p. 1319-1337.

[46]. van Kampen, J., J. Boon, and M. van Sint Annaland, *Steam adsorption on molecular sieve 3A for sorption enhanced reaction processes.* ADSORPTION-JOURNAL OF THE INTERNATIONAL ADSORPTION SOCIETY, 2020. **27**(4): p. 577-589.

[47]. Ng, E.-P. and S. Mintova, *Nanoporous materials with enhanced hydrophilicity and high water sorption capacity.* MICROPOROUS AND MESOPOROUS MATERIALS, 2008. **114**(1-3): p. 1-26.

[48]. Simo, M., S. Sivashanmugam, C.J. Brown, and V. Hlavacek, *Adsorption/Desorption of Water and Ethanol on 3A Zeolite in Near-Adiabatic Fixed Bed.* INDUSTRIAL & ENGINEERING CHEMISTRY RESEARCH, 2009. **48**(20): p. 9247-9260.

[49]. Furukawa, H., F. Gandara, Y.B. Zhang, J. Jiang, W.L. Queen, M.R. Hudson, and O.M. Yaghi, *Water adsorption in porous metal-organic frameworks and related materials.* JOURNAL OF THE AMERICAN CHEMICAL SOCIETY, 2014. **136**(11): p. 4369-81.

[50]. Sreedhar, I., Y. Varun, S.A. Singh, A. Venugopal, and B.M. Reddy, *Developmental*

trends in CO_2 methanation using various catalysts. Catalysis Science & Technology, 2019. **9**(17): p. 4478-4504.

[51]. Nie, X., W. Li, X. Jiang, X. Guo, and C. Song, *Recent advances in catalytic CO_2 hydrogenation to alcohols and hydrocarbons*, in *Advances in Catalysis, Vol 65*, C. Song, Editor. 2019. p. 121-233.

[52]. Yan, Y., Y. Dai, H. He, Y. Yu, and Y. Yang, *A novel W-doped Ni-Mg mixed oxide catalyst for CO_2 methanation.* Applied Catalysis B: Environmental, 2016. **196**: p. 108-116.

[53]. Li, Y., Q. Zhang, R. Chai, G. Zhao, F. Cao, Y. Liu, and Y. Lu, *Metal-foam-structured Ni–Al_2O_3 catalysts: Wet chemical etching preparation and syngas methanation performance.* Applied Catalysis A: General, 2016. **510**: p. 216-226.

[54]. Aziz, M.A.A., A.A. Jalil, S. Triwahyono, and A. Ahmad, *CO_2 methanation over heterogeneous catalysts: recent progress and future prospects.* GREEN CHEMISTRY, 2015. **17**(5): p. 2647-2663.

[55]. Walspurger, S., W.G. Haije, and B. Louis, *CO_2 Reduction to Substitute Natural Gas: Toward a Global Low Carbon Energy System.* ISRAEL JOURNAL OF CHEMISTRY, 2014. **54**(10): p. 1432-1442.

[56]. Bacariza, M.C., I. Graça, J.M. Lopes, and C. Henriques, *Tuning Zeolite Properties towards CO_2 Methanation: An Overview.* ChemCatChem, 2019. **11**(10): p. 2388-2400.

[57]. Fechete, I. and J.C. Vedrine, *Nanoporous materials as new engineered catalysts for the synthesis of green fuels.* MOLECULES, 2015. **20**(4): p. 5638-66.

[58]. Aziz, M.A.A., A.A. Jalil, S. Triwahyono, R.R. Mukti, Y.H. Taufiq-Yap, and M.R. Sazegar, *Highly active Ni-promoted mesostructured silica nanoparticles for CO_2 methanation.* Applied Catalysis B: Environmental, 2014. **147**: p. 359-368.

[59]. Beaumont, S.K., S. Alayoglu, C. Specht, N. Kruse, and G.A. Somorjai, *A nanoscale demonstration of hydrogen atom spillover and surface diffusion across silica using the kinetics of CO_2 methanation catalyzed on spatially separate Pt and Co nanoparticles.* NANO LETTERS, 2014. **14**(8): p. 4792-6.

[60]. Li, W., X. Nie, X. Jiang, A. Zhang, F. Ding, M. Liu, Z. Liu, X. Guo, and C. Song, *ZrO_2 support imparts superior activity and stability of Co catalysts for CO_2 methanation.* Applied Catalysis B: Environmental, 2018. **220**: p. 397-408.

[61]. Franken, T. and A. Heel, *Are Fe based catalysts an upcoming alternative to Ni in CO_2 methanation at elevated pressure?* Journal of CO_2 Utilization, 2020. **39**.

[62]. Merkache, R., I. Fechete, M. Maamache, M. Bernard, P. Turek, K. Al-Dalama, and F. Garin, *3D ordered mesoporous Fe-KIT-6 catalysts for methylcyclopentane (MCP) conversion and carbon dioxide (CO_2) hydrogenation for energy and environmental applications.* Applied Catalysis A: General, 2015. **504**: p. 672-681.

[63]. Wang, X., G. Yang, J. Zhang, S. Chen, Y. Wu, Q. Zhang, J. Wang, Y. Han, and Y. Tan, *Synthesis of isoalkanes over a core (Fe-Zn-Zr)-shell (zeolite) catalyst by CO_2 hydrogenation.* Chem Commun (Camb), 2016. **52**(46): p. 7352-5.

[64]. Primo, A., J. He, B. Jurca, B. Cojocaru, C. Bucur, V.I. Parvulescu, and H. Garcia, *CO_2 methanation catalyzed by oriented MoS_2 nanoplatelets supported on few layers graphene.* Applied Catalysis B: Environmental, 2019. **245**: p. 351-359.

[65]. Mori, S., W.C. Xu, T. Ishidzuki, N. Ogasawara, J. Imai, and K. Kobayashi, *Mechanochemical activation of catalysts for CO_2 methanation.* Applied Catalysis A: General, 1996. **137**(2): p. 255-268.

[66]. Hastings, W.R., C.J. Cameron, M.J. Thomas, and M.C. Baird, *Carbon monoxide and carbon dioxide hydrogenation catalyzed by supported ruthenium carbonyl clusters. A novel procedure for encapsulating triruthenium dodecacarbonyl within the pores*

of Na-Y zeolite. Inorganic Chemistry, 1988. **27**(17): p. 3024-3028.

[67]. Abe, T., M. Tanizawa, K. Watanabe, and A. Taguchi, *CO_2 methanation property of Ru nanoparticle-loaded TiO_2 prepared by a polygonal barrel-sputtering method.* Energy & Environmental Science, 2009. **2**(3): p. 315-321.

[68]. Lee, W.T., A.P. van Muyden, F.D. Bobbink, Z. Huang, and P.J. Dyson, *Indirect CO_2 Methanation: Hydrogenolysis of Cyclic Carbonates Catalyzed by Ru-Modified Zeolite Produces Methane and Diols.* Angew Chem Int Ed Engl, 2019. **58**(2): p. 557-560.

[69]. Bando, K.K., H. Arakawa, and N. Ichikuni, *CO_2 hydrogenation over micro- and mesoporous oxides supported Ru catalysts.* CATALYSIS LETTERS, 1999. **60**(3): p. 125-132.

[70]. Swalus, C., M. Jacquemin, C. Poleunis, P. Bertrand, and P. Ruiz, *CO_2 methanation on Rh/γ-Al_2O_3 catalyst at low temperature: "In situ" supply of hydrogen by Ni/activated carbon catalyst.* Applied Catalysis B: Environmental, 2012. **125**: p. 41-50.

[71]. Karelovic, A. and P. Ruiz, *Mechanistic study of low temperature CO_2 methanation over Rh/TiO_2 catalysts.* JOURNAL OF CATALYSIS, 2013. **301**: p. 141-153.

[72]. Sápi, A., U. Kashaboina, K.B. Ábrahámné, J.F. Gómez-Pérez, I. Szenti, G. Halasi, J. Kiss, B. Nagy, T. Varga, Á. Kukovecz, and Z. Kónya, *Synergetic of Pt Nanoparticles and H-ZSM-5 Zeolites for Efficient CO_2 Activation: Role of Interfacial Sites in High Activity.* Frontiers in Materials, 2019. **6**.

[73]. Beaumont, S.K., S. Alayoglu, C. Specht, W.D. Michalak, V.V. Pushkarev, J. Guo, N. Kruse, and G.A. Somorjai, *Combining in situ NEXAFS spectroscopy and CO(2) methanation kinetics to study Pt and Co nanoparticle catalysts reveals key insights into the role of platinum in promoted cobalt catalysis.* JOURNAL OF THE AMERICAN CHEMICAL SOCIETY, 2014. **136**(28): p. 9898-901.

[74]. Kikkawa, S., K. Teramura, H. Asakura, S. Hosokawa, and T. Tanaka, *Isolated Platinum Atoms in Ni/γ-Al_2O_3 for Selective Hydrogenation of CO_2 toward CH_4.* The Journal of Physical Chemistry C, 2019. **123**(38): p. 23446-23454.

[75]. Luo, L., M. Wang, Y. Cui, Z. Chen, J. Wu, Y. Cao, J. Luo, Y. Dai, W.X. Li, J. Bao, and J. Zeng, *Surface Iron Species in Palladium-Iron Intermetallic Nanocrystals that Promote and Stabilize CO_2 Methanation.* Angew Chem Int Ed Engl, 2020. **59**(34): p. 14434-14442.

[76]. Karelovic, A. and P. Ruiz, *Improving the Hydrogenation Function of Pd/γ-Al_2O_3 Catalyst by Rh/γ-Al_2O_3 Addition in CO_2 Methanation at Low Temperature.* ACS Catalysis, 2013. **3**(12): p. 2799-2812.

[77]. Weatherbee, G., *Hydrogenation of CO_2 on group VIII metals IV. Specific activities and selectivities of silica-supported Co, Fe, and Ru.* JOURNAL OF CATALYSIS, 1984. **87**(2): p. 352-362.

[78]. Falbo, L., M. Martinelli, C.G. Visconti, L. Lietti, C. Bassano, and P. Deiana, *Kinetics of CO_2 methanation on a Ru-based catalyst at process conditions relevant for Power-to-Gas applications.* Applied Catalysis B: Environmental, 2018. **225**: p. 354-363.

[79]. Le, T.A., T.W. Kim, S.H. Lee, and E.D. Park, *Effects of Na content in Na/Ni/SiO_2 and Na/Ni/CeO_2 catalysts for CO and CO_2 methanation.* CATALYSIS TODAY, 2018. **303**: p. 159-167.

[80]. Petala, A. and P. Panagiotopoulou, *Methanation of CO_2 over alkali-promoted Ru/TiO_2 catalysts: I. Effect of alkali additives on catalytic activity and selectivity.* Applied Catalysis B: Environmental, 2018. **224**: p. 919-927.

[81]. Chen, H., Y. Mu, Y. Shao, S. Chansai, S. Xu, C.E. Stere, H. Xiang, R. Zhang, Y. Jiao, C.J.C.S. Hardacre, and Technology, *Coupling non-thermal plasma with Ni*

catalysts supported on BETA zeolite for catalytic CO_2 methanation. Catalysis Science & Technology, 2019. **9**(15): p. 4135-4145.

[82]. Pierson, H.O., *Handbook of Chemical Vapor Deposition (CVD) - Principles, Technology and Applications (2nd Edition).* 1999: William Andrew Publishing/Noyes.

[83]. Schlögl, R., *Handbook of Heterogeneous Catalysis*. 2008, Wiley-VCH Verlag GmbH & Co. KGaA.

[84]. Terreni, J., M. Trottmann, R. Delmelle, A. Heel, P. Trtik, E.H. Lehmann, and A. Borgschulte, *Observing Chemical Reactions by Time-Resolved High-Resolution Neutron Imaging.* The Journal of Physical Chemistry C, 2018. **122**(41): p. 23574-23581.

[85]. Borgschulte, A., R. Delmelle, R.B. Duarte, A. Heel, P. Boillat, and E. Lehmann, *Water distribution in a sorption enhanced methanation reactor by time resolved neutron imaging.* PHYSICAL CHEMISTRY CHEMICAL PHYSICS, 2016. **18**(26): p. 17217-23.

[86]. Chen, Y., S. Ji, C. Chen, Q. Peng, D. Wang, and Y. Li, *Single-Atom Catalysts: Synthetic Strategies and Electrochemical Applications.* Joule, 2018. **2**(7): p. 1242-1264.

[87]. Zhang, L., Y. Ren, W. Liu, A. Wang, and T. Zhang, *Single-atom catalyst: a rising star for green synthesis of fine chemicals.* NATL SCI REV, 2018. **5**(5): p. 653-672.

[88]. Abbet, S., A. Sanchez, U. Heiz, W.-D. Schneider, A.M. Ferrari, G. Pacchioni, and N. Rösch, *Acetylene cyclotrimerization on supported size-selected Pd n clusters (1≤ n≤ 30): one atom is enough!* J AM CHEM SOC, 2000. **122**(14): p. 3453-3457.

[89]. Yan, H., H. Cheng, H. Yi, Y. Lin, T. Yao, C. Wang, J. Li, S. Wei, and J. Lu, *Single-atom Pd1/graphene catalyst achieved by atomic layer deposition: remarkable performance in selective hydrogenation of 1, 3-butadiene.* J AM CHEM SOC, 2015. **137**(33): p. 10484-10487.

[90]. Peters, A.W., Z. Li, O.K. Farha, and J.T. Hupp, *Atomically precise growth of catalytically active cobalt sulfide on flat surfaces and within a metal–organic framework via atomic layer deposition.* ACS Nano, 2015. **9**(8): p. 8484-8490.

[91]. Zhang, J., X. Wu, W.-C. Cheong, W. Chen, R. Lin, J. Li, L. Zheng, W. Yan, L. Gu, and C. Chen, *Cation vacancy stabilization of single-atomic-site Pt 1/Ni (OH)x catalyst for diboration of alkynes and alkenes.* NAT COMMUN, 2018. **9**(1): p. 1002.

[92]. Qiu, H.J., Y. Ito, W. Cong, Y. Tan, P. Liu, A. Hirata, T. Fujita, Z. Tang, and M. Chen, *Nanoporous Graphene with Single-Atom Nickel Dopants: An Efficient and Stable Catalyst for Electrochemical Hydrogen Production.* ANGEW CHEM INT EDIT, 2015. **54**(47): p. 14031-14035.

[93]. Han, Y., Y.-G. Wang, W. Chen, R. Xu, L. Zheng, J. Zhang, J. Luo, R.-A. Shen, Y. Zhu, W.-C. Cheong, C. Chen, Q. Peng, D. Wang, and Y. Li, *Hollow N-Doped Carbon Spheres with Isolated Cobalt Single Atomic Sites: Superior Electrocatalysts for Oxygen Reduction.* J AM CHEM SOC, 2017. **139**(48): p. 17269-17272.

[94]. Yin, P., T. Yao, Y. Wu, L. Zheng, Y. Lin, W. Liu, H. Ju, J. Zhu, X. Hong, Z. Deng, G. Zhou, S. Wei, and Y. Li, *Single Cobalt Atoms with Precise N-Coordination as Superior Oxygen Reduction Reaction Catalysts.* ANGEW CHEM INT EDIT, 2016. **55**(36): p. 10800-10805.

[95]. Chen, Y., S. Ji, Y. Wang, J. Dong, W. Chen, Z. Li, R. Shen, L. Zheng, Z. Zhuang, D. Wang, and Y. Li, *Isolated Single Iron Atoms Anchored on N-Doped Porous Carbon as an Efficient Electrocatalyst for the Oxygen Reduction Reaction.* ANGEW CHEM INT EDIT, 2017. **56**(24): p. 6937-6941.

[96]. Qu, Y., Z. Li, W. Chen, Y. Lin, T. Yuan, Z. Yang, C. Zhao, J. Wang, C. Zhao, X.

Wang, F. Zhou, Z. Zhuang, Y. Wu, and Y. Li, *Direct transformation of bulk copper into copper single sites via emitting and trapping of atoms.* Nat. Catal., 2018. **1**(10): p. 781-786.

[97]. Liu, L., M. Lopez-Haro, C.W. Lopes, C. Li, P. Concepcion, L. Simonelli, J.J. Calvino, and A. Corma, *Regioselective generation and reactivity control of subnanometric platinum clusters in zeolites for high-temperature catalysis.* NATURE MATERIALS, 2019. **18**(8): p. 866-873.

[98]. Kistler, J.D., N. Chotigkrai, P. Xu, B. Enderle, P. Praserthdam, C.Y. Chen, N.D. Browning, and B.C. Gates, *A single-site platinum CO oxidation catalyst in zeolite KLTL: microscopic and spectroscopic determination of the locations of the platinum atoms.* Angew Chem Int Ed Engl, 2014. **53**(34): p. 8904-7.

[99]. Liu, Y., Z. Li, Q. Yu, Y. Chen, Z. Chai, G. Zhao, S. Liu, W.C. Cheong, Y. Pan, Q. Zhang, L. Gu, L. Zheng, Y. Wang, Y. Lu, D. Wang, C. Chen, Q. Peng, Y. Liu, L. Liu, J. Chen, and Y. Li, *A General Strategy for Fabricating Isolated Single Metal Atomic Site Catalysts in Y Zeolite.* JOURNAL OF THE AMERICAN CHEMICAL SOCIETY, 2019. **141**(23): p. 9305-9311.

[100]. Li, L., J. Zheng, Y. Liu, W. Wang, Q. Huang, and W. Chu, *Impacts of SiC Carrier and Nickel Precursor of NiLa/support Catalysts for CO_2 Selective Hydrogenation to Synthetic Natural Gas (SNG).* ChemistrySelect, 2017. **2**(13): p. 3750-3757.

[101]. Bando, K.K., K. Soga, K. Kunimori, N. Ichikuni, K. Okabe, H. Kusama, K. Sayama, and H. Arakawa, *CO_2 hydrogenation activity and surface structure of zeolite-supported Rh catalysts.* APPLIED CATALYSIS A-GENERAL, 1998. **173**(1): p. 47-60.

[102]. Scirè, S., C. Crisafulli, R. Maggiore, S. Minicò, and S. Galvagno, *Influence of the support on CO_2 methanation over Ru catalysts: an FT-IR study.* CATALYSIS LETTERS, 1998. **51**(1/2): p. 41-45.

[103]. Jwa, E., S.B. Lee, H.W. Lee, and Y.S. Mok, *Plasma-assisted catalytic methanation of CO and CO_2 over Ni–zeolite catalysts.* FUEL PROCESSING TECHNOLOGY, 2013. **108**: p. 89-93.

[104]. Azzolina-Jury, F. and F. Thibault-Starzyk, *Mechanism of Low Pressure Plasma-Assisted CO_2 Hydrogenation Over Ni-USY by Microsecond Time-resolved FTIR Spectroscopy.* TOPICS IN CATALYSIS, 2017. **60**(19-20): p. 1709-1721.

[105]. Bacariza, M.C., I. Graça, S.S. Bebiano, J.M. Lopes, and C. Henriques, *Magnesium as Promoter of CO_2 Methanation on Ni-Based USY Zeolites.* ENERGY & FUELS, 2017. **31**(9): p. 9776-9789.

[106]. Bacariza, M.C., R. Bértolo, I. Graça, J.M. Lopes, and C. Henriques, *The effect of the compensating cation on the catalytic performances of Ni/USY zeolites towards CO_2 methanation.* Journal of CO_2 Utilization, 2017. **21**: p. 280-291.

[107]. Bacariza, M.C., I. Graça, J.M. Lopes, and C. Henriques, *Enhanced activity of CO_2 hydrogenation to CH_4 over Ni based zeolites through the optimization of the Si/Al ratio.* MICROPOROUS AND MESOPOROUS MATERIALS, 2018. **267**: p. 9-19.

[108]. Bacariza, M.C., I. Graça, S.S. Bebiano, J.M. Lopes, and C. Henriques, *Micro- and mesoporous supports for CO_2 methanation catalysts: A comparison between SBA-15, MCM-41 and USY zeolite.* CHEMICAL ENGINEERING SCIENCE, 2018. **175**: p. 72-83.

[109]. Bacariza, M.C., I. Graça, J.M. Lopes, and C. Henriques, *Ni-Ce/Zeolites for CO_2 Hydrogenation to CH_4: Effect of the Metal Incorporation Order.* ChemCatChem, 2018. **10**(13): p. 2773-2781.

[110]. Bacariza, M.C., M. Maleval, I. Graça, J.M. Lopes, and C. Henriques, *Power-to-methane over Ni/zeolites: Influence of the framework type.* MICROPOROUS AND

MESOPOROUS MATERIALS, 2019. **274**: p. 102-112.

[111]. Rasmussen, K.H., F. Goodarzi, D.B. Christensen, J. Mielby, and S. Kegnæs, *Stabilization of Metal Nanoparticle Catalysts via Encapsulation in Mesoporous Zeolites by Steam-Assisted Recrystallization.* ACS Applied Nano Materials, 2019. **2**(12): p. 8083-8091.

[112]. Wang, C., E. Guan, L. Wang, X. Chu, Z. Wu, J. Zhang, Z. Yang, Y. Jiang, L. Zhang, X. Meng, B.C. Gates, and F.S. Xiao, *Product Selectivity Controlled by Nanoporous Environments in Zeolite Crystals Enveloping Rhodium Nanoparticle Catalysts for* CO_2 *Hydrogenation.* JOURNAL OF THE AMERICAN CHEMICAL SOCIETY, 2019. **141**(21): p. 8482-8488.

[113]. Chen, Y., B. Qiu, Y. Liu, and Y. Zhang, *An active and stable nickel-based catalyst with embedment structure for* CO_2 *methanation.* Applied Catalysis B: Environmental, 2020. **269**.

[114]. Czuma, N., K. Zarębska, M. Motak, M.E. Gálvez, and P. Da Costa, *Ni/zeolite X derived from fly ash as catalysts for* CO_2 *methanation.* FUEL, 2020. **267**: p. 117139.

[115]. da Costa-Serra, J.F., C. Cerdá-Moreno, and A. Chica, *Zeolite-Supported Ni Catalysts for* CO_2 *Methanation: Effect of Zeolite Structure and Si/Al Ratio.* Applied Sciences, 2020. **10**(15).

[116]. Vogt, C., M. Monai, G.J. Kramer, and B.M. Weckhuysen, *The renaissance of the Sabatier reaction and its applications on Earth and in space.* Nature Catalysis, 2019. **2**(3): p. 188-197.

[117]. Vogt, C., M. Monai, E.B. Sterk, J. Palle, A.E.M. Melcherts, B. Zijlstra, E. Groeneveld, P.H. Berben, J.M. Boereboom, E.J.M. Hensen, F. Meirer, I.A.W. Filot, and B.M. Weckhuysen, *Understanding carbon dioxide activation and carbon-carbon coupling over nickel.* Nat Commun, 2019. **10**(1): p. 5330.

[118]. Massa, F., A. Coppola, and F. Scala, *A thermodynamic study of sorption-enhanced* CO_2 *methanation at low pressure.* Journal of CO_2 Utilization, 2020. **35**: p. 176-184.

[119]. Catarina Faria, A., C.V. Miguel, and L.M. Madeira, *Thermodynamic analysis of the* CO_2 *methanation reaction with in situ water removal for biogas upgrading.* Journal of CO_2 Utilization, 2018. **26**: p. 271-280.

[120]. Delmelle, R., J. Terreni, A. Remhof, A. Heel, J. Proost, and A. Borgschulte, *Evolution of Water Diffusion in a Sorption-Enhanced Methanation Catalyst.* Catalysts, 2018. **8**(9).

[121]. Lappas, A. and E. Heracleous, *Production of biofuels via Fischer–Tropsch synthesis: biomass-to-liquids*, in *Handbook of biofuels production*. 2016, Elsevier. p. 549-593.

[122]. Lee, B., H. Lee, S. Kim, H.-S. Cho, W.-C. Cho, B.-H. Jeon, C.-H. Kim, and H. Lim, *Quantification of economic uncertainty for synthetic natural gas production in a* H_2O *permeable membrane reactor as simultaneous power-to-gas and* CO_2 *utilization technologies.* ENERGY, 2019. **182**: p. 1058-1068.

[123]. Wei, L., W. Haije, N. Kumar, J. Peltonen, M. Peurla, H. Grénman, and W. de Jong, *Influence of nickel precursors on the properties and performance of Ni impregnated zeolite 5A and 13X catalysts in* CO_2 *methanation.* CATALYSIS TODAY, 2021. **362**: p. 35-46.

[124]. Yang, H.Q., Z.H. Xu, M.H. Fan, R. Gupta, R.B. Slimane, A.E. Bland, and I. Wright, *Progress in carbon dioxide separation and capture: A review.* Journal of Environmental Sciences, 2008. **20**(1): p. 14-27.

[125]. Shuai, C., L. Shen, L. Jiao, Y. Wu, and Y. Tan, *Identifying key impact factors on carbon emission: Evidences from panel and time-series data of 125 countries from 1990 to 2011.* Applied Energy, 2017. **187**: p. 310-325.

[126]. Rahman, F.A., M.M.A. Aziz, R. Saidur, W.A.W.A. Bakar, M.R. Hainin, R. Putrajaya,

and N.A. Hassan, *Pollution to solution: Capture and sequestration of carbon dioxide (CO_2) and its utilization as a renewable energy source for a sustainable future.* Renewable and Sustainable Energy Reviews, 2017. **71**: p. 112-126.

[127]. Boot-Handford, M.E., J.C. Abanades, E.J. Anthony, M.J. Blunt, S. Brandani, N. Mac Dowell, J.R. Fernández, M.-C. Ferrari, R. Gross, and J.P. Hallett, *Carbon capture and storage update.* Energy & Environmental Science, 2014. **7**(1): p. 130-189.

[128]. Reiner, D.M., *Learning through a portfolio of carbon capture and storage demonstration projects.* Nature Energy, 2016. **1**(1): p. 15011.

[129]. House, K.Z., A.C. Baclig, M. Ranjan, E.A. van Nierop, J. Wilcox, and H.J. Herzog, *Economic and energetic analysis of capturing CO_2 from ambient air.* PROCEEDINGS OF THE NATIONAL ACADEMY OF SCIENCES OF THE UNITED STATES OF AMERICA, 2011. **108**(51): p. 20428-33.

[130]. Wei, L., H. Yang, B. Li, X. Wei, L. Chen, J. Shao, and H. Chen, *Absorption-enhanced steam gasification of biomass for hydrogen production: Effect of calcium oxide addition on steam gasification of pyrolytic volatiles.* INTERNATIONAL JOURNAL OF HYDROGEN ENERGY, 2014. **39**(28): p. 15416-15423.

[131]. Li, B., H. Yang, L. Wei, J. Shao, X. Wang, and H. Chen, *Hydrogen production from agricultural biomass wastes gasification in a fluidized bed with calcium oxide enhancing.* INTERNATIONAL JOURNAL OF HYDROGEN ENERGY, 2017. **42**(8): p. 4832-4839.

[132]. Wang, J., K. Sakanishi, I. Saito, T. Takarada, and K. Morishita, *High-yield hydrogen production by steam gasification of HyperCoal (ash-free coal extract) with potassium carbonate: comparison with raw coal.* Energy & Fuels, 2005. **19**(5): p. 2114-2120.

[133]. Pasman, H.J. and W.J. Rogers, *Risk assessment by means of Bayesian networks: A comparative study of compressed and liquefied H_2 transportation and tank station risks.* International Journal of Hydrogen Energy, 2012. **37**(22): p. 17415-17425.

[134]. Götz, M., J. Lefebvre, F. Mörs, A. McDaniel Koch, F. Graf, S. Bajohr, R. Reimert, and T. Kolb, *Renewable Power-to-Gas: A technological and economic review.* RENEWABLE ENERGY, 2016. **85**: p. 1371-1390.

[135]. Frontera, P., A. Macario, M. Ferraro, and P. Antonucci, *Supported Catalysts for CO_2 Methanation: A Review.* Catalysts, 2017. **7**(2): p. 59.

[136]. Schaaf, T., J. Grünig, M.R. Schuster, T. Rothenfluh, and A. Orth, *Methanation of CO_2-storage of renewable energy in a gas distribution system.* Energy, Sustainability and Society, 2014. **4**(1): p. 2.

[137]. Borgschulte, A., N. Gallandat, B. Probst, R. Suter, E. Callini, D. Ferri, Y. Arroyo, R. Erni, H. Geerlings, and A. Züttel, *Sorption enhanced CO_2 methanation.* Physical Chemistry Chemical Physics, 2013. **15**(24): p. 9620-9625.

[138]. Wei, W. and G. Jinlong, *Methanation of carbon dioxide: an overview.* Frontiers of Chemical Science and Engineering, 2011. **5**(1): p. 2-10.

[139]. He, S., Q. Jing, W. Yu, L. Mo, H. Lou, and X. Zheng, *Combination of CO_2 reforming and partial oxidation of methane to produce syngas over Ni/SiO_2 prepared with nickel citrate precursor.* CATALYSIS TODAY, 2009. **148**(1-2): p. 130-133.

[140]. He, S., Z. Mei, N. Liu, L. Zhang, J. Lu, X. Li, J. Wang, D. He, and Y. Luo, *Ni/SBA-15 catalysts for hydrogen production by ethanol steam reforming: Effect of nickel precursor.* INTERNATIONAL JOURNAL OF HYDROGEN ENERGY, 2017. **42**(21): p. 14429-14438.

[141]. Chick, L.A., L.R. Pederson, G.D. Maupin, J.L. Bates, L.E. Thomas, and G.J. Exarhos, *Glycine-nitrate combustion synthesis of oxide ceramic powders.* MATERIALS LETTERS, 1990. **10**(1-2): p. 6-12.

[142]. Delmon, B., *Preparation of heterogeneous catalysts.* JOURNAL OF THERMAL

ANALYSIS AND CALORIMETRY, 2007. **90**(1): p. 49-65.

[143]. Zhang, H.-M., Y. Teraoka, and N. Yamazoe, *Preparation of Perovskite-type Oxides with Large Surface Area by Citrate Process.* CHEMISTRY LETTERS, 1987. **16**(4): p. 665-668.

[144]. Adams, J.M. and D.A. Haselden, *The structure of dehydrated zeolite 5A () by neutron profile refinement.* JOURNAL OF SOLID STATE CHEMISTRY, 1984. **51**(1): p. 83-90.

[145]. Hunger, J., I.A. Beta, H. Bohlig, C. Ling, H. Jobic, and B. Hunger, *Adsorption structures of water in NaX studied by DRIFT spectroscopy and neutron powder diffraction.* JOURNAL OF PHYSICAL CHEMISTRY B, 2006. **110**(1): p. 342-53.

[146]. Joos, L., J.A. Swisher, and B. Smit, *Molecular simulation study of the competitive adsorption of H_2O and CO_2 in zeolite 13X.* LANGMUIR, 2013. **29**(51): p. 15936-42.

[147]. Luengnaruemitchai, A. and A. Kaengsilalai, *Activity of different zeolite-supported Ni catalysts for methane reforming with carbon dioxide.* CHEMICAL ENGINEERING JOURNAL, 2008. **144**(1): p. 96-102.

[148]. Zhang, C., Y.-M. Chai, and C.-G. Liu, *Effect of different precursor species on the metal dispersion of a Ni/γ-Al_2O_3 adsorbent for sulfur adsorption.* Applied Petrochemical Research, 2017. **7**(1): p. 33-40.

[149]. Li, F., X. Yi, and W. Fang, *Effect of Organic Nickel Precursor on the Reduction Performance and Hydrogenation Activity of Ni/Al_2O_3 Catalysts.* CATALYSIS LETTERS, 2009. **130**(3-4): p. 335-340.

[150]. Still, E.R. and P. Wikberg, *Solution studies of systems with polynuclear complex formation. 2. The nickel(II) citrate system.* INORGANICA CHIMICA ACTA, 1980. **46**: p. 153-155.

[151]. Field, T.B., J.L. McCourt, and W.A.E. McBryde, *Composition and Stability of Iron and Copper Citrate Complexes in Aqueous Solution.* Canadian Journal of Chemistry, 1974. **52**(17): p. 3119-3124.

[152]. Brockner, W., C. Ehrhardt, and M. Gjikaj, *Thermal decomposition of nickel nitrate hexahydrate, $Ni(NO_3)_2{\cdot}6H_2O$, in comparison to $Co(NO_3)_2{\cdot}6H_2O$ and $Ca(NO_3)_2{\cdot}4H_2O$.* THERMOCHIMICA ACTA, 2007. **456**(1): p. 64-68.

[153]. Abelló, S., C. Berrueco, and D. Montané, *High-loaded nickel–alumina catalyst for direct CO_2 hydrogenation into synthetic natural gas (SNG).* FUEL, 2013. **113**: p. 598-609.

[154]. Abate, S., K. Barbera, E. Giglio, F. Deorsola, S. Bensaid, S. Perathoner, R. Pirone, and G. Centi, *Synthesis, Characterization, and Activity Pattern of Ni–Al Hydrotalcite Catalysts in CO_2 Methanation.* INDUSTRIAL & ENGINEERING CHEMISTRY RESEARCH, 2016. **55**(30): p. 8299-8308.

[155]. Lensveld, D.J., J.G. Mesu, A.J. Van Dillen, and K.P. de Jong, *Synthesis and characterisation of MCM-41 supported nickel oxide catalysts.* Microporous and Mesoporous Materials, 2001. **44**: p. 401-407.

[156]. Zheng, H., L. Han, H. Ma, Y. Zheng, H. Zhang, D. Liu, and S. Liang, *Adsorption characteristics of ammonium ion by zeolite 13X.* JOURNAL OF HAZARDOUS MATERIALS, 2008. **158**(2-3): p. 577-84.

[157]. Melo, C.R., H.G. Riella, N.C. Kuhnen, E. Angioletto, A.R. Melo, A.M. Bernardin, M.R. da Rocha, and L. da Silva, *Synthesis of 4A zeolites from kaolin for obtaining 5A zeolites through ionic exchange for adsorption of arsenic.* Materials Science and Engineering: B, 2012. **177**(4): p. 345-349.

[158]. Sun, S., N. Tsubaki, and K. Fujimoto, *The reaction performances and characterization of Fischer–Tropsch synthesis Co/SiO_2 catalysts prepared from mixed cobalt salts.* Applied Catalysis A: General, 2000. **202**(1): p. 121-131.

[159]. Fang, K., J. Ren, and Y. Sun, *Effect of nickel precursors on the performance of Ni/AlMCM-41 catalysts for n-dodecane hydroconversion.* Journal of Molecular Catalysis A: Chemical, 2005. **229**(1-2): p. 51-58.

[160]. Yang, X.F., A. Wang, B. Qiao, J. Li, J. Liu, and T. Zhang, *Single-atom catalysts: a new frontier in heterogeneous catalysis.* ACCOUNTS OF CHEMICAL RESEARCH, 2013. **46**(8): p. 1740-8.

[161]. Suzuki, M., K. Tsutsumi, and H. Takahashi, *Characterization and catalytic activity of nickel-zeolite catalysts. I. Reduction properties of nickel ions in zeolites.* Zeolites, 1982. **2**(1): p. 51-58.

[162]. Yavuz, O., Y. Altunkaynak, and F. Guzel, *Removal of copper, nickel, cobalt and manganese from aqueous solution by kaolinite.* WATER RESEARCH, 2003. **37**(4): p. 948-52.

[163]. Shannon, R., *Revised effective ionic radii and systematic studies of interatomic distances in halides and chalcogenides.* Acta Crystallographica Section A, 1976. **32**(5): p. 751-767.

[164]. Jadhav, P.D., R.V. Chatti, R.B. Biniwale, N.K. Labhsetwar, S. Devotta, and S.S. Rayalu, *Monoethanol Amine Modified Zeolite 13X for CO_2 Adsorption at Different Temperatures.* ENERGY & FUELS, 2007. **21**(6): p. 3555-3559.

[165]. Yong, H.H., H.C. Park, Y.S. Kang, J. Won, and W.N. Kim, *Zeolite-filled polyimide membrane containing 2,4,6-triaminopyrimidine.* JOURNAL OF MEMBRANE SCIENCE, 2001. **188**(2): p. 151-163.

[166]. Hedwig, G.R., J.R. Liddle, and R.D. Reeves, *Complex formation of nickel (II) ions with citric acid in aqueous solution: a potentiometric and spectroscopic study.* Australian Journal of Chemistry, 1980. **33**(8): p. 1685-1693.

[167]. Ho, S.-C. and T.-C. Chou, *The role of anion in the preparation of nickel catalyst detected by TPR and FTIR spectra.* INDUSTRIAL & ENGINEERING CHEMISTRY RESEARCH, 1995. **34**(7): p. 2279-2284.

[168]. Abu-Zied, B.M. and A.M. Asiri, *An investigation of the thermal decomposition of nickel citrate as a precursor for Ni NiO composite nanoparticles.* THERMOCHIMICA ACTA, 2017. **649**: p. 54-62.

[169]. De Jesus, J.C., I. González, A. Quevedo, and T. Puerta, *Thermal decomposition of nickel acetate tetrahydrate: an integrated study by TGA, QMS and XPS techniques.* Journal of Molecular Catalysis A: Chemical, 2005. **228**(1-2): p. 283-291.

[170]. Sánchez-Sánchez, M.C., R.M. Navarro, and J.L.G. Fierro, *Ethanol steam reforming over Ni/MxOy–Al_2O_3 (M=Ce, La, Zr and Mg) catalysts: Influence of support on the hydrogen production.* International Journal of Hydrogen Energy, 2007. **32**(10): p. 1462-1471.

[171]. Aziz, M.A.A., A.A. Jalil, S. Triwahyono, and M.W.A. Saad, *CO_2 methanation over Ni-promoted mesostructured silica nanoparticles: Influence of Ni loading and water vapor on activity and response surface methodology studies.* CHEMICAL ENGINEERING JOURNAL, 2015. **260**: p. 757-764.

[172]. Zhu, P., Q. Chen, Y. Yoneyama, and N. Tsubaki, *Nanoparticle modified Ni-based bimodal pore catalysts for enhanced CO_2 methanation.* RSC Adv., 2014. **4**(110): p. 64617-64624.

[173]. Garbarino, G., D. Bellotti, P. Riani, L. Magistri, and G. Busca, *Methanation of carbon dioxide on Ru/Al_2O_3 and Ni/Al_2O_3 catalysts at atmospheric pressure: Catalysts activation, behaviour and stability.* INTERNATIONAL JOURNAL OF HYDROGEN ENERGY, 2015. **40**(30): p. 9171-9182.

[174]. Wei, L., N. Kumar, W. Haije, J. Peltonen, M. Peurla, H. Grénman, and W. de Jong, *Can bi-functional nickel modified 13X and 5A zeolite catalysts for CO_2 methanation*

be improved by introducing ruthenium? Molecular Catalysis, 2020. **494**: p. 111115.

[175]. De Jong, W. and J.R.e. Van Ommen, *Biomass, a sustainable energy source for the future – fundamentals of conversion processes*. 2014, New York (USA): John Wiley & Sons.

[176]. Mueller, K. and W. Arlt, *Status and Development in Hydrogen Transport and Storage for Energy Applications.* Energy Technology, 2013. **1**(9): p. 501-511.

[177]. Poullikkas, A., *A comparative overview of large-scale battery systems for electricity storage.* Renewable and Sustainable Energy Reviews, 2013. **27**(Supplement C): p. 778-788.

[178]. Lebarbier, V.M., R.A. Dagle, L. Kovarik, K.O. Albrecht, X. Li, L. Li, C.E. Taylor, X. Bao, and Y. Wang, *Sorption-enhanced synthetic natural gas (SNG) production from syngas: A novel process combining CO methanation, water-gas shift, and* CO_2 *capture.* Applied Catalysis B: Environmental, 2014. **144**(1): p. 223-232.

[179]. Wan Abu Bakar, W.A., R. Ali, and N.S. Mohammad, *The effect of noble metals on catalytic methanation reaction over supported Mn/Ni oxide based catalysts.* Arabian Journal of Chemistry, 2015. **8**(5): p. 632-643.

[180]. Gao, J., Q. Liu, F. Gu, B. Liu, Z. Zhong, and F. Su, *Recent advances in methanation catalysts for the production of synthetic natural gas.* RSC Advances, 2015. **5**(29): p. 22759-22776.

[181]. Hubble, R.A., J.Y. Lim, and J.S. Dennis, *Kinetic studies of* CO_2 *methanation over a Ni/gamma-*Al_2O_3 *catalyst.* FARADAY DISCUSSIONS, 2016. **192**: p. 529-544.

[182]. Jalama, K., *Carbon dioxide hydrogenation over nickel-, ruthenium-, and copper-based catalysts: Review of kinetics and mechanism.* Catalysis Reviews, 2017. **59**(2): p. 95-164.

[183]. Abu Bakar, W.A.W., R. Ali, and S. Toemen, *Catalytic methanation reaction over supported nickel–ruthenium oxide base for purification of simulated natural gas.* Scientia Iranica, 2012. **19**(3): p. 525-534.

[184]. Chen, B.H., Z.S. Chao, H. He, C. Huang, Y.J. Liu, W.J. Yi, X.L. Wei, and J.F. An, *Towards a full understanding of the nature of Ni(II) species and hydroxyl groups over highly siliceous HZSM-5 zeolite supported nickel catalysts prepared by a deposition-precipitation method.* DALTON TRANSACTIONS, 2016. **45**(6): p. 2720-39.

[185]. Burattin, P., M. Che, and C. Louis, *Molecular approach to the mechanism of deposition− precipitation of the Ni (II) phase on silica.* The Journal of Physical Chemistry B, 1998. **102**(15): p. 2722-2732.

[186]. Nares, R., J. Ramírez, A. Gutiérrez-Alejandre, C. Louis, and T. Klimova, *Ni/Hβ-Zeolite Catalysts Prepared by Deposition−Precipitation.* The Journal of Physical Chemistry B, 2002. **106**(51): p. 13287-13293.

[187]. Tada, S., R. Kikuchi, A. Takagaki, T. Sugawara, S.T. Oyama, K. Urasaki, and S. Satokawa, *Study of RuNi/*TiO_2 *catalysts for selective CO methanation.* Applied Catalysis B: Environmental, 2013. **140-141**: p. 258-264.

[188]. Kimura, M., T. Miyao, S. Komori, A. Chen, K. Higashiyama, H. Yamashita, and M. Watanabe, *Selective methanation of CO in hydrogen-rich gases involving large amounts of* CO_2 *over Ru-modified Ni-Al mixed oxide catalysts.* Applied Catalysis A: General, 2010. **379**(1-2): p. 182-187.

[189]. Jin, D., J. Gao, Z. Hou, Y. Guo, X. Lu, Y. Zhu, and X. Zheng, *Microwave assisted in situ synthesis of USY-encapsulated heteropoly acid (HPW-USY) catalysts.* Applied Catalysis A: General, 2009. **352**(1-2): p. 259-264.

[190]. Arena, F., R. Dario, and A. Parmaliana, *A characterization study of the surface acidity of solid catalysts by temperature programmed methods.* Applied Catalysis A: General, 1998. **170**(1): p. 127-137.

[191]. Lónyi, F. and J. Valyon, *On the interpretation of the NH3-TPD patterns of H-ZSM-5 and H-mordenite.* Microporous and Mesoporous Materials, 2001. **47**(2): p. 293-301.

[192]. Peebles, D.E., D.W. Goodman, and J.M. White, *Methanation of carbon dioxide on nickel(100) and the effects of surface modifiers.* The Journal of Physical Chemistry, 1983. **87**(22): p. 4378-4387.

[193]. Eckle, S., H.-G. Anfang, and R.J. Behm, *Reaction Intermediates and Side Products in the Methanation of CO and CO_2 over Supported Ru Catalysts in H_2-Rich Reformate Gases.* The Journal of Physical Chemistry C, 2011. **115**(4): p. 1361-1367.

[194]. Mills, G.A. and F.W. Steffgen, *Catalytic Methanation.* Catalysis Reviews, 1974. **8**(1): p. 159-210.

[195]. Sharma, S., Z. Hu, P. Zhang, E.W. McFarland, and H. Metiu, *CO_2 methanation on Ru-doped ceria.* JOURNAL OF CATALYSIS, 2011. **278**(2): p. 297-309.

[196]. Bligaard, T., J.K. Nørskov, S. Dahl, J. Matthiesen, C.H. Christensen, and J. Sehested, *The Brønsted–Evans–Polanyi relation and the volcano curve in heterogeneous catalysis.* JOURNAL OF CATALYSIS, 2004. **224**(1): p. 206-217.

[197]. Dongapure, P., S. Bagchi, S. Mayadevi, and R.N. Devi, *Variations in activity of Ru/TiO_2 and Ru/Al_2O_3 catalysts for CO_2 hydrogenation: An investigation by in-situ infrared spectroscopy studies.* Molecular Catalysis, 2020. **482**: p. 110700.

[198]. Vesselli, E., L. De Rogatis, X. Ding, A. Baraldi, L. Savio, L. Vattuone, M. Rocca, P. Fornasiero, M. Peressi, A. Baldereschi, R. Rosei, and G. Comelli, *Carbon dioxide hydrogenation on Ni(110).* JOURNAL OF THE AMERICAN CHEMICAL SOCIETY, 2008. **130**(34): p. 11417-22.

[199]. Roiaz, M., E. Monachino, C. Dri, M. Greiner, A. Knop-Gericke, R. Schlogl, G. Comelli, and E. Vesselli, *Reverse Water-Gas Shift or Sabatier Methanation on Ni(110)? Stable Surface Species at Near-Ambient Pressure.* JOURNAL OF THE AMERICAN CHEMICAL SOCIETY, 2016. **138**(12): p. 4146-54.

[200]. Rolniak, P.D. and R.J.A.J. Kobayashi, *Adsorption of methane and several mixtures of methane and carbon dioxide at elevated pressures and near ambient temperatures on 5A and 13X molecular sieves by tracer perturbation chromatography.* 1980. **26**(4): p. 616-625.

[201]. Montanari, T., E. Finocchio, E. Salvatore, G. Garuti, A. Giordano, C. Pistarino, and G. Busca, *CO_2 separation and landfill biogas upgrading: A comparison of 4A and 13X zeolite adsorbents.* ENERGY, 2011. **36**(1): p. 314-319.

[202]. Wei, L., H. Grénman, W. Haije, N. Kumar, A. Aho, K. Eränen, L. Wei, and W. de Jong, *Sub-nanometer ceria-promoted Ni 13X zeolite catalyst for CO_2 methanation.* Applied Catalysis A: General, 2021. **612**: p. 118012.

[203]. Wang, A., J. Li, and T. Zhang, *Heterogeneous single-atom catalysis.* Nature Reviews Chemistry, 2018. **2**(6): p. 65-81.

[204]. Yang, T., R. Fukuda, S. Hosokawa, T. Tanaka, S. Sakaki, and M. Ehara, *A Theoretical Investigation on CO Oxidation by Single-Atom Catalysts M1/gamma-Al_2O_3 (M=Pd, Fe, Co, and Ni).* ChemCatChem, 2017. **9**(7): p. 1222-1229.

[205]. Liang, S., C. Hao, and Y. Shi, *The Power of Single-Atom Catalysis.* ChemCatChem, 2015. **7**(17): p. 2559-2567.

[206]. Rogge, S.M.J., A. Bavykina, J. Hajek, H. Garcia, A.I. Olivos-Suarez, A. Sepulveda-Escribano, A. Vimont, G. Clet, P. Bazin, F. Kapteijn, M. Daturi, E.V. Ramos-Fernandez, F.X.L.I. Xamena, V. Van Speybroeck, and J. Gascon, *Metal-organic and covalent organic frameworks as single-site catalysts.* CHEM SOC REV, 2017. **46**(11): p. 3134-3184.

[207]. Chen, L., T. Horiuchi, T. Osaki, and T. Mori, *Catalytic selective reduction of NO with propylene over Cu-Al_2O_3 catalysts: influence of catalyst preparation method.*

Applied Catalysis B-Environmental, 1999. **23**(4): p. 259-269.

[208]. Emeis, C.A., *Determination of Integrated Molar Extinction Coefficients for Infrared Absorption Bands of Pyridine Adsorbed on Solid Acid Catalysts.* J CATAL, 1993. **141**(2): p. 347-354.

[209]. Abate, S., K. Barbera, E. Giglio, F. Deorsola, S. Bensaid, S. Perathoner, R. Pirone, and G. Centi, *Synthesis, Characterization, and Activity Pattern of Ni–Al Hydrotalcite Catalysts in* CO_2 *Methanation.* IND ENG CHEM RES, 2016. **55**(30): p. 8299-8308.

[210]. Lensveld, D.J., J.G. Mesu, A.J. Van Dillen, and K.P. de Jong, *Synthesis and characterisation of MCM-41 supported nickel oxide catalysts.* MICROPOR MESOPOR MAT, 2001. **44**: p. 401-407.

[211]. Speight, J.G., *Lange's handbook of chemistry*. Vol. 1. 2005: McGraw-Hill New York.

[212]. Luengnaruemitchai, A. and A. Kaengsilalai, *Activity of different zeolite-supported Ni catalysts for methane reforming with carbon dioxide.* CHEM ENG J, 2008. **144**(1): p. 96-102.

[213]. Graça, I., L.V. González, M.C. Bacariza, A. Fernandes, C. Henriques, J.M. Lopes, and M.F. Ribeiro, CO_2 *hydrogenation into* CH_4 *on NiHNaUSY zeolites.* APPL CATAL B-ENVIRON, 2014. **147**(Supplement C): p. 101-110.

[214]. Laachir, A., V. Perrichon, A. Badri, J. Lamotte, E. Catherine, J.C. Lavalley, J. El Fallah, L. Hilaire, F. Le Normand, E. Quéméré, G.N. Sauvion, and O. Touret, *Reduction of* CeO_2 *by hydrogen. Magnetic susceptibility and Fourier-transform infrared, ultraviolet and X-ray photoelectron spectroscopy measurements.* J. Chem. Soc., Faraday Trans., 1991. **87**(10): p. 1601-1609.

[215]. Xavier, K.O., R. Sreekala, K.K.A. Rashid, K.K.M. Yusuff, and B. Sen, *Doping effects of cerium oxide on Ni/*Al_2O_3 *catalysts for methanation.* CATAL TODAY, 1999. **49**(1-3): p. 17-21.

[216]. Zimmer, P., A. Tschöpe, and R. Birringer, *Temperature-Programmed Reaction Spectroscopy of Ceria- and Cu/Ceria-Supported Oxide Catalyst.* J CATAL, 2002. **205**(2): p. 339-345.

[217]. Nie, W., X. Zou, X. Shang, X. Wang, W. Ding, and X. Lu, CeO_2 *-assisted Ni nanocatalysts supported on mesoporous* γ-Al_2O_3 *for the production of synthetic natural gas.* FUEL, 2017. **202**: p. 135-143.

[218]. Socrates, G., *Infrared and Raman characteristic group frequencies: tables and charts*. 2004: John Wiley & Sons.

[219]. Suarez-Toriello, V.A., C.E. Santolalla-Vargas, J.A. de los Reyes, A. Vazquez-Zavala, M. Vrinat, and C. Geantet, *Influence of the solution pH in impregnation with citric acid and activity of Ni/W/*Al_2O_3 *catalysts.* J MOL CATAL A-CHEM, 2015. **404**: p. 36-46.

[220]. Strathmann, T.J. and S.C.B. Myneni, *Speciation of aqueous Ni(II)-carboxylate and Ni(II)-fulvic acid solutions: Combined ATR-FTIR and XAFS analysis 1 1Associate editor: G. Sposito.* GEOCHIM COSMOCHIM AC, 2004. **68**(17): p. 3441-3458.

[221]. Ding, X., J. Ma, X. Zhou, X. Zhao, S. Hao, C. Deng, and G. Li, *Preparation of cerium dioxide microspheres by internal gelation with cerium citrate as precursor.* J SOL-GEL SCI TECHN, 2019. **90**(2): p. 296-304.

[222]. Jiang, Y.-F., C.-Z. Yuan, X. Xie, X. Zhou, N. Jiang, X. Wang, M. Imran, and A.-W. Xu, *A Novel Magnetically Recoverable Ni-*CeO_{2}*–x/Pd Nanocatalyst with Superior Catalytic Performance for Hydrogenation of Styrene and 4-Nitrophenol.* ACS APPL MATER INTER, 2017. **9**(11): p. 9756-9762.

[223]. Lv, M., J. Zhou, and Y. Zhang, *Synergistic catalysis between nano-Ni and nano semiconductor* CeO_2 *of Ni hybird nanostructured catalysts for high efficient selective hydrogenation.* CATAL SCI TECHNOL, 2019.

[224]. Wang, Y., Z. Chen, P. Han, Y. Du, Z. Gu, X. Xu, and G. Zheng, *Single-Atomic Cu with Multiple Oxygen Vacancies on Ceria for Electrocatalytic* CO_2 *Reduction to* CH_4*.* ACS CATAL, 2018. **8**(8): p. 71147119.

[225]. Arandiyan, H., Y. Wang, J. Scott, S. Mesgari, H. Dai, and R. Amal, *In Situ Exsolution of Bimetallic Rh–Ni Nanoalloys: a Highly Efficient Catalyst for* CO_2 *Methanation.* ACS APPL MATER INTER, 2018. **10**(19): p. 16352-16357.

[226]. Li, W., X. Nie, X. Jiang, A. Zhang, F. Ding, M. Liu, Z. Liu, X. Guo, and C. Song, ZrO_2 *support imparts superior activity and stability of Co catalysts for* CO_2 *methanation.* Applied Catalysis B-Environmental, 2018. **220**: p. 397-408.

[227]. Wang, F., S. He, H. Chen, B. Wang, L. Zheng, M. Wei, D.G. Evans, and X. Duan, *Active site dependent reaction mechanism over* Ru/CeO_2 *catalyst toward* CO_2 *methanation.* J AM CHEM SOC, 2016. **138**(19): p. 6298-6305.

[228]. Graciani, J., K. Mudiyanselage, F. Xu, A.E. Baber, J. Evans, S.D. Senanayake, D.J. Stacchiola, P. Liu, J. Hrbek, J. Fernandez Sanz, and J.A. Rodriguez, *Catalysis. Highly active copper-ceria and copper-ceria-titania catalysts for methanol synthesis from CO(2).* SCIENCE, 2014. **345**(6196): p. 546-50.

[229]. Lijun Wu, H.J.W., A. R. Moodenbaugh, R. F. Klie, Yimei Zhu, D. O. Welch, and M. Suenaga, *Oxidation state and lattice expansion of* CeO_2*-x nanoparticles as a function of particle size.* PHYSICAL REVIEW B, 2004. **69**: p. 125415(9).

[230]. Yu, K., N. Kumar, A. Aho, J. Roine, I. Heinmaa, D.Y. Murzin, and A. Ivaska, *Determination of acid sites in porous aluminosilicate solid catalysts for aqueous phase reactions using potentiometric titration method.* J CATAL, 2016. **335**: p. 117-124.

[231]. Benaliouche, F., Y. Boucheffa, P. Ayrault, S. Mignard, and P. Magnoux, NH_3*-TPD and FTIR spectroscopy of pyridine adsorption studies for characterization of Ag-and Cu-exchanged X zeolites.* MICROPOR MESOPOR MAT, 2008. **111**(1-3): p. 80-88.

[232]. Wang, C., Q. Liu, J. Song, W. Li, P. Li, R. Xu, H. Ma, and Z. Tian, *High quality diesel-range alkanes production via a single-step hydrotreatment of vegetable oil over Ni/zeolite catalyst.* CATALYSIS TODAY, 2014. **234**: p. 153-160.

[233]. Pan, Q., Peng, Jiaxi, Sun, Tianjun, Wang, Sheng, Wang, Shudong, *Insight into the reaction route of* CO_2 *methanation: Promotion effect of medium basic sites.* catcom.2013.10.034, 2014. **10**(34): p. 74-78.

[234]. Yan, Y., Y.H. Dai, H. He, Y.B. Yu, and Y.H. Yang, *A novel W-doped Ni-Mg mixed oxide catalyst for* CO_2 *methanation.* APPL CATAL B-ENVIRON, 2016. **196**: p. 108-116.

[235]. Strathmann, T.J. and S.C.B. Myneni, *Speciation of aqueous Ni(II)-carboxylate and Ni(II)-fulvic acid solutions: Combined ATR-FTIR and XAFS analysis.* GEOCHIMICA ET COSMOCHIMICA ACTA, 2004. **68**(17): p. 3441-3458.

[236]. Suárez-Toriello, V.A., C.E. Santolalla-Vargas, J.A. de los Reyes, A. Vázquez-Zavala, M. Vrinat, and C. Geantet, *Influence of the solution pH in impregnation with citric acid and activity of* $Ni/W/Al_2O_3$ *catalysts.* Journal of Molecular Catalysis A: Chemical, 2015. **404-405**: p. 36-46.

[237]. Wang, Y., Z. Chen, P. Han, Y. Du, Z. Gu, X. Xu, and G. Zheng, *Single-Atomic Cu with Multiple Oxygen Vacancies on Ceria for Electrocatalytic* CO_2 *Reduction to* CH_4*.* ACS Catalysis, 2018. **8**(8): p. 7113-7119.

[238]. Wei, L., H. Azad, W. Haije, H. Grénman, and W. de Jong, *Pure methane from* CO_2 *hydrogenation using a sorption enhanced process with catalyst/zeolite bifunctional materials.* Applied Catalysis B: Environmental, 2021. **297**: p. 120399.

[239]. Mebrahtu, C., F. Krebs, S. Abate, S. Perathoner, G. Centi, and R. Palkovits, CO_2 *Methanation: Principles and Challenges*, in *Horizons in Sustainable Industrial*

Chemistry and Catalysis, S. Albonetti, S. Perathoner, and E.A. Quadrelli, Editors. 2019, Elsevier. p. 85-103.

[240]. Duyar, M.S., M.A.A. Treviño, and R.J. Farrauto, *Dual function materials for CO_2 capture and conversion using renewable H_2*. Applied Catalysis B: Environmental, 2015. **168-169**: p. 370-376.

[241]. Ruiz, A.Z., D. Brhwiler, T. Ban, and G. Calzaferri, *Synthesis of Zeolite L. Tuning Size and Morphology*. Monatshefte fr Chemie - Chemical Monthly, 2005. **136**(1): p. 77-89.

[242]. Insuwan, W. and K.J.E.j. Rangsriwatananon, *Morphology-controlled synthesis of zeolite and physicochemical properties.* Engineering journal, 2012. **16**(3): p. 1-12.

[243]. Azad, M.H., *Sorption enhanced Methanation of Carbon Dioxide: Experimental research of nickel modified zeolites for sorption enhanced CO_2 methanation*, in *Process and Energy*. 2020, Delft University of Technology.

[244]. Qasem, N.A.A. and R. Ben-Mansour, *Adsorption breakthrough and cycling stability of carbon dioxide separation from $CO_2/N_2/H_2O$ mixture under ambient conditions using 13X and Mg-MOF-74.* APPLIED ENERGY, 2018. **230**: p. 1093-1107.

[245]. Hu, X., L. Liu, X. Luo, G. Xiao, E. Shiko, R. Zhang, X. Fan, Y. Zhou, Y. Liu, Z. Zeng, and C.e. Li, *A review of N-functionalized solid adsorbents for post-combustion CO_2 capture.* APPLIED ENERGY, 2020. **260**: p. 114244.

[246]. Rodrigues, A.E., Y.-j. Wu, L.M. Madeira, and R. Faria, *Sorption enhanced reaction processes*. Vol. 1. 2017: World Scientific.

[247]. Bacariza, M.C., I. Graça, A. Westermann, M.F. Ribeiro, J.M. Lopes, and C. Henriques, *CO_2 Hydrogenation Over Ni-Based Zeolites: Effect of Catalysts Preparation and Pre-reduction Conditions on Methanation Performance.* TOPICS IN CATALYSIS, 2015. **59**(2-4): p. 314-325.

[248]. Kapteijn, F. and J.A. Moulijn, *Handbook of heterogeneous catalysis, Chap.9.1 Laboratory Catalytic Reactors: Aspects of Catalyst Testing*. 1997: Wiley.

[249]. Koschany, F., D. Schlereth, and O. Hinrichsen, *On the kinetics of the methanation of carbon dioxide on coprecipitated NiAl(O).* Applied Catalysis B: Environmental, 2016. **181**: p. 504-516.

[250]. Vidal Vázquez, F., J. Kihlman, A. Mylvaganam, P. Simell, M.-L. Koskinen-Soivi, and V. Alopaeus, *Modeling of nickel-based hydrotalcite catalyst coated on heat exchanger reactors for CO_2 methanation.* CHEMICAL ENGINEERING JOURNAL, 2018. **349**: p. 694-707.

[251]. Boon, J., E. van Dijk, Ö. Pirgon-Galin, W. Haije, and R. van den Brink, *Water–gas shift kinetics over FeCr-based catalyst: effect of hydrogen sulphide.* CATALYSIS LETTERS, 2009. **131**(3-4): p. 406-412.

[252]. Zhang, Z., Y. Tian, L. Zhang, S. Hu, J. Xiang, Y. Wang, L. Xu, Q. Liu, S. Zhang, and X. Hu, *Impacts of nickel loading on properties, catalytic behaviors of Ni/γ–Al_2O_3 catalysts and the reaction intermediates formed in methanation of CO_2.* INTERNATIONAL JOURNAL OF HYDROGEN ENERGY, 2019. **44**(18): p. 9291-9306.

[253]. Chuah, G.K., S. Jaenicke, and T.H. Xu, *The effect of digestion on the surface area and porosity of alumina.* MICROPOROUS AND MESOPOROUS MATERIALS, 2000. **37**(3): p. 345-353.

[254]. Galhotra, P., J.G. Navea, S.C. Larsen, V.H.J.E. Grassian, and E. Science, *Carbon dioxide (C16O2 and C18O2) adsorption in zeolite Y materials: effect of cation, adsorbed water and particle size.* 2009. **2**(4): p. 401-409.

[255]. Choong, C.K.S., L. Huang, Z. Zhong, J. Lin, L. Hong, and L. Chen, *Effect of calcium addition on catalytic ethanol steam reforming of Ni/Al_2O_3: II. Acidity/basicity, water*

adsorption and catalytic activity. Applied Catalysis A: General, 2011. **407**(1-2): p. 155-162.

[256]. Daza, Y.A. and J.N. Kuhn, *CO_2 conversion by reverse water gas shift catalysis: comparison of catalysts, mechanisms and their consequences for CO_2 conversion to liquid fuels.* RSC Advances, 2016. **6**(55): p. 49675-49691.

[257]. Kattel, S., P. Liu, and J.G. Chen, *Tuning Selectivity of CO_2 Hydrogenation Reactions at the Metal/Oxide Interface.* JOURNAL OF THE AMERICAN CHEMICAL SOCIETY, 2017. **139**(29): p. 9739-9754.

[258]. Andersson, M.P., F. Abild-Pedersen, I.N. Remediakis, T. Bligaard, G. Jones, J. Engbæk, O. Lytken, S. Horch, J.H. Nielsen, and J. Sehested, *Structure sensitivity of the methanation reaction: H_2-induced CO dissociation on nickel surfaces.* JOURNAL OF CATALYSIS, 2008. **255**(1): p. 6-19.

[259]. Granitsiotis, G., *Methanation of Carbon Dioxide: Experimental research of separation enhanced methanation of CO_2*, in *Process and Energy*. 2017, Delft University of Technology.

[260]. Gierman, H., *Design of laboratory hydrotreating reactors.* Applied Catalysis, 1988. **43**(2): p. 277-286.

[261]. Cussler, E.L. and E.L. Cussler, *Diffusion: mass transfer in fluid systems*. 2009: Cambridge university press.

[262]. Chu, C. and K. Ng, *Flow in packed tubes with a small tube to particle diameter ratio.* AICHE JOURNAL, 1989. **35**(1): p. 148-158.

[263]. Ergun, S., *Fluid flow through packed columns.* CHEMICAL ENGINEERING PROGRESS, 1952. **48**: p. 89-94.

[264]. Dixon, A.G., *Correlations for wall and particle shape effects on fixed bed bulk voidage.* The Canadian Journal of Chemical Engineering, 1988. **66**(5): p. 705-708.